

**NON-DESTRUCTIVE ELECTRICAL CHARACTERIZATION OF
CONTROLLED WASPALLOY MICROSTRUCTURES**

A Dissertation
Presented to
The Academic Faculty

by

V. Siva Kumar G. Kelekanjeri

In Partial Fulfillment
of the Requirements for the Degree
Doctor of Philosophy in the
School of Materials Science and Engineering

Georgia Institute of Technology
May 2007

**NON-DESTRUCTIVE ELECTRICAL CHARACTERIZATION OF
CONTROLLED WASPALOY MICROSTRUCTURES**

Approved by:

Dr. Rosario A. Gerhardt, Advisor
School of Materials Science and
Engineering
Georgia Institute of Technology

Dr. Thomas H. Sanders, Jr.
School of Materials Science and
Engineering
Georgia Institute of Technology

Dr. Stephen Antolovich
School of Materials Science and
Engineering
Georgia Institute of Technology

Dr. Arun M. Gokhake
School of Materials Science and
Engineering
Georgia Institute of Technology

Dr. Laurence J. Jacobs
School of Materials Science and
Engineering
Georgia Institute of Technology

Date Approved: April 2nd, 2007

ACKNOWLEDGEMENTS

I would like to express my appreciation for Dr. Rosario A. Gerhardt for her advice, guidance and unstinted support during the course of this dissertation. Working with Dr. Gerhardt, I had the flexibility and freedom to explore the project from very diverse viewpoints. I would like to thank her especially for the extensive time investment on a very regular and consistent basis to facilitate the progress of my research. I would like to acknowledge the funding for this research from the United States Department of Energy under grant DE-FG02-03-ER46035. I am thankful to the committee members- Dr. Tom Sanders, Dr. Arun Gokhale, Dr. Steve Antolovich and Dr. Larry Jacobs for their readiness to serve on the committee. I would like to acknowledge Dr. Runqing Ou for his help with the experimental set up of *ac* impedance and *dc* resistivity measurements. Special thanks to Lewis Moss, who tirelessly worked on preparing the specimens for small angle scattering work, but for whom, the USAXS analysis would not be an integral part of this dissertation. I appreciate the assistance provided by Dr. Y. Y. Su with regards to electrochemical etching experiments for highlighting the microstructure of Waspaloy. I would like to thank David Maybury for taking time out of his work schedule to teach me the basics and operation of the AFM. Thanks to the EM Center staff- Yolande Berta and Todd Walters for help and advice with the SEM on several occasions. I would like to acknowledge the helpful discussions and advice provided by Dr. Siva Gurrum and COMSOL staff on analytical and FE modeling of electrical measurements. I appreciate the help from Dr. Tom Sanders for taking time out of his busy schedule to provide a feedback on the analysis of coarsening data. I am thankful to Dr. Steve Antolovich for his

valuable suggestions, that helped me gain a better understanding of solution-treated microstructures.

Finally, I would like to express my gratitude to family and friends for being there when I needed them the most.

TABLE OF CONTENTS

	Page
ACKNOWLEDGEMENTS	iii
LIST OF TABLES	ix
LIST OF FIGURES	x
SUMMARY	xv
<u>CHAPTER</u>	
1 INTRODUCTION	1
2 LITERATURE SURVEY	5
2.1 NDE techniques for probing the microstructure of metallic systems	5
2.1.1 NDE using electrical methods	5
2.1.2 NDE using acoustic techniques	9
2.1.3 NDE using scattering techniques	10
2.2 Literature survey on coarsening	13
2.2.1 Coarsening theory	13
2.2.2 Temporal change of other microstructural parameters during coarsening	19
2.2.3 Specific applications of coarsening theory to nickel-base superalloys	21
3 EXPERIMENTAL PROCEDURE	26
3.1 Heat-treatments	26
3.2 Metallography	29
3.3 Microscopy and X-ray diffraction	33
3.4 Ultra Small Angle X-ray Scattering	34

3.5 DC four-point probe resistivity	35
3.5.1 Calculation of specimen resistivity	39
3.5.2 Calculation of standard deviation in ρ	40
3.6 AC impedance measurements	40
4 RESULTS AND DISCUSSION OF HEAT-TREATMENT EXPERIMENTS	47
4.1 Microstructural evolution in Set I experiments	47
4.1.1 Characterization results	47
4.1.2 Analysis and discussion	64
4.1.3 Conclusions	86
4.2 Microstructural evolution in Set III experiments	88
4.2.1 Characterization results	88
4.2.2 Discussion	102
4.2.3 Conclusions	110
5 MODELING AC AND DC ELECTRICAL MEASUREMENTS	113
5.1 Analytical treatment of two-probe impedance measurement	114
5.1.1 Introduction	114
5.1.2 Problem description	115
5.1.3 Analytical approach	117
5.1.3.1 Formulation and generic solution	117
5.1.3.2 Boundary conditions	119
5.1.3.3 Determination of coefficients and constants	120
5.1.3.3.1 Symmetry and anti-symmetry conditions	121
5.1.3.3.2 Validation of 1D solution for $f(r)$	122
5.1.3.4 Semi-infinite solution	126
5.1.4 Finite element approach	127

5.1.5	Simulation results and discussion	129
5.1.5.1	Electric field profiles	129
5.1.5.2	Geometric effects on field distribution	133
5.1.5.3	Limiting thickness analysis	137
5.1.6	Calculation of specimen impedance for a two-probe	141
5.1.7	Conclusions	147
5.2	Determination of correction factors for a DC four-point probe measurement	148
5.2.1	Introduction	148
5.2.2	Problem formulation	152
5.2.3	Analytical approach	154
5.2.3.1	Closed-form solution	154
5.2.3.2	Determination of a convergent solution	159
5.2.4	Finite element approach	160
5.2.5	Analytical approximation to geometric correction factors	162
5.2.6	Results and discussion	167
5.2.7	Conclusions	176
5.3	Calculation of specimen impedance for AC four-point probe measurements	178
5.3.1	Measurements on wire specimens	178
5.3.2	Measurements on cylindrical disk specimens	179
6	AC ELECTRICAL MEASUREMENTS ON CONDUCTING SPECIMENS	184
6.1	AC two-probe impedance on cylindrical disk specimens	184
6.2	AC four-point probe impedance on wire specimens	188
6.3	AC four-point probe impedance on cylindrical disk specimens	192
6.4	Conclusions	196

7	AFM-BASED LOCALIZED ELECTRICAL CHARACTERIZATION	198
7.1	Description of measurement techniques	198
7.2	Results and discussion	203
7.3	Conclusions	218
8	CONCLUSIONS AND FUTURE WORK	220
8.1	Conclusions	220
8.2	Future work	222
	APPENDIX A: INTEGRALS AND IDENTITIES	224
	APPENDIX B: NOMENCLATURE USED IN MODELING CHAPTER	227
	APPENDIX C: MATLAB CODE IMPLEMENTATION IN ANALYTICAL MODELS	229
	REFERENCES	254
	VITA	259

LIST OF TABLES

	Page
Table 3.1: Composition of primary constituents in as-received Waspaloy	27
Table 3.2: List of specimens categorized under Set I heat-treatments	30
Table 3.3: List of specimens categorized under Set II heat-treatments	31
Table 3.4 List of specimens categorized under Set III heat-treatments	32
Table 4.1: Four-probe resistivity of solution-treated and vacancy stabilized specimens	52
Table 4.2: List of k_I , D and f_e for specimens aged at 800°C with the three different pre-solution-treatments	81
Table 4.3: Computations of γ - γ' lattice misfit for selected specimens in the three aging sets	100
Table 4.4: Calculations of elastic moduli for directions in $\langle 200 \rangle$ or $\langle 111 \rangle$ oriented grains	104
Table 7.1: List of specimens with the specific surface finish and the corresponding measurement parameters for EFM experiments	205
Table 7.2: List of specimens with the specific surface finish and the corresponding measurement parameters for SKPM experiments	208
Table 7.3: List of specimens with the specific surface finish and the corresponding measurement parameters for I-AFM experiments	214

LIST OF FIGURES

	Page
Figure 2.1: Anomalous-USAXS spectra at different energies near Ni-K edge for Waspaloy aged at 649°C for 50 hours	12
Figure 2.2: Binary phase diagram of a precipitation hardening system	14
Figure 2.3: Free energy vs composition diagram to illustrate the chemical potential difference	14
Figure 2.4: Schematic illustrating the transfer of flux from a smaller precipitate of radius, r_1 to a larger one of radius r_2	17
Figure 3.1: Schematic showing the basic principle of a four-point probe measurement	37
Figure 3.2: Illustration showing the underlying principle of a delta measurement	38
Figure 3.3: Schematic illustrating a four-point probe <i>ac</i> measurement on a wire specimen	42
Figure 3.4: Schematic illustrating a four-point probe <i>ac</i> measurement on a cylindrical disk Waspaloy specimen	45
Figure 4.1: Representative optical micrographs of grain structures solution-treated at 1045°C-(a), 1090°C-(b) and 1145°C-(c)	48-49
Figure 4.2: SEM micrographs of as-solution-treated and subsequently stabilized microstructures	50
Figure 4.3: Plot showing the variation of the lattice parameter of the matrix (γ) phase with solution-treatment temperature	51
Figure 4.4: Plot showing the DC four-point probe resistivity as a function of treatment temperature	52
Figure 4.5: SEM micrographs showing microstructural evolution upon aging at 800°C after a prior solution-treatment at 1045°C	55-56
Figure 4.6: SEM micrographs showing microstructural evolution upon aging at 800°C after a prior solution-treatment at 1090°C	56-58
Figure 4.7: SEM micrographs showing microstructural evolution upon aging at 800°C after a prior solution-treatment at 1145°C	58-59
Figure 4.8: Plot of the DC four-point probe resistivity versus logarithm of the	

aging time	60
Figure 4.9: Plot of normalized USAXS intensity versus the wave vector for specimens solution-treated at 1045°C	62
Figure 4.10: Plot of normalized USAXS intensity versus the wave vector for specimens solution-treated at 1090°C	62
Figure 4.11: Plot of normalized USAXS intensity versus the wave vector for specimens solution-treated at 1145°C	63
Figure 4.12: Plot of the mean γ' precipitate radius as a function of the aging time	67
Figure 4.13: Plot of the γ' precipitate density as a function of the aging time	70
Figure 4.14: Plot of the fraction of precipitates below the mean radius as a function of the aging time	71
Figure 4.15: Plot of the cube of mean γ' precipitate radius as a function of the aging time	73
Figure 4.16: Comparison between the size distribution of γ' precipitates	74
Figure 4.17: Evolution of the particle size distributions with aging time for sets of specimens pre-solution-treated at 1045°C and 1090°C and 1145°C	77-78
Figure 4.18: Plot of the volume fraction of the γ' precipitates as a function of $\frac{I}{\langle r \rangle}$	79
Figure 4.19: Plot of the residual resistivity- $\rho_{stab} - \rho_{\gamma}(t)$ versus $t^{\frac{1}{3}}$	85
Figure 4.20: Solution-treated microstructures (at 1145°C) showing polygonal etch	89
Figure 4.21: SEM micrographs showing microstructural evolution upon aging at 725°C	90-91
Figure 4.22: SEM and AFM micrographs of specimens at 1, 2 and 10 hrs of aging at 725°C	92-94
Figure 4.23: SEM micrographs showing microstructural evolution upon aging at 800°C	96-97
Figure 4.24: SEM micrographs showing microstructural evolution upon aging	

at 875°C	97-99
Figure 4.25: Plot showing the variations in the lattice parameter of the matrix (γ)	100
Figure 4.26: Plot of the DC four-point probe resistivity as a function of the aging	102
Figure 4.27: Illustrations showing (a) square shaped etch-pits in [200] oriented grains and (b) hexagon shaped pits in [111] oriented grains	104
Figure 5.1: Schematic illustrating the measurement geometry comprising of the specimen with coaxially placed electrodes	116
Figure 5.2: Illustration of the problem geometry (r - z cross-section) detailing the various sub-domains and boundaries as modeled in FEMLAB	128
Figure 5.3: Plots showing the axial field profiles- $E_z(r, z)$	131
Figure 5.4: Plots showing the radial field profiles- $E_r(r, z)$	132
Figure 5.5: Plots showing the skin-effect field $E_z(r, z) \Big _{(r_c, \frac{t_o}{2})}$ as a function of specimen thickness- t_o	134
Figure 5.6: Plot showing the constriction field $E_z(r, z) \Big _{(r_c, \frac{t_o}{6})}$ versus t_o	136
Figure 5.7: Plots showing the axial field at 1MHz as a function of r	139
Figure 5.8: Plot of the frequency dependent resistance computed from both analytical (open symbols) and finite element models (solid line)	144
Figure 5.9: Plot of the frequency dependent inductance from both analytical (open symbols) and finite element models (solid line)	144
Figure 5.10: Plot showing the magnetic field- $H_\phi(r, z)$ versus r_o	146
Figure 5.11: Plot of the complex impedance magnitude versus frequency from both analytical (open symbols) and finite element models (solid line)	146
Figure 5.12: Schematic showing the placement of four probes at random locations- $(r_i, \theta_i, 0)$ on the circular face-A of a specimen	152
Figure 5.13: Schematic showing the top view of a cylindrical specimen - PNR arrangement	164

Figure 5.14: Schematic showing the top view of a cylindrical specimen - PAR arrangement	164
Figure 5.15: Plots showing the comparison between geometric correction factors obtained via the closed-form, COMSOL and analytical approximation solutions as a function of specimen thickness	168
Figure 5.16: Plots showing the comparison between geometric correction factors obtained via the closed-form, COMSOL and analytical approximation solutions as a function of specimen radius	171
Figure 5.17: Plots showing the geometric factor (CF solution) variations as a function of specimen thickness	173
Figure 5.18: Plots showing the geometric factor (CF solution) variations as a function of specimen radius	175
Figure 5.19: Schematic showing the arrangement of current probes (at $\pm s$) and voltage probes (at $\pm s/2$) on the circular face of a cylindrical specimen	182
Figure 6.1: Plots of experimentally measured resistance- (a) and reactance- (b) as a function of the frequency of a cylindrical Waspaloy disk specimen	185
Figure 6.2: Plots of computed resistance- (a) and reactance- (b) as a function of the frequency of a cylindrical Waspaloy disk specimen	186
Figure 6.3: Plot of the resistance versus frequency showing the measured (open symbols) and the computed profiles (solid line) for wires	189
Figure 6.4: Plot of the inductance versus frequency showing the measured (open symbols) and the computed profiles (solid line) for wires	189
Figure 6.5: Surface plots of the axial electric field- E_z at various frequencies	190
Figure 6.6: Surface plots of the axial normalized magnetic field- H_{norm} at various Frequencies	191
Figure 6.7: Plot of the resistance versus frequency showing the as-measured, short- corrected and computed profiles of a cylindrical Waspaloy specimen	193
Figure 6.8: Plot of the reactance versus frequency showing the as-measured, short- corrected and computed profiles of a cylindrical Waspaloy specimen	194
Figure 6.9: Plot of the absolute value of the impedance as a function of the frequency showing the effect of thickness variations	195

Figure 7.1: Schematic showing the experimental set-up of an EFM/SKPM	199
Figure 7.2: Schematic showing the experimental set-up of an I-AFM	202
Figure 7.3: AFM micrographs of IIIDS-875-75 specimen with a preferential γ'	204
Figure 7.4: AFM micrographs of IBS-800-100 specimen with a preferential γ etch	204
Figure 7.5: AFM micrographs of IID-875-100 specimen in the as-polished	205
Figure 7.6: AFM micrographs of IID-725-5 specimen with a preferential γ' etch showing etch-pit contrast	207
Figure 7.7: Schematic illustrating the topography dependent non-linear tip-surface interaction during EFM/SKPM measurement	209
Figure 7.8: AFM micrographs of IBS-800-100 specimen with a preferential γ etch	211
Figure 7.9: AFM micrographs of IIIDS-875-100specimen in the as-polished	211
Figure 7.10: AFM micrographs of IIIDS-875-75specimen with a preferential γ'	212
Figure 7.11: AFM micrographs of IID-725-5 specimen with a preferential γ' etch showing etch-pit contrast	213
Figure 7.12: AFM micrographs of IID-725-5 specimen with a preferential γ' etch showing etch-pit contrast	215
Figure 7.13 AFM micrographs of IIIDS-875-75 specimen with a preferential γ'	215
Figure 7.14 AFM micrographs of IID-875-100 specimen with a preferential γ etch	216
Figure 7.15 AFM micrographs of IID-875-100 specimen in the as-polished	217

SUMMARY

In this research, controlled Waspaloy microstructures are produced with the objective of studying microstructural evolution in this alloy via non-destructive electrical measurements. Waspaloy is a precipitation-hardenable γ - γ' nickel-base superalloy that is used in turbine blade applications demanding superior strength retention capabilities at elevated temperatures. Overall, three different sets of microstructures were produced that varied systematically as a function of the matrix (γ) grain size and γ' precipitate size distribution or just the latter. Initial solutionizing treatments conducted at 1045°C, 1090°C and 1145°C resulted in average γ grain size of 13, 52 and 89 μm respectively. A vacancy stabilization treatment at 1045°C followed the solutionizing treatments in Set I experiments, after which the specimens were aged at 800°C for durations ranging from 0.1 hrs to 100 hrs. In Sets II and III, the matrix grain size was kept unchanged by an initial solution-treatment at 1145°C. The stabilization treatment at 1045°C was only conducted in Set II after the solution-treatment. Aging experiments were then conducted at 700°C (or 725°C in Set III), 800°C and 875°C to study the growth kinetics of γ' precipitate distribution. The specimens with controlled microstructures were investigated using scanning electron microscopy (SEM), atomic force microscopy (AFM), x-ray diffraction (XRD), ultra small-angle x-ray scattering (USAXS) and *dc* four-point probe resistivity. The applicability of two and four-probe *ac* impedance techniques was also investigated.

Characterization of Heat-treated Specimens

Solution-treated SEM microstructures showed the presence of polygonal etch-pit shapes, which was proposed to be due to the condensation of excess quenched-in vacancies along crystallographically soft-directions in the γ phase. The etch-pits evolved upon subsequent aging into progressively irregular shapes, concurrent with γ' growth inside the pits. SEM and USAXS observations clearly supported the progressive coarsening of the γ' distribution with increasing aging time at 800°C. Complementary evidence from *dc* resistivity measurements confirmed that γ' nucleation was complete by 0.1 hrs of aging at 800°C. Coarsening studies indicated an LSW type volume diffusion mechanism of coarsening in Waspaloy, with an average coarsening rate constant of 3.25×10^{-29} [m³/sec] for Set I specimens aged at 800°C. This is an order of magnitude smaller compared to values quoted in the literature for binary Ni-Al systems. The resistivity decrease during initial stages of γ' coarsening was attributed to the progressive decrease in the 'scattering power' of the γ' distribution. The variations in the later stages were related to compositional changes during coarsening. Resistivity variations as a function of the aging time at 800°C did not show any dependence on the prior solution-treatment temperature in Set I specimens. Resistivity measurements also showed a drastic shortening in the first-stage coarsening with increase in the aging temperature from 725°C to 800°C, while this stage was completely absent at 875°C. In Set III specimens, the γ - γ' lattice misfit was found to increase with increasing aging duration at the same temperature or with increasing kinetics.

Modeling Electrical Measurements

Closed-form analytical derivation of the electric field distribution inside a metallic cylindrical disk specimen was conducted for an ideal two-probe impedance measurement. The closed-form solutions for the axial and radial electric fields accounted for both skin-effect and constriction effect and were expressed in terms of Bessel functions. A finite-element solution to the same problem was obtained using FEMLAB 3.1 to validate the closed-form solution and the solutions showed excellent match with each other. The constriction effect was dominant near the electrode contacts and decayed with distance away from the contacts both in terms of r and z . The skin-effect was predominant at high frequencies (10^4 Hz to 10^6 Hz) near the end regions of the disk (large r). The frequency dependent resistance and inductance of a typical Waspaloy disk specimen computed using the closed-form electric field solution, remained invariant up to 100 kHz. With further rise in frequency, the inductance decreased progressively due to a in the magnetic energy storage. The resistance however increased progressively due to an increase in the overall Joule heat-loss.

Geometrical correction factors for *dc* four-point probe resistivity measurements on cylindrical specimens using a collinear probe array were computed based on an analytical derivation of the potential distribution inside the specimen. The correction factors computed using the derived closed-form solution were in good agreement with those determined from COMSOL finite element simulations. Additionally, the factors from the closed-form and COMSOL solutions lied within the bounds predicted by approximate analytical correction factors available in the literature.

Micro Electrical Characterization

AFM-based localized electrical examination of sub-grain Waspaloy microstructures was successfully conducted using electrostatic force microscopy (EFM), scanning Kelvin probe microscopy (SKPM) and current-AFM (I-AFM) electrical modes. I-AFM experiments revealed that the conductivity of the γ' phase was lower than that of the γ phase. γ - γ' contrast and etch-pit contrast were clearly observed in EFM and SKPM experiments using two different etchants that led to opposite γ - γ' topographic contrasts. However, the tip-surface interaction in both EFM and SKPM is non-linear owing to the inhomogeneous surface topography and the surface potential distribution.

CHAPTER 1

INTRODUCTION

Nickel-base superalloys are an important class of high-temperature materials and find their use in land and air-based turbine engine components¹. The important properties of superalloys that make them suitable for such applications are good strength-retention at high temperatures, creep-resistance, hot-corrosion resistance, low-temperature ductility etc. The strength-retention ability of superalloys is primarily attributed to the presence of nanometer-sized γ' precipitates that reinforce the matrix phase via precipitation hardening². The matrix is a nickel-rich austenitic phase that contributes to solid-solution hardening in combination with elements like Cr, Co, Mo etc¹. The addition of carbon to the alloy composition is to promote the formation of carbides along grain boundaries, which enhance the creep resistance of the alloy. In addition to these phases, topologically close-packed phases such as σ , δ and Laves may form during processing, all of which are considered undesirable¹.

The microstructure of these alloys is known to change in service after several thousand hours at high homologous temperatures. As an example, coarsening of γ' precipitates can result in Waspaloy that can impair the strength-retention properties of the alloy³. In the case of directionally-solidified alloys, coarsening of γ' precipitates renders the blade material vulnerable to creep damage⁴. It is therefore important to make the connection between microstructural variations and related changes in mechanical properties. Conventional microscopy techniques are indispensable in furnishing detailed structure and composition-related information at different length scales. However, they

are destructive and in addition, a time-consuming means of arriving at the average statistical representation of the microstructure and not ideal for fast characterization.

Non-destructive evaluation (NDE) techniques provide an alternative and a complementary approach to microscopy for carrying out fast-throughput routine characterization of materials. The majority of NDE techniques may be classified into one of the following categories- (a) scattering methods, (b) acoustic methods and (c) electrical-based techniques. Applications of specific techniques from each of these categories, which are relevant to superalloys are discussed in the literature survey chapter. At a general level, NDE techniques may be sensitive to different attributes of the microstructure such as impurities, second phase particles, grain boundaries, as well as defects such as vacancies and dislocations, surface roughness, etc. The application of two or more NDE techniques may yield complementary information as one technique tends to be more sensitive to a particular microstructural heterogeneity than others. The sensitivity of a given technique to a defect or heterogeneity is primarily dependent on the wavelength of the probing signal in relation to the size of the features. Additionally, the information depth or volume of the specimen that is sampled by the probing signal may also vary from one technique to another. It is therefore desirable to use more than one technique for the study of a given material system to obtain a comprehensive understanding of the structure of the specimen. Once the groundwork is conducted, where correlations between the NDE parameter(s) and the microstructure are developed, the technique may then be used for a routine analysis.

In this research, Waspaloy, a precipitation-hardenable nickel-base superalloy, was chosen as the baseline material to produce systematically varying controlled

microstructures via suitably designed heat-treatments. The microstructures were controlled in terms of the matrix (γ) grain size and the precipitate size distribution. In all, three different sets of microstructures were produced according to the following scheme- Set I with three different grain sizes of the matrix, but identical γ' distributions (at a specific aging time) obtained by aging at 800°C for times up to 100 hrs and Sets II and III with a fixed matrix grain size, but different γ' distributions (at a specific aging time) obtained by aging at 700°C (or 725°C in Set III), 800°C and 875°C. A detailed description of the heat-treatments pertinent to the different sets is given in section 3.1. The motivation for this research was to be able to develop correlations between microstructural studies and non-destructive electrical measurements of the systematically varying specimens for reasons explained in the preceding paragraphs. Structural analysis of the specimens was conducted at different length scales using light microscopy, scanning electron microscopy (SEM) and atomic force microscopy (AFM). The four-point *dc* resistivity technique was the primary macro electrical characterization tool used for analyzing the resistivity variations among the specimens. Besides, the *dc* resistivity technique, the feasibility of two-probe and four-probe *ac* impedance techniques was also investigated. In addition to electrically based techniques, scattering techniques such as Ultra Small Angle X-ray Scattering (USAXS) and X-ray diffraction (XRD) were used for statistical quantification of microstructure and lattice parameter studies respectively. The results of characterization experiments of heat-treated specimens are described in detail in Chapter 4.

Analytical and finite-element models (FEM) of both *dc* and *ac* macro electrical measurements (Chapter 5) were developed to gain a better understanding of the measured

electrical response from the specimens. A closed-form (CF) analytical solution for the electric field distribution inside a cylindrical metallic specimen was derived for the case of an ideal two-probe impedance measurement. This was subsequently used for computing the overall specimen complex impedance. The *dc* model deals with the derivation for a CF geometric correction factor for a *dc* four-point probe resistivity measurement of a finitely thick cylindrical conducting specimen. A brief procedure is also given for computing the four-probe *ac* impedance of a cylindrical disk metallic specimen using a closed-form analytical solution available in the literature.

The results from investigations of two-probe and four-probe *ac* impedance measurements and associated comparison with computed spectra are given in Chapter 6.

Finally, electrical characterization of heat-treated Waspaloy microstructures on a microscale (Chapter 7) was conducted using AFM-based techniques, with the objective of studying the electrical properties of the constituent phases at least qualitatively. Specifically, γ - γ' electrical contrast was investigated using electrostatic force microscopy (EFM), surface potential microscopy (SPM) and current-atomic force microscopy (I-AFM).

CHAPTER 2

LITERATURE SURVEY

2.1 NDE techniques for probing the microstructure of metallic systems

The majority of the non-destructive probing techniques can be categorized into one of the following classes – (1) electrical techniques, (2) acoustic techniques and (3) scattering techniques. In this subsection, examples of these techniques used by various researchers for conducting microstructural investigations or understanding material related properties in metallic alloys will be reported. This review is not intended to be a comprehensive survey of the broad spectrum of NDE techniques available, but rather provides a short summary of the available NDE techniques used to characterize metallic materials.

2.1.1 NDE using electrical methods

The use of electrical methods for non-destructive characterization relies on the ability of the defects or a dispersed phase to impede the propagation of the probing signal. Electrical resistivity measurements have been widely used for studying microstructural evolution in precipitation-hardenable systems over several decades. Frequency-based techniques such as eddy current method have the potential for mapping sub-surface residual stress in metallic materials. Some examples of the application of these techniques are given below.

Pre-aging studies of Al-Zn-Mg-Cu based alloy systems were conducted by Ferragut et al⁵. using electrical resistivity and synchrotron-radiation small angle x-ray scattering (SR-SAXS), to investigate the decomposition kinetics and mechanisms of

solute migration in the formation of pre-precipitates. The resistivity changes during pre-aging were mainly related to the volume fraction growth of GP zones or pre-precipitate solute clusters, which were described using the Johnson-Mehl-Avrami (JMA) type equation⁶. A good correlation between the changes tracked via resistivity and SR-SAXS measurements was found to exist for one specific case⁵.

Panseri et al.⁷ conducted extensive investigations of the effect of quenching and aging temperatures on the pre-precipitation in Al-10%Zn by resistivity measurements. They report significant amounts of clustering of solute atoms during quenching itself and the rate of pre-precipitation during aging to increase with the quenching temperature. The rate of pre-precipitation was found to depend on the excess number of quenched-in vacancies, which stopped when all the vacancies were eliminated. The variation of the maximum increase in resistivity as a function of aging temperature was attributed to the number of solute cluster-zones that formed. An equilibrium number of zones was indicated to exist for each aging temperature and the lower the aging temperature, the higher the number of zones that formed⁷.

White et al.⁸ conducted kinetic studies of γ' nucleation-growth and coarsening in Nimonic PE16 alloy in the temperature range of 580°C to 780°C using electrical resistivity and electron microscopy studies. The experimentally observed resistivity was found to increase upon progressive aging to a maximum and then decrease monotonically, characteristic of sequential nucleation-growth and coarsening stages respectively. The overall resistivity was modeled as the sum of the following individual resistivity components using Matthiessen's rule⁹- matrix- ρ_m , impurities in solution-

$\rho_i \left(\frac{n_i}{n_o} \right)$, impurities present as small clusters- $\rho_s \left(\frac{n_s}{n_o} \right)$ and impurities present as large clusters- $\rho_l \left(\frac{n_l}{n_o} \right)$. The quantities- n_i , n_s , n_l and n_o were designated as the fraction of impurity atoms present in solution, small clusters, large clusters and the total number of atoms respectively. The parameters- n_i , n_s and n_l were obtained as solutions to first-order kinetic differential equations which described the nucleation-growth and growth-coarsening reactions. The values of ρ_s and ρ_l determined from the model were found to go through a maximum as a function of the temperature. This behavior was reasoned as due to the variation in the fraction of (Ni+Al+Ti) atoms that are able to form the precipitate phase due to changes in solubility with temperature. The activation energies for the nucleation-growth and coarsening regimes were reported to be 1.11 eV and 1.83 eV respectively⁸.

Dorward¹⁰ studied the over aging kinetics in Al-Zn-Mg-Cu alloy 7050 at 157-182°C for times up to 3000 hrs using electrical resistivity as one of the characterization techniques. The measured resistivity was found to show a linear behavior with $t^{-1/3}$ with increasing aging time- t , analogous to the solute concentration in the matrix (as derived by Ardell¹¹). The changes in the solute concentration of the matrix phase arise due to particle curvature effects, that is described by the Gibbs-Thomson equation^{6, 12}. This is detailed in the next section (2.2) on the literature survey of coarsening kinetics. The important conclusion of this study was that in the overaged state, the changes in resistivity were no longer due to scattering of conduction electrons by the precipitate

distribution, but were in fact due to changes in the solute concentration as a consequence of coarsening¹⁰.

Noble et al¹³. studied the coarsening kinetics of δ' precipitates in Al-Li alloys upon aging at 130-150°C using electrical resistivity measurements. The basic nature of this study is similar to that by Dorward¹⁰, in that the resistivity changes during coarsening were linked to changes in solute concentration in the matrix phase. In this case however, the authors separate the matrix component of resistivity from the overall measured resistivity by isolating contributions from δ' precipitates and thermal vibrations¹³. The matrix component of resistivity which is a measure of the solute concentration in the matrix showed a linear behavior with $\frac{1}{\langle r_t \rangle}$, a direct consequence of the Gibbs-Thomson solubility effect¹³. Here $\langle r_t \rangle$ is the mean precipitate radius at a time t .

An apparent increase in the electrical conductivity of shot-peened nickel-base superalloys was found by Blodgett et al., in contrast to other materials via eddy current measurements¹⁴. This phenomenon, found at higher probing frequencies, was attributed to residual stress effects, as the presence of surface roughness, increased dislocation density or increased permeability generally decreases the apparent electrical conductivity. The excess conductivity in shot-peened specimens was found to scale with the peening intensity. The measured conductivity difference was reported to be approximately proportional to the remaining subsurface residual stress in partially relaxed shot-peened Waspaloy specimens and vanished completely in the case of fully relaxed specimens¹⁴. The authors indicate a close correlation between residual stress measurements made via the eddy current technique and x-ray diffraction¹⁵. The authors also report the sensitivity

of the technique to surface roughness or the presence of near-surface microcracks, which force the eddy current to propagate along a more tortuous path than it normally would, without any artifacts. This apparent reduction in electrical conductivity due to the presence of surface roughness, is indicated to play a significant role in the evaluation of engine components after long-term service. This is due to the reduction in the primary material effects due to thermomechanical relaxation, while, the surface roughness contribution is unaltered or may even increase due to corrosion or fretting¹⁵.

2.1.2 NDE using acoustic techniques

Near-surface material properties in shot peened Waspaloy were investigated by Lavrentyev et al.¹⁶ using ultrasonic wave velocity measurements. Rayleigh wave velocity measurements were made on smooth and shot-peened Waspaloy samples with the objective of isolating the effects of surface roughness, residual stress and near-surface grain reorientation. Their results indicated that neither of the above factors dominated the experimentally observed Rayleigh wave velocity change all by itself. They suggested that the increase in dislocation density induced by shot peening was responsible for the observed changes in velocity¹⁶.

Haldipur et al.¹⁷ conducted localized ultrasonic measurements within jet-engine nickel alloy billets to correlate the measured parameters to the corresponding grain structure of the alloy. Ultrasonic attenuation and backscattered noise were found to be independent of the inspection direction at any given position within the billet. However, significant variations were noted with change in position within the billet. Metallographic examination revealed an equiaxed and untextured microstructure with variations in average grain diameter with position, which was consistent with observations drawn from

acoustic measurements. The attenuation and the figure-of-merit, a measure of the backscattered noise, were reported to increase with increasing grain diameter, which also agreed with predicted model results for equiaxed microstructures¹⁷.

Kang et al¹⁸. report the use of non-linear ultrasound technique for assessing the remnant creep life of a directionally solidified nickel-base superalloy. Specimens were subjected to creep loading at 871°C at three different stress levels as follows: 358 MPa, 289 MPa and 227 MPa. The specimens were tested using transmission ultrasound technique at periodically interrupted intervals that correspond to different creep life fractions of the alloy. A strong correlation was reported between the third order harmonic of the transmitted wave and the exhausted creep life fraction. In addition, the second order harmonic showed a good correlation with the extent of plastic deformation. The latter result was reported based on separate tensile tests on the same specimen. The authors thus, indicate the significance of the ultrasound technique as a potential non-destructive method for assessing creep damage in superalloys¹⁸.

2.1.3 NDE using scattering techniques

Nathal et al.¹⁹ conducted in situ X-ray diffraction experiments on Alloy H to monitor the lattice parameter variations during aging at 1000°C for times up to 975 hrs. Measurements were conducted on [001] oriented single crystals using Cu K α radiation. The lattice parameter of the γ' phase was found to be constant throughout the aging experiment. The γ peak could not be resolved prior to 215 hrs of aging, indicative of a relatively small misfit. It is reported that the γ' morphology changed from cubic to irregular plate shapes after longer aging durations, indicative of a semi-coherent γ - γ' interface. The loss of coherency was confirmed by measuring the γ' lattice parameter

from a bulk specimen and γ' extracted from the bulk specimen that resulted in identical values. The increase in the lattice mismatch with aging was reasoned to be due to changes in the γ lattice parameter, which is initially constrained to a large degree owing to the large volume fraction of the γ' phase¹⁹.

Wang et al.²⁰ conducted insitu characterization of the changes occurring in equilibrium and non-equilibrium microstructures of CM247CC nickel-base superalloy during aging at 1000°C using neutron diffraction. The non-equilibrium microstructure obtained after a solutionizing treatment, when aged for 5 hours at 1000°C, showed no apparent change in the (110) γ' peak intensity, while, the lattice mismatch increased non-linearly as a function of the aging time. In a second experiment, a near-equilibrium microstructure was obtained by slow cooling from 1190°C to 1000°C. In this case, the (110) γ' peak intensity continued to rise when cooling from 1100°C to 1000°C and 1.5 hours into the aging schedule and showed no change on further aging. The lattice mismatch more or less reflected the same trend. The authors were able to make conclusions about the growth and dissolution phenomena based on the above results²⁰.

Royer et al.²¹ report the use of high-resolution synchrotron diffraction for non-destructive microstructural investigations of AM1 single crystal nickel-base superalloy. Specimens subjected to creep tests at different stress states at 1000°C, were measured in directions parallel and perpendicular to the loading direction. Specifically, the mosaicity of (002) and (200) planes, and the lattice parameter distribution were mapped both parallel and perpendicular to the rafts. The mosaicity was found to depend strongly on the localized volume of material that contributes to diffraction. The lattice mismatch of the (002) reflections was reported positive, while, that for (200) reflections was negative, and

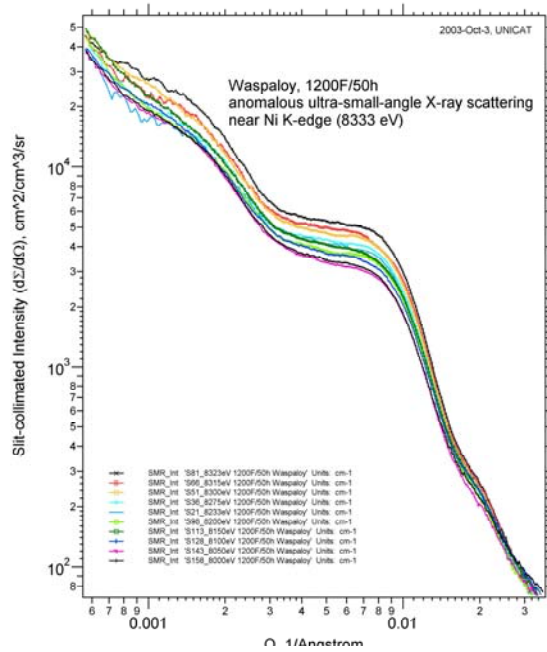


Figure 2.1 Anomalous-USAXS spectra at different energies near Ni-K edge for Waspaloy aged at 649°C for 50 hours²².

the mismatch was indicated to be a strong function of the applied stress and the resultant deformation²¹.

Jemian et al.²² conducted anomalous USAXS (A-USAXS) measurements for investigating the changes occurring in the precipitate population in thermally exposed Waspaloy. Long-term thermal exposure was conducted at 649°C for 12623 hours. A series of measurements with different energies near the Ni-K edge (8.34 keV) were made to enhance the scattering from γ' precipitates. The measurements spanned a q range of 0.001 nm⁻¹ to 1 nm⁻¹, where $q = (4\pi/\lambda)\sin\theta$, λ is the incident wavelength and 2θ is the scattering angle. The experimentally measured intensity as a function of q , displayed three distinct Guinier regions (see Figure 2.1), corresponding to scattering from primary

and secondary γ' precipitates and contributions from coarser features such as intragranular and grain-boundary carbides. Their work clearly demonstrates the ability of the present technique in rapid acquisition of statistically significant microstructural information²².

2.2 Literature Survey on Coarsening

In this section of the literature survey, the general theory of Ostwald ripening that governs the microstructural changes during coarsening will be described first. Then specific examples of applications of the coarsening theory by several researchers in studies of binary Ni-Al, Ni-Ti or commercial Ni-base superalloy systems will be discussed.

2.2.1 Coarsening Theory

The precipitation of a second phase from a supersaturated solid solution is known to proceed in the succession of (a) nucleation, (b) growth and (c) coarsening of second phase precipitates. In real systems, it is possible for (a) and (b) as well as (b) and (c) to proceed simultaneously²³. In a system consisting of a dispersion of fine second phase precipitates in a parent phase, a reduction in the global free energy of the system is brought about by a decrease in the interfacial energy of the system²³. The physical mechanism by which a reduction in the interfacial energy is achieved is based on the increased solute solubility in matrix regions in equilibrium with small particles, known as the ‘Gibbs-Thomson’ solubility effect⁶. The increased solubility of smaller precipitates is associated with the larger ratio of surface area to volume. As the curvature increases, there are fewer perfect bonds associated with surface atoms. This ultimately leads to a

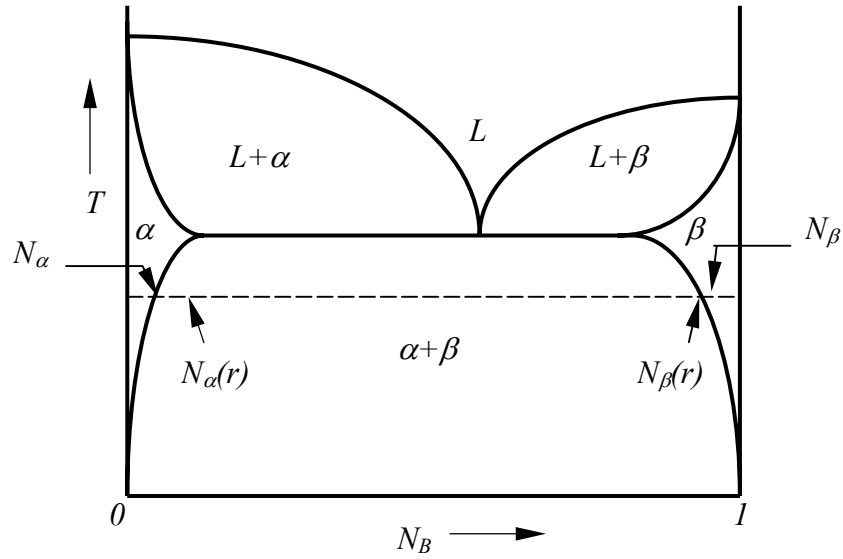


Figure 2.2 Binary phase diagram (temperature vs composition) of a precipitation hardening system, showing the shift in composition from equilibrium values of N_α and N_β to $N_\alpha(r)$ and $N_\beta(r)$, for a system consisting of a fine dispersion of β phase precipitates.

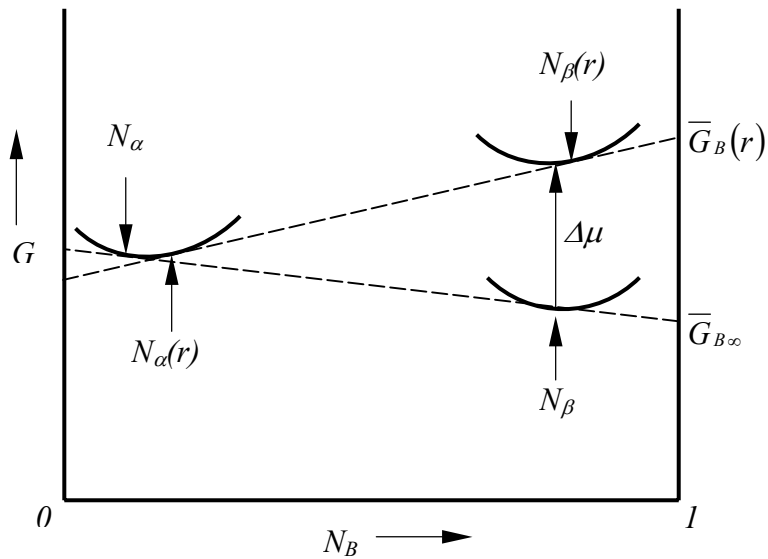


Figure 2.3 Free energy versus composition diagram to illustrate the chemical potential difference between an equilibrium dispersion of precipitates (N_β) and a fine dispersion ($N_\beta(r)$) that exists during the initial stages of coarsening.

$N_\alpha(r)$ and $N_\beta(r)$ due to the presence of a fine dispersion of precipitates is shown in the phase diagram in Figure 2.2. The corresponding increase in the chemical potential may be seen in the free energy vs composition diagram in Figure 2.3.

The change in the chemical potential- $\Delta\mu$ (associated with the curved interface) upon transfer of dn moles of atomic fraction N_β from a precipitate with a planar interface ($r = \infty$) to a precipitate of radius r is given as⁶:

$$\Delta\mu = \sigma \frac{dA}{dn} \quad (1)$$

where A is the area of the precipitate and σ is the isotropic matrix-precipitate interfacial energy. This equation may be rewritten in terms of the molar volume of the precipitate- V_m as follows⁶:

$$\Delta\mu = \sigma \frac{2V_m}{r} \quad (2)$$

The chemical potential difference- $\Delta\mu$ may be expressed in terms of the free energies- $G_B(r)$ and $G_B(\infty)$ and the compositions- N_α and N_β using Figure 2.2 as follows⁶:

$$\frac{\Delta\mu}{N_\beta - N_\alpha} = \frac{G_B(r) - G_B(\infty)}{1 - N_\alpha} \quad (3)$$

The above equation may be further modified by writing the free energies in terms of the composition and activity terms. Skipping this for brevity, the final result by combining equations (2) and (3) is as follows⁶:

$$\ln \left[\frac{N_\alpha(r)}{N_\alpha} \right] = \frac{2\sigma V_m}{RT r} \quad (4)$$

where, R is the universal gas constant. This is the commonly quoted form of the Gibbs-Thomson equation^{6, 12} and is derived based on the assumption of the two phases being almost pure, i.e. $N_\alpha \rightarrow 0$ and $N_\beta \rightarrow 1$. With $N_\alpha \rightarrow 0$, the activity coefficient- γ_α may be assumed to be a constant in the dilute limit. If the precipitate size is larger than a few nanometers, then the above equation may be simplified as⁶:

$$N_\alpha(r) = N_\alpha \left[1 + \frac{2\sigma V_m}{RT r} \right] \quad (5)$$

However, if the two phases- α and β are not terminal solid solutions, then the complete Gibbs-Thomson equation is given as⁶:

$$N_\alpha(r) = N_\alpha \left[1 + \frac{(1 - N_\alpha)}{(N_\beta - N_\alpha)} \left(\frac{2\sigma V_m}{RT \varepsilon_\alpha r} \right) \right] \quad (6)$$

In the above equation, $\varepsilon_\alpha = 1 + \frac{\partial \ln \gamma_\alpha}{\partial \ln N_\alpha}$ is the Darken factor, which is significant for

precipitates that form as an intermediate phase. The composition term- $\left(\frac{1 - N_\alpha}{N_\beta - N_\alpha} \right)$ is of

a greater significance in the case of non-terminal solid solutions, where the effect of this term is to increase the solute solubility of the matrix in equilibrium with a precipitate of finite radius- r ⁶.

The Gibbs-Thomson solubility effect described in the previous section is the starting point for explaining the coarsening mechanism and the associated kinetics. In the treatment of coarsening, it is generally assumed that the rate-controlling step is that of lattice diffusion and that there is no barrier to atom transfer across the precipitate-matrix interface. Consider the illustration (Figure 2.4) showing atom transfer between two precipitates of radii r_1 and r_2 ($r_1 > r_2$) of equilibrium solute concentrations- $N_\alpha(r_1)$ and

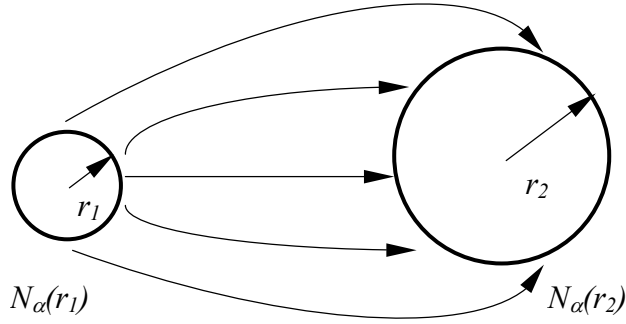


Figure 2.4 Schematic illustrating the transfer of flux from a smaller precipitate of radius, r_1 to a larger one of radius r_2 due to a composition gradient, $N_\alpha(r_1) > N_\alpha(r_2)$.

precipitate of smaller radius- r_1 should be greater than $N_\alpha(r_2)$ that corresponds to the larger particle. In this scenario, the diffusive flux of atoms will be from 1 to 2, resulting in the growth of the larger precipitate at the expense of the smaller one. The smaller precipitate continues to shrink at a growing rate during the process, as a consequence of the Gibbs-Thomson equation, until it disappears eventually⁶. In a system consisting of a distribution of spherical precipitates of different sizes, the expression for the expected growth rate is given as follows⁶:

$$\left(\frac{dr}{dt}\right) = \left(\frac{2D\sigma N_\alpha V_m}{RT r}\right) \left(\frac{1}{\langle r \rangle} - \frac{1}{r}\right) \quad (7)$$

where D is the diffusion coefficient of solute in the matrix, N_α is the solute concentration in the matrix in equilibrium with a particle of infinite radius and $\langle r \rangle$ is the mean radius of the precipitate distribution. A few inferences may be drawn based on the above equation for the growth rate as follows⁶:

(a) Precipitates smaller than $\langle r \rangle$ shrink at an accelerating rate with progressively decreasing r .

(b) Precipitates larger than $\langle r \rangle$ grow continuously with the growth rate- $\left(\frac{dr}{dt}\right)$ increasing from zero at $r = \langle r \rangle$ to a maximum at $r = 2\langle r \rangle$ and then decreases beyond $2\langle r \rangle$.

(c) The growth rate of precipitates larger than $\langle r \rangle$ falls as $\langle r \rangle$ increases.

The growth rate equation may be used to find an approximate variation of $\langle r \rangle$ with t by

assuming that $\left(\frac{d\langle r \rangle}{dt}\right) \approx \left(\frac{dr}{dt}\right)_{max}$ at $r = 2\langle r \rangle$. The final result is the well-known $t^{\frac{1}{3}}$ law

that describes the coarsening kinetics which is expressed as follows⁶:

$$\langle r_t \rangle^3 - \langle r_o \rangle^3 = \frac{3D\sigma N_a V_m}{2RT} t = k_l t \quad (8)$$

where $\langle r_t \rangle$ is the radius at a time t , $\langle r_o \rangle$ is the radius at $t = 0$ and k_l is the coarsening rate constant. This result is obtained from Greenwood's treatment of Ostwald ripening and the distribution in this case has a cut-off value of $\frac{r_{max}}{\langle r \rangle} = 2$. A similar result for the

coarsening kinetics is obtained by a more rigorous LSW treatment, with a factor of $\frac{8}{9}$

instead of $\frac{3}{2}$ on the RHS of equation (8)⁶. The equation however needs to be modified if

the phases involved are not terminal solid solutions. Specifically, the composition

correction term in the Gibbs-Thomson equation- $\frac{(1-N_a)}{\varepsilon_\alpha(N_\beta - N_a)}$ and the amount of solute

needed for precipitate growth- $(N_\beta - N_\alpha)$ needs to be included to describe the kinetics correctly. The modified version of equation (8) is given as follows⁶:

$$\langle r_t \rangle^3 - \langle r_o \rangle^3 = \frac{8D\sigma N_\alpha V_m}{9RT} \frac{(1 - N_\alpha)}{(N_\beta - N_\alpha)^2 \varepsilon_\alpha} t \quad (9)$$

So far, in the above equations for coarsening, a near zero volume fraction of the precipitates was assumed, so that there is no overlap between the diffusion fields of two precipitates. A final modification to the coarsening equation arises from the effect of finite volume fraction of the precipitates. In this case, the ratio of the radius to the interparticle spacing between precipitates- $\left(\frac{r}{\lambda}\right)$ is non-negligible, resulting in the overlap of diffusion fields between precipitates. This effect of volume fraction of precipitates was incorporated into the coarsening equation first by Ardell²⁴ via the volume fraction parameter- $k(f_v)$. It may generally be stated that the coarsening kinetics is accelerated upon increasing the volume fraction of the precipitates²⁴. The minimum value for $k(f_v)$ is therefore equal to 1, which corresponds to the ideal LSW treatment of a zero volume fraction situation. Results from further investigations on the effect of volume fraction on the coarsening behavior by different researchers will be given later.

2.2.2 Temporal change of other microstructural parameters during coarsening

It is assumed in the ideal LSW treatment that the coarsening reaction proceeds at a constant volume fraction of the precipitates⁶. At the onset of the true stage coarsening, the average solute concentration of the alloy- $\overline{N_\alpha}$ is nearly equal to the solute concentration in the matrix in equilibrium with a particle of mean radius- $\langle r \rangle$, i.e.

$N_\alpha(\langle r \rangle)^6$. However, the solute solubility associated with a fine dispersion of precipitates can be significantly greater than larger ones due to the Gibbs-Thomson solubility effect, as explained earlier. This effect was accounted for by Ardell¹¹, who showed that the volume fraction during coarsening is not a constant, but in fact increases with time. The volume fraction of precipitates- $f_v(t)$, according to the lever rule may be written as¹¹:

$$f_v(t) = \frac{N_o - N_\alpha(\langle r \rangle)}{N_\beta - N_\alpha(\langle r \rangle)} \quad (10)$$

By using the Gibbs-Thomson equation to substitute for $N_\alpha(\langle r \rangle)$, the above equation is modified as¹¹:

$$f_v(t) = f_e - \frac{2(1-f_e)\sigma N_\alpha V_m}{RT(N_\beta - N_\alpha)} \frac{1}{\langle r \rangle} \quad (11)$$

The above equation may be written in terms of t by assuming that $\langle r \rangle \approx (k_1 t)^{1/3}$ as follows¹¹:

$$f_v(t) = f_e - \frac{2(1-f_e)\sigma N_\alpha V_m}{RT(N_\beta - N_\alpha)} \frac{1}{k_1^{1/3}} t^{-1/3} \quad (12)$$

Thus the volume fraction of precipitates- $f_v(t)$ follows a linear increase with $t^{-1/3}$ until the equilibrium volume fraction, $f_e = \frac{N_o - N_\alpha}{N_\beta - N_\alpha}$ is reached as $\langle r \rangle \rightarrow \infty$. If supersaturation driven growth persists for a time t_1 before the onset of the true coarsening reaction, then the linear behavior of $f_v(t)$ will be in terms of $(t-t_1)^{-1/3}$ instead of $t^{-1/3}$.

The variation of the precipitate density- $W(t)$ with t may be obtained by defining the following relationship between $W(t)$ and $f_v(t)$ ¹¹:

$$f_v(t) = \frac{4}{3} \pi \langle r \rangle^3 W(t) \quad (13)$$

Using this relation, the temporal variation of the particle density may be expressed as follows¹¹:

$$W(t) = \frac{3f_e}{4\pi k_1} (t-t_1)^{-1} - \frac{3(1-f_e)\sigma N_\alpha V_m}{2\pi RT(N_\beta - N_\alpha)k_1^{4/3}} (t-t_1)^{-4/3} \quad (14)$$

Equivalently, $W(t)(t-t_1)$ follows a linear behavior as a function of $(t-t_1)^{-1/3}$.

Finally, the time variation of the solute concentration in the matrix- $N_\alpha(t)$ vs t can be obtained by substituting for the mean radius- $\langle r_t \rangle$ in equation (5) from the coarsening equation (see equation (8)), as follows¹¹:

$$N_\alpha(t) - N_\alpha = N_\alpha \frac{2\sigma V_m}{RTk_1^{1/3}} (t-t_1)^{-1/3} \quad (15)$$

2.2.3 Specific applications of coarsening theory to nickel-base alloys

Reports of coarsening studies in simple binary nickel-base alloys and commercial superalloys and the subsequent use of coarsening data for computation of thermodynamic or material-related parameters such as D , Q or σ will be the prime focus of this section.

Rao et al.²⁵ reported the effects of long-term exposure in the range of 700°C to 850°C on the coarsening behavior of a Ni-Fe base Nimonic PE16 superalloy. The coarsening kinetics of γ' investigated up to 1500 hrs was reported to follow the $t^{1/3}$ law, suggestive of volume diffusion of the solute(s)- Al and Ti in the matrix. The activation

energy for solute diffusion obtained from the slope of a plot of $\ln(k_1T)$ vs $\frac{1}{T}$ was computed to be 280 kJ mol⁻¹. Here k_1 is the coarsening rate constant introduced in equation (8). The reported value of 280 kJ mol⁻¹ compared favorably with the activation energy values of 270 kJ mol⁻¹ and 257 kJ mol⁻¹ for diffusion of Al and Ti in Ni respectively²⁵.

In another investigation by Stevens et al.²⁶, the results of γ' coarsening kinetics in IN-738 superalloy in the temperature range of 750°C to 850°C were reported. The alloy consisted of a bimodal γ' distribution- spheroids (0.05 μm radius) and cuboids (0.5 μm radius) after initial heat-treatment. Upon aging, both classes of precipitates were indicated to obey volume-diffusion controlled coarsening kinetics; however, the cuboids were reported to coarsen at the expense of the spheroids, until the latter disappeared. The activation energy for coarsening of γ' spheroids in this alloy was reported to be 269 kJ mol⁻¹. The volume fraction of γ' cuboids increased upon aging to a maximum value of 0.45 and remained constant thereafter with a simultaneous decrease in the volume fraction of γ' spheroids²⁶.

Ges et al.²⁷ reported coarsening studies in IN-713C for times up to 20000 hrs at 950°C. Their results indicated that γ' coarsening described by linear volumetric growth was only valid for aging times shorter than 2500 hrs. The coarsening rate of γ' was reported to slow down and eventually reach saturation for aging times greater than 2500 hrs. Therefore, the following exponential relationship was suggested for the coarsening kinetics beyond 2500 hrs instead of the LSW linear law²⁷:

$$\langle r_t \rangle^3 = V - (V - \langle r_o \rangle^3) e^{-at} \quad (16)$$

In the above equation, $\langle r_t \rangle^3 + V = \text{const.}$ and was interpreted as the molar volume that contributes to precipitate coarsening and α is the volumetric growth velocity. It was suggested that after longer aging periods, the precipitates would grow to be of volume V , disregarding the morphological changes²⁷.

Xiao et al.²⁸ conducted HREM investigations of both pre-coarsening and true coarsening stages in a Ni-12 at% Al alloy in response to aging at 500°C for times up to 264 hrs. Nucleation and coarsening regimes were distinctly identified as separated by a critical radius- r^* of 1.22 nm. The nucleation period was characterized by an increase in the precipitate density- $W(t)$ and a slight increase in the mean radius- $\langle r \rangle$. The coarsening phase governed by volume-diffusion controlled kinetics showed a monotonic decrease in the precipitate density and an increase in $\langle r \rangle$. Correspondingly, the volume fraction of the precipitates was reported to increase from 0 to 0.07 up to 264 hrs of coarsening. The diffusion coefficient- D and the precipitate-matrix interfacial energy- σ were computed in two separate ways using the coarsening data- (i) slopes of $\langle r_t \rangle^3$ vs t and $f_v(t)$ vs $t^{-1/3}$ plots and (ii) slope and intercept of $W(t)$ vs t plot. The parameters involved in the slopes and intercepts of these plots may be noted from equations (8), (12) and (14) presented earlier. The computed values of D , σ are reported to be $1.65 \times 10^{-21} \text{ m}^2 \text{ s}^{-1}$, 0.014 J m^{-2} and $1.55 \times 10^{-21} \text{ m}^2 \text{ s}^{-1}$, 0.021 J m^{-2} using (i) and (ii) respectively. Thus independent measurements of $\langle r_t \rangle$ and $f_v(t)$ or $\langle r_t \rangle$ and $W(t)$ during precipitate coarsening facilitate the estimation of both D and σ instead of the product $D\sigma$ just from a plot of $\langle r_t \rangle^3$ vs t ²⁸.

Lastly, the effects of volume fraction of the precipitates on the coarsening kinetics are addressed. The LSW theory of diffusion controlled particle coarsening was modified by Ardell²⁴ to account for the effect of volume fraction- f_v on particle coarsening, usually referred to as the MLSW theory. The modification was carried out under the assumption that the solute diffusion distance to or from a precipitate will in general depend on a characteristic distance that is a function of the spatial distribution of the precipitates. The MLSW theory preserves the basic $t^{1/3}$ kinetics predicted by the LSW theory; however an increased coarsening rate is predicted by the MLSW theory even for small values of f_v ²⁴. Additionally, the theory predicts a rapid broadening of the precipitate size distribution (PSD) with increasing f_v , approaching the PSD for interface controlled coarsening in the limit of $f_v = 1$. The predictions of the MLSW theory are however inconsistent with the experimental observations of coarsening behavior in Ni-base γ - γ' alloys, in that neither the coarsening rate nor the PSD's are significantly affected by f_v ²⁴. Ardell²⁹ compared the normalized coarsening rate constants- $\frac{k_I(f_v)}{k_I(0)}$ as a function of the volume fraction of γ' precipitates from ten different investigations on binary Ni-Al alloys by different research groups. Ardell²⁹ concluded that there was no dependence of either the true coarsening kinetics or the PSD's on f_v over a wide range of volume fractions (1% to nearly 60%) investigated. The absence of the volume fraction effect on the coarsening kinetics was attributed by Ardell to elastic interaction effects between precipitates. It was suggested that the retardation of coarsening kinetics was

through the co-operative effects of the shear moduli difference between the γ and γ' phases and the role played by elastic anisotropy²⁹.

In the present research, a combination of electrical and scattering NDE techniques is used in conjunction with microscopy and USAXS techniques for studying microstructural evolution in controlled Waspaloy microstructures. Specifically, correlations are developed among *dc* electrical resistivity measurements, SEM microstructures, USAXS data and x-ray lattice parameter measurements with the objective of understanding the mechanisms responsible for microstructural evolution. In addition, the feasibility of using *ac* impedance techniques for non-destructive examination purposes is also investigated. Coarsening data obtained from USAXS experiments are analyzed using methods proposed by Ardell^{6, 11} for binary Ni-X systems. The coarsening rate constants and the diffusion coefficients computed from the USAXS data are compared to those from binary Ni-Al systems and the observed differences are discussed.

CHAPTER 3

EXPERIMENTAL PROCEDURE

This section describes in detail, the heat-treatment procedure used for obtaining the controlled Waspaloy microstructures with varying grain size and precipitate size distributions. Subsequently, the different characterization techniques used for microstructural examination as well as macro electrical characterization are detailed.

3.1 Heat-treatments

As stated before, heat-treatments were conducted with the objective of varying the microstructural parameters systematically, viz. the grain size and γ' precipitate size distribution. Industrial grade Waspaloy obtained from Fry Steel was the starting material for the heat-treatment experiments. The nominal composition of the alloy is given in Table 3.1. Heat-treatments were conducted in a Carbolite model CTF 12/65/500 horizontal tube furnace under flowing argon conditions. Specimens were seated on a ceramic tray that was positioned at the furnace center, with radiation shields placed on either sides of the tray inside the tube. The radiation shields prevented the heat from escaping to the ends of the tube. A uniform heat-zone of 21 cm was quoted by the manufacturer for this arrangement. The tube was then sealed at both ends via end-caps that had provisions for gas inlet, outlet and thermocouple insertion. A type N thermocouple was used for external temperature monitoring, which was approximately positioned at the furnace center and below the specimen tray. All the heat-treatments conducted in this work were programmed to be of three steps- ramp-up, dwell and ramp-down sequentially. At the conclusion of the dwell duration, the specimen was manually

Table 3.1 Composition (atomic %) of primary constituents in as-received Waspaloy

Element	Atomic %
Ni	56.1
Cr	21.2
Co	12.3
Mo	2.5
Ti	3.6
Fe	1.3
Al	2.7

removed from the furnace and subjected to a rapid quench in a 5 wt% brine solution at 50°C.

Overall, three different sets of heat-treatment experiments were conducted in this research, which will hereafter be referred to using roman numerals. A heating rate of 5.5°C/min was used for all the heat-treatments in Sets I and II, while a rate of 3.3°C/min was used in Set III of experiments. The first set (I) of heat-treatments was conducted with the objective of investigating the electrical properties of microstructures with varying grain size but similar precipitate size distributions. Solution-treatments were conducted initially at 1045°C, 1090°C and 1145°C for 4 hours to vary the matrix (γ) grain size and to homogenize the microstructure of the alloy in the as-received condition. The solution-treatments at temperatures of 1045°C, 1090°C and 1145°C will be denoted by capital letters- ‘E’, ‘B’ and ‘D’ respectively. This scheme will be used to reflect the order in which the heat-treatment experiments were conducted to vary the grain size. The solution-treated specimen bars were next subjected to a vacancy-stabilization treatment for 3 hours, which was intended to homogenize the discrepancies in the quenched-in vacancy concentration after the solution-treatments. The letter ‘S’ will be concatenated to the solution-treatment code to indicate the stabilization treatment. The vacancy

stabilization temperature was chosen to be at 1045°C corresponding to the lowest solution-treatment temperature. This is in comparison to the γ' solvus temperature of ~1020°C, as quoted by the manufacturer. The solution-treated and stabilized specimen bars were subsequently aged at 800°C for the following aging times- 0., 0.5, 1, 2, 5, 10, 20, 50, 75 and 100 hours. Slices were sampled from the original specimen bar at each specific aging interval and the bar was then replaced in the furnace for further aging. As an example, the microstructure resulting from the sequence of heat-treatments- 1090°C solution-treatment, 1045°C vacancy stabilization treatment and 800°C aging treatment for 75 hours is identified as IBS-800-75.

The second (II) and the third (III) sets of heat-treatments were conducted with the objective of studying the coarsening kinetics of this alloy at different aging temperatures. The initial step that was common to both sets of experiments was a solutionizing treatment at 1145°C (code 'D'). This was in order to keep the matrix (γ) grain size invariant for subsequent coarsening experiments in both cases. The vacancy stabilization treatment at 1045°C was conducted as an intermediate step before aging in the second set of experiments only. This serves to minimize vacancy cluster formation and associated effects on γ' nucleation during subsequent aging. Subsequently, the specimen bars were aged at 700°C, 800°C and 875°C in the second set of experiments for aging times ranging from 0.5 to 100 hrs. In the third set of experiments, specimens were aged directly after the solution-treatment, at temperatures of 725°C, 800°C and 875°C. Additionally, in the third set of experiments, aging experiments were carried out at 600°C for much shorter aging durations, viz. 2, 4, 6 and 9 min to investigate the kinetics during the early stages of

precipitation. The summary of specimens produced in Sets I, II and III experiments are listed in Tables 3.2, 3.3 and 3.4 respectively.

3.2 Metallography

A Buehler ISOMET 1000 Low Speed Saw was used for sampling slices from heat-treated specimen bars. The as-cut slices were then mounted inside a bakelite mold using a Buehler SIMPLEMET molding press. The mounted specimens were then rough ground using a 400 grit SiC abrasive paper on a Buehler Phoenix Beta Grinder/Polisher. Subsequently, the specimens were polished sequentially using 9 μm and 3 μm diamond suspensions on ULTRAPOL SILK and TEXMET 1000 polishing cloths respectively. Finally, the specimens were fine polished in a suspension of four parts colloidal silica to one part 30% H_2O_2 for 6 min and colloidal alumina suspension for 30 sec. A CHEMOMET Microcloth was used for the fine polishing step.

An etchant consisting of a mix of 3:2:2 ratio by volumes of HCl, HNO_3 and CH_3COOH was used for delineating the grain structure³⁰. Highlighting the γ' phase for microscopic examination was accomplished in two ways viz. preferential etching of the γ' phase and preferential dissolution of the matrix (γ) phase surrounding the γ' precipitates. An etchant comprising a mix of 10 ml each of HCl, HNO_3 , H_2O and 0.3g of molybdc acid reagent (A-etchant) was used for preferential etching of the γ' phase. Preferential dissolution of the γ phase was achieved using an electrolytic polishing procedure³⁰ in a solution of 66% methanol and 33% HNO_3 (B-etchant). The electropolishing was conducted at room temperature with voltage and current density settings of 50V and 0.46 A/cm^2 respectively.

Table 3.2 List of specimens categorized under Set I heat-treatments

Specimen ID	Solution-treatment	Stabilization-treatment	Aging treatment
IE	1045°C, 4 hrs	-	-
IES	1045°C, 4 hrs	1045°C, 3 hrs	-
IB	1090°C, 4 hrs	-	-
IBS	1090°C, 4 hrs	1045°C, 3 hrs	-
ID	1145°C, 4 hrs	-	-
IDS	1145°C, 4 hrs	1045°C, 3 hrs	-
IES-800-0.5	1045°C, 4 hrs	1045°C, 3 hrs	800°C, 0.5 hrs
IES-800-1	1045°C, 4 hrs	1045°C, 3 hrs	800°C, 1 hrs
IES-800-2	1045°C, 4 hrs	1045°C, 3 hrs	800°C, 2 hrs
IES-800-5	1045°C, 4 hrs	1045°C, 3 hrs	800°C, 5 hrs
IES-800-10	1045°C, 4 hrs	1045°C, 3 hrs	800°C, 10 hrs
IES-800-20	1045°C, 4 hrs	1045°C, 3 hrs	800°C, 20 hrs
IES-800-50	1045°C, 4 hrs	1045°C, 3 hrs	800°C, 50 hrs
IES-800-75	1045°C, 4 hrs	1045°C, 3 hrs	800°C, 75 hrs
IES-800-100	1045°C, 4 hrs	1045°C, 3 hrs	800°C, 100 hrs
IBS-800-0.1	1090°C, 4 hrs	1045°C, 3 hrs	800°C, 0.1 hrs
IBS-800-0.5	1090°C, 4 hrs	1045°C, 3 hrs	800°C, 0.5 hrs
IBS-800-1	1090°C, 4 hrs	1045°C, 3 hrs	800°C, 1 hrs
IBS-800-2	1090°C, 4 hrs	1045°C, 3 hrs	800°C, 2 hrs
IBS-800-5	1090°C, 4 hrs	1045°C, 3 hrs	800°C, 5 hrs
IBS-800-10	1090°C, 4 hrs	1045°C, 3 hrs	800°C, 10 hrs
IBS-800-20	1090°C, 4 hrs	1045°C, 3 hrs	800°C, 20 hrs
IBS-800-50	1090°C, 4 hrs	1045°C, 3 hrs	800°C, 50 hrs
IBS-800-75	1090°C, 4 hrs	1045°C, 3 hrs	800°C, 75 hrs
IBS-800-100	1090°C, 4 hrs	1045°C, 3 hrs	800°C, 100 hrs
IDS-800-0.5	1145°C, 4 hrs	1045°C, 3 hrs	800°C, 0.5 hrs
IDS-800-1	1145°C, 4 hrs	1045°C, 3 hrs	800°C, 1 hrs
IDS-800-2	1145°C, 4 hrs	1045°C, 3 hrs	800°C, 2 hrs
IDS-800-5	1145°C, 4 hrs	1045°C, 3 hrs	800°C, 5 hrs
IDS-800-10	1145°C, 4 hrs	1045°C, 3 hrs	800°C, 10 hrs
IDS-800-20	1145°C, 4 hrs	1045°C, 3 hrs	800°C, 20 hrs
IDS-800-50	1145°C, 4 hrs	1045°C, 3 hrs	800°C, 50 hrs
IDS-800-75	1145°C, 4 hrs	1045°C, 3 hrs	800°C, 75 hrs
IDS-800-100	1145°C, 4 hrs	1045°C, 3 hrs	800°C, 100 hrs

Table 3.3 List of specimens categorized under Set II heat-treatments

Specimen ID	Solution-treatment	Stabilization-treatment	Aging treatment
IID	1145°C, 4 hrs	-	-
IIDS	1145°C, 4 hrs	1045°C, 3 hrs	-
IIDS-700-0.5	1145°C, 4 hrs	1045°C, 3 hrs	700°C, 0.5 hrs
IIDS-700-1	1145°C, 4 hrs	1045°C, 3 hrs	700°C, 1 hr
IIDS-700-2	1145°C, 4 hrs	1045°C, 3 hrs	700°C, 2 hrs
IIDS-700-5	1145°C, 4 hrs	1045°C, 3 hrs	700°C, 5 hrs
IIDS-700-10	1145°C, 4 hrs	1045°C, 3 hrs	700°C, 10 hrs
IIDS-700-20	1145°C, 4 hrs	1045°C, 3 hrs	700°C, 20 hrs
IIDS-700-50	1145°C, 4 hrs	1045°C, 3 hrs	700°C, 50 hrs
IIDS-700-75	1145°C, 4 hrs	1045°C, 3 hrs	700°C, 75 hrs
IIDS-700-100	1145°C, 4 hrs	1045°C, 3 hrs	700°C, 100 hrs
IIDS-800-0.5	1145°C, 4 hrs	1045°C, 3 hrs	800°C, 0.5 hrs
IIDS-800-1	1145°C, 4 hrs	1045°C, 3 hrs	800°C, 1 hrs
IIDS-800-2	1145°C, 4 hrs	1045°C, 3 hrs	800°C, 2 hrs
IIDS-800-5	1145°C, 4 hrs	1045°C, 3 hrs	800°C, 5 hrs
IIDS-800-10	1145°C, 4 hrs	1045°C, 3 hrs	800°C, 10 hrs
IIDS-800-20	1145°C, 4 hrs	1045°C, 3 hrs	800°C, 20 hrs
IIDS-800-50	1145°C, 4 hrs	1045°C, 3 hrs	800°C, 50 hrs
IIDS-800-75	1145°C, 4 hrs	1045°C, 3 hrs	800°C, 75 hrs
IIDS-800-100	1145°C, 4 hrs	1045°C, 3 hrs	800°C, 100 hrs
IIDS-875-0.5	1145°C, 4 hrs	1045°C, 3 hrs	875°C, 0.5 hrs
IIDS-875-1	1145°C, 4 hrs	1045°C, 3 hrs	875°C, 1 hr
IIDS-875-2	1145°C, 4 hrs	1045°C, 3 hrs	875°C, 2 hrs
IIDS-875-5	1145°C, 4 hrs	1045°C, 3 hrs	875°C, 5 hrs
IIDS-875-10	1145°C, 4 hrs	1045°C, 3 hrs	875°C, 10 hrs
IIDS-875-20	1145°C, 4 hrs	1045°C, 3 hrs	875°C, 20 hrs
IIDS-875-50	1145°C, 4 hrs	1045°C, 3 hrs	875°C, 50 hrs
IIDS-875-75	1145°C, 4 hrs	1045°C, 3 hrs	875°C, 75 hrs
IIDS-875-100	1145°C, 4 hrs	1045°C, 3 hrs	875°C, 100 hrs

Table 3.4 List of specimens categorized under Set III heat-treatments

Specimen ID	Solution-treatment	Stabilization-treatment	Aging treatment
IID	1145°C, 4 hrs	-	-
IID-725-0.5	1145°C, 4 hrs	-	725°C, 0.5 hrs
IID-725-1	1145°C, 4 hrs	-	725°C, 1 hr
IID-725-2	1145°C, 4 hrs	-	725°C, 2 hrs
IID-725-5	1145°C, 4 hrs	-	725°C, 5 hrs
IID-725-10	1145°C, 4 hrs	-	725°C, 10 hrs
IID-725-20	1145°C, 4 hrs	-	725°C, 20 hrs
IID-725-50	1145°C, 4 hrs	-	725°C, 50 hrs
IID-725-75	1145°C, 4 hrs	-	725°C, 75 hrs
IID-725-100	1145°C, 4 hrs	-	725°C, 100 hrs
IID-800-0.5	1145°C, 4 hrs	-	800, 0.5 hrs
IID-800-1	1145°C, 4 hrs	-	800°C, 1 hrs
IID-800-2	1145°C, 4 hrs	-	800°C, 2 hrs
IID-800-5	1145°C, 4 hrs	-	800°C, 5 hrs
IID-800-10	1145°C, 4 hrs	-	800°C, 10 hrs
IID-800-20	1145°C, 4 hrs	-	800°C, 20 hrs
IID-800-50	1145°C, 4 hrs	-	800°C, 50 hrs
IID-800-75	1145°C, 4 hrs	-	800°C, 75 hrs
IID-800-100	1145°C, 4 hrs	-	800°C, 100 hrs
IID-875-0.5	1145°C, 4 hrs	-	875°C, 0.5 hrs
IID-875-1	1145°C, 4 hrs	-	875°C, 1 hr
IID-875-2	1145°C, 4 hrs	-	875°C, 2 hrs
IID-875-5	1145°C, 4 hrs	-	875°C, 5 hrs
IID-875-10	1145°C, 4 hrs	-	875°C, 10 hrs
IID-875-20	1145°C, 4 hrs	-	875°C, 20 hrs
IID-875-50	1145°C, 4 hrs	-	875°C, 50 hrs
IID-875-75	1145°C, 4 hrs	-	875°C, 75 hrs
IID-875-100	1145°C, 4 hrs	-	875°C, 100 hrs
IID-600-2m	1145°C, 4 hrs	-	600°C, 2 min
IID-600-4m	1145°C, 4 hrs	-	600°C, 4 min
IID-600-6m	1145°C, 4 hrs	-	600°C, 6 min
IID-600-9m	1145°C, 4 hrs	-	600°C, 9 min

3.3 Microscopy and X-ray Diffraction

Optical micrographs of specimens for observing grain contrast were acquired on a LEICA DM IRM digital light microscope. Sub-grain microstructures were examined in a LEO 1530 and a LEO 1550 scanning electron microscope (SEM) at magnifications ranging from 500X to 200,000X. Images were acquired using both secondary electron and INLENS detectors. Chemical composition analysis was conducted on the LEO 1530 SEM using an oxygen-sensitive Oxford 7246 energy dispersive spectrometer.

Topographic examination of sub-grain microstructures was also conducted via scanning probe microscopy (SPM) besides high-magnification SEM. The setup consisted of an XE-100 PSIA advanced scanning probe microscope supplemented by a TS 150 Herzan active vibration isolation system. Images were acquired using both contact and non-contact scan modes. Cantilever types NSC36 and NCHR supplied by PSIA were used for contact and non-contact modes respectively. The scanner set-up in the XE-100 SPM is separated into an XY scanner for horizontal motion and a Z scanner for vertical motion respectively. The XY and the Z scanners move in response to the applied voltage; the higher the applied voltage, the larger the range of motion. Depending on the resolution needed, the SPM may be operated either in a High Voltage or a Low Voltage mode. In both the High and the Low Voltage modes, it is further possible to control the resolution of the z-scanner by adjusting the Z-scanner range. The vertical resolution in the High and the Low voltage modes for a Z-scanner range of 1.0 are 0.18 nm and 0.025 nm respectively. The High Voltage mode was generally used for scan sizes larger than $1\mu\text{m} \times 1\mu\text{m}$. However, the Low Voltage mode was used when a higher resolution was needed for typical scan sizes below $1\mu\text{m} \times 1\mu\text{m}$.

X-ray diffraction (XRD) was primarily used for determining the lattice parameter of the γ and γ' phases. High-resolution diffraction experiments were conducted on a Philips PW 1800 $\theta/2\theta$ automated powder diffractometer (APD) with a Bragg Brentano geometry and Cu-K α radiation. Scans were conducted in the range of 22° to 155° with a step size of $\Delta 2\theta = 0.02^\circ$, allowing 5 seconds per step.

3.4 Ultra Small Angle X-ray Scattering

Ultra Small Angle X-ray Scattering (USAXS) experiments were conducted on the first set (I) of heat-treated specimens, viz. E, B and D solution-treatments followed by stabilization treatment at 1045°C and finally aging at 800°C. The objective was primarily to obtain the size distribution and the volume fraction of γ' precipitates. Specimen preparation for USAXS analysis consisted of rough grinding in the sequence of 240, 400, 800 and 1200 grit abrasive papers of the as-cut slices (~1 to 1.5mm thick) to the point where the slice peeled off the mount easily. Subsequently, small pieces (~5mm x 5mm) were cut from the original slice using a metal cutting tool. The reverse side of these pieces was then thinned by the same sequential procedure using a Gatan disc grinder. The final thicknesses of the specimens for USAXS experiments were approximately around 10 μ m.

USAXS experiments in slit-smear configuration were performed using the synchrotron source installed at the 32 ID beam line at the Advanced Photon Source, Argonne National Laboratories. The thinned specimens were mounted on a sample pallet that could accommodate up to thirty specimens in a single experiment. The energy of the x-rays used in the USAXS experiments was 11 keV, corresponding to a wavelength of 1.1271 angstroms. Each specimen was measured multiple times to verify the

homogeneity of the specimen. Sample transmission obtained from USAXS measurements were used to compute the correct thicknesses of the specimens by using the calculated absorption length for Waspaloy for 11 keV x-rays. The data were then calibrated to absolute intensity using the correct thicknesses. The slit-smear data obtained from the USAXS experiments were analyzed using the Igor Pro (Wavemetrics Inc.) graphing and analysis package. Data reduction was accomplished using the Indra package and the reduced data were modeled using the Irena package. Modeling the scatter population, viz. the γ' distribution, was conducted under the assumption of a dilute limit, but interparticle interferences were accounted for whenever necessary. A built-in least squares fitting tool in the Igor Pro package was used for fitting the parameters of the model distribution, viz. the mean size of the scatterers- $\langle r \rangle$ and the volume fraction of the scatterers- f_v . Additionally, the number or the volume distribution of the scatterers could also be obtained directly from the modeling results.

3.5 DC Four-point Probe Resistivity

DC four-point probe resistivity was one of the macro electrical characterization techniques used for investigating the electrical response of heat-treated Waspaloy specimens. The probe system consisted of a Signatone model SP4-40045TFS probe head mounted on a Signatone model S301-6 probe station. The probe head was comprised of four equally spaced spring-loaded collinear tungsten probes at ~ 1 mm spacing, which contacted the specimen directly. The probe tips (in brand new condition) had a contact radius of $127\mu\text{m}$. The leads from the probes were connected to a Keithley 2182A nanovoltmeter and a Keithley 6221 AC/DC current source meter, the combination referred to as a Delta Mode System. Current was made to flow in and out of the specimen

through the outer probes, while voltage was measured across the inner probes connected to a high impedance circuit. A schematic illustrating the set-up for a four-probe measurement is shown in Figure 3.1.

Specimens for measurement were in the form of cylindrical slices of 13 mm diameter and thickness in the range of 1.5 to 3 mm. The circular face on which the measurement was conducted was polished to 0.05 μm roughness. The opposite face rested on an insulating supporting block during the measurement. Measurements were made by centering the probe array on the polished circular face of the specimen. Up to eight measurements per specimen were made along four different diametric orientations and two at each orientation using currents of 40 and 50 mA.

Low-resistance measurements are affected by thermoelectric EMF's, which originate from dissimilar metal contacts in the measurement circuit³¹. These can lead to serious errors in the measured voltage of the actual device under test (DUT). Moreover, thermoelectric EMF's may also vary with time, which entails an involved measurement technique to obtain an error free reading. Keithley Instruments Inc., have devised a new measurement technique known as the Delta method³¹ to eliminate thermoelectric EMF's in low-resistance measurements. In the following, a description of this method is provided.

The underlying principle of the Delta method³¹ is that voltage measurements are acquired successively by alternating the polarity of the source current. Each resistance calculation of the DUT is derived from three consecutive voltage measurements. The resistance calculation is explained with reference to the voltage and current profiles shown in Figure 3.2. In the voltage profile, V_{M1} , V_{M2} and V_{M3} are the measured voltages

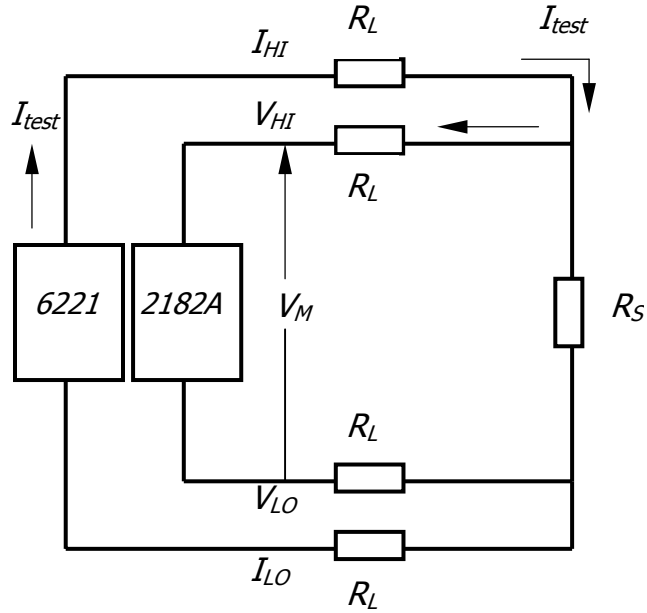


Figure 3.1 Schematic showing the basic principle of a four-point probe measurement³¹. A test current- I_{test} sourced by Keithley 6221 Current Source Meter flows through the specimen of resistance R_S . R_L refers to lead resistance of the wires. The magnitude of the sensing current- I_{sense} is negligible compared to I_{test} due to the high impedance associated with 2182A and therefore, the measured voltage- V_M by 2182A nanovoltmeter is primarily across the specimen.

across the DUT upon alternating the source current. It may be assumed that each voltage measurement is offset by a constant thermal EMF (V_{EMF}) and a linearly varying voltage offset (δV_{EMF}). The linear drift approximation is only valid for short measurement cycle times that are small in comparison with the thermal time constant of the DUT. Therefore it is essential that the current source and nanovoltmeter be fast enough to yield a short measurement cycle time. The first three measured voltage readings may be expressed as³¹:

$$V_{M1} = V_1 + V_{EMF} \quad (1a)$$

$$V_{M2} = V_2 + V_{EMF} + \delta V_{EMF} \quad (1b)$$

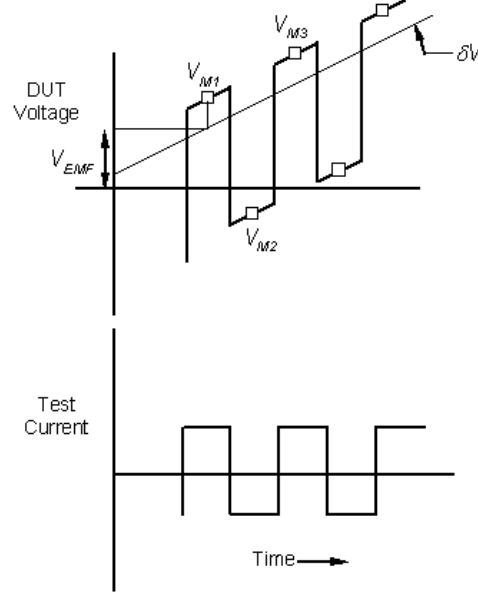


Figure 3.2 Illustration showing the underlying principle of a delta measurement³¹. V_{M1} , V_{M2} and V_{M3} refer to three successive delta measurements obtained by reversing the polarity of the current as shown in the second schematic. V_{EMF} is the constant thermal EMF offset affecting every delta measurement and δV_{EMF} is the linearly varying voltage offset.

$$V_{M3} = V_3 + V_{EMF} + 2\delta V_{EMF} \quad (1c)$$

where V_1 , V_2 and V_3 are the voltage drops across the DUT due to the applied current; V_{M1} is the measured voltage at zero time and V_{EMF} is the constant thermoelectric voltage offset at the same time. The constant thermoelectric EMF and the linearly varying drift are eliminated by the following procedure³¹:

$$V_A = \frac{V_{M1} - V_{M2}}{2} = \frac{(V_1 - V_2)}{2} - \frac{\delta V_{EMF}}{2} \quad (2a)$$

$$V_B = \frac{V_{M3} - V_{M2}}{2} = \frac{(V_3 - V_2)}{2} + \frac{\delta V_{EMF}}{2} \quad (2b)$$

$$V_{final} = \frac{V_A + V_B}{2} = \frac{(V_1 + V_3 - 2V_2)}{4} \quad (3)$$

The measured resistance R_{final} is then obtained as the ratio of V_{final} to the amplitude of the sourced current, I_{source} :

$$R_{final} = \frac{V_{final}}{I_{source}} \quad (4)$$

3.5.1 Calculation of specimen resistivity

Resistivity values were computed from the measured resistance by incorporating appropriate correction factors to account for finite specimen geometry. A general expression relating the specimen resistivity ρ to the experimentally measured resistance R_{final} in a four-probe measurement is as follows³²:

$$\rho = GR_{final} \quad (5)$$

where, G is referred to as the geometric correction factor. Generally speaking, G is a function of both the probe arrangement as well as the dimensions of the specimen. For a specimen of cylindrical geometry of radius r_o and thickness d , the expression for the geometric correction factor may be written as follows³²:

$$G = 2\pi s C\left(\frac{r_o}{s}\right) T\left(\frac{d}{s}\right) \quad (6)$$

where, $C\left(\frac{r_o}{s}\right)$ is the correction factor associated with a finite contour³³ and $T\left(\frac{d}{s}\right)$ is the thickness correction factor³⁴. The pre-factor $2\pi s$ (s is the probe spacing) is the geometric correction factor corresponding to an infinite slab of the same material³⁵. A detailed treatment of correction factors for four-point resistivity measurements on cylindrical specimens may be found in a later chapter.

3.5.2 Calculation of standard deviation in ρ

The standard deviation in the specimen resistivity was computed by the following procedure. Considering differentials of physical quantities on both sides of equation (5):

$$d\rho = GdR + RdG = G\langle d \rangle dR + 2\pi s \langle R \rangle C \left(\frac{r_o}{s} \right) dT \left(\frac{d}{s} \right) \quad (7)$$

where, dR and dT are the respective standard deviations in the measured resistance and the thickness correction factor. G is the overall geometric correction factor of the specimen corresponding to the mean thickness $\langle d \rangle$ and $\langle R \rangle$ is the average resistance.

dT was obtained as the standard deviation in $T \left(\frac{d}{s} \right)$ corresponding to each specific thickness measurement.

3.6 AC Impedance Measurements

The underlying objective of conducting AC impedance measurements on Waspaloy was to investigate the frequency response behavior due to the presence of inhomogeneities in the matrix, viz. γ' precipitates, carbides etc. Impedance measurements were initially conducted using a two-probe method on HP 4192A Impedance Analyzer with an Agilent 16034E test fixture.

AC four-point probe impedance measurements were conducted on a SR830 Stanford Research Systems DSP Lock-In Amplifier. A lock-in amplifier is basically a sensitive ac nanovoltmeter that enables accurate measurement of small signals that may possibly be obscured by noise signals of much larger magnitude. This is made possible by phase sensitive detection, wherein the signal of interest is isolated by choosing a specific reference frequency and a phase. Noise signals that are not in the vicinity of the

reference frequency are discarded and therefore do not affect the measurement. The internal oscillator of the lock-in amplifier is capable of sourcing a sine signal (available at the SINE OUT BNC) up to 102 kHz with an amplitude range of 4mV to 5V. Complex voltage measurements (V_x, V_y) were conducted using the differential (A-B) input of the lock-in. In this case, the measured voltage is the difference between the center conductors of the A and B inputs.

AC four-point probe measurements were initially performed on wire specimens and the set-up was subsequently replicated for measuring actual cylindrical slice specimens. The experimental set-up for wire specimens, shown in Figure 3.3, was developed along similar lines as that used by Gosselin et al.³⁶ for skin-effect measurements. The set-up for wire measurements consisted of a 12 AWG copper wire specimen of ~30 cm length onto which four 32 AWG copper lead wires were soldered for current and voltage connections. The lead wires for voltage were soldered equidistantly on either side from the center of the specimen wire. The voltage lead wires were cut sufficiently long and were twisted together from the solder connections along the entire length of the wires (see Figure 3.3). This was in order to minimize any loops in the circuitry, which can lead to spurious voltage pick-up due to the presence of alternating magnetic fields. The current lead wires were soldered on either ends of the specimen wire. The specimen wire with the soldered lead wires was then carefully led into a copper tube (2.54 cm diameter, 20 cm length) through insulating plugs at the ends of the tube (see Figure 3.3). The arrangement was such that the voltage connections remained inside the copper tube while, the ends of the specimen wire bearing the current contacts were outside the shield. The co-axial arrangement of the specimen surrounded by the copper

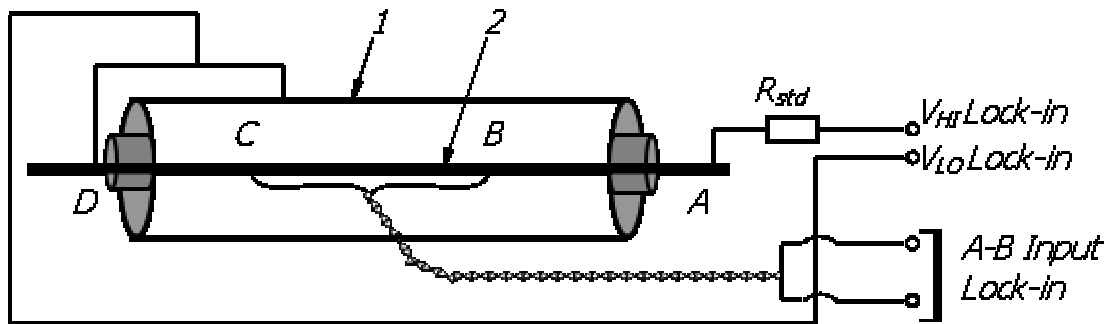


Figure 3.3 Schematic illustrating a four-point probe *ac* measurement on a wire specimen. The specimen (denoted by '2') is placed inside a hollow copper shield tube (denoted by '1') in the form of a coaxial cell arrangement. Points 'A' and 'D' represent the current injection and extraction points, while 'B' and 'C' refer to the voltage pick-up points. The voltage pick-up wires are braided to minimize effects of induced voltage from the magnetic field (after Gosselin et al.³⁶).

tube enables shielding the AC measurement from electromagnetic radiation. Additionally, the copper shield acts as a common ground point for the LOW current lead wire from the specimen and the outer conductor of the SINE OUT BNC of the lock-in amplifier. The HIGH current lead wire from the specimen was connected in series to a fixed resistor, which was then connected to the center conductor of the SINE OUT BNC. The braided voltage lead wires extending from inside the shield were connected to the differential (A-B) input of the lock-in for voltage measurement. The amplitude of complex current through the specimen wire was obtained by measuring the voltage across the resistor independently by a Keithley 2000 Digital Multimeter (DMM).

Four-point probe AC measurements on wire specimens conducted in the above described fashion need to be corrected for voltage contributions arising from the circuitry, referred to as short compensation. To enable this, a new wire specimen was prepared by shorting the voltage lead wires on the specimen by a single solder

connection. The current lead wires were soldered at either ends of the specimen as before. This will be referred to as the ‘short specimen’ hereafter. Short compensation was achieved by subtracting the voltage measured from the short specimen from the original wire specimen at all the frequencies investigated. The resulting voltages will be referred to as the short-corrected voltages.

Short-corrected voltage measurements from the specimen were taken at two different values of source voltage and the corresponding source currents were measured using the DMM. The real and imaginary components of the specimen impedance were then obtained by the following procedure³⁶:

$$V_{x1} = V_{ins} + I_{o1}R(\omega) \quad (8a)$$

$$V_{x2} = V_{ins} + I_{o2}R(\omega) \quad (8b)$$

$$V_{y1} = V_{ins} + I_{o1}\omega(L_{ins} + L(\omega)) \quad (9a)$$

$$V_{y2} = V_{ins} + I_{o2}\omega(L_{ins} + L(\omega)) \quad (9b)$$

In the above set of equations, V_{xj} and V_{yj} refer to the real and imaginary components of the measured voltage corresponding to the flow of a source current I_{oj} ($j = 1$ and 2). The quantities- V_{ins} , L_{ins} , $R(\omega)$ and $L(\omega)$ denote the residual voltage and inductance due to the instrumentation, the frequency dependent resistance and inductance of the specimen respectively. The resistance- $R(\omega)$ and the inductance- $L(\omega)$ of the specimen were obtained from the above set of equations as follows:

$$R(\omega) = \frac{V_{x2} - V_{x1}}{I_{o2} - I_{o1}} \text{ and} \quad (10)$$

$$L(\omega) = \frac{1}{\omega} \left(\frac{V_{y2} - V_{y1}}{I_{o2} - I_{o1}} \right) \quad (11)$$

As stated before, the experimental set-up for AC four-point probe measurements on cylindrical slice specimens was developed based on that used for wire measurements. The set-up, shown in Figures 3.4 (a) and (b), consisted of a probe head that was mounted on an aluminum support, which was attached to a thick aluminum base. An XYZ stage with an insulating platform attachment on the Z stage was also affixed to the aluminum base. The specimen seated on the platform was moved closer to the probe head for measurement using the motion controls on the stage. The aluminum base with the XYZ stage and the probe head mount was enclosed inside a copper box (cuboid-shaped), analogous to the copper tube used in wire specimen measurements. The box was designed so that the front face was left open for manipulating stage motion, which could later be sealed after connection between the specimen and the probes was established. The probe head for AC four-point probe measurements was the same as that used for making DC four-point measurements as described earlier. However, the manner in which the lead wires from the probes were drawn outside the probe head was modified significantly (see Figure 3.4 (b)). The current lead wires from the two end probes were led out from either side of the probe head. The voltage wires were twisted together as in the wire specimen measurements and drawn out from the center of the probe head. The two current lead wires and the pair of voltage wires were drawn out from three separate holes on the back face of the box. Connections between the different lead wires and the lock-in were identical to that used in wire measurements. Short compensation in case of slice specimens was conducted by using a sheet of copper (1cm x 1cm) as the short specimen.

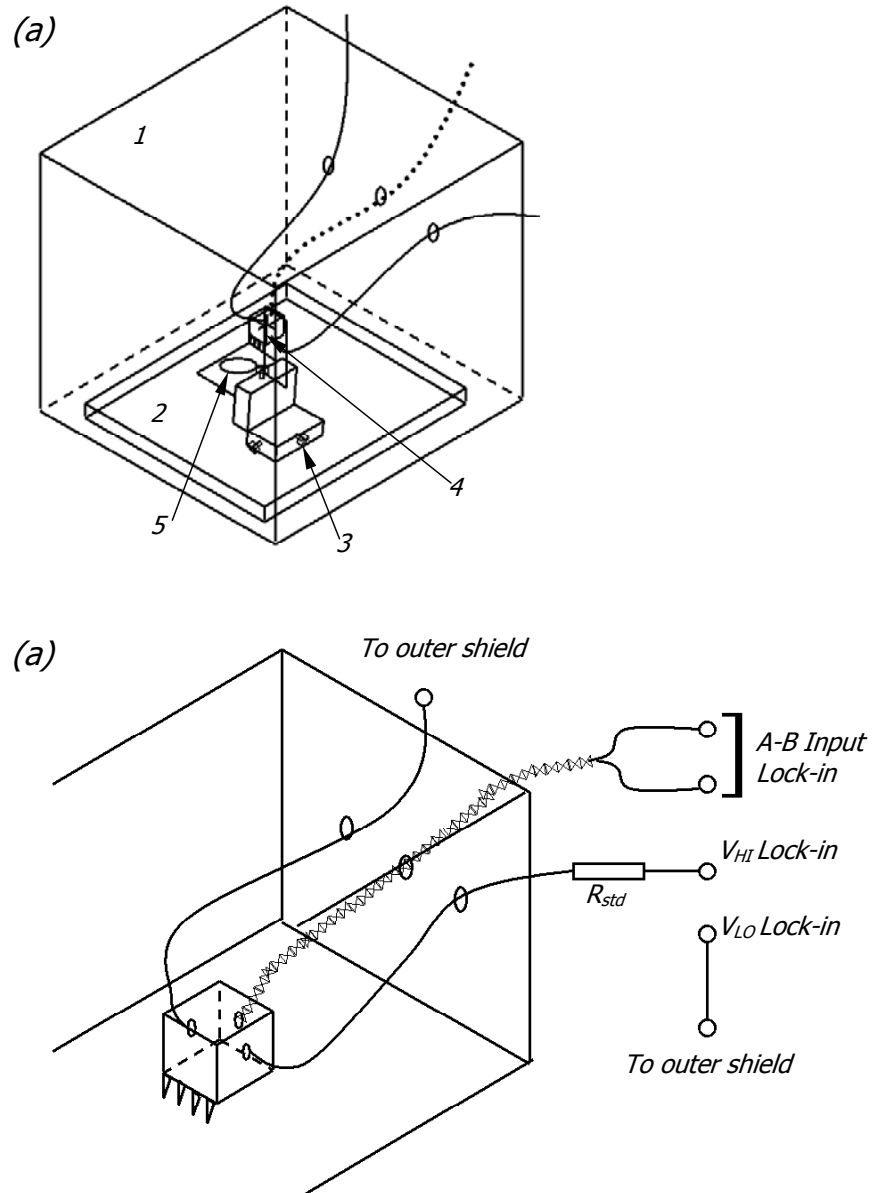


Figure 3.4 Schematic illustrating a four-point probe ac measurement on a cylindrical disk Waspaloy specimen is shown in (a). The numerals denote the following: (1) Copper shield box, (2) aluminum base, (3) xyz stage, (4) four-point probe and (5) a Waspaloy specimen, A magnified view of the four-point probe is shown in (b), where the current wires are drawn from opposite sides of the probe head and the twisted voltage pick-up wires are drawn from the center.

Four probe impedance measurements were conducted on the specimen of interest in the frequency range of 200 Hz to 100 kHz. At each frequency, two separate voltage measurements were made by switching the 'A' and 'B' voltage inputs i.e. (A-B) and (B-A) differential measurements. The average of the difference between these measurements was taken as the final measured reading. This procedure referred to as the 'Common Mode Reversal' or CMR technique helps in minimizing voltage errors due to common mode signals^{37, 38}. Common mode signals are those signals that arise equally on both A and B inputs i.e. common mode noise or common mode signal³⁸. If the signal source and the lock-in amplifier are connected to different ground points, they may not be at the same potential. This residual voltage due to ground loops results in imperfect cancellation of the signal appearing on the A and B inputs, leading to a common mode error³⁸. The CMR measurement was performed at two different source voltages for an actual specimen and a copper sheet specimen.

Next, a computed response for the four-probe impedance of the copper sheet specimen was obtained by making use of a closed-form analytical solution for the electric field distribution inside the specimen, developed by Bowler³⁹. Details of this computation are described in section 5.3.2. The residual impedance was then obtained as the difference between the measured and the computed impedances for the copper sheet specimen respectively. The actual specimen impedance was finally obtained as the difference between the measured specimen response and the residual impedance determined previously from the copper sheet specimen.

CHAPTER 4

RESULTS AND DISCUSSION OF HEAT-TREATMENT

EXPERIMENTS

In this chapter, the characterization results from the different sets of heat-treated specimens, described in the experimental procedure chapter, are presented and discussed. The first part of the chapter deals with Set I specimens, where aging experiments are conducted at 800°C after different prior solution-treatments at 1045°C, 1090°C and 1145°C. In the second part of the chapter, the microstructural evolution in Set III specimens, which are aged at 725°C, 800°C and 875°C after initial solution-treatment at 1145°C, is discussed.

4.1 Microstructural evolution in Set I experiments

4.1.1 Characterization Results

The grain structures resulting from solution-treatments at 1045°C, 1090°C and 1145°C (denoted as E, B and D respectively) are presented in Figure 4.1. As expected, the grain size shows progressive increase with increase in the solution-treatment temperature with average values of 13, 52 and 89µm. The average grain size post vacancy stabilization (denoted by the letter ‘S’) at 1045°C increased by not more than 15% of the as-solution-treated grain sizes. Representative scanning electron micrographs of specimens in the different solution-treated and stabilized conditions are shown in

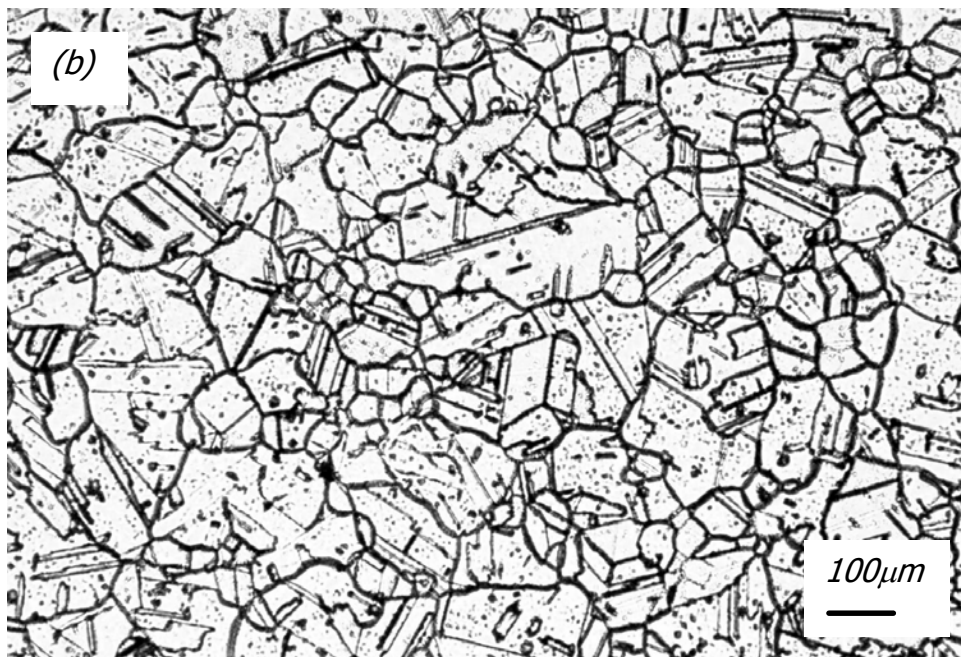
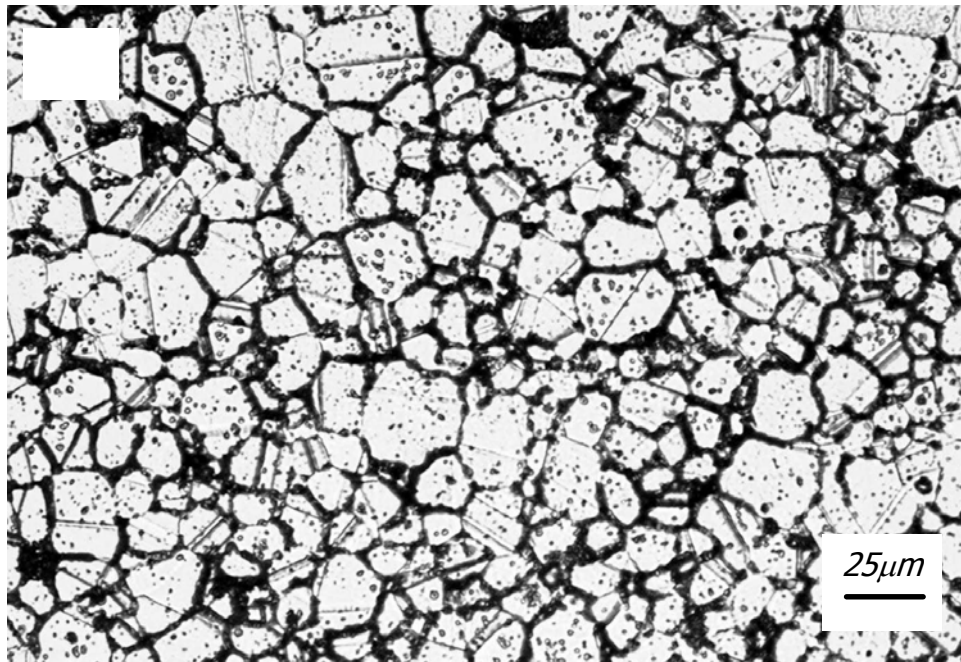


Figure 4.1 Representative optical micrographs of grain structures solution-treated at 1045°C-(a) and 1090°C-(b).

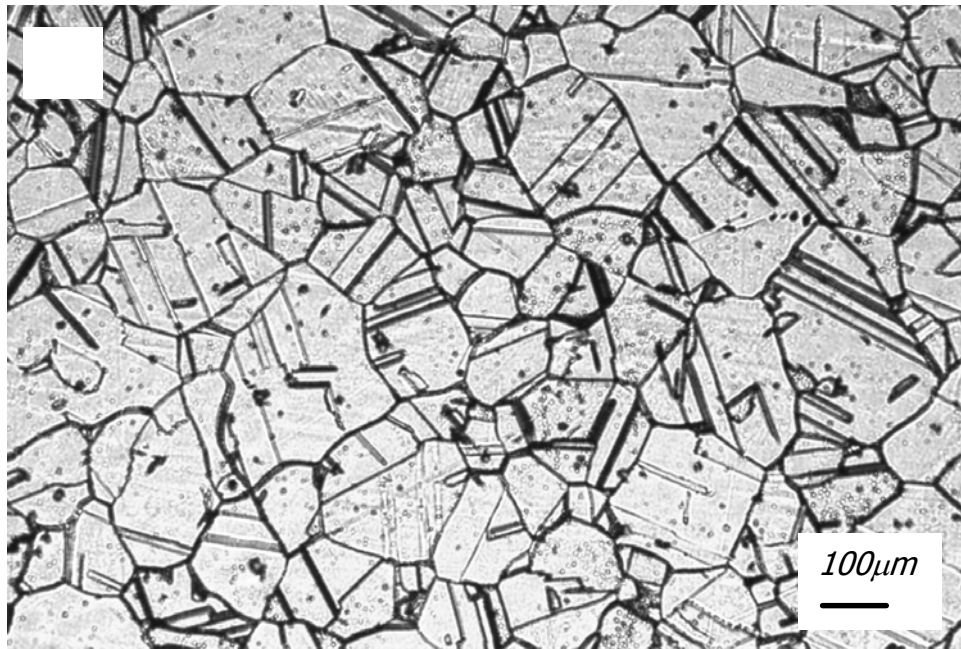


Figure 4.1 (c) Representative optical micrograph of grain structure solution-treated at 1145°C.

Figure 4.2. The presence of polygonal etch-pits, usually seen as square or hexagon shapes inside the grains, is common to all the microstructures. It is postulated that the formation of these polygonal etch pits is related to the condensation of excess quenched in vacancies onto preferential elastically soft directions. Further details on the formation and evolution of etch-pits are treated in sections 4.2.1 and 4.2.2 of this chapter. No evidence of γ' precipitation was noted from high-resolution SEM micrographs of solution-treated or stabilized specimens.

A plot of the lattice parameter of the γ phase as a function of the solution-treatment temperature is shown in Figure 4.3. Each data point represents an average obtained from multiple specimens that are different solution-treatment iterations at the

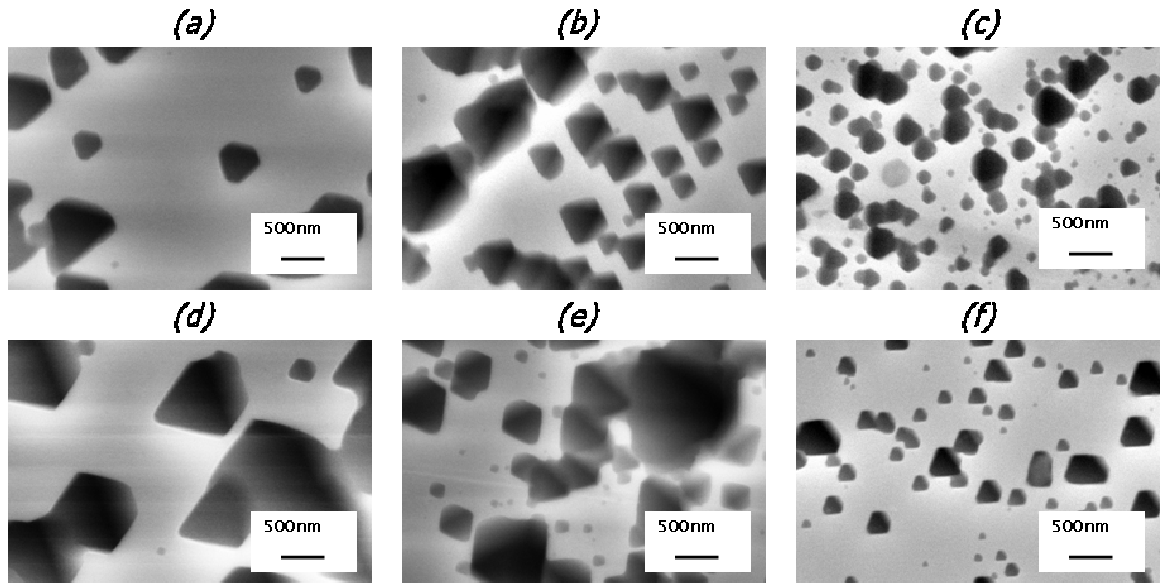


Figure 4.2 SEM micrographs of as-solution-treated and subsequently stabilized microstructures corresponding to initial solution-treatment temperatures of 1145°C- (a) & (b), 1090°C- (c) and (d), 1045°C- (e) and (f) respectively.

A plot of the lattice parameter of the γ phase as a function of the solution-treatment temperature is shown in Figure 4.3. Each data point represents an average obtained from multiple specimens that are different solution-treatment iterations at the same temperature. In spite of the large standard deviations, it is clear that the average lattice parameter shows an increase with increasing solution-treatment temperature.

The lattice parameter values of solution-treated and vacancy stabilized specimens that are specifically used for later aging treatments at 800°C are listed in Table 4.1. The vacancy stabilization treatment, as mentioned earlier, is intended to eliminate the discrepancies in the quenched-in excess vacancy concentration after the solution-treatments. The increasing trend in the lattice parameter with solution-treatment temperature is consistent with the plot presented in the previous paragraph in Figure 4.3. The post-vacancy stabilization treatment (at 1045°C) of the solution-treated specimens (at

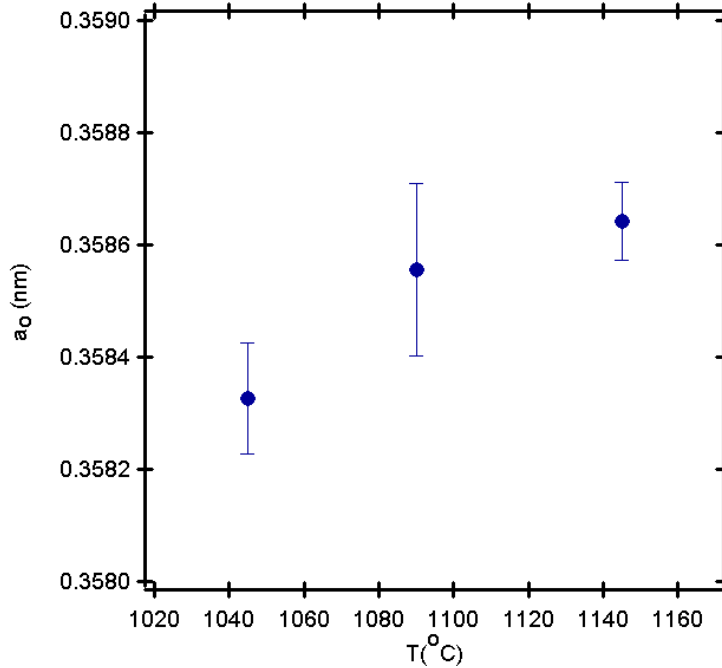


Figure 4.3 Plot showing the variation of the lattice parameter of the matrix (γ) phase with solution-treatment temperature.

1145°C and 1090°C) resulted in a slight decrease of the lattice parameter as seen from Table 4.1. The match between the lattice parameters of the stabilized (at 1045°C) specimens, with B (1090°C) and D (1145°C) pre-solution-treatments is very good. The notably higher lattice parameter (after stabilization) in case of the specimen pre-solution-treated at 1045°C, is not clearly understood. For this particular treatment, there was a temperature differential inside the furnace causing the treatment temperature to lie in proximity to the γ' solvus. Any compositional changes in the matrix associated with the possible precipitation of γ' during the stabilization treatment could potentially lead to a change in the lattice parameter.

A plot of the resistivity versus temperature is shown in Figure 4.4 for multiple iterations of different solutionizing and subsequent stabilization treatments. The as-

Table 4.1 Four-probe resistivity of solution-treated and vacancy stabilized specimens

Solutionizing temperature [°C]	ρ [$\mu\Omega\text{-cm}$] (solution-treated)	ρ [$\mu\Omega\text{-cm}$] (stabilized)	a_o (nm) (solution-treated)	a_o (nm) (stabilized)
1145	124.41	126.20	0.3587	0.3584
1090	125.78	125.44	0.3585	0.3584
1045	127.65	129.86	0.3583	0.3586

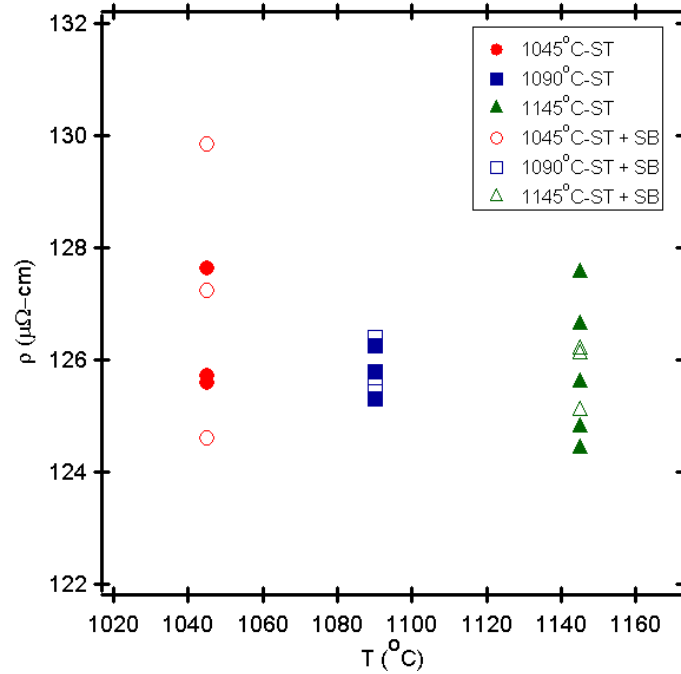


Figure 4.4 Plot showing the DC four-point probe resistivity as a function of treatment temperature in case of as-solution-treated and solution-treated + stabilized specimens. Multiple specimens were measured for each treatment. Closed symbols denote as-solution-treated specimens and open symbols denote the solution-treatment with the post vacancy-stabilization treatment.

solution-treated specimens are represented using closed symbols, while the solution-treated and subsequently stabilized specimens are denoted with open symbols. It is clear from the plot that there is no noticeable trend in the resistivity as a function of the solution-treatment temperature. Almost all the resistivity values of solution-treated and

stabilized specimens lie in a range between 124.41 [$\mu\Omega\cdot\text{m}$] and 127.652 [$\mu\Omega\cdot\text{m}$], with the exception of one specimen. The large scatter observed here is attributed to slightly dissimilar quenching conditions from one specimen to another. The dissimilarity in the quench is because the time taken to remove a specimen from the furnace at the conclusion of the heat-treatment and subject it to a quench is variable. Therefore, uncontrolled events such as association of vacancies and formation of cooling γ' are possible during this time interval, which can affect the measured resistivity. The markedly higher resistivity for one of the (1045°C solutionized + 1045°C stabilized) specimens is thought to be due to the presence of fine γ' upon precipitation during the stabilization treatment. This is a consequence of temperature differential inside the furnace causing the treatment temperature to lie in proximity to the γ' solvus.

The resistivity values of solution-treated and stabilized specimens that are later subjected to aging at 800°C are reported in Table. 4.1. These values were used previously in the resistivity plot reported in Figure 4.4.

Subsequent to the vacancy stabilization treatment, the specimens were aged at 800°C for times ranging from 0.1 to 100 hours in order to study the aging kinetics. The micrographs showing the microstructural evolution in response to aging at 800°C for the three pre-solution treatment cases (E: 1045°C, B: 1090°C and D: 1145°C) are presented in Figures 4.5 through 4.7. No observable γ' (via SEM) was noted in specimens sampled at 0.1 hrs or 0.5 hrs into the aging treatment in any of the three pre-solution-treatment cases. The rather large microstructural features observed in the SEM at these early aging durations are etch-pits, which transformed from perfect polygonal shapes (seen after solutionizing or stabilization treatments in Figure 4.2) into more rounded shapes upon

aging. γ' precipitates were present abundantly in case of specimens solution-treated initially at 1145°C after 1 hr of aging at 800°C (see Figure 4.7 (b)). The amount of γ' that could be observed using the SEM diminished drastically with decreasing pre-solution-treatment temperature. After 2 hours of aging at 800°C, γ' was clearly observable in all three pre-solution-treatment cases- B, D and E (see Figures 4.5(c), 4.6(d) and 4.7(c)). The larger features in the microstructures at 1 hr and 2 hrs are etch-pits that have evolved from rounded shapes into more irregular shapes and should not be confused with γ' . Aging for longer times led to the eventual disappearance of the etch-pits. A detailed treatment of the etch-pit evolution is dealt with in the next section, as stated earlier. Progressive growth of γ' was noted upon aging at 800°C for longer aging times viz., 5, 10, 20, 50, 75 and 100 hours in all three pre-solution treatment cases. This is clearly seen from the series of micrographs- 4.5 (d)-(i), 4.6 (e)-(j) and 4.7 (d)-(i) for pre-solution treatment cases of 1045°C, 1090°C and 1145°C respectively. The nominal size of γ' as perceived visually was the largest in case of specimens pre-solution-treated at 1145°C at all the aging sampling times. Precipitate sizes corresponding to pre-solution-treatments of 1090°C and 1045°C were comparable. These observations based on SEM micrographs will be justified in the following using precipitate size distribution data, obtained using ultra small angle x-ray scattering (USAXS). The present observations however, signify that the aging kinetics is faster in case of specimens that were solution-treated at 1145°C, in spite of the vacancy-stabilization treatment. This conclusion seems to suggest that the faster aging kinetics in set D (1145°C pre-solution-treatment) as compared to B (1090°C pre-solution-treatment) or E (1045°C pre-solution-treatment) may be influenced by residual vacancy contributions even after the stabilization treatment.

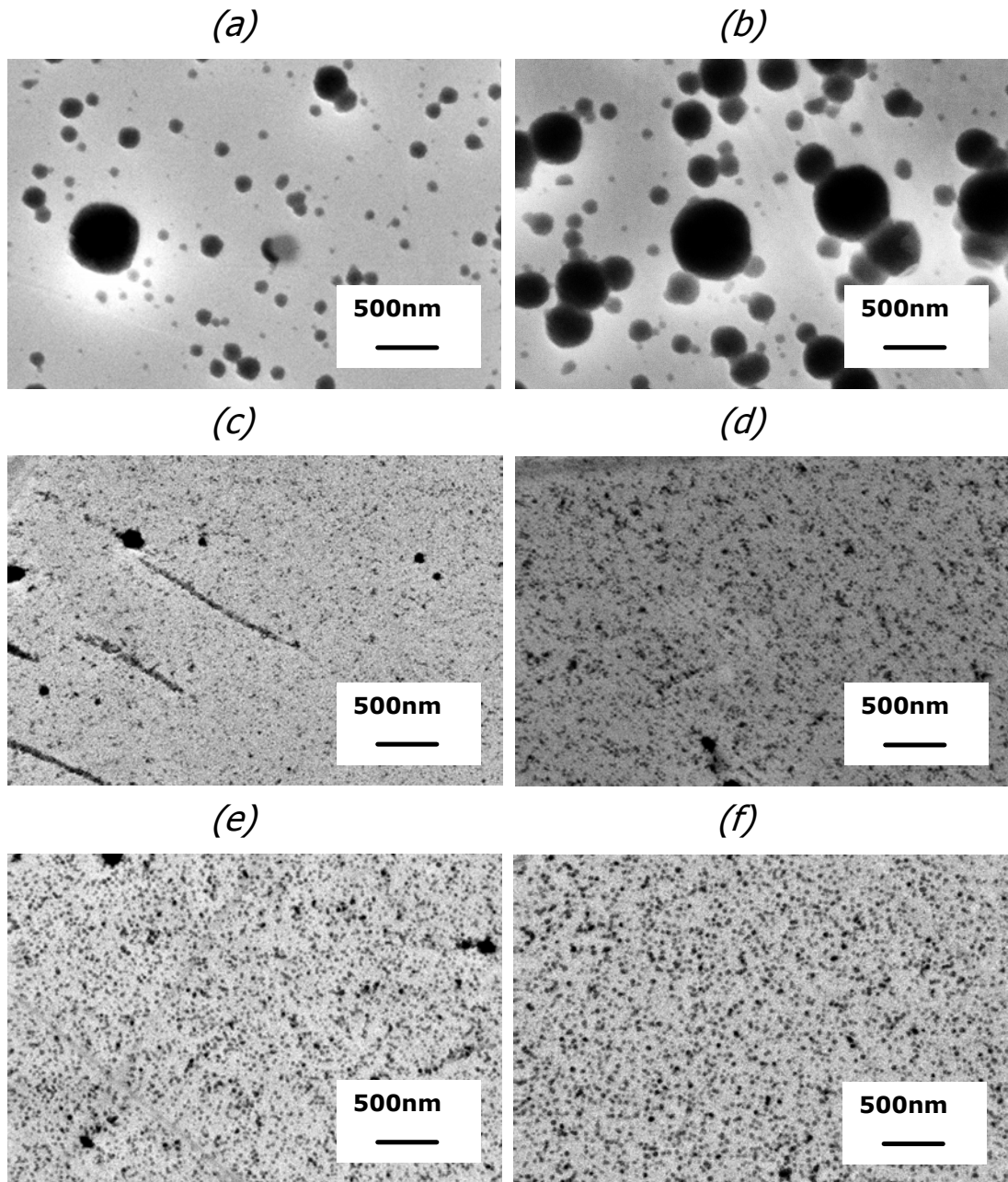


Figure 4.5 SEM micrographs showing microstructural evolution upon aging at 800°C for aging times of (a) 0.5, (b) 1, (c) 2, (d) 5, (e) 10 and (f) 20 hrs respectively. The specimens were solution-treated at 1045°C and stabilized at 1045°C prior to aging at 800°C.

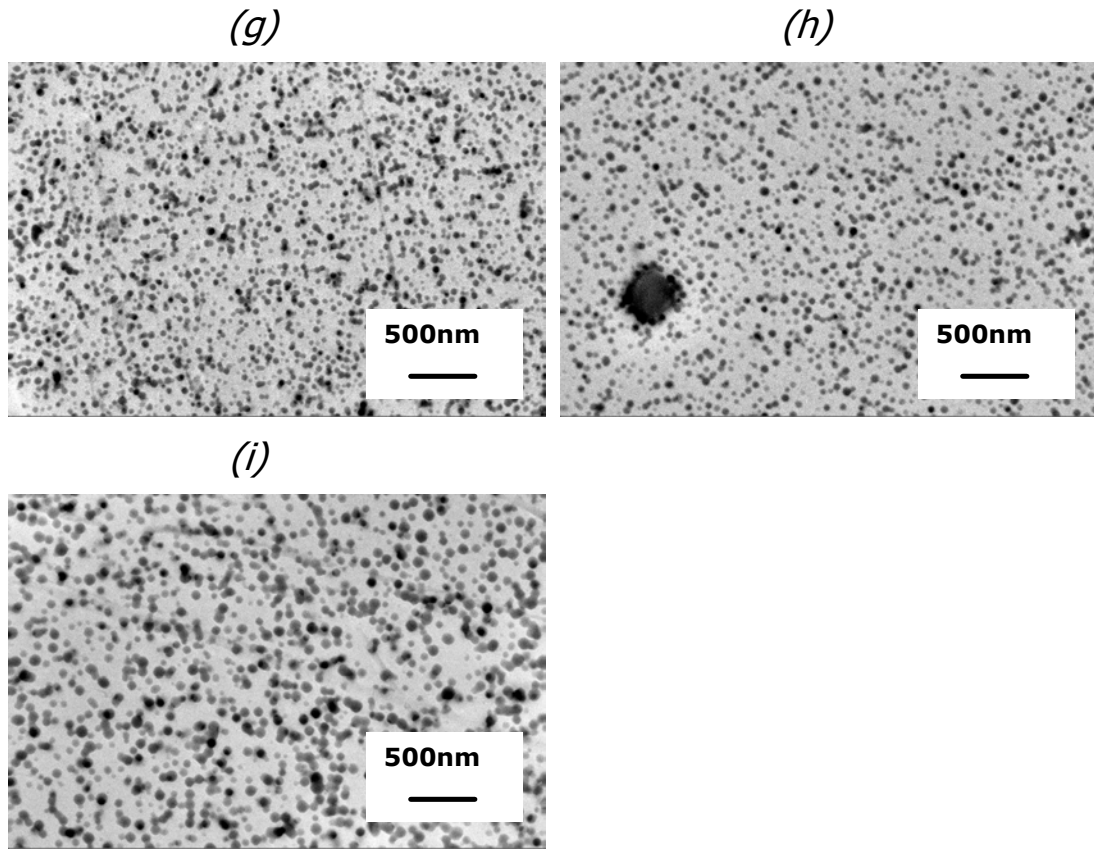


Figure 4.5 SEM micrographs showing microstructural evolution upon aging at 800°C for aging times of (g) 50, (h) 75 and (i) 100 hrs respectively. The specimens were solution-treatment at 1045°C and stabilized at 1045°C prior to aging at 800°C.

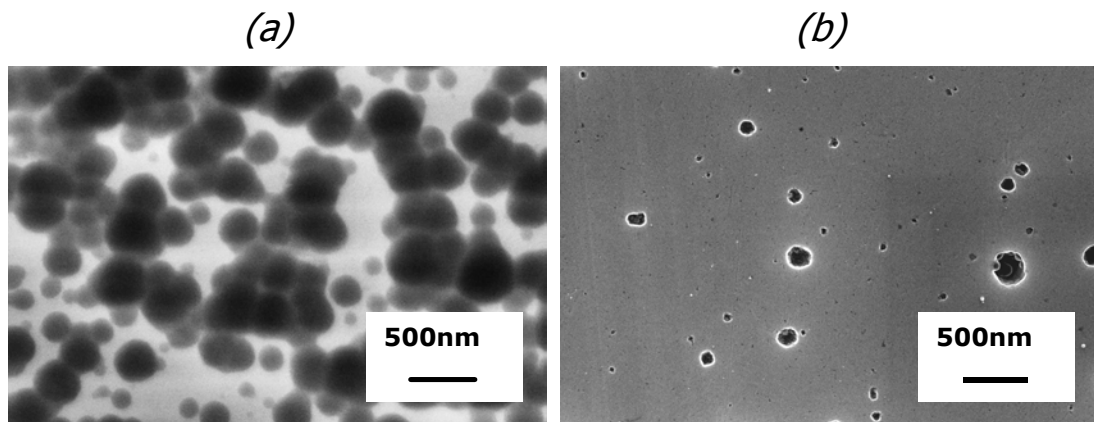


Figure 4.6 SEM micrographs showing microstructural evolution upon aging at 800°C for aging times of (a) 0.1 and (b) 0.5 hrs respectively. The specimens were solution-treatment at 1090°C and stabilized at 1045°C prior to aging at 800°C.

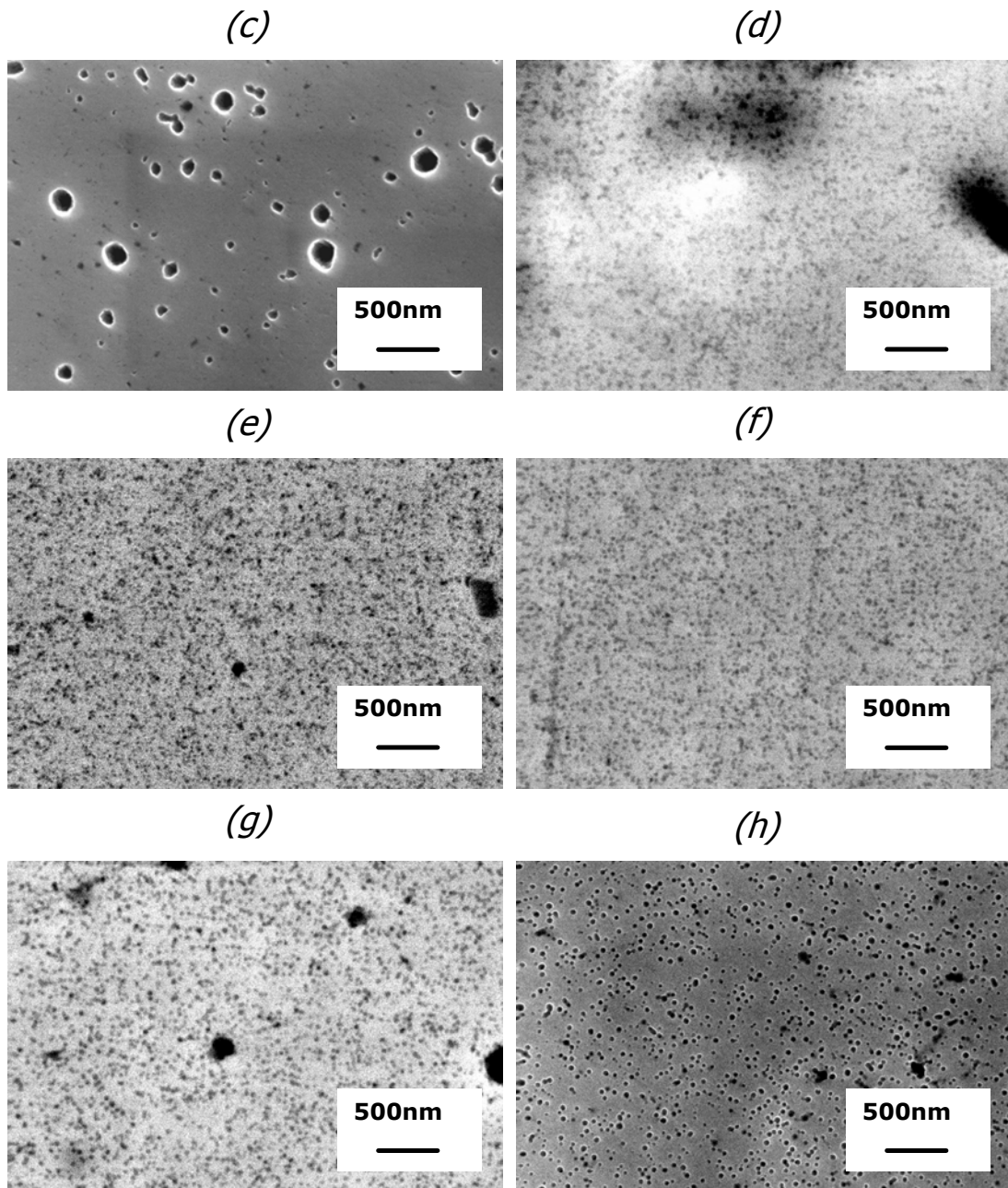


Figure. 4.6 SEM micrographs showing microstructural evolution upon aging at 800°C for aging times of (c) 1, (d) 2, (e) 5, (f) 10, (g) 20 and (h) 50 hrs respectively. The specimens were solution-treatment at 1090°C and stabilized at 1045°C prior to aging at 800°C.

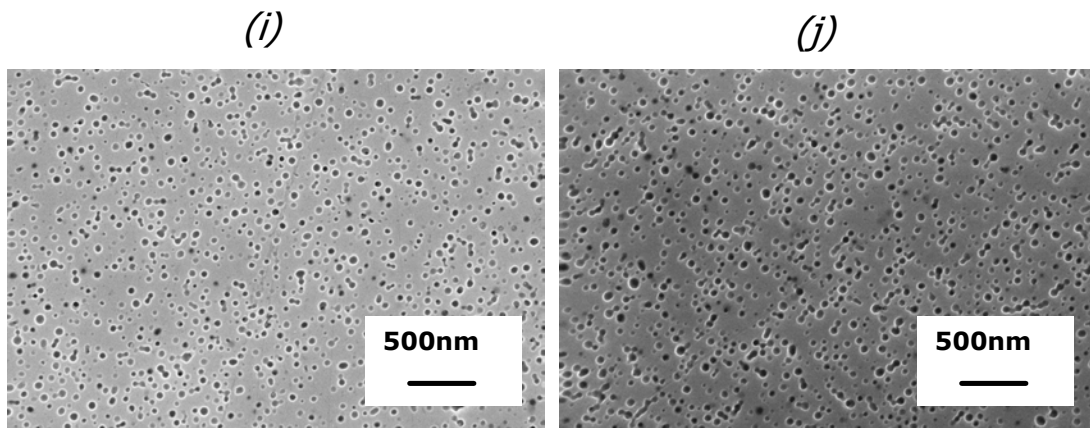


Figure 4.6 SEM micrographs showing microstructural evolution upon aging at 800°C for aging times of (i) 75 and (j) 100 hrs respectively. The specimens were solution-treatment at 1090°C and stabilized at 1045°C prior to aging at 800°C.

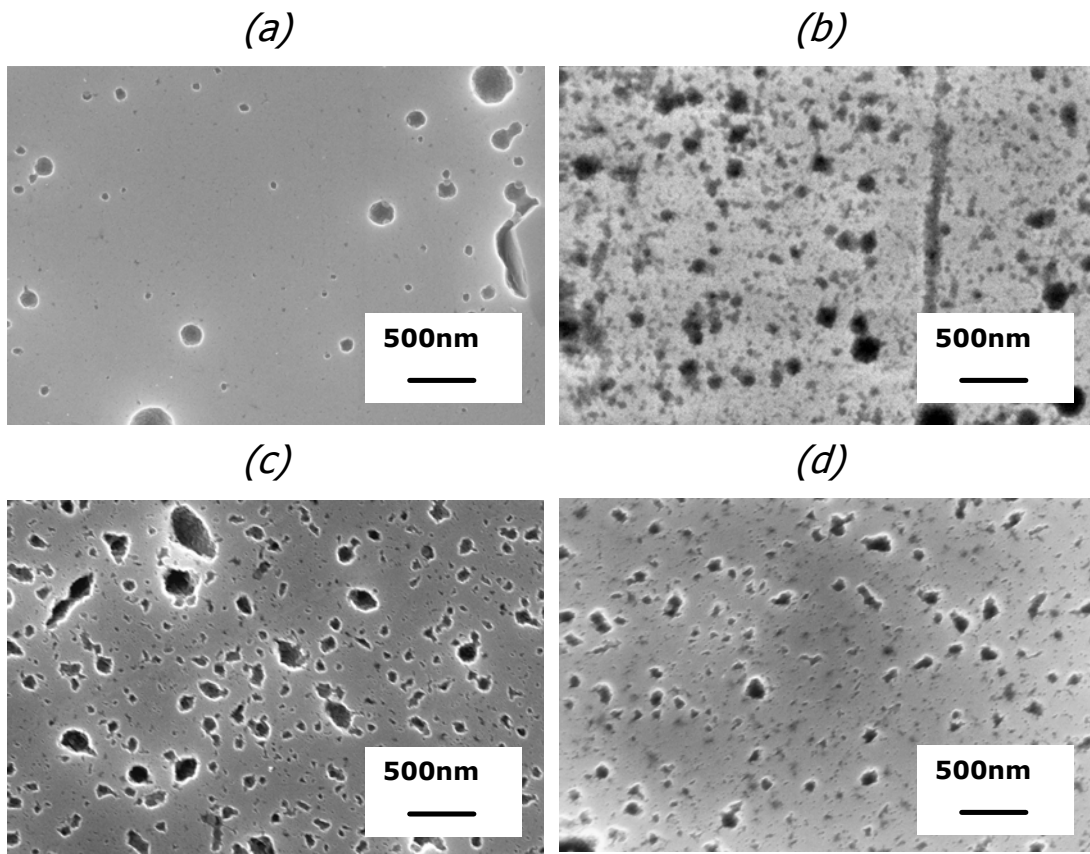


Figure 4.7 SEM micrographs showing microstructural evolution upon aging at 800°C for aging times of (a) 0.5, (b) 1, (c) 2 and (d) 5 hrs respectively. The specimens were solution-treatment at 1145°C and stabilized at 1045°C prior to aging at 800°C.

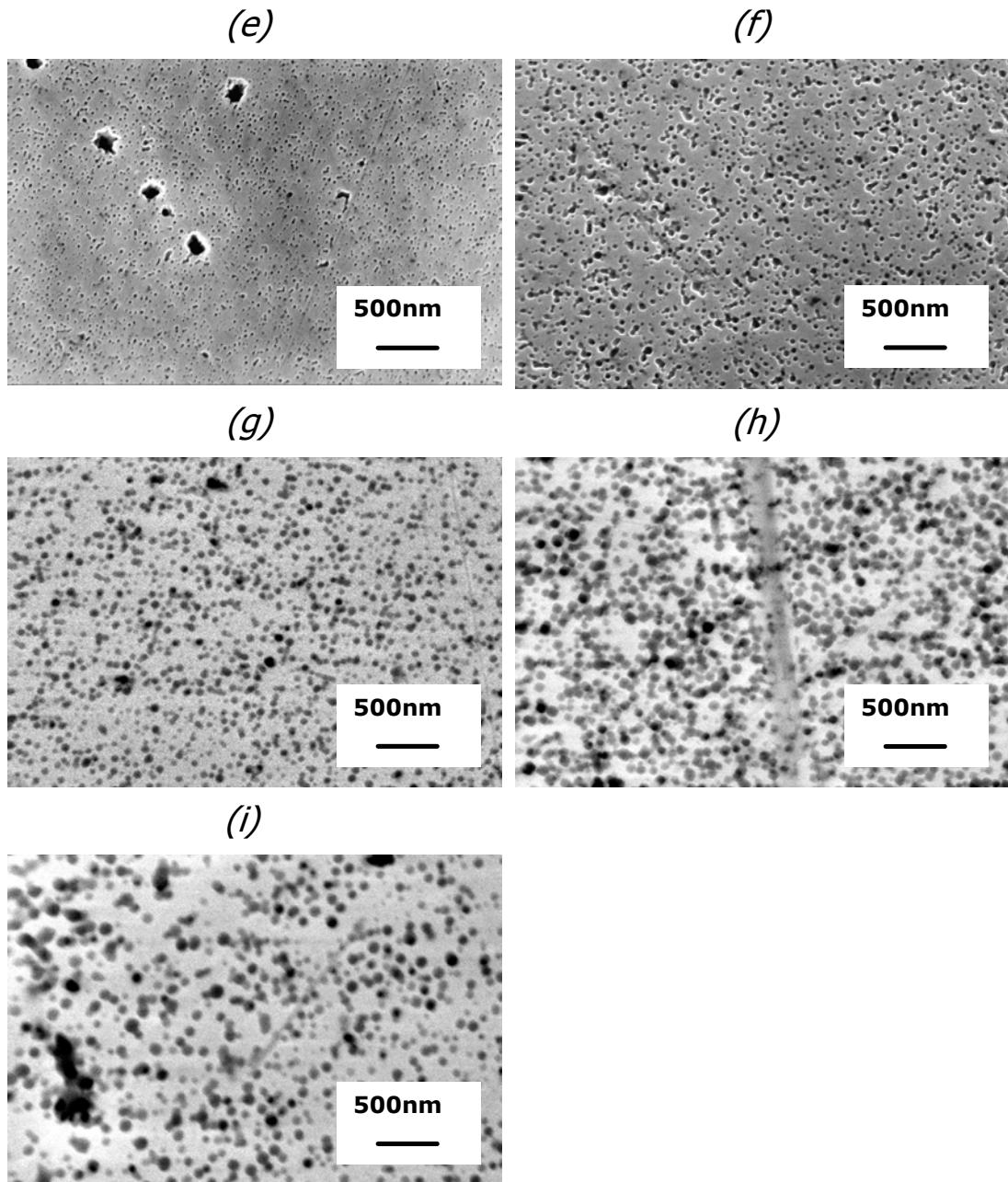


Figure 4.7 SEM micrographs showing microstructural evolution upon aging at 800°C for aging times of (e) 10, (f) 20, (g) 50, (h) 75 and (i) 100 hrs respectively. The specimens were solution-treatment at 1145°C and stabilized at 1045°C prior to aging at 800°C.

Figure 4.8 shows a plot of the DC four-point probe resistivity values of specimens aged at 800°C for all the three pre-solution-treatment cases as a function of the aging time. The first set of data points at 0.01 hrs correspond to specimens in the vacancy stabilized condition. As mentioned earlier, the resistivity of the IES (1045°C solution-treated + 1045°C stabilized) specimen is possibly influenced by γ' precipitation during the stabilization treatment due to a temperature differential inside the furnace. With the

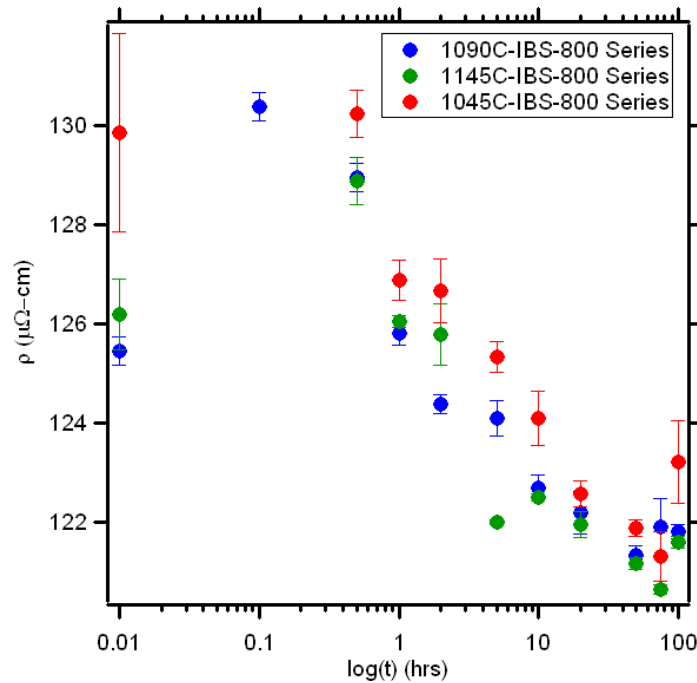


Figure 4.8 Plot of the DC four-point probe resistivity versus logarithm of the aging time for specimens pre-solution-treated at 1045°C, 1090°C and 1145°C and aged at 800°C.

exception of this specimen, a rise in resistivity from the stabilized condition is noted upon aging, with a maximum increase of 4.95 [nΩ.m] in case of the IBS-800-0.1 specimen. Upon further aging up to 1 hr, the resistivity is noted to decrease monotonically for the B (1090°C pre-solution-treatment) series, at which point it is nearly equal to the as-

stabilized resistivity. The same is also true of E (1045°C) and D (1145°C) series specimens, in which cases, the earliest aging sampling time is 0.5 hrs instead of 0.1 hrs. Further decrease in resistivity beyond 1 hr all the way up to 100 hrs is noted for the three pre-solution-treatment cases, the reasons for which are discussed later.

Slit-smear data obtained from USAXS measurements are shown as plots of the intensity- I versus the wave vector- q in Figure 4.9 through 4.11 for specimens at the different aging intervals corresponding to the three pre-solution treatment cases. It should be mentioned that the wave vector is inversely related to the real space dimension of the scattering particles. A typical I versus q plot shows two or three linear regions (with finite slopes) separated by plateau(s) in between. Each linear region is referred to as a Guinier region that corresponds to scattering from a distinct size distribution of particles. Guinier region(s) in the high q region correspond to scattering from the γ' distribution(s) because of their relatively small real space dimensions. The linear region in the low q regime may be attributed to scattering from relatively larger microstructural features such as the grain structure and carbides. The clear presence of a Guinier region in the high q regime was noted in all the aged specimens for times ranging from 0.1 hrs to 100 hrs for the three pre-solution-treatment cases. This is a clear indication of the existence of γ' precipitates even at the smallest aging times, which could not be seen in the SEM. Plots of I vs q were data-fitted using a least squares fitting tool in the Igor Pro package for obtaining the γ' size distribution, the mean size- $\langle r \rangle$ and the volume fraction- f_v , by assuming a lognormal size distribution.

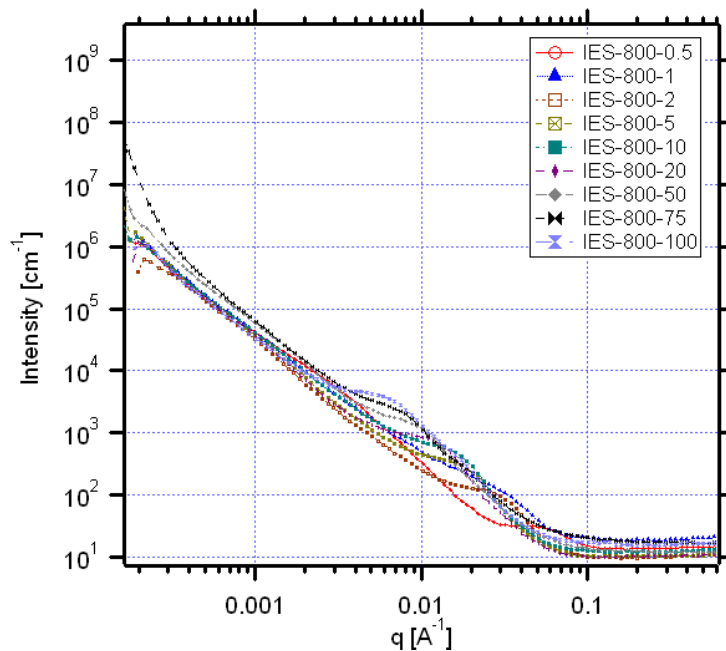


Figure 4.9 Plot of normalized USAXS intensity versus the wave vector for specimens solution-treated at 1045°C (denoted by ‘E’), stabilized at 1045°C and subsequently aged at 800°C for times up to 100 hrs.

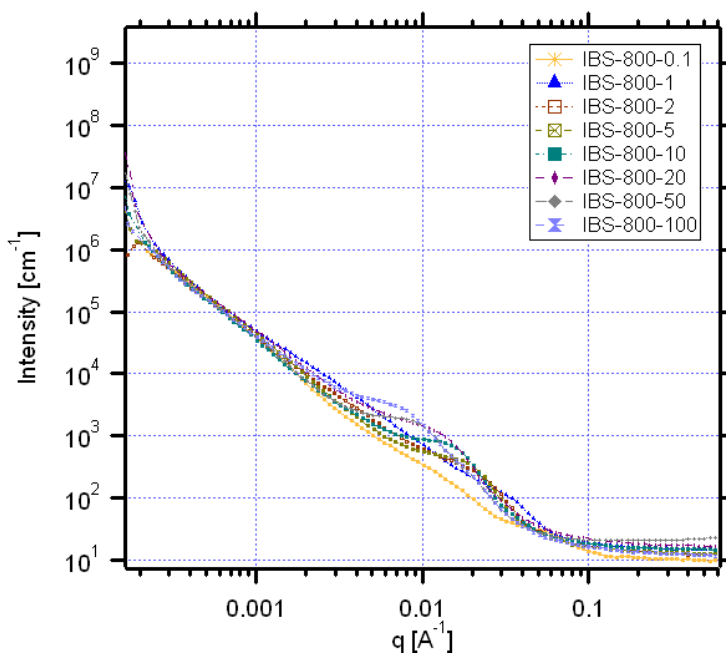


Figure 4.10 Plot of normalized USAXS intensity versus the wave vector for specimens solution-treated at 1090°C (denoted by ‘B’), stabilized at 1045°C and subsequently aged at 800°C for times up to 100 hrs.

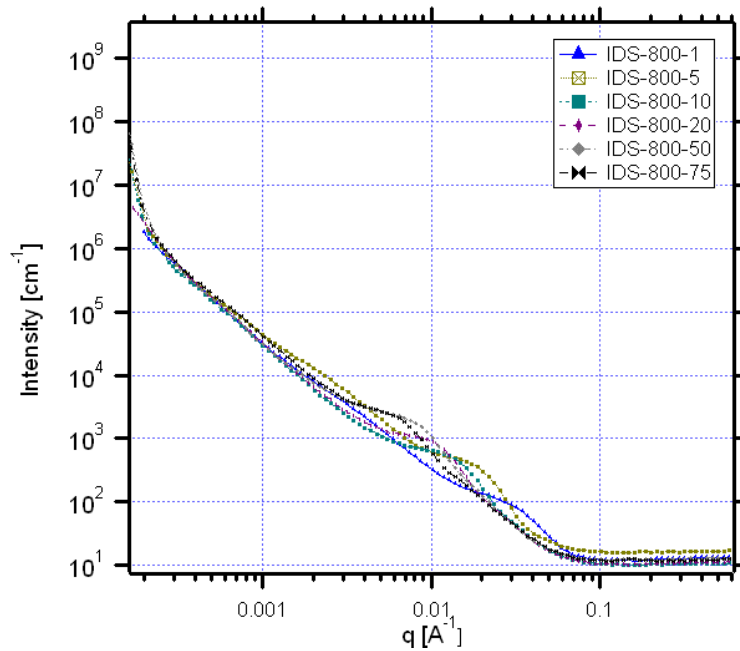


Figure 4.11 Plot of normalized USAXS intensity versus the wave vector for specimens solution-treated at 1145°C (denoted by 'D'), stabilized at 1045°C and subsequently aged at 800°C for times up to 100 hrs.

scattering particles. A typical I versus q plot shows two or three linear regions (with finite slopes) separated by plateau(s) in between. Each linear region is referred to as a Guinier region that corresponds to scattering from a distinct size distribution of particles. Guinier region(s) in the high q region correspond to scattering from the γ' distribution(s). The linear region in the low q regime may be attributed to scattering from relatively larger microstructural features such as the grain structure and carbides. The clear presence of a Guinier region in the high q regime was noted in all the aged specimens for times ranging from 0.1 hrs to 100 hrs for the three pre-solution-treatment cases. This is a clear indication of the existence of γ' precipitates even at the smallest aging times, which could not be seen in the SEM. Plots of I vs q were data-fitted using a least squares

fitting tool in the Igor Pro package for obtaining the γ' size distribution, the mean size- $\langle r \rangle$ and the volume fraction- f_v , by assuming a lognormal size distribution.

4.1.2 Analysis and Discussion

The increase in the lattice parameter with solution-treatment temperature shown in Figure 4.3 is because of the thermal dilatation of the lattice and lattice relaxation around vacancies that form at the solution-treatment temperature¹². It is however not possible to obtain the vacancy concentration just from x-ray lattice parameter measurements. A measure of the quenched-in vacancy concentration can only be obtained if simultaneous dilatometric measurements are conducted along with the lattice parameter measurements¹². There is no doubt however, that the quenched-in vacancy concentration should increase with increasing solution-treatment temperature. The quenched-in vacancy concentrations corresponding to the three solution-treatment temperatures were computed by making the following assumptions- (a) matrix is pure Ni and (b) vacancy formation enthalpy (ΔH_f^v) of 1.72 eV for Ni obtained from positron annihilation spectroscopy⁴⁰. The concentration of monovacancies as a function of temperature is given by the following expression:

$$C_v = A \exp\left(-\frac{E_f^v}{kT}\right) = \exp\left(\frac{S_f^v}{k}\right) \exp\left(-\frac{E_f^v}{kT}\right) \quad (1)$$

where, E_f^v and S_f^v are the formation energy and entropy associated with a monovacancy.

However, $\Delta H_f^v = E_f^v - PV_f^v \approx E_f^v$ and $\Delta G_f^v = \Delta H_f^v - TS_f^v \approx \Delta H_f^v$, where P, V_f^v and ΔG_f^v refer to the pressure, volume of a monovacancy and the free energy associated with the formation of a monovacancy respectively. It is assumed that the entropy contribution is

negligible as compared to the formation enthalpy term. Incorporating these assumptions, the expression for C_v may be rewritten as:

$$C_v \approx \exp\left(-\frac{\Delta H_f^v}{kT}\right) \quad (2)$$

Based on this expression, the quenched-in vacancy concentration at solution-treatment temperatures of 1045°C, 1090°C and 1145°C were computed to be 2.65×10^{-7} , 4.37×10^{-7} and 7.72×10^{-7} respectively.

The as-stabilized lattice parameters of specimens previously solution-treated at 1090°C and 1145°C show a good match as seen from Table 4.1. It is however possible that the formation of vacancy clusters may impact the measured values. Quenched-in vacancies from higher temperatures (1090°C and 1145°C) after the solution-treatments may aggregate to form divacancies during the stabilization treatment. The lattice around a divacancy is more relaxed than around a single vacancy¹². Therefore, the increase in the lattice parameter brought about by a divacancy is lower than that due to two single vacancies. For this reason, the presence of divacancies can result in a lower value of the measured parameter than if all the vacancies were to exist as single ones.

Next, the resistivity plot of solution-treated and stabilized specimens shown in Figure 4.4 is discussed. The contributions to solution-treated resistivity can arise from the solid solution elements in the Ni-rich matrix phase (γ), excess quenched-in vacancies, carbide distribution and grain boundaries. The effect of carbides and grain boundaries on the overall resistivity is presumed to be a minor one, considering the rather large scale of dispersion of these features. The concentration of quenched-in vacancies (in pure Ni matrix) as discussed in a previous paragraph is in the range of 10^{-7} to 10^{-6} for the above

solution temperatures. The concentration of solid solution impurity elements is several orders of magnitude higher than the excess vacancy concentration (see Table 3.1 for concentration of solid-solution elements). Therefore, it is proposed that the measured resistivity in the solution-treated condition is primarily influenced by the presence of solid-solution alloying elements. The observed differences in resistivity among the different solution-treatments may be due to slight variations in the quench or in the alloy composition from one bar to another.

Since the stabilization treatment is also conducted above the γ' solvus, the arguments presented for explaining the resistivity of solution-treated specimens are equally valid here.

Next, the results from USAXS analysis, SEM observations and four-point probe resistivity are discussed. The mean γ' precipitate radius- $\langle r \rangle$ plotted as a function of the aging time is shown in Figure 4.12 for the three pre-solution-treatment cases E (1045°C), B (1090°C) and D (1145°C) upon aging at 800°C. A clear increase in $\langle r \rangle$ with progressive aging is seen from the figure for the three pre-solution-treatment cases. It is also evident that the specimens pre-solution-treated at 1145°C have the largest $\langle r \rangle$ of the three cases for most of the aging sampling times. These observations are in good agreement with the conclusions drawn earlier based on visual comparison of the SEM micrographs presented in Figures 4.5 through 4.7.

Lattice parameter analysis was not conducted for the present set of aged specimens with the three different pre-solution-treatments. However, lattice parameter variations in response to aging at 800°C for a different set of specimens with a pre-

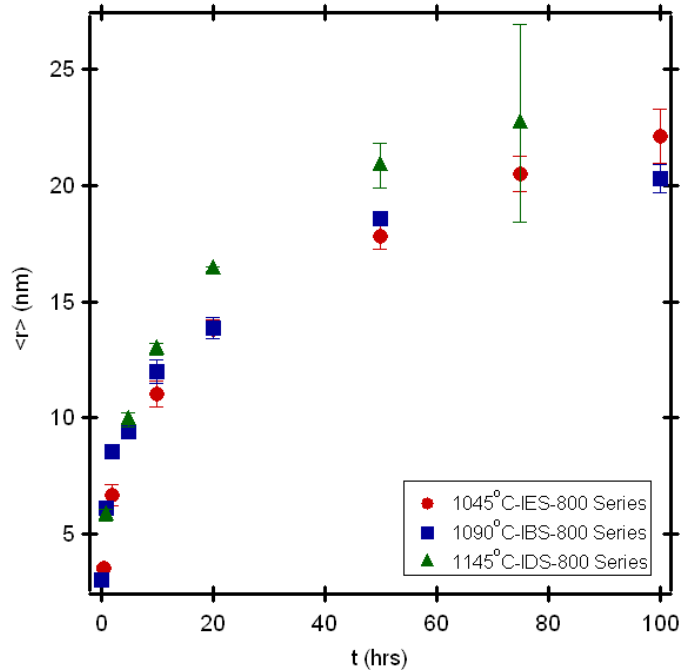


Figure 4.12 Plot of the mean γ' precipitate radius as a function of the aging time for specimens pre-solution-treated at 1045°C, 1090°C and 1145°C and aged at 800°C.

solution-treatment of 1145°C and without the stabilization treatment are presented in sections 4.2.1 and 4.2.2. The stabilization treatment (at 1045°C) results only in a slight decrease of the lattice parameter from the as-solution-treated condition (for 1145°C and 1090°C) as discussed earlier based on the data in Table 4.1. It is expected that the lattice parameter changes that will ensue upon aging at 800°C in the present sets of specimens will be very similar to that presented later.

The increase in the DC four-point probe resistivity upon initial aging from the as-stabilized condition (with the exception of the IES (1045°C solution-treated + 1045°C stabilized) specimen) was mentioned in the results section, with reference to Figure 4.8. The only plausible explanation for this rise is due to the presence of very fine γ'

precipitates that form upon aging. Their presence is clearly confirmed via USAXS experiments as mentioned in an earlier paragraph, although they were not sighted in the SEM. The increase in resistivity seen in the early stages of aging is dependent on two factors, viz. the interparticle spacing- λ between the γ' precipitates and the mean free path- Λ of the conduction electrons in the material. The γ' interparticle spacing is directly related to the mean γ' precipitate radius- $\langle r \rangle$. The closer the value of $\langle r \rangle$ to Λ , the more effective the γ' size distribution is in scattering the conduction electrons and therefore the greater the resistivity. The classical estimate of Λ in pure nickel using Drude's free electron model⁹ is computed to be 0.3 nm, which compares to an $\langle r \rangle$ of 3 nm for the aged specimen at 0.1 hrs with the 1090°C pre-solution-treatment from USAXS analysis. The exact position of the resistivity maximum- ρ_{max} that would correspond to a critical γ' radius- $\langle r_c \rangle$ leading to the maximum scattering of conduction electrons⁸, is unknown from the present data. This is due to the lack of data for sampling times below 0.1 hrs. The increase in resistivity up to ρ_{max} if observed, may be attributed to the nucleation and growth phase of γ' precipitates, beyond which the resistivity decreases due to γ' coarsening. From the present data it can only be concluded that γ' nucleation should have been completed by 0.1 hrs because the resistivity decreases monotonically upon further aging. Therefore, the measured resistivity data of specimens from 0.1 hrs and beyond are related to microstructural changes during γ' coarsening. This argument is supported by the progressive increase of the mean precipitate radius- $\langle r \rangle$ with aging time shown in Figure 4.12 and the SEM micrographs reported in Figures 4.5-4.7 for the three pre-

solution-treatment cases. Further discussion on the resistivity changes in the coarsening regime is presented later.

It is seen from Figure 4.12 that the growth rate- $\frac{d\langle r \rangle}{dt}$ decreases as the mean precipitate radius- $\langle r \rangle$ increases. This may be understood by examining the simplified expression for the maximum growth rate- $\left(\frac{dr}{dt}\right)_{max}$ from Greenwood's treatment of Ostwald ripening⁶:

$$\left(\frac{d\langle r \rangle}{dt}\right) \approx \left(\frac{dr}{dt}\right)_{max} = \frac{D\sigma N_{\alpha} V_m}{2R_B T \langle r \rangle^2} \quad (3)$$

In the above equation, D is the diffusion coefficient of the solute, σ is the specific interfacial energy between the matrix (γ) and the precipitate (γ') phases, N_{α} is the solute content in equilibrium with a particle of infinite radius, V_m is the molar volume of the precipitate, R_B is the gas constant and T is the aging temperature. The decrease in the growth rate with increasing precipitate radius- $\langle r \rangle$, is featured in the above equation as an inverse proportionality with $\langle r \rangle^2$. As the precipitate becomes larger, more of the solute needs to diffuse up to the precipitate for further growth and therefore a slower growth rate is expected for larger precipitates⁶.

A plot of the precipitate density or the total no. of precipitates per cm^3 - $W(t)$ obtained from analysis of USAXS data vs logarithm of the aging time is shown in Figure 4.13 for the three pre-solution-treatment cases. The precipitate density was obtained by integrating the number distribution of precipitates (obtained upon data fitting the USAXS spectra) over the observed range of precipitate sizes. A clear decrease in $W(t)$ is noted as

coarsening proceeds with minor exceptions. This is a direct consequence of Ostwald ripening⁶, where larger precipitates continue to grow at the expense of smaller ones due to a concentration gradient in solute in the matrix regions surrounding the precipitates. At any given instant during coarsening, precipitates that are smaller than the mean radius- $\langle r \rangle$ are shrinking and eventually disappear, leading to a reduction in the precipitate density. An expression for the temporal variation of the precipitate density- $W(t)$ during coarsening was given in an earlier chapter on literature survey of coarsening. The reduction in the no. of precipitates per unit area for aging times beyond 5 hrs may be observed qualitatively from the series of SEM micrographs in Figures 4.5 through 4.7 for the three pre-solution-treatment cases.

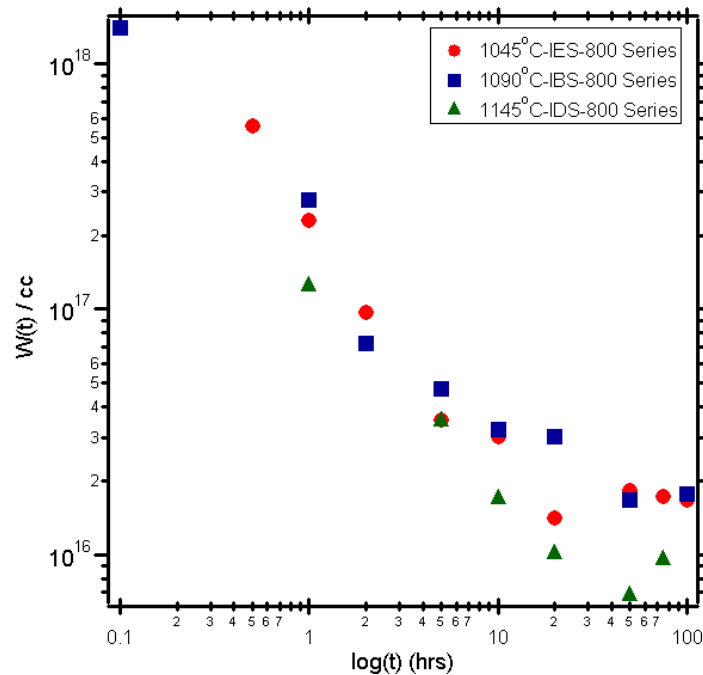


Figure 4.13 Plot of the γ' precipitate density as a function of the aging time for specimens pre-solution-treated at 1045°C, 1090°C and 1145°C and aged at 800°C.

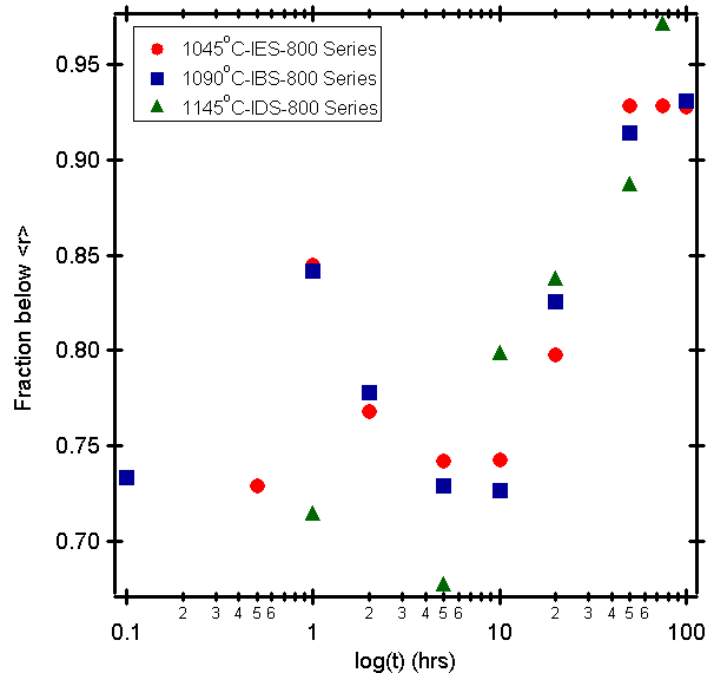


Figure 4.14 Plot of the fraction of precipitates below the mean radius as a function of the aging time for specimens pre-solution-treated at 1045°C, 1090°C and 1145°C and aged at 800°C.

Next, a plot of the number fraction of particles with radii below $\langle r \rangle$ vs the aging time is shown in Figure 4.14. It is noted that the number fraction increases with progressive aging starting from 5 hrs in the D (1145°C) set of specimens. The fraction levels off at the higher aging times in B (1090°C) and E (1045°C) sets of specimens. It is speculated that the random behavior during the early aging times (below 5 hrs) may be due to non-negligible pre-coarsening time or the incubation period before the onset of the ‘true coarsening reaction’. As per Greenwood’s treatment of Ostwald ripening⁶, particles whose radii are larger than the mean radius- $\langle r \rangle$ grow at the expense of those smaller than $\langle r \rangle$. Generally speaking, the range- $[\langle r \rangle, r_{max}]$ over which coarsening takes place also

increases with increasing $\langle r \rangle$ upon coarsening. However, the growth rate of particles larger than $\langle r \rangle$ falls as $\langle r \rangle$ increases, as expressed by equation (3), which is also experimentally observed as reported in Figure 4.11. As a consequence of this, the probability of finding a particle that is significantly larger than $\langle r \rangle$ decreases with increase in $\langle r \rangle$ due to coarsening. This is probably why the number fraction of particles with radii below $\langle r \rangle$ increases with the aging time (for times from 5 hrs) in Figure 4.14.

Figure 4.15 shows a plot of $\langle r \rangle^3$ vs t which is indicative of the coarsening kinetics in the three different pre-solution treatments cases upon aging at 800°C. The $\langle r \rangle^3$ vs t coarsening kinetics results from volume-diffusion of solute through the matrix during coarsening and is generally described using the LSW equation as follows⁶:

$$\langle r_i \rangle^3 - \langle r_o \rangle^3 = \frac{8D\sigma N_\alpha V_m}{9RT} \frac{(1 - N_\alpha)}{(N_\beta - N_\alpha)^2 \epsilon_\alpha} t = k_I t \quad (4)$$

Details on the derivation of the coarsening equation originally by Greenwood, the LSW modification and corrections to the LSW equation in cases of non-terminal solid solutions are discussed in section 2.2.1 of the literature survey chapter. It is seen that the data points for the E (1045°C) and D (1145°C) sets of specimens yield good linear fits. The straight line fit for the B (1090°C) set of specimens is only fair. However, there is no reason to expect a departure from the $\langle r \rangle^3$ vs t kinetics in this case because the aging treatments are conducted in an identical fashion to those of E and D pre-solution-treatment cases. Additionally, the coarsening sequence shown in the series of micrographs in Figures 4.5 and 4.6 for the E and B cases are very similar. The slope of

the straight line fits yields the coarsening rate constant- k_l , which is primarily dependent on the diffusion coefficient of the solute in the matrix- D , the specific interfacial energy- σ and the solute content- N_α .

It is clear from Figure 4.15 that the coarsening rate constant- k_l is larger for the D set of specimens pre-solution treated at 1145°C compared to sets B (1090°C) and E (1045°C). It is believed that this discrepancy in the coarsening kinetics originates from differences in the precipitate size distributions (PSD's) during the initial stages of coarsening. The evolution of the PSD's at the different aging sampling times is shown in Figure 4.16 as plots of the frequency of occurrence- $g(r/\langle r \rangle)$ of a particle in terms of the reduced radius- $(r/\langle r \rangle)$ for the three pre-solution-treatment cases.

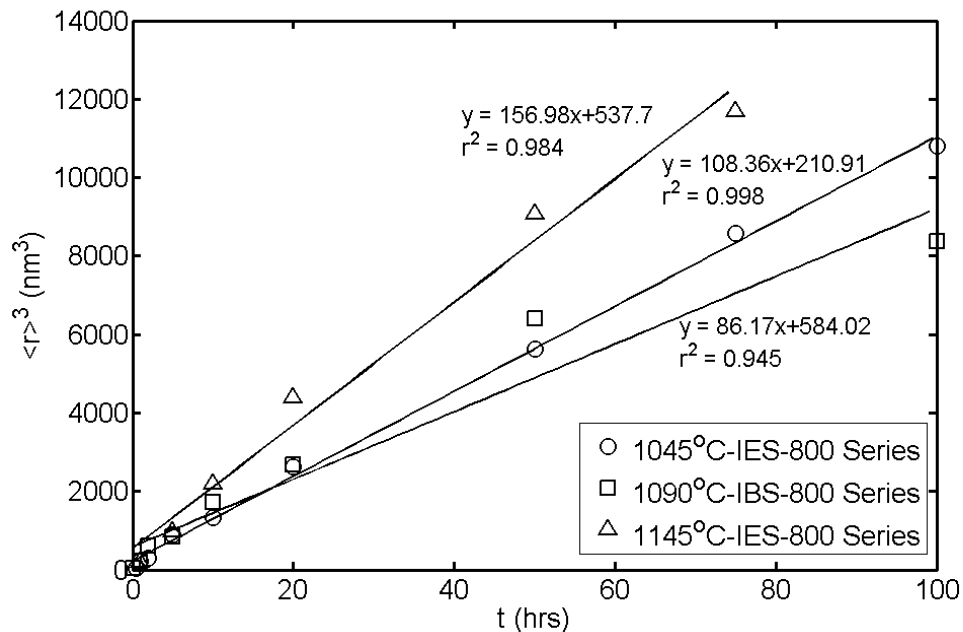


Figure 4.15 Plot of the cube of mean γ' precipitate radius as a function of the aging time for specimens pre-solution-treated at 1045°C, 1090°C and 1145°C and aged at 800°C. The slope is indicative of the coarsening kinetics.

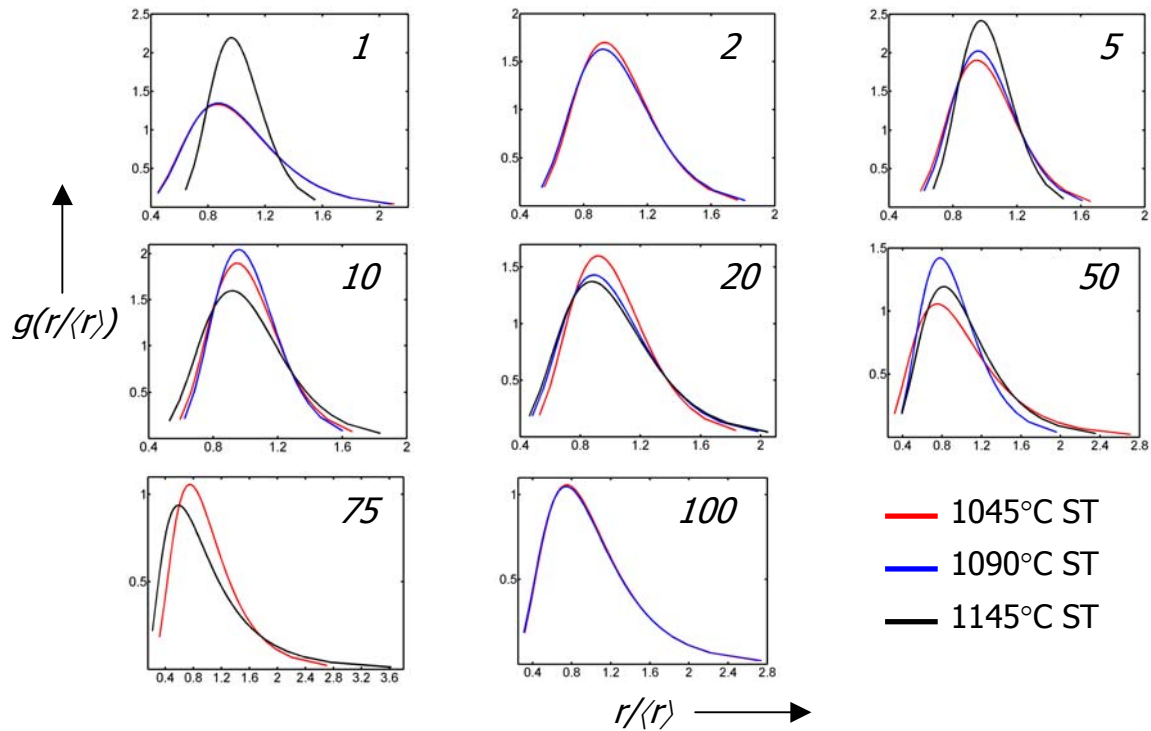


Figure 4.16 Comparison between the size distribution of γ' precipitates for the three different pre-solution-treatment cases (1045°C, 1090°C and 1145°C) shown as plots of the frequency of occurrence of a particle in terms of the reduced radius. The respective aging durations are indicated on individual plots. PSD plots at 2 and 100 hrs show distributions for 1045°C and 1090°C pre-solution treated specimens only and the plot at 75 hrs shows data for 1045°C and 1145°C pre-solution treated specimens only.

The PSD plots are derived directly from volume distribution of precipitates obtained from fitting the USAXS spectra by assuming a lognormal distribution of precipitates. It is noted from Figure 4.16 that the D (1145°C) specimens have a much tighter distribution at aging times of 1 and 5 hrs compared to the B (1090°C) and E (1045°C) cases. The reason for the cut-off values- $\frac{r_{max}}{\langle r \rangle}$ exceeding 2.0 in B and E cases (at 1 hr) is possibly because of widespread γ' nucleation times. Besides, a combined precipitation and coarsening stage is also possible prior to a true stage coarsening

reaction, if supersaturation driven growth ($\overline{N}_\alpha > N_\alpha(\langle r \rangle)$) persists⁶. Here \overline{N}_α is the average solute content of the alloy and $N_\alpha(\langle r \rangle)$ is the solute content of the matrix in equilibrium with a precipitate size of $\langle r \rangle$. In addition to having a significantly tighter distribution, the frequency of occurrence of particles just above and below $\langle r \rangle$ is much higher in D set of specimens compared to B or E at aging times of 1 and 5 hrs (see Figure 4.16 (a) and (c)). A third difference is that the specimens with the D (1145°C) pre-solution-treatment also have a lower particle density- $W(t)$ compared to the B (1090°C) and E (1045°C) cases as seen from Figure 4.13. These differences facilitate faster evolution upon coarsening in case of D specimens as compared to B or E specimens, even though they all have a similar value of $\langle r \rangle$ at the early aging times- 1 and 5 hrs (see Figure 4.12). It is suggested that these differences owe themselves to the nucleation stage of γ' , which can potentially be affected by residual excess vacancy contributions from initial solution-treatments even after the post vacancy stabilization treatment. The nucleation stage can also be influenced by non-idealities in quenching that can result in clustering of vacancies and precipitation of cooling γ' .

Beyond 5 hrs, the distributions become wider (see Figure 4.16) with cut-off values ranging between 1.6 and 2.75 typically, although the IDS-800-75 specimen (1145°C pre-solution-treatment and aged at 800°C for 75 hrs) presents a rather large cut-off value of ~ 3.6 . It is also seen that the distributions beyond 5 hrs are skewed towards larger precipitate sizes as a result of the widening. With the exception of 50 hrs, the PSD's are always wider in D (1145°C) set of specimens as compared to B (1090°C) or E (1045°C). This in addition to the lower precipitate density- $W(t)$ in case D (see Figure

4.13) is indicative of the faster coarsening kinetics. In cases B (1090°C) and E (1045°C), although the parameters- $\langle r \rangle$, $W(t)$ and the PSD's are similar for most aging intervals (see Figures 4.11, 4.13 and 4.16), some differences do exist which contribute to slightly different coarsening kinetics. The notable differences between B (1090°C) and E (1045°C) sets of specimens exist at 20 hrs and 50 hrs in the particle density- $W(t)$ and the PSD as seen from Figures 4.13 and 4.16 (e) and (f) respectively. The retarded growth kinetics in case B (1090°C) from 50 to 100 hrs is not well understood given that both $\langle r \rangle$ and $W(t)$ are very similar (to E) in both cases and it also has a significantly tighter distribution as compared to E at 50 hrs (see Figure 4.16 (f)). The lack of data at 75 hrs for B (1090°C) also makes the above interpretation difficult.

The particle size distributions for all the aging durations that belong to a specific series are summarized in Figures 4.17 (a)-(c) for the 1045°C, 1090°C and 1145°C sets of specimens respectively. In general, the PSD's show widening at longer aging times, which is evident from Figure 4.17 (a)-(c). One of the reasons for the widening of the PSD's is inherent to the nature of the coarsening process, where the range of precipitate sizes composing the distribution continues to increase with progressive coarsening. Based on the plots, it may be inferred that the PSD's reach a steady state only for the 1045°C set of specimens. This may be seen from Figure 4.17 (a), where the PSD's at 50, 75 and 100 hrs clearly overlap with each other. In case of the 1090°C and 1145°C sets of specimens, the aging experiments may need to be prolonged to attain a steady state, based on the present data (Figure 4.17 (b) and (c)).

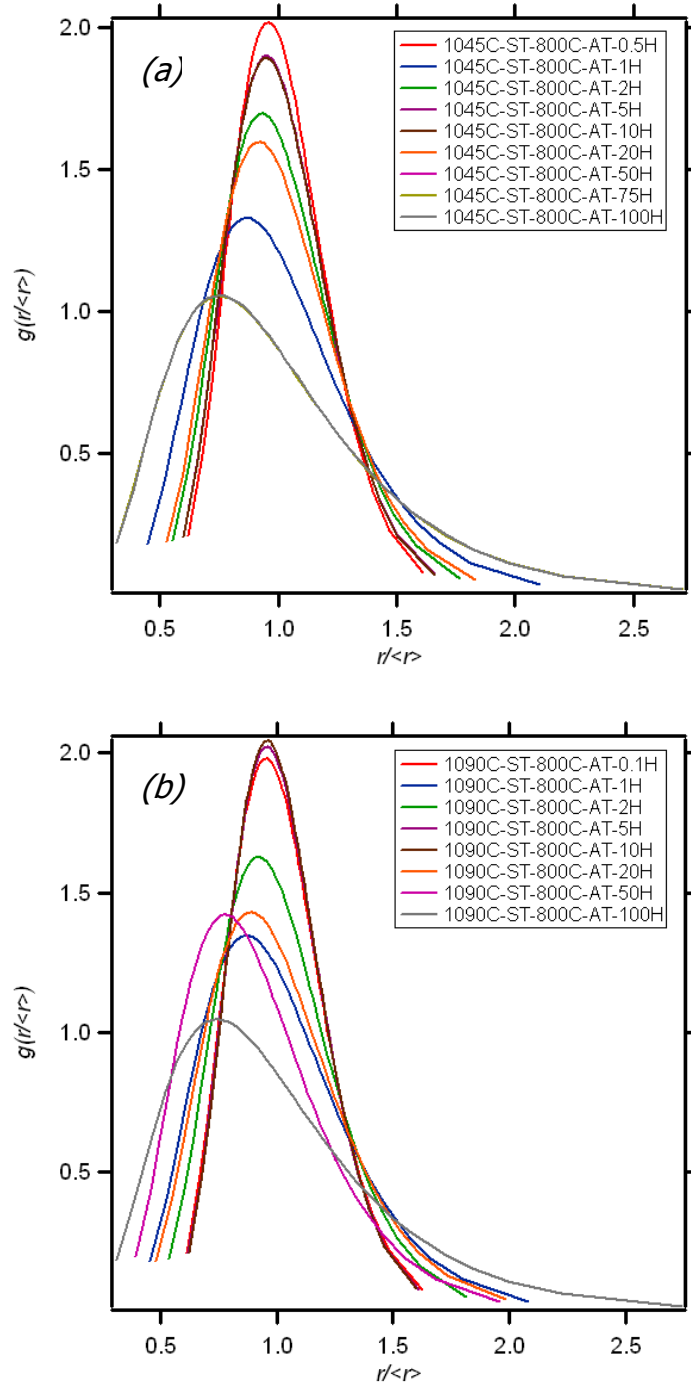


Figure 4.17 Evolution of the particle size distributions with aging time for sets of specimens pre-solution-treated at 1045°C and 1090°C in (a) and (b) respectively.

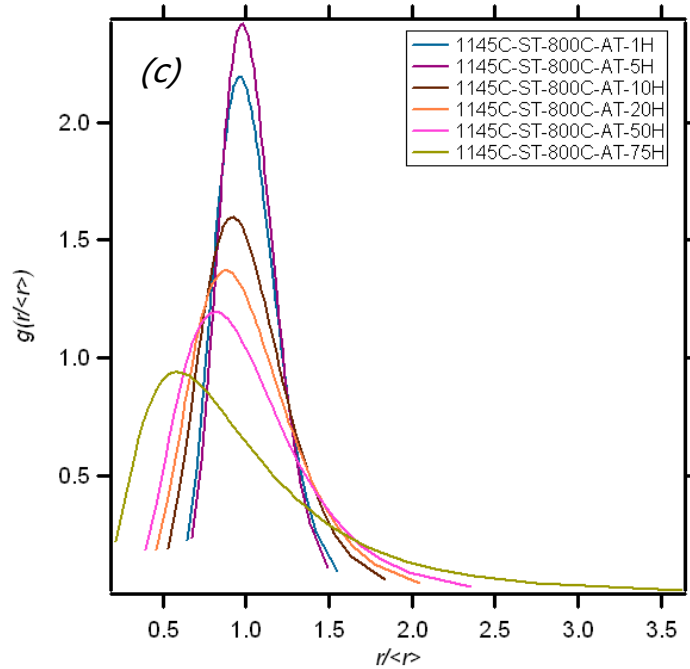


Figure 4.17 Evolution of the particle size distributions with aging time for the set of specimens pre-solution-treated at 1145°C.

A plot of the volume fraction of the γ' - f_v vs $\frac{t}{\langle r \rangle}$ is shown in Figure 4.18 for the three different pre-solution-treatment cases. The general trend that is common to all three cases is that f_v shows a plateau behavior initially followed by a steep rise for longer aging durations. It should be mentioned that data points at longer aging times presented a larger degree of scatter (not shown here), which may be an indication of some level of non-homogeneity in the γ' dispersion or the need for more extensive sampling. The plateau behavior extends up to 5 hrs in specimens with the B (1090°C) pre-solution-treatment and even longer (up to 20 hrs) in D (1145°C) and E (1045°C) cases. The reason for this initial plateau behavior is not clearly understood. The increase in f_v noted for

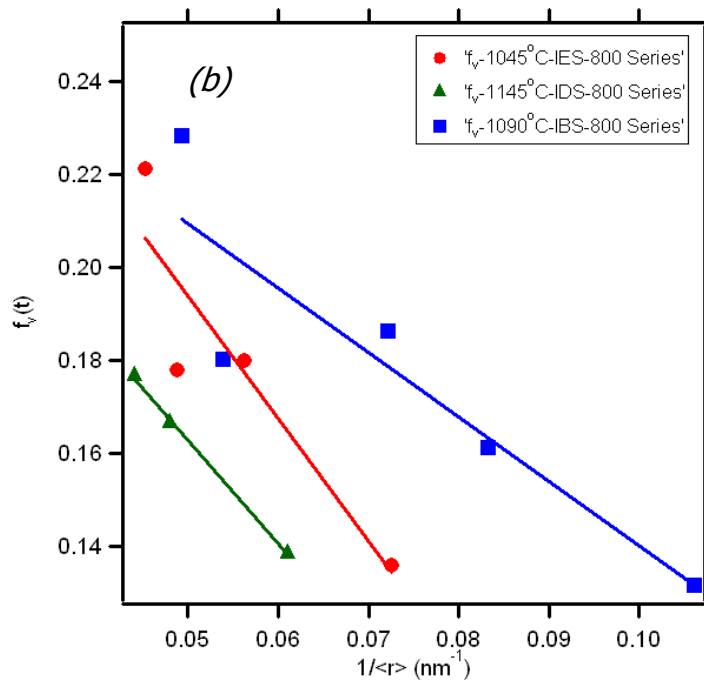
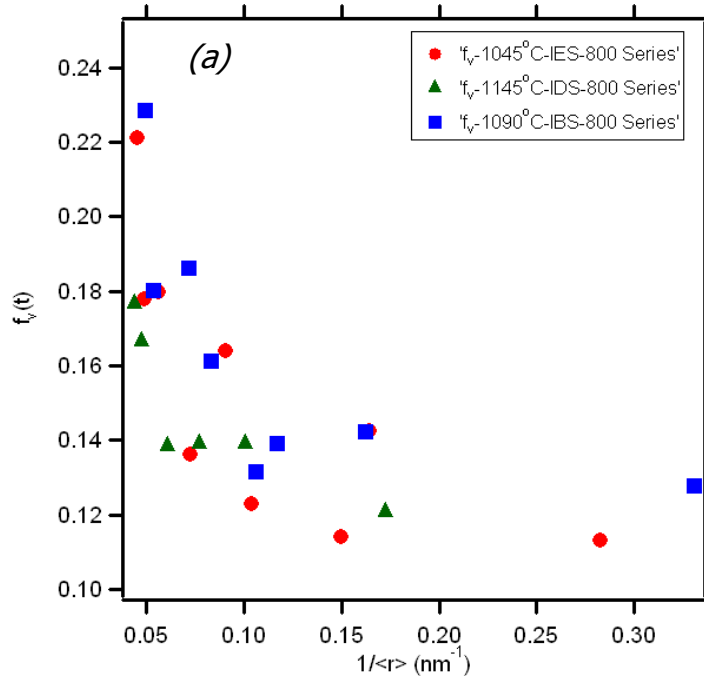


Figure 4.18 Plot of the volume fraction of the γ' precipitates as a function of $\frac{1}{\langle r \rangle}$ in (a) and linear fits to data at higher aging times in (b), for specimens pre-solution-treated at 1045°C, 1090°C and 1145°C and aged at 800°C.

longer aging times after the plateau is expected during coarsening as a result of the change of Gibbs-Thomson solubility⁶. For a finely dispersed system of precipitates, the solubility $N_\alpha(\langle r \rangle)$ can be significantly larger than N_α (for a particle of infinite radius) because of the curvature associated with the small precipitates^{6, 12}. As the mean radius- $\langle r \rangle$ increases, the solubility $N_\alpha(\langle r \rangle)$ decreases with a corresponding rise in f_v . The theoretical limit of f_v occurs at f_e , at which stage, the particle is of an infinite radius with a corresponding solubility of N_α ^{6, 11}. The temporal change of the precipitate volume fraction due to Ardell¹¹ may be written as follows:

$$f_v(t) = f_e - \frac{2(1-f_e)\sigma N_\alpha(1-N_\alpha)V_m}{RT\varepsilon_\alpha(N_\beta - N_\alpha)^2} \frac{I}{\langle r \rangle} \quad (5)$$

Figure 4.18 (b) shows linear fits for the volume fraction data at longer aging times for the three pre-solution-treatment cases, as expressed by the above equation.

Table 4.2 shows a compilation of the coarsening rate constant- k_I , the diffusion coefficient- D and the equilibrium volume fraction- f_e of the three different aging series with prior solution-treatments at 1045°C, 1090°C and 1145°C. The values of f_e were obtained from the intercepts of the linear fits of volume fraction data in Figure 4.18 (b). The diffusion coefficients for each case were computed from the coarsening rate constant- k_I and the slope of f_v plot (see equations (4) and (5)). The computed diffusion coefficients do not scale in the same order as the coarsening rate constants for the sets of specimens with 1045°C and 1090°C pre-solution-treatments, as seen clearly from Table 4.2. This lack of correlation between k_I and D values could possibly be related to the large degree of scatter in f_v data at longer aging times, which was ignored for this

analysis. Additionally, the volume fraction effect on coarsening, which is not accounted for in the present calculations, may also have an impact.

Table 4.2 List of k_l , D and f_e values obtained for the specimens aged at 800°C with the three different pre-solution-treatments.

Series/Pre-solution-treatment temp. (°C)	k_l [m ³ /sec]	D [m ² /sec]	f_e
IES/ 1045	3.01×10^{-29}	1.74×10^{-20}	0.33
IBS/ 1090	2.39×10^{-29}	2.80×10^{-20}	0.28
IDS/ 1145	4.36×10^{-29}	3.21×10^{-20}	0.27

The effect of γ' volume fraction on the acceleration of coarsening kinetics and the broadening of the PSD's has been a much debated issue over the years in coarsening studies of binary Ni-Al alloys. However, there was no evidence of the effect of volume fraction in enhancing the coarsening kinetics or widening the PSD's in a conclusive study conducted by Ardell²⁹.

Consider the following calculation of D based on Ardell's analysis of binary Ni-Al data at 800°C⁶. The values of k_l , f_e and N_α taken directly from Ardell's analysis are 5.85×10^{-28} [m³s⁻¹], 0.014 and 0.131 respectively. A typical interfacial energy- σ of 0.014 [Jm⁻²] for Ni-Al and N_β of 0.25 were also assumed⁶. The value of D at 800°C was then computed to be 1.88×10^{-18} [m²s⁻¹] by substituting the known parameters in the expression for the coarsening rate constant (see equation (4)). It is seen that this value is roughly two orders of magnitude higher than the diffusion coefficients obtained from the present data (see Table 4.2). One possible explanation for this discrepancy is because of the presence of multiple solute elements in Waspaloy, viz. Al, Ti, Mo and Cr as opposed to a single

solute in Ardell's case. The overall diffusion coefficient in a system with multiple solutes is determined by the slowest diffusing element (probably Mo), which essentially controls the coarsening rate kinetics.

The resistivity changes occurring during coarsening will be discussed finally based on the data presented already in Figure 4.8. As argued before, the observed changes in resistivity with progressive aging, 0.1 to 100 hrs for case B (1090°C) and 0.5 to 100 hrs for D (1145°C) and E (1045°C) are related to γ' coarsening. The initial decrease in resistivity in set B (1090°C), i.e. from 0.1 hrs to 1 hr is due to progressive coarsening of γ' precipitates, corresponding to an increase in $\langle r \rangle$ from 3 nm to 6.2 nm (see Figure 4.12). During this stage of coarsening, the measured resistivity- ρ_t may be argued to depend inversely on the average interparticle spacing- λ_t of the precipitate distribution. Assuming a direct proportionality between λ_t and $\langle r_t \rangle$, the following relationship may be written between ρ_t and $\langle r_t \rangle$:

$$\rho_t = \frac{A}{\langle r \rangle} \quad (6)$$

where, A is a proportionality constant. Combining the above equation with the LSW coarsening equation (2), the following is obtained:

$$\frac{1}{\rho_t^3} - \frac{1}{\rho_o^3} = k_2 t \quad (7)$$

Here ρ_o refers to the resistivity at the beginning of coarsening, which is taken to be at $t = 0$. Equations (6) and (7) essentially imply that the decrease in the measured resistivity during initial stages of coarsening is because of a decrease in the scattering efficiency of conduction electrons resulting from γ' coarsening.

This explanation is satisfactory only for the early aging durations because the scattering of the conduction electrons due to the precipitates becomes less significant as the distribution coarsens, i.e. when $\langle r \rangle > \Lambda$ ^{10, 13}. This condition seems to have been achieved after 1 hr of aging, where the resistivity becomes comparable to the initial resistivity in the as-stabilized condition, as seen from Figure 4.8. From this point and beyond, the measured resistivity of the alloy is primarily influenced by the solid solution impurities as the scattering due to γ' has only a minor effect on the overall resistivity^{10, 13}. However, as γ' coarsening proceeds the solute content of the matrix- $N_\alpha(\langle r \rangle)$ decreases progressively till the theoretical limit N_α is reached, with a corresponding increase in the volume fraction from f_v to f_e ^{6, 11}. This is discussed in the literature survey section on coarsening. Therefore the decrease in resistivity noted beyond 1 hr may be associated with the changes in the solute concentration of the matrix. The same argument is also true of aged specimens that were pre-solution-treated at 1045°C and 1145°C, for which the resistivity data are shown in Figure 4.8.

The changes in the resistivity of the matrix- $\rho_\gamma(t)$ if separated from the overall measured resistivity- $\rho_{tot}(t)$ may be related to the changes in the solute concentration $N_\alpha(\langle r \rangle)$ by the following argument. The as-stabilized resistivity- ρ_{stab} is primarily influenced by the solid solution impurities- both γ' and non γ' forming elements. For the present analysis, contributions arising from quenched-in excess vacancies are assumed to be negligible for reasons stated previously. The resistivity of the matrix- $\rho_\gamma(t)$ should be influenced by solid solution impurities consisting of non γ' formers and remainder of γ'

forming elements. Therefore, the difference- $\rho_{stab} - \rho_{\gamma}(t)$ should then yield a measure of the loss of γ' forming elements. For the sake of simplicity, it is desirable to treat all of the γ' forming elements in terms of an 'average solute'. The difference- $\rho_{stab} - \rho_{\gamma}(t)$ is then linearly related to the loss of solute concentration as follows:

$$\rho_{stab} - \rho_{\gamma}(t) = P(N_o - \overline{N_{\alpha}(t)}) \quad (8)$$

where N_o is the average solute content of the alloy initially and $\overline{N_{\alpha}(t)}$ is the average solute content after time t . The change of the mean solute concentration in the matrix- $\overline{N_{\alpha}(t)}$ as a function of time during coarsening is given by Ardell^{6, 11} as:

$$\overline{N_{\alpha}(t)} - N_{\alpha} = k_4(t - t_1)^{\frac{1}{3}} \quad (9)$$

Incorporating this relation into equation (8), the difference- $\rho_{stab} - \rho_{\gamma}(t)$ may be written as:

$$\rho_{stab} - \rho_{\gamma}(t) = P(N_o - N_{\alpha}) - Pk_4(t - t_1)^{\frac{1}{3}} \quad (10)$$

The above equation suggests that a plot of $\rho_{stab} - \rho_{\gamma}(t)$ vs $t^{\frac{1}{3}}$ should yield a linear behavior.

The resistivity contribution arising only from the matrix- $\rho_{\gamma}(t)$ is separated from the overall measured resistivity- $\rho_{tot}(t)$ by using the equation given by Böttcher⁴¹ as follows:

$$(1 - f_{\gamma}) \frac{\sigma_{\gamma} - \sigma_{tot}}{\sigma_{\gamma} + 2\sigma_{tot}} = f_{\gamma} \frac{\sigma_{\gamma'} - \sigma_{tot}}{\sigma_{\gamma'} + 2\sigma_{tot}} \quad (11)$$

In the above equation, f_v is the volume fraction of the γ' phase, σ_{tot} , σ_γ and $\sigma_{\gamma'}$ refer to the overall measured conductivity, conductivity of the γ and γ' phases respectively. The conductivity of the γ' phase- $\sigma_{\gamma'}$ is computed from Wiedemann-Franz relation using a thermal conductivity of 28.2 [$\text{Wm}^{-1}\text{K}^{-1}$] for Ni_3Al quoted by Terada et al⁴². The value of $\sigma_{\gamma'}$ is computed to be 3.76 [MSm^{-1}]. The computed values of $\rho_\gamma(t)$ are then used to plot $\rho_{stab} - \rho_\gamma(t)$ vs $t^{\frac{1}{3}}$ as shown in Figure 4.19. It is evident from the plot that the points yield a reasonable fit to a straight line, according to equation (10).

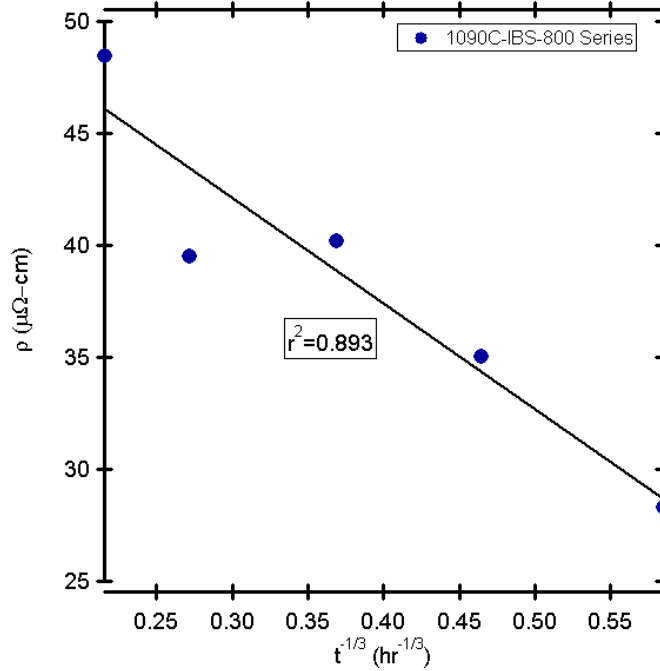


Figure 4.19 Plot of the residual resistivity- $\rho_{stab} - \rho_\gamma(t)$ versus $t^{\frac{1}{3}}$ for specimens pre-solution-treated at 1090°C and aged at 800°C. The linear fit indicates that the variations in the residual resistivity bear a good correlation to concentration loss of γ' forming elements.

4.1.3 Conclusions

The DC four-point probe resistivity of specimens in the solution-treated and as-stabilized condition is primarily affected by the presence of solid-solution alloying elements. The scatter observed in the data is attributed to slight variations in the quench from specimen to specimen, that can lead to uncontrolled events such as precipitation of cooling γ' and association or loss of vacancies.

SEM micrographs of solution-treated and as-stabilized specimens showed clear presence of faceted etch-pits mostly in square and non-regular hexagon shapes. This phenomenon is believed to be related to the condensation of quenched-in excess vacancies, which is covered in a greater depth in the next chapter.

SEM and USAXS observations indicated progressive growth of γ' precipitates upon aging at 800°C in case of all three pre-solution-treatments. It was confirmed based on resistivity measurements that the nucleation of γ' was complete within 0.1 hrs of aging at 800°C. The primary mechanism of microstructural evolution beyond 0.1 hrs was γ' coarsening.

γ' coarsening kinetics was fastest in the case of IDS-800 series as compared to IBS-800 or IES-800 series. This conclusion was supported by USAXS data in the form of $\langle r \rangle^3$ vs t and also qualitatively by SEM micrographs. Concurrently, the IDS-800 series showed a lower particle density- $Z(t)$ compared to the other series at all the aging times. The explanation for the faster kinetics in the IDS-800 series was based on the PSD plots- $g(r/\langle r \rangle)$ vs $r/\langle r \rangle$. The γ' size distribution during initial stages of aging was found to be significantly tighter in case of the IDS-800 series, which also had a lower particle density

compared to the IBS-800 or the IES-800 series. The faster evolution in the IDS-800 series is attributed primarily to these reasons. The above mentioned differences in the PSD's are thought to arise during the nucleation stage itself, which could be affected by residual vacancy concentrations from the pre-solution-treatments.

The volume fraction of γ' - $f_v(t)$ also derived from USAXS experiments showed a linear behavior with $\frac{1}{\langle r \rangle}$ for longer aging durations as a consequence of the Gibbs-Thomson solubility relation.

The coarsening rate constants for the present data at 800°C are at least an order of magnitude lower than that reported for binary Ni-Al alloys in the literature. A plausible explanation for this is because of the presence of multiple solutes in Waspaloy, in which case, the slowest diffusing element controls the overall coarsening kinetics. The diffusion coefficients computed from the coarsening data did not correlate with the kinetic behavior predicted by the coarsening rate constants for the sets of specimens with 1045°C and 1090°C prior solution-treatments. The reason for this is speculated to be due to the effect of volume fraction of precipitates on coarsening, which is not taken into account in the calculations.

The resistivity decrease during initial stages of coarsening (up to 2 hrs) is attributed to the decrease in the scattering power of the γ' precipitate distribution. The resistivity variations beyond this stage are attributed to changes in the 'average solute' concentration in the matrix, as the scattering contribution from the precipitates becomes less significant. Beyond 2 hrs, the difference- $\rho_{stab} - \rho_\gamma(t)$ is related to the loss of 'average solute' concentration- $N_o - \overline{N_\alpha(t)}$. A linear relationship between $\rho_{stab} - \rho_\gamma(t)$

and $t^{-\frac{1}{3}}$ is obtained by expressing the concentration loss in terms of t using Ardell's relationship.

4.2 Microstructural evolution in Set III experiments

4.2.1 Characterization Results

In this section, the results from microstructural evolution in specimens aged at 725°C, 800°C and 875°C will be presented in the form of SEM micrographs and data from lattice parameter and DC four-point probe resistivity measurements. The underlying objective is to correlate the resistivity changes to the variations in the microstructure upon evolution due to progressive aging.

Figures 4.20 (a) and (b) show the sub-grain microstructures of two different solution-treated specimens in the etched condition. These microstructures were highlighted using an etchant comprising 10 ml each of HCl, HNO₃, H₂O and 0.3g of molybdic acid reagent (will be referred to as 'A-etchant'). The microstructures in the solution-treated condition show the presence of etch pits with polygon shapes, predominantly as a square or a non-regular hexagon. It is observed that the shape of the etch-pits within a single grain is always a constant, which is demonstrated in Figure 4.20 (c) in two grains across a grain boundary. The micrograph in Figure 4.20 (c) was acquired from a different specimen also quenched directly from the super-solvus regime. Moreover, the etch-pits are clearly aligned along a specific direction within the grain. The occurrence of the etch-pits as squares or hexagons varied only from one grain to another, possibly depending on the grain orientation. No presence of γ' was to be seen even in the high resolution micrographs.

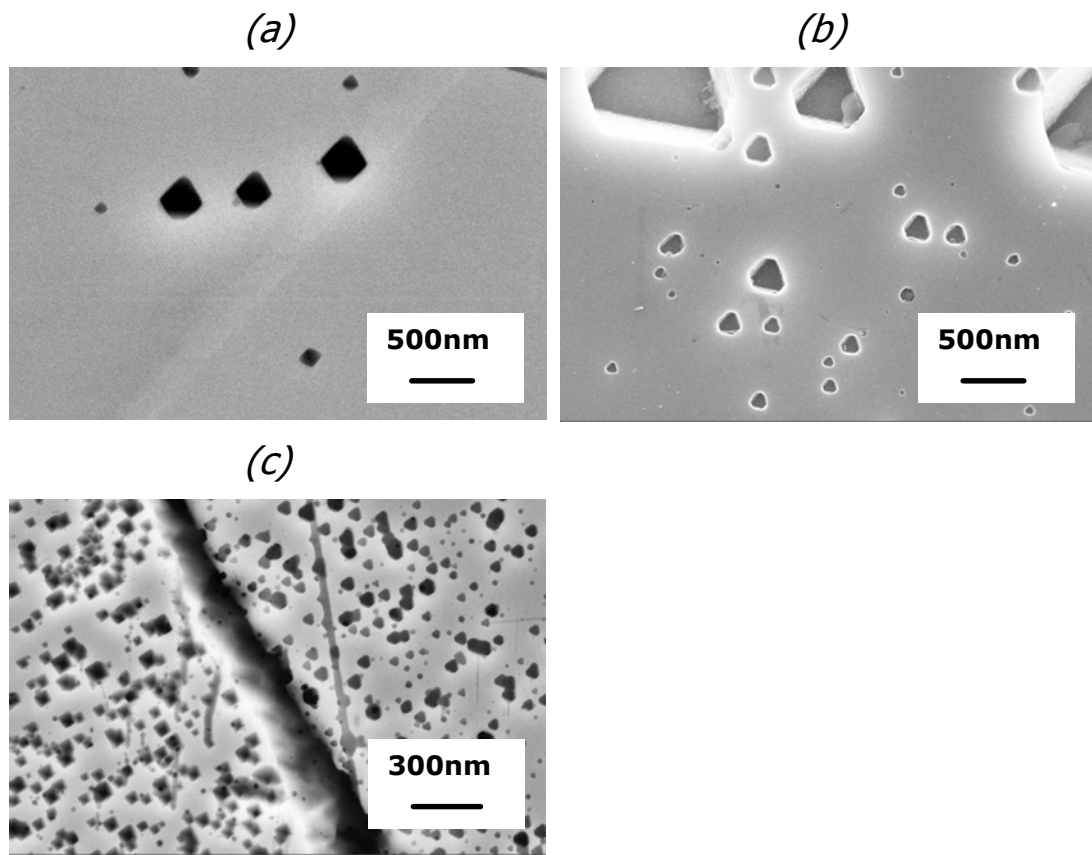


Figure 4.20 Solution-treated microstructures (at 1145°C) showing polygonal etch-pits primarily as square and non-regular hexagon shapes in (a) and (b) respectively. The micrograph in (c) shows etch-pits of different shapes in two neighboring grains.

SEM micrographs representing microstructural evolution upon aging at 725°C are reported in the series of micrographs in Figure 4.21. All the microstructures shown here were highlighted using the A-etchant, which was used previously in the case of solution-treated specimens (Figure 4.20). The polygonal etch-pit shapes evidenced in the solution-treated microstructures are also seen here for the early aging durations of 0.5 hrs and 1 hr in Figures 4.21 (a) and (b) respectively. Upon further aging, the polygonal shapes transform progressively into rounded pit-shapes at 2 hrs (Figure 4.21 (c)) and into more irregular shapes at 5 and 10 hrs (Figures 4.21 (d) and (e)). There is no clear evidence of γ'

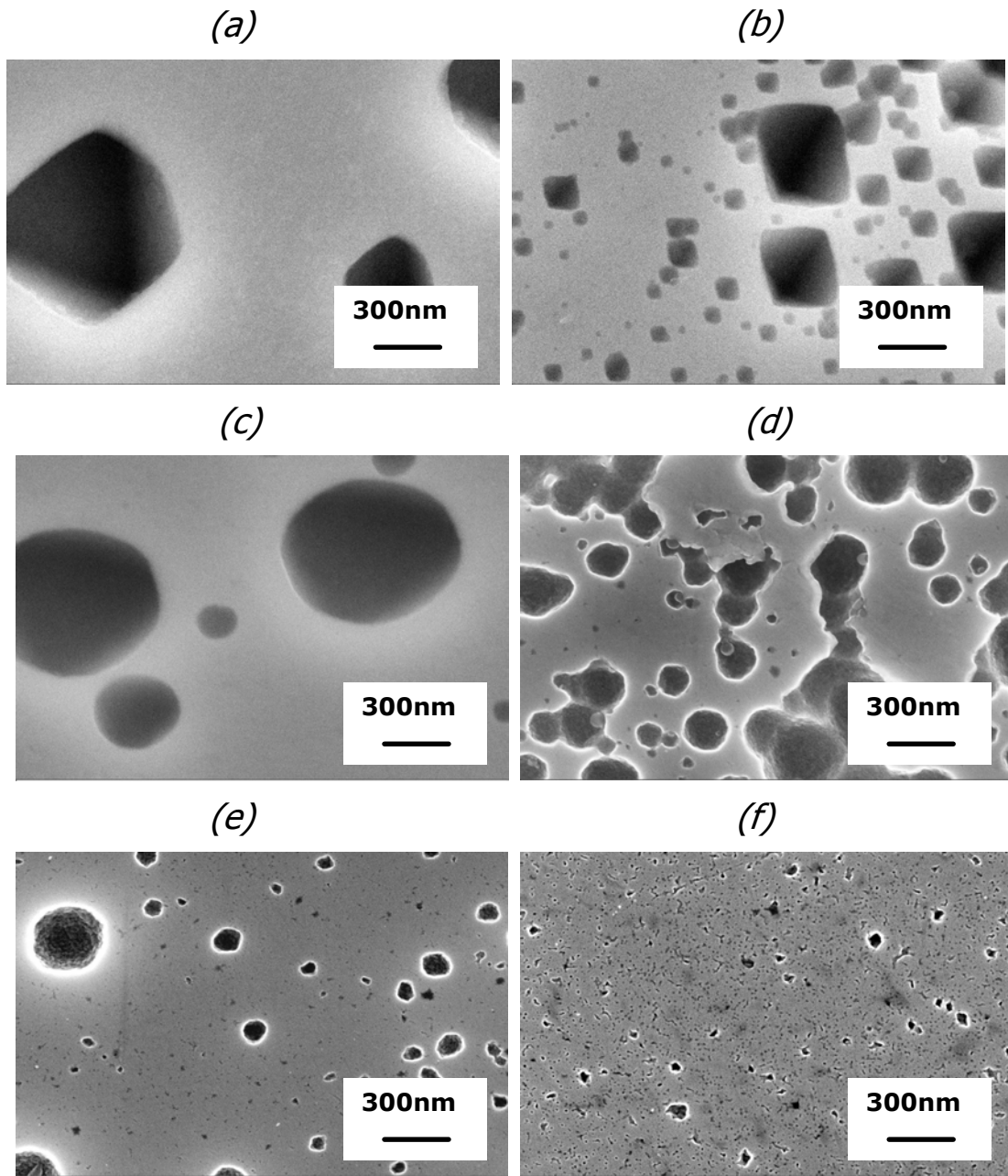


Figure 4.21 SEM micrographs showing microstructural evolution upon aging at 725°C for aging times of (a) 0.5, (b) 1, (c) 2, (d) 5, (e) 10 and (f) 20 hrs respectively. Initial solution-treatment was conducted at 1145°C prior to aging at 725°C.

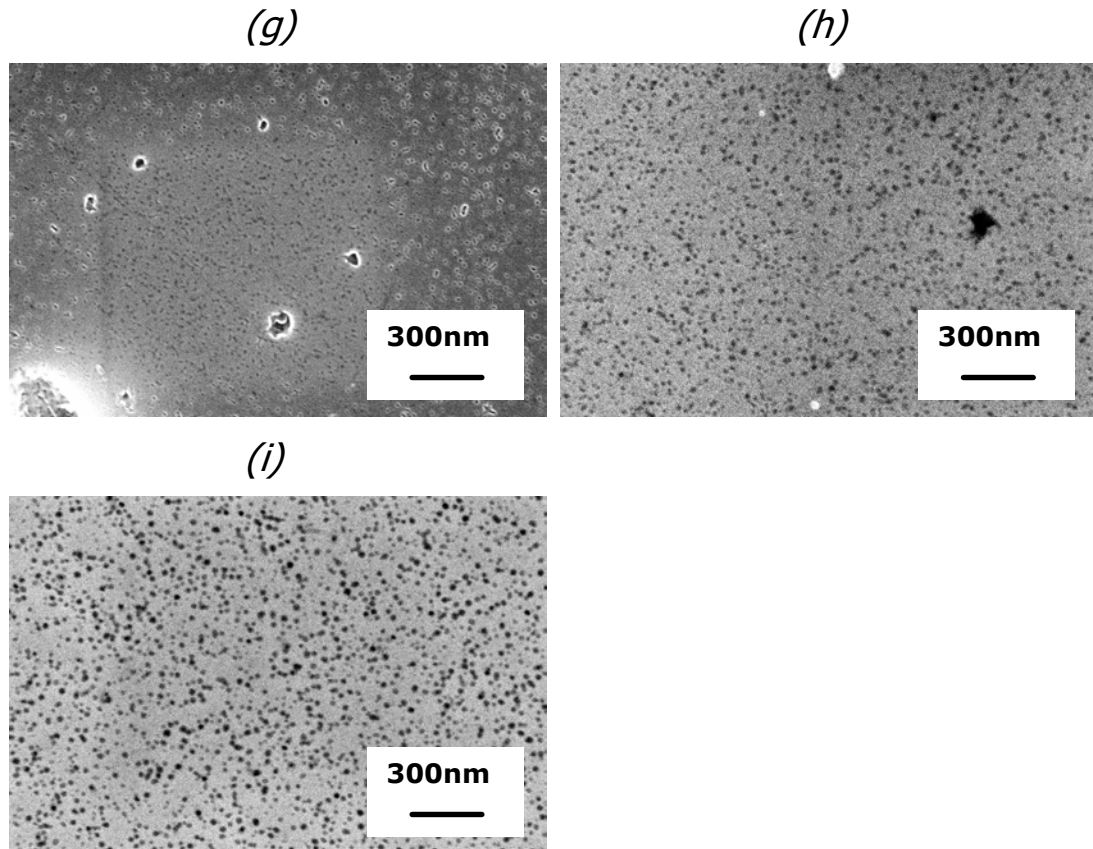


Figure 4.21 SEM micrographs showing microstructural evolution upon aging at 725°C for aging times of (g) 50, (h) 75 and (i) 100 hrs respectively. Initial solution-treatment was conducted at 1145°C prior to aging at 725°C.

that is noted from the above set of microstructures up to 10 hrs highlighted using the A-etchant. Micrographs corresponding to longer aging times- 20 to 100 hrs, show the presence of γ' clearly as seen from Figures 4.21 (f) through (i) respectively. The microstructural evolution for these longer aging times consists of progressive γ' growth alongside the gradual annihilation of the irregular etch-pit features.

SEM and AFM micrographs of specimens corresponding to aging durations of 1, 2 and 10 hrs highlighted using the B-etchant are shown in Figure 4.22. The B-etchant caused the preferential removal of the γ phase retaining the γ' phase, creating the

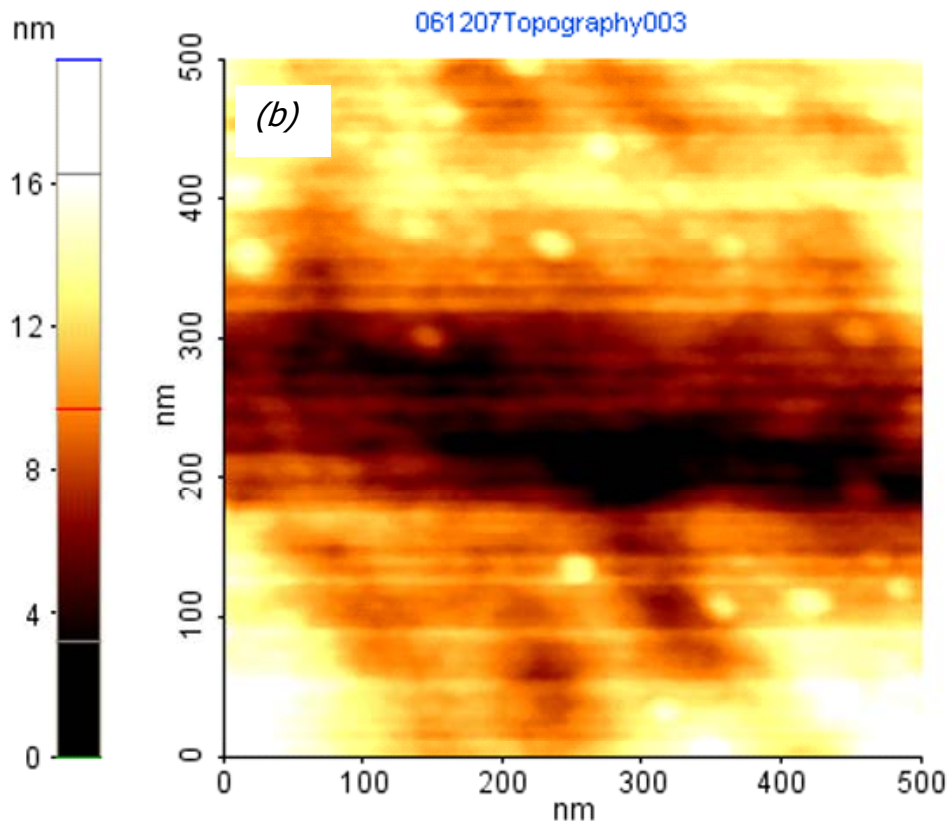
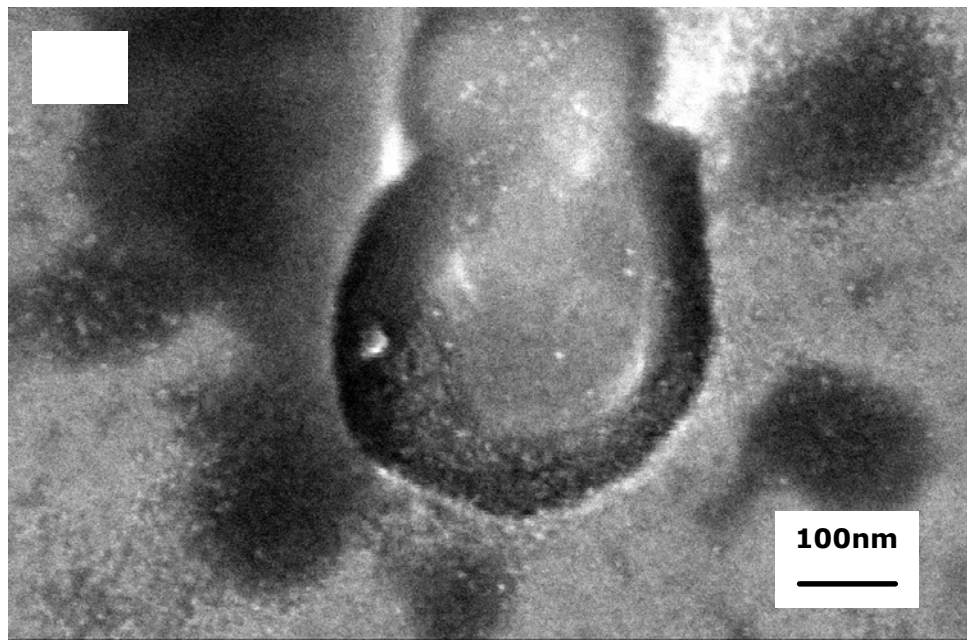


Figure 4.22 SEM and AFM micrographs of specimen after 1 hr of aging at 725°C shown in (a) and (b) respectively.

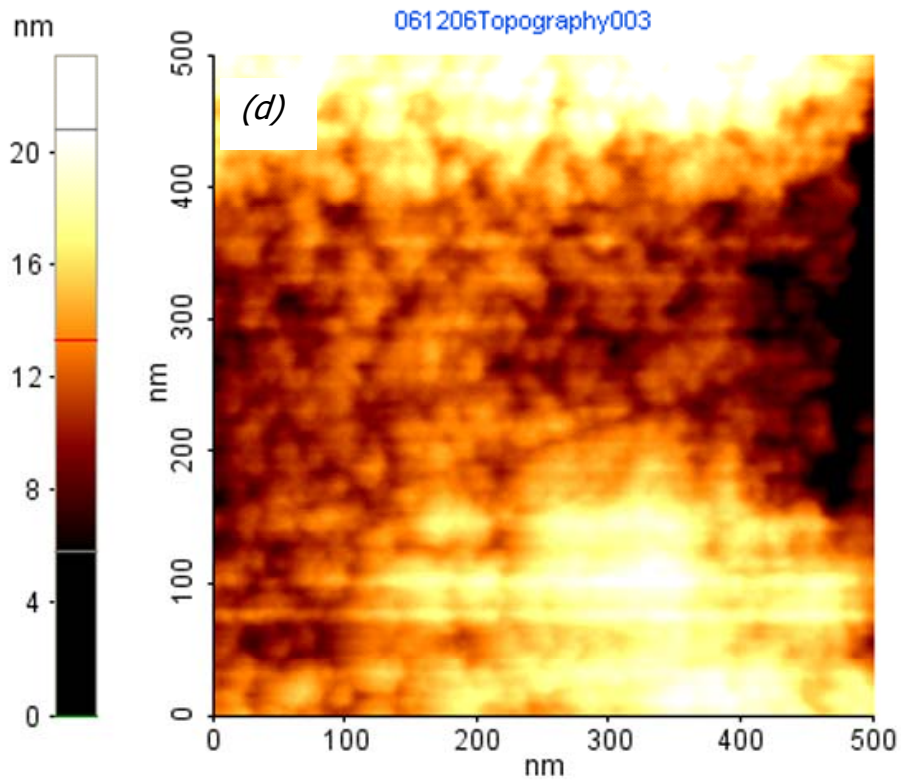
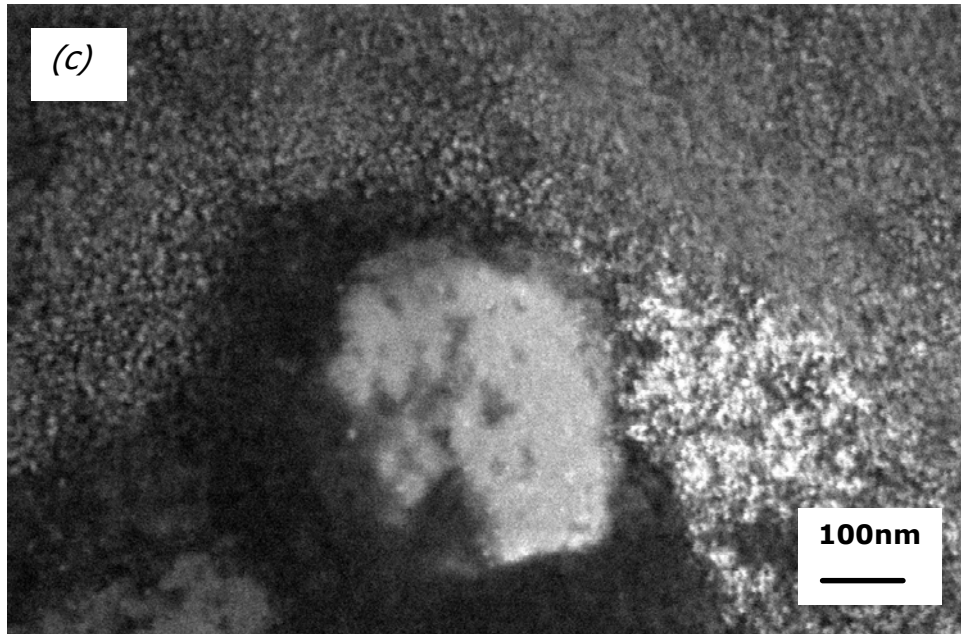


Figure 4.22 SEM and AFM micrographs of specimen after 2 hrs of aging at 725°C shown in (c) and (d) respectively.

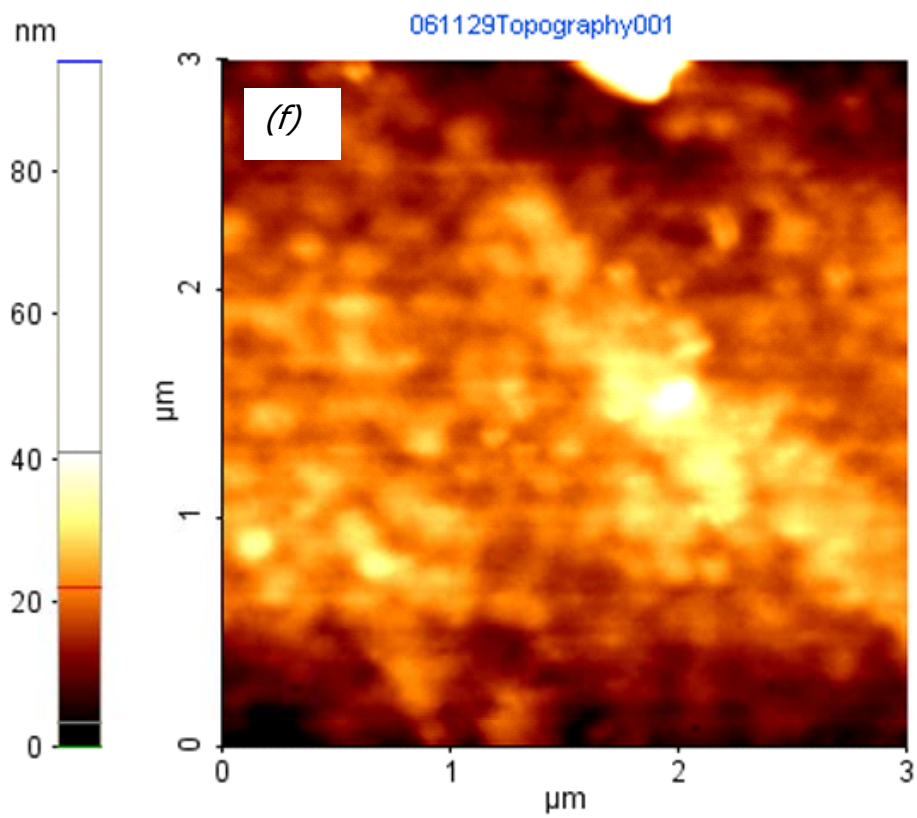


Figure 4.22 SEM and AFM micrographs of specimen after 2 hrs of aging at 725°C shown in (e) and (f) respectively.

opposite effect of the A-etchant. Besides, the B-etchant did not produce any etch-pit contrast that was observed using the A-etchant. The presence of γ' precipitates at 1, 2 and 10 hrs is seen from Figures 4.22 (a) & (b), (c) & (d) and (e) and (f) respectively. This clearly confirms the existence of the γ' precipitates at shorter aging times, despite the fact

The set of micrographs demonstrating microstructural evolution in response to aging at 800°C and 875°C is shown in Figures 4.23 and 4.24 respectively. The sequence of events described in case of the evolution at 725°C is also true of the higher temperatures. However, the snapshots of all the events cannot be captured at the same aging intervals because of the faster kinetics. In the case of the 800°C series for instance, the evolution begins with the etch-pits mostly in rounded or irregular shapes after 0.5 hrs of aging (see Figure 4.23 (a)). Here, the irregular shaped etch-pit features are annihilated much faster than that was seen for the 725°C series (see Figure 4.21). The clear presence of γ' was noted after 2 hrs of aging and further aging up to 100 hrs led to progressive γ' growth as may be seen from Figures 4.23 (c) through (i). The faster kinetics at 800°C relative to 725°C is obvious from the faster etch-pit evolution and additionally, the larger γ' precipitate sizes resulting from aging at the different sampling times (see Figures 4.21 and 4.23).

The microstructures resulting from aging at 875°C is shown in the set of micrographs in Figures 4.24 (a) through (i). The kinetics of microstructural evolution is evidently the fastest here of all the aging temperatures investigated, both in terms of the etch-pit evolution and γ' growth. For the 875°C series, the etch-pit evolution seemed to be complete within 2 hrs of aging (see Figures 4.24 (a) through (c)). The precipitate sizes at the different aging sampling times are also the largest here of the three aging

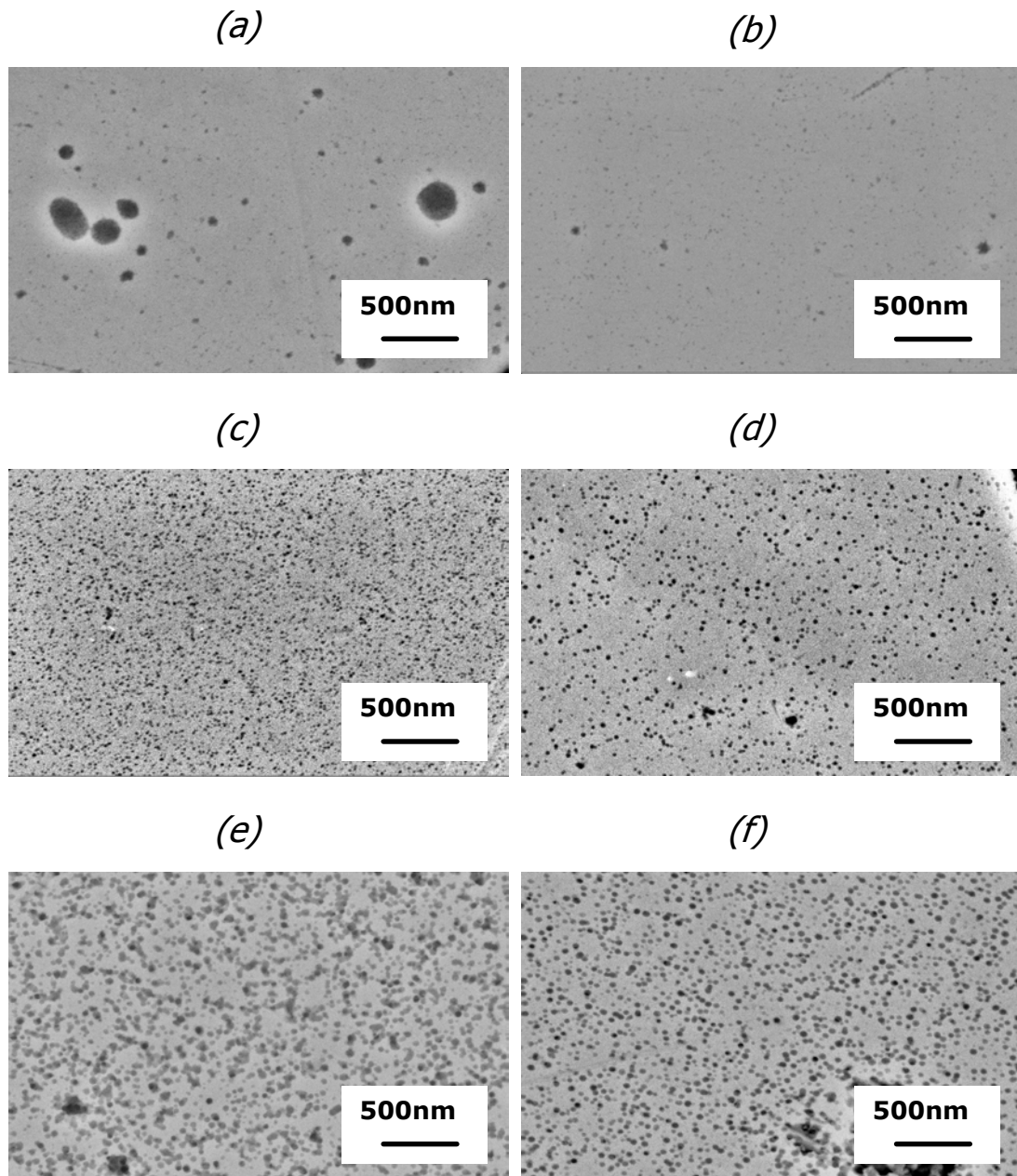


Figure 4.23 SEM micrographs showing microstructural evolution upon aging at 800°C for aging times of (a) 0.5, (b) 1, (c) 2, (d) 5, (e) 10 and (f) 20 hrs respectively. Initial solution-treatment was conducted at 1145°C prior to aging at 800°C.

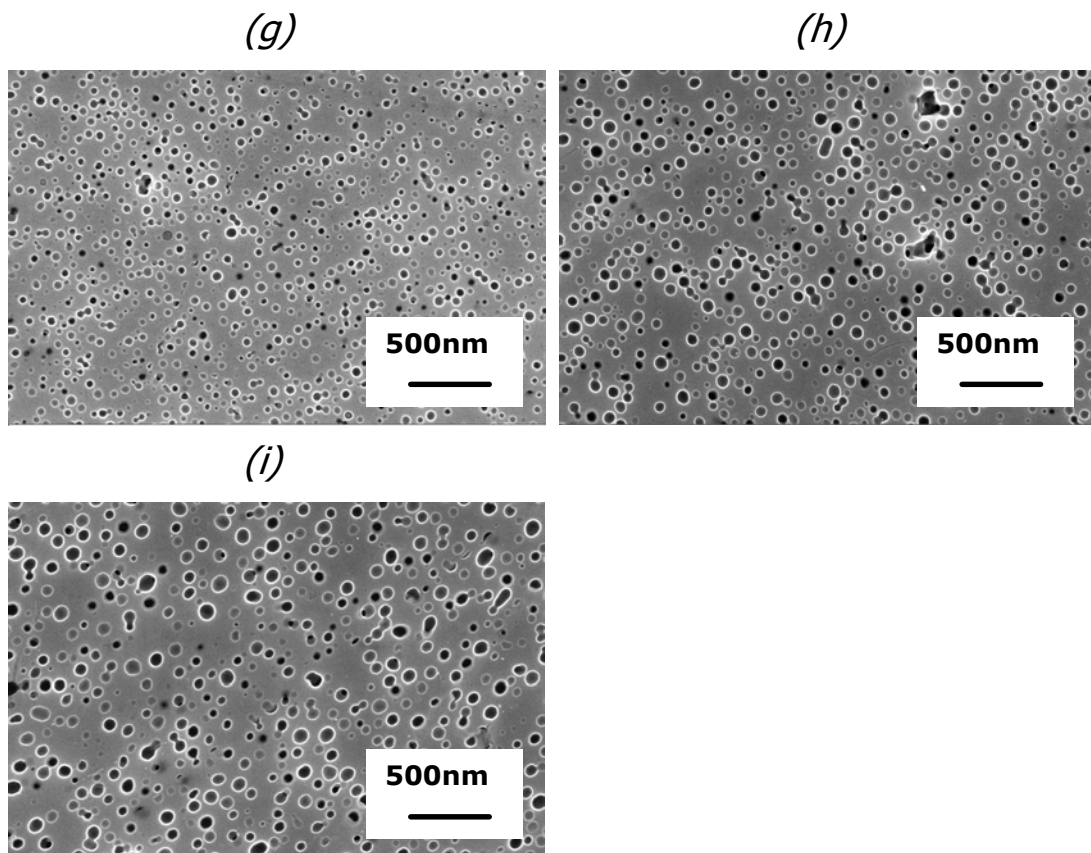


Figure 4.23 SEM micrographs showing microstructural evolution upon aging at 800°C for aging times of (g) 50, (h) 75 and (i) 100 hrs respectively. Initial solution-treatment was conducted at 1145°C prior to aging at 800°C.

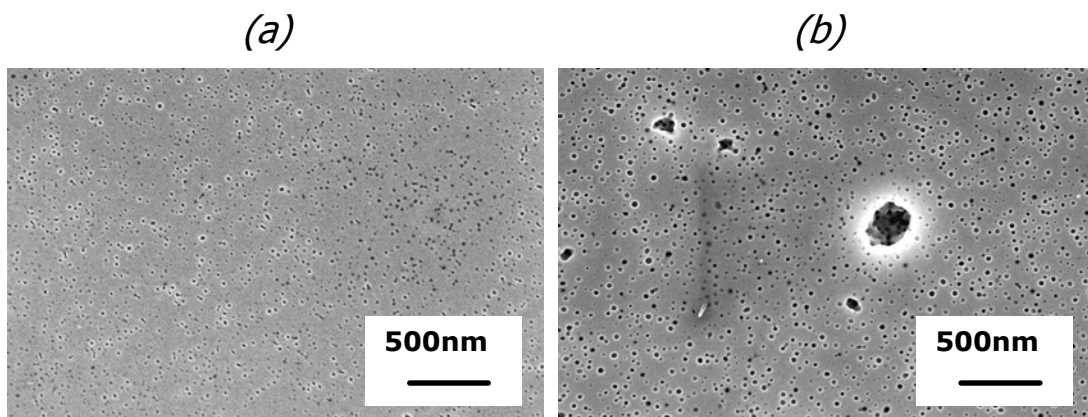


Figure 4.24 SEM micrographs showing microstructural evolution upon aging at 875°C for aging times of (a) 0.5 and (b) 1hr respectively. Initial solution-treatment was conducted at 1145°C prior to aging at 875°C.

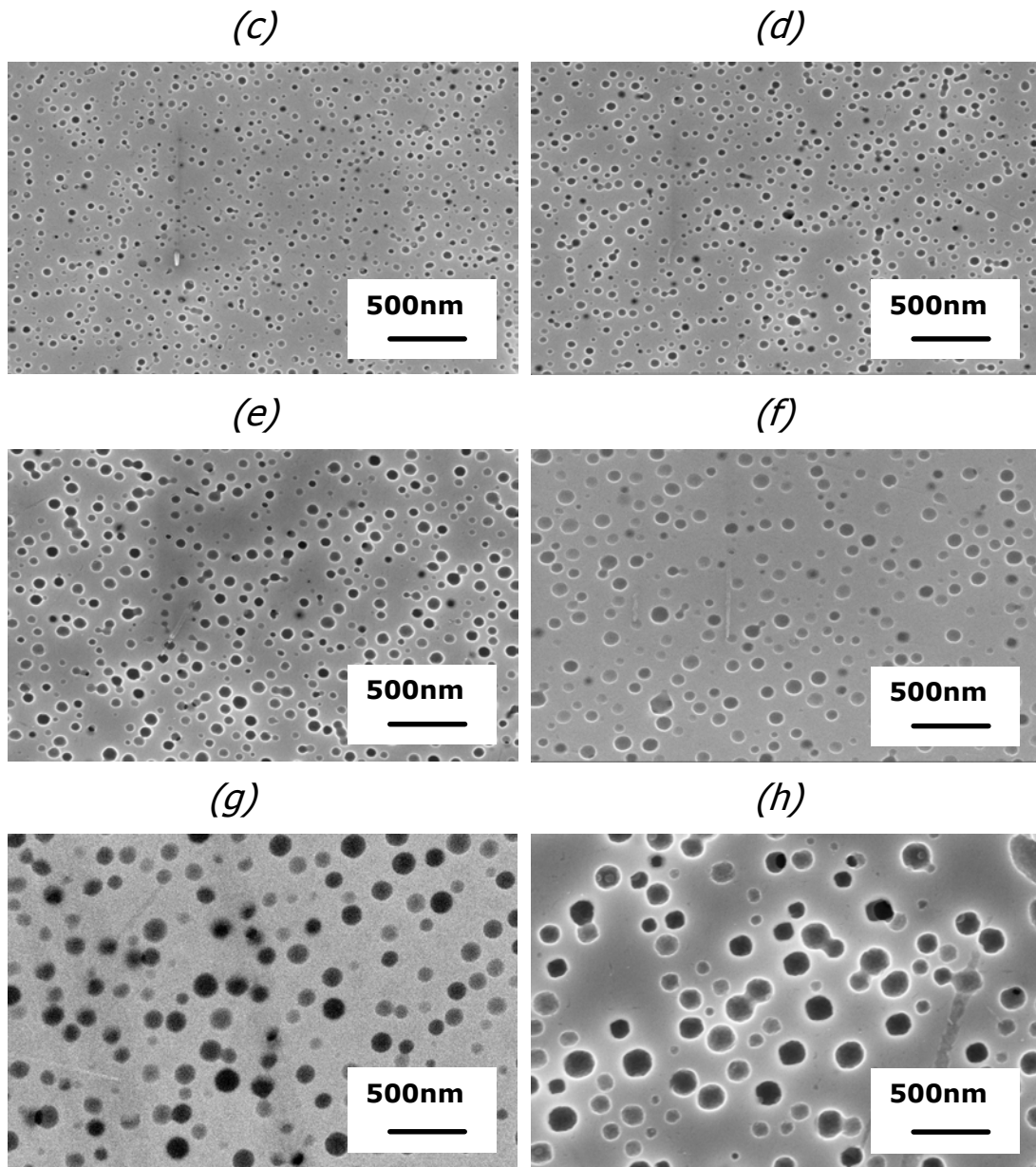


Figure. 4.24 SEM micrographs showing microstructural evolution upon aging at 875°C for aging times of (c) 2, (d) 5, (e) 10, (f) 20, (g) 50 and (h) 75 hrs respectively. Initial solution-treatment was conducted at 1145°C prior to aging at 875°C.

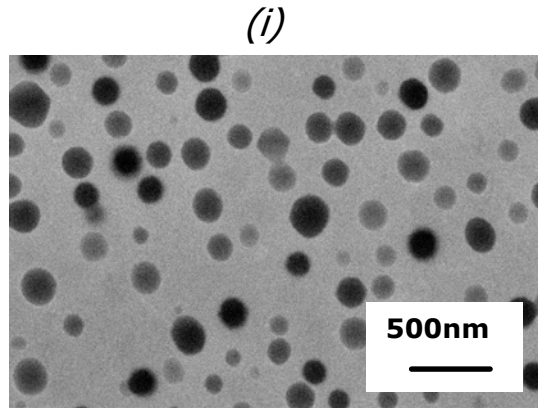


Figure. 4.24 SEM micrographs showing microstructural evolution upon aging at 875°C for aging times of (i) 100 hrs respectively. Initial solution-treatment was conducted at 1145°C prior to aging at 875°C.

temperatures (see Figures 4.21, 4.23 and 4.24). Microstructures aged for durations beyond 20 hrs at 875°C revealed some γ' precipitates that were incompletely round and resembled corner-rounded cubic shapes. Very minor faceting if any was noted at 800°C in the case of the specimen aged for 100 hrs.

A plot of the variations in the lattice parameter of the matrix (γ) phase- $a_o(\gamma)$ in response to progressive aging at 725°C, 800°C and 875°C is shown in Figure 4.25. The data points at 0.01 hrs correspond to the specimens in the as-solution-treated condition. It is seen from the plot that the general trend that is common to all the aging sets is that the lattice parameter shows a decrease from the as-solution-treated value with progressive aging. The factors that play a role in the observed lattice parameter changes are discussed later.

Table 4.3 shows the lattice misfit for selected cases from the three sets of aged specimens that were computed based on the lattice parameter obtained from (331) reflections of the γ and γ' phases. Lattice misfit values are only given for these cases, as

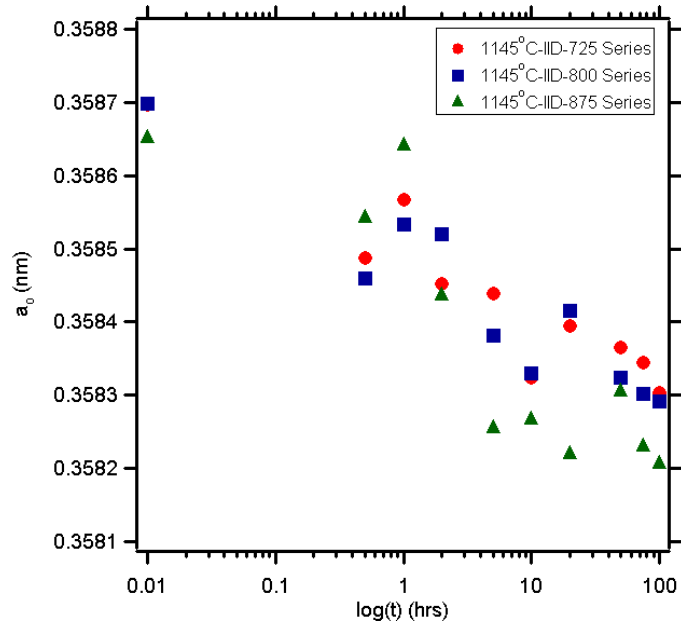


Figure 4.25 Plot showing the variations in the lattice parameter of the matrix (γ) phase as a function of the aging time (0 to 100 hrs) for the three aging temperatures- 725°C, 800°C and 875°C. The data points at 0.01 hrs refer to specimens in the as-solution-treated condition.

Table 4.3 Computations of γ - γ' lattice misfit for selected specimens in the three aging sets

Aging temperature (°C)	Aging time (hrs)	Lattice misfit (% δ)
725	50	0.1033
725	100	0.1648
800	100	0.2654
875	10	0.2093
875	20	0.2177
875	50	0.2428
875	75	0.2345
875	100	0.2373

unambiguous identification of high angle γ' reflections was not possible for all the specimens. It is seen that the lattice mismatch values are the lowest in the case of the IID-725 specimens as compared to those aged at 800°C and 875°C. In both IID-725 and

IIID-875 sets of specimens, the mismatch is noted to increase with increasing aging time. The table also shows a relatively high mismatch of 0.265% in the case of IIID-800-100 specimen, which is the only computation for the IIID-800 series.

Figure 4.26 shows a plot of the DC four-point probe resistivity of specimens for the three different aging series as a function of the aging time. As before, the time at 0.01 hrs is indicative of specimens in the solution-treated condition. Upon aging from the solution-treated condition, a maximum increase in resistivity of 12.41 [nΩ.m] is noted in the case of the 725°C series specimen at 0.5 hrs. The amount of initial increase in resistivity upon aging decreases drastically with increasing aging temperature, as is evident from the plot. In fact, the 875°C series does not show an increase in resistivity upon aging from the solution-treated condition. Next, the resistivity is noted to decrease monotonically from 0.5 hrs up to 50 hrs for the 725°C series at which point it is nearly equal to the initial solution-treated value. This condition is achieved at a much shorter aging time (even below 1hr) in the case of specimens aged at 800°C. For the 875°C set of specimens, this condition is well past even before the first sampling time of 0.5 hrs due to the rapid kinetics. After this stage has been reached, the resistivity shows a slight decrease culminating more or less in a plateau behavior, seen for the 800°C and the 875°C series of specimens. The specific reasons for resistivity changes during aging with due reference to the microstructures are discussed later.

The data set for the 600°C aging experiments is only partial and was collected in order to observe resistivity changes during very early aging times (see Figure 4.26). A rise in resistivity upon initial aging is observed here similar to the 725°C data set; however, the amount of increase is much smaller compared to that in the latter.

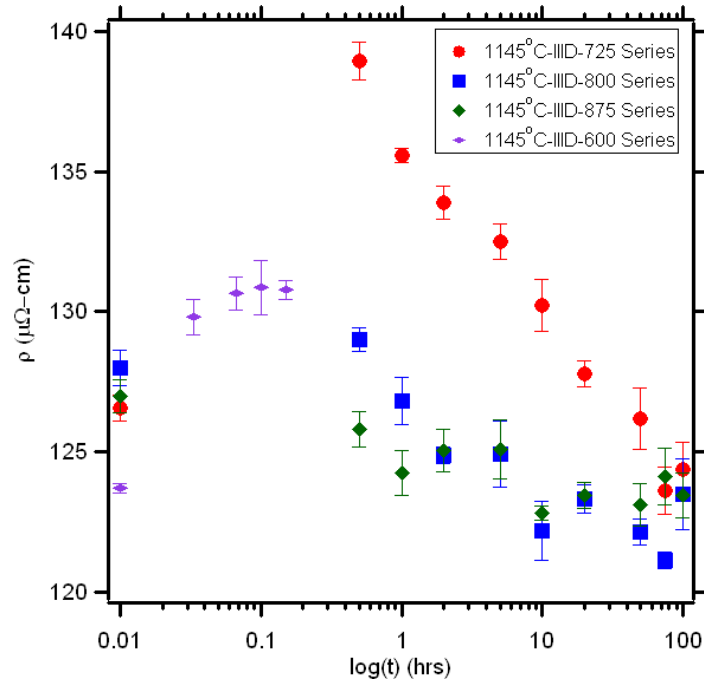


Figure 4.26 Plot of the DC four-point probe resistivity as a function of the aging time (0 to 100 hrs) for the three different aging series- 725°C, 800°C and 875°C. The data points at 0.01 hrs refer to specimens in the as-solution-treated condition.

The clear difference between the 600°C data set and the other sets is that the resistivity increases monotonically with progressive aging in the former for the durations sampled. The reasons for the observed difference are also discussed later.

4.2.2 Discussion

The formation of polygonal etch-pits in the shapes of square and hexagon in the solution-treated microstructures, shown in Figure 4.20 is discussed first. It is believed that upon quenching, the excess vacancies are condensed onto specific soft-directions of the matrix (γ) phase, which is highlighted as an etch-pit by the A-etchant. During quenching, it is possible for the vacancies to aggregate into dislocation loops, which might have a bearing on the formation of etch-pits. However, the formation of dislocation

loops can only be verified if detailed transmission electron microscopy studies are conducted. In a cubic material, soft directions such as $\langle 100 \rangle$ have relatively lower elastic moduli compared to other directions. It is therefore easier to accommodate any lattice strains arising due to the creation of vacancies preferentially along the soft directions. Table 4.4 shows calculations of elastic moduli for directions that can be accommodated in either in the $\{200\}$ or $\{111\}$ planes- $\langle 100 \rangle$, $\langle 110 \rangle$, $\langle 211 \rangle$, and $\langle 321 \rangle$ directions for pure nickel using the following formula⁴³:

$$\frac{1}{E} = s_{11} - 2 \left[(s_{11} - s_{12}) - \frac{1}{2} s_{44} \right] (l^2 m^2 + m^2 n^2 + n^2 l^2) \quad (8)$$

where s_{11} , s_{12} and s_{44} refer to components of elastic compliances; l , m and n are the components of the unit vector along the direction of interest.

It is suggested that square-shaped etch-pits are formed in $\langle 200 \rangle$ oriented grains, with the soft directions being $\langle 100 \rangle$, that run along the sides of the etch-pit. A schematic of this description is shown in Figure 4.27. The formation of a regular hexagonal etch-pit bounded by $\langle 110 \rangle$ soft directions on a $\langle 111 \rangle$ oriented grain is also shown in Figure 4.27. It is however evident from the micrographs that the etch-pits are observed to be non-regular hexagons instead of perfect regular ones as shown in the schematic. One possible explanation for this may be advanced based on the nature of image formation in the SEM. It is known that undistorted representation of real objects in an image is only true for those features that lie in a plane perpendicular to the optic axis. Features that are present on planes that are tilted with reference to the optic axis appear to be shortened in the image, unless a correction factor for the predetermined degree of tilt is applied⁴⁴. The occurrence of etch-pits as non-regular hexagons could be as a result of this phenomenon,

Table 4.4 Calculations of elastic moduli for directions in $\langle 200 \rangle$ or $\langle 111 \rangle$ oriented grains

Direction	$(l^2 m^2 + m^2 n^2 + n^2 l^2)$	E (GPa)
$\langle 100 \rangle$	0	134
$\langle 110 \rangle$	0.25	231
$\langle 211 \rangle$	0.25	231
$\langle 321 \rangle$	0.25	231

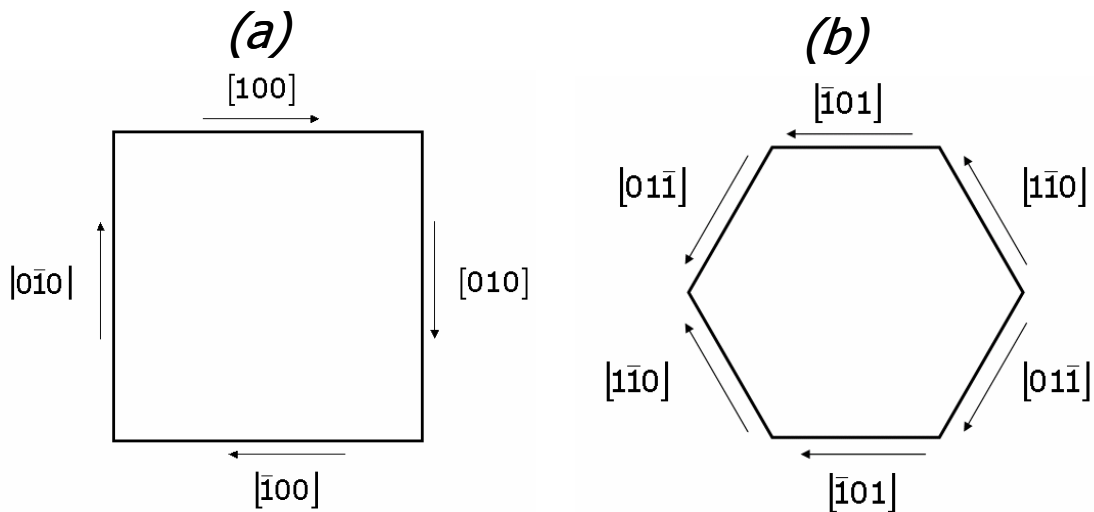


Figure 4.27 Illustrations showing (a) square shaped etch-pits in $[200]$ oriented grains and (b) hexagon shaped pits in $[111]$ oriented grains, with the respective soft directions being $\langle 100 \rangle$ and $\langle \bar{1}\bar{1}0 \rangle$.

if the respective grains are oriented at large tilt angles from the optic axis. The alternate reasoning is that non-regular hexagons are formed by bounding directions that are not all $\langle 110 \rangle$ type, that however have the same elastic modulus. For instance, in a $\langle 111 \rangle$ oriented grain, $\langle 211 \rangle$ and $\langle 321 \rangle$ directions have the same elastic modulus as $\langle 110 \rangle$. In this case, the interior angles of the hexagon are not equal due to dissimilar bounding directions.

Finally, the formation of etch-pits is also possible in grains with other orientations, and the etch-pit shapes will be governed by the corresponding soft directions that can be accommodated within the grain.

The high values of $a_o(\gamma)$ noted in the solution-treated specimens (see Figure 4.25), is primarily because of the increased thermal dilatation of the lattice due to the high treatment temperature¹². Contributions arising from the quenched-in excess vacancies in the form of lattice relaxation effects also affect the measured lattice parameter¹².

Contributions to the as-solution-treated resistivity (see Figure 4.26) can arise from three factors- viz. solid solution impurities alloyed with nickel, quenched-in excess vacancies from the solution-treatment temperature, carbide distribution and grain boundaries. The influence of the carbides and grain boundaries can be taken to be negligible considering the large scale of dispersion of these features, as mentioned previously. The quenched-in vacancy concentration corresponding to the solution-treatment temperature of 1145°C is calculated to be $\sim 10^{-6}$ (see 4.1.2), assuming a vacancy formation enthalpy (H_f^v) of 1.72 eV for pure nickel⁴⁰. Considering that this fraction of vacancies is negligible compared to the atomic fractions of solid solution impurities, the latter should have the dominant influence on the solution-treated resistivity.

Upon aging from the solution-treated condition, the resistivity is noted to increase for the 725°C and 800°C sets of specimens (see Figure 4.26) as mentioned previously in the results section. This initial increase in resistivity that is noted upon aging can only be explained by the presence of fine γ' precipitates that form upon aging. Even though no evidence of this is presented for the earliest aging time of 0.5 hrs, SEM and AFM

micrographs show the clear presence of γ' precipitates after 1 and 2 hrs of aging at 725°C (see Figure 4.22). The fine γ' distribution that is present during the initial stages of aging is effective at scattering the conduction electrons, causing an increase in the measured resistivity. The 'scattering power' of the precipitates depends on the γ' interparticle spacing relative to the mean free path- Λ of conduction electrons in the material, as mentioned in section 4.1.2. The interparticle spacing is directly related to the mean precipitate radius- $\langle r \rangle$ of the γ' distribution. The closer the value of $\langle r \rangle$ to Λ , the more effective the γ' size distribution is in scattering the conduction electrons and therefore greater the resistivity. The subsequent decrease in resistivity beyond 0.5 hrs for the 725°C and 800°C series of specimens (see Figure 4.26) suggests that nucleation of γ' must have been completed by 0.5 hrs. A nucleation phase is generally characterized by an increasing resistivity, which may be described using Johnson-Mehl-Avrami (JMA) kinetics⁶. Ideally, the maximum in resistivity coincides with the completion of the nucleation stage, which also corresponds to the critical radius- r^* of the precipitates that contributes to the maximum scattering⁸. From the present data, the position of the resistivity maximum that corresponds to r^* is unknown because aging times under 0.5 hrs were not sampled.

Based on the argument in the previous paragraph, it is then clear that the drop in resistivity with increasing aging time should be related to γ' coarsening. Microstructural evidence for this is presented in the series of SEM micrographs in Figures 4.23 and 4.24 for the 800°C and 875°C set of specimens respectively. For the 725°C specimens, the microstructural evolution seen up to 10 hrs is predominantly that of the etch-pits, while γ' coarsening is clear only after 20 hrs of aging. The presence of γ' at 1, 2 and 10 hrs of aging was however confirmed using the B-etchant (see Figure 4.22), as stated previously.

It is also seen upon a closer examination of the micrograph in Figure 4.21 (e), highlighted using the A-etchant, that the irregular etch-pit features show small protrusions. These small protrusions seen inside the pit regions are in fact the γ' precipitates.

Based on the above evidence, it is theorized that the evolution of etch-pits occurs in response to the gradual coarsening of γ' precipitates inside the pit regions during aging. During γ' coarsening, there is diffusion of solute within the matrix, changes in the coherency strains and elastic interaction between the precipitates that lead to the observed changes in the etch-pit shapes. The etch-pit shapes finally lose their identity after significant γ' coarsening has occurred at which point they are visible in the SEM.

The drop in the lattice parameter noted upon initial aging from the solution-treated condition (see Figure 4.25) can potentially be affected by three factors- viz. reduced thermal dilatation of the lattice, reduction in the excess vacancy concentration and changes in the matrix composition due to γ' precipitation. It is reasonable to expect that the combination of thermal dilatation and changes in the matrix composition would be the predominant factors causing the observed decrease at this stage.

The changes in the lattice parameter noted upon further aging (see Figure 4.25) may arise from two contributions- viz. changes in the matrix composition during coarsening and changes in the coherency strains between the matrix and the γ' precipitates. The changes in the solute concentration of the matrix during coarsening, is a consequence of the Gibbs-Thomson solubility effect^{6, 12} that was mentioned in an earlier chapter. The Gibbs-Thomson solubility effect essentially describes the increased solute solubility of a system of very fine particles arising from the curvature effect^{6, 12}. Due to this effect, as the γ' precipitates coarsen, the solute concentration in the matrix in

equilibrium with a γ' precipitate of an average size decreases with time. Accompanying this effect is the increase in the volume fraction of the γ' phase, until an equilibrium is reached, at which point the average γ' radius approaches infinity.

The other factor that contributes to the observed changes in the lattice parameter upon aging is the changes in the coherency strains between the matrix and the precipitate phases¹⁹. It is known that γ' coarsening is driven by a reduction in the interfacial energy of the system because of the large interfacial energy of a fine dispersion of precipitates initially⁶. However, as the precipitates coarsen, the lattice structure around the γ' is distorted, resulting in an increase in the lattice misfit between the matrix and the precipitate phases, which contributes to the coherency strains⁴⁵. Evidence for the increase in lattice misfit with increasing aging time as well as enhanced kinetics may be seen from Table 4.3. The relatively high mismatch values at the longest aging times for the IID-875 series is in agreement with the earlier SEM observations of rounded cubic γ' shapes in these microstructures (see Figure 4.24).

The monotonic decrease in resistivity with progressive aging up to 50 hrs for the 725°C specimens (see Figure 4.26) is attributed to the decrease in the scattering power of the γ' distribution (see equations (6) and (7) in 4.1.2) as a result of the coarsening process. This is consistent with the microstructures discussed earlier, presented in Figures 4.21 and 4.22. The resistivity after 50 hrs of aging at 725°C, is nearly equal to the solution-treated resistivity, as mentioned earlier. The contribution to the overall resistivity due to scattering from the γ' distribution becomes less significant beyond 50 hrs of aging. This is because, the mean radius- $\langle r \rangle$ of the γ' precipitates at this stage becomes much larger than the mean free path of the conduction electrons- λ as a result of the coarsening. The

primary contribution to the measured resistivity past this stage comes from the solid solution impurities in the matrix phase^{10, 13}. The changes in the measured resistivity after 50 hrs of aging at 725°C may be related to the changes in the solute concentration in the matrix as a result of the coarsening process⁴⁶. This is as a result of the Gibbs-Thomson solubility effect^{6, 12}, which is explained in a previous paragraph.

The amount of initial increase in resistivity for the 800°C set is much smaller as compared to the previous case at 725°C. This is because of the faster kinetics at 800°C that results in a coarser γ' distribution with a much less scattering power than the corresponding specimen at 725°C. Secondly, the measured resistivity after 1 hr of aging falls below the solution-treated resistivity, indicating that the scattering due to the γ' distribution is less significant past this stage. As explained for the 725°C case, the resistivity changes due to coarsening beyond this stage may be attributed to the changes in the solute concentration in the matrix. The corresponding coarsening sequence for the 800°C set of specimens is shown in Figure 4.23.

The third aging set at 875°C which has the fastest kinetics, does not show any increase in resistivity upon initial aging from the solution-treated condition, as is evident from Figure 4.26. This is because the starting γ' distribution is coarse enough so as not to impede the propagation of conduction electrons to any significant extent. Subsequent microstructures are progressively coarser than the initial one as may be seen from Figure 4.24. In this case, the kinetics is so fast that all the resistivity changes associated with γ' coarsening may be attributed to changes in the solute concentration in the matrix.

The final set of aging treatments is conducted at 600°C to demonstrate that the nucleation stage of γ' is in fact seen if the kinetics is slowed down significantly. In all,

only five data points (under 0.5 hrs) including the solution-treated specimen, were collected for this set. The initial rise in resistivity upon aging is noted here similar to the 725°C set (see Figure 4.26); however, the magnitude of rise is significantly smaller than that noted in the 725°C set. Moreover, a gradual increase is noted in the average resistivity with further aging at 600°C. This is clearly suggestive of a nucleation and growth regime, where the measured resistivity is expected to increase until a maximum is reached, corresponding to the completion of this reaction. This is also the stage at which the mean γ' radius approaches the critical, i.e. $\langle r \rangle = r^*$, which leads to the maximum scattering of the conduction electrons⁸.

4.2.3 Conclusions

The microstructures of solution-treated specimens observed using an SEM, showed the presence of polygonal etch-pits mostly in the shapes of squares or non-regular hexagons. The etch-pits within a single grain were all the same shape and were aligned along a specific direction within the grain, suggesting a dependence of the pit formation on the grain orientation. The formation mechanism of the etch-pits was attributed to the condensation of excess quenched-in vacancies along crystallographically soft directions, eg. $\langle 100 \rangle$. The softer directions have relatively lower elastic moduli and can therefore accommodate lattice distortions much easily than other directions. The formation of specific etch-pit shapes is explained based on the accommodation of a certain soft direction in a grain of a given orientation. Based on this explanation, square and hexagonal etch-pits were argued to form in $\langle 200 \rangle$ and $\langle 111 \rangle$ oriented grains respectively.

Microstructural evolution in response to aging at 725°C, showed progressive transformation of the etch-pit shapes from perfectly faceted polygons to corner-rounded polygons and to more irregular shapes. The transformation is attributed to the progressive growth of the γ' precipitates inside the pits and the concomitant effects of solute-diffusion, lattice distortion due to coherency strains and elastic interaction effects between γ' precipitates. The same phenomenon is also true of aging at 800°C and 875°C; however, the slow progression of events seen at the lower aging temperature is masked effectively by the faster kinetics prevailing at these higher temperatures.

The changes in the lattice parameter of the γ phase was attributed to two factors-changes occurring in the solute concentration of the matrix and coherency strains arising due to lattice misfit between the γ and γ' phases. It was observed in a few selected cases that the lattice misfit increased from shorter aging times at 725°C to longer aging times at 800°C or 875°C.

The four-probe resistivity showed a marked increase from the solution-treated value upon aging at 725°C, which was attributed to the presence of fine γ' precipitates that serve as scattering sites of conduction electrons. The extent of the increase in resistivity decreased drastically with increasing aging temperature, which is a result of the faster γ' growth kinetics. The absence of a nucleation regime in the IID-725, IID-800 and IID-875 data sets was clearly indicated by a decrease in resistivity noted upon further aging (after 0.5 hrs). The decrease in resistivity affected by a reduction in the scattering power of the γ' precipitates is a valid explanation only for the IID-725 series up to 50 hrs of aging and during early stages of aging for the IID-800 series. The resistivity variations that occur outside these range of times and in the case of the IID-

875 series are associated with the changes in the 'average solute' concentration in the matrix. Finally, aging experiments at 600°C for durations shorter than 0.5 hrs do reveal the existence of a nucleation regime, characterized by an increasing resistivity.

CHAPTER 5

MODELING AC AND DC ELECTRICAL MEASUREMENTS

This chapter pertains to the development of analytical and finite-element models for gaining an understanding of two-probe, four-probe AC impedance measurements and four-point probe DC measurements. In the first part of the chapter an analytical derivation is presented for the electric field distribution in a cylindrical metallic specimen for a two-probe impedance measurement. A validation for the analytical solution is also provided by a finite element solution obtained by using FEMLAB 3.1, a commercially available finite element package. The effect of varying the specimen geometry on the electric field behavior is also discussed. Subsequently, the analytical expressions for the electric and magnetic fields are used to compute the complex impedance of the specimen via energy methods.

The second part of the chapter deals with the computation of geometric correction factors for cylindrical specimens of finite shape subject to a four point probe DC resistivity measurement. A derivation of the closed-form analytical solution as a solution to Laplace's equation for the potential difference between the voltage probes is presented first. The potential difference obtained from the closed-form solution is subsequently used for computing the geometric correction factors. Next, a comparison among the correction factors computed via the closed-form solution, COMSOL finite-element solution and analytical approximation factors (available in the literature) is presented. Lastly, the effect of varying the specimen geometry and probe arrangement on the correction factor is also considered.

In the final part of the chapter, impedance calculations are presented for four-probe AC measurements on wire specimens and cylindrical disk specimens. The impedance of wire specimens is computed based on a solution for the ‘skin-effect’ in wires, developed by Giacoletto⁴⁷. The impedance of disk specimens is evaluated using a closed-form analytical solution developed by Bowler³⁹. The closed-form solution describes the electric field distribution inside a semi-infinite metal plate (of finite thickness) upon injection of alternating current at the surface. The calculations are intended for understanding the frequency response of a metallic specimen to the flow of alternating current in a four-probe configuration.

5.1 Analytical treatment of two-probe impedance measurement

5.1.1 Introduction

A two-probe impedance measurement relies on the application of an *ac* signal across a specimen placed in between source and sink electrodes. The measurement in essence can be treated as current injection into the specimen at the source electrode and current extraction at the sink electrode. The objective of this treatment is to develop a continuum solution for the electric field distribution inside a cylindrical disk metallic specimen, which is relevant to understanding the impedance response from two-probe impedance measurements. The treatment is valid only for the specific case wherein, the electrodes are placed on opposite circular faces of the specimen and sharing the same axis of symmetry. An analytical formulation of this problem is developed by using Maxwell’s equations for conductors^{48, 49} and closed form analytical expressions for the resultant field distribution are derived in terms of Bessel series⁵⁰⁻⁵⁴.

One instance from the literature may be cited, where a closed-form solution in the frequency domain is available for a problem that parallels the current one. Ney^{55, 56} proposed a closed-form solution for the electric field distribution in a solid non-perfectly conducting flat ground plane arising from electromagnetic interference. The electromagnetic interference effect is assumed to be due to external currents entering and exiting the ground plane at contacts on opposite sides. The contacts are modeled to be symmetric with respect to the ground plane and the contact width is assumed to be much smaller compared to the width of the ground plane. The solution accounted for skin-effect due to finite conductivity of the ground plane, as well as constriction effect as a result of confinement of current lines near the contact points^{55, 56}.

5.1.2 Problem description

The problem may simply be described as the injection of an alternating current $I_o \exp(-j\omega t)$ of angular frequency- ω , into a cylindrical metallic disk specimen via a source electrode and extraction by means of a sink electrode. The electrodes are modeled as perfect contacts of radius r_c and negligible thickness contacting the specimen of radius r_o ($r_o \gg r_c$) and thickness t_o ($t_o < r_o$) as illustrated in Figure 5.1 (a). The contact electrodes and the specimen share the same axis of symmetry. The impressed current at the source electrode, is assumed to be along the z direction. Due to a difference in the electrode contact radius and that of the specimen, there will be spreading of the current flow lines in the r direction within the specimen. This phenomenon is referred to as striction effect or constriction^{55, 56}, wherein confinement or expansion of current flow lines occurs due to a discrepancy in the section width between the two conductors. An alternate effect is that of current crowding near the surface of a conductor at high

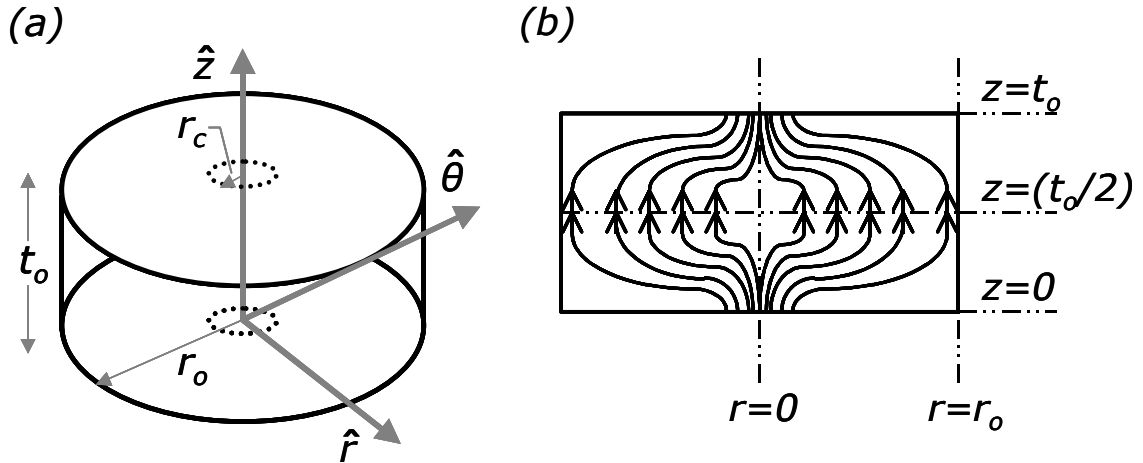


Figure 5.1 (a). Schematic illustrating the measurement geometry comprising of the specimen with coaxially placed electrodes (dotted line) in a cylindrical co-ordinate system. The illustration in (b) shows the current flow contour incorporating both skin and constriction effects inside the specimen (r - z cross-section).

frequencies, an effect generally known as the skin-effect^{47, 57}. The skin-effect is pertinent only for current flow along the z direction. Therefore, electric fields along both axial (z) and radial (r) directions (E_z and E_r) will be present within the specimen. However, there is no apparent electric field in the tangential (ϕ) direction. Hence due to ϕ -symmetry, modeling can be confined to the r - z plane. A cross-section of the problem configuration contained in the r - z plane illustrating the skin and the constriction effects is shown in Figure 5.1 (b). Since symmetry also prevails about the z axis, the modeling space can be reduced further to one half of the r - z plane from $r = 0$ to $r = r_o$.

5.1.3 Analytical approach

5.1.3.1. Formulation and generic solution

The analytical solution for the electric field distribution inside the specimen (of uniform conductivity- σ and magnetic permeability- μ) is obtained by solving the following two-dimensional diffusion equation^{47, 55}:

$$\nabla^2 \bar{E} = \mu\sigma \left(\frac{\partial \bar{E}}{\partial t} \right) = j\omega\mu\sigma \bar{E} \quad (1)$$

Two independent partial differential equations (PDE's) in E_z and E_r result upon expanding the vector Laplacian⁵⁴ in the above equation using cylindrical co-ordinates.

$$\frac{\partial^2 E_r}{\partial r^2} + \frac{\partial^2 E_r}{\partial z^2} + \frac{1}{r} \frac{\partial E_r}{\partial r} - \frac{E_r}{r^2} = j\omega\mu\sigma E_r \quad (2)$$

$$\frac{\partial^2 E_z}{\partial r^2} + \frac{\partial^2 E_z}{\partial z^2} + \frac{1}{r} \frac{\partial E_z}{\partial r} = j\omega\mu\sigma E_z \quad (3)$$

Equations (2) and (3) can each be separated into two independent PDE's in r and z using the product method^{50, 53, 55} as follows:

$$E_r(r, z) = F_1(r)G_1(z) \quad (4)$$

$$E_z(r, z) = F_2(r)G_2(z) \quad (5)$$

Substituting these expressions into equations (2) and (3), the following ordinary differential equations (ODE's) are obtained in terms of the new radial and axial functions viz., $F_1(r)$, $F_2(r)$, $G_1(z)$ and $G_2(z)$:

$$\frac{[F_1'']_r}{F_1} + \frac{1}{r} \frac{[F_1']_r}{F_1} - \frac{1}{r^2} = k_1^2 \quad (6)$$

$$\frac{[F_2'']_r}{F_2} + \frac{1}{r} \frac{[F_2']_r}{F_2} = k_2^2 \quad (7)$$

$$\frac{[G_1'']_z}{G_1} = \gamma^2 - k_1^2 \quad (8)$$

$$\frac{[G_2'']_z}{G_2} = \gamma^2 - k_2^2 \quad (9)$$

where k_1 and k_2 are arbitrary constants and $\gamma^2 = j\omega\mu\sigma$.

Equations (6) and (7) are Bessel's ODE's of order one and zero respectively, for which the standard solutions^{50, 53} can be expressed as:

$$F_1(r) = C_1 J_1(\lambda_1 r) + C_2 Y_1(\lambda_1 r) \quad (10)$$

$$F_2(r) = C_3 J_0(\lambda_2 r) + C_4 Y_0(\lambda_2 r) \quad (11)$$

where J_ν and Y_ν are Bessel functions of the first and the second kind of order ν respectively; $\lambda_1 = jk_1$, $\lambda_2 = jk_2$ and C_i ($i = 1, 2, 3$ and 4) are the corresponding coefficients. Y_ν solutions are singular^{6,9} at the origin and can be excluded right away as the final solution must be continuous at the origin.

The solutions for ODE's (8) and (9) involving z can be expressed as follows^{6,9,12}:

$$G_1(z) = C_5 e^{-\xi_1 z} + C_6 e^{\xi_1 z} \quad (12)$$

$$G_2(z) = C_7 e^{-\xi_2 z} + C_8 e^{\xi_2 z} \quad (13)$$

where $\xi_i^2 = \gamma^2 - k_i^2$ ($i = 1, 2$) and C_l ($l = 5, 6, 7$ and 8) are the various coefficients.

Grouping the radial (r) and axial (z) solutions, the complete solutions for $E_r(r, z)$ and $E_z(r, z)$ can be written as follows:

$$E_r(r, z) = (C_5' e^{-\xi_1 z} + C_6' e^{\xi_1 z}) J_1(\lambda_1 r) \quad (14)$$

$$E_z(r, z) = (C_7' e^{-\xi_2 z} + C_8' e^{\xi_2 z}) J_0(\lambda_2 r) \quad (15)$$

where C_l' ($l = 5, 6, 7$ and 8) are the modified coefficients resulting from grouping the radial and axial solutions together.

5.1.3.2. Boundary conditions

In order to determine the electric field distribution uniquely at a given point within the specimen, it is essential to determine all the constants in the above field expressions. The constants can be solved for by examining the boundary conditions governing the problem, which are listed as follows:

- (a) Source and sink specifications:

$$\begin{aligned} (E_z)_{z=0,t_o} &= \frac{I_o}{\pi r_c^2 \sigma} \quad (0 \leq r \leq r_c) \\ &= 0 \quad (r_c < r \leq r_o) \end{aligned} \quad (16)$$

$$\left(\frac{\partial E_z}{\partial r} \right)_{z=0,t_o} = -\frac{I_o}{\pi r_c^2 \sigma} \delta(r_c - r) \quad (17)$$

- (b) Limiting normal current on curved surface:

$$(E_r)_{r=r_o} = 0 \quad \forall z \quad (18)$$

- (c) Constancy of current via Ampere's law^{48, 49}:

$$\oint_c H_\phi(r)_{r=r_o} r_o d\phi = I_o \quad (19)$$

In the above equations, I_o is the total current injected into the specimen and H_ϕ is the magnetic field in the azimuthal (ϕ) direction. The magnetic field \bar{H} is governed by the following Maxwell curl equation^{48, 49}:

$$\nabla \times \bar{E} = -\mu \left(\frac{\partial \bar{H}}{\partial t} \right) \quad (20)$$

The final expression for H_ϕ in terms of the electric field components (E_r and E_z) is then obtained as:

$$H_\phi(r, z) = \frac{I}{j\omega\mu} \left(\frac{\partial E_z}{\partial r} - \frac{\partial E_r}{\partial z} \right) \quad (21)$$

5.1.3.3. Determination of coefficients and constants

First, the limiting current boundary condition imposed on $E_r(r, z)$, listed in equation (18) is examined. A non-trivial solution for this condition is obtained by setting:

$$J_1(\lambda_1 r) \Big|_{r=r_0} = 0, \text{ which has infinite roots}^{50, 53}, \text{ given by } - \lambda_{1i} = \frac{\beta_{1i}}{r_0} (i = 1, 2, 3, \dots), \text{ where}$$

β_{1i} is a root of $J_1(x)$. Therefore, via the principle of superposition, the expressions for $E_r(r, z)$ and $E_z(r, z)$ in equations (14) and (15) can be rewritten as:

$$E_r(r, z) = \sum_m \left(C'_{5m} e^{-\xi_{1m} z} + C'_{6m} e^{\xi_{1m} z} \right) J_1(\lambda_{1m} r) \quad (22)$$

$$E_z(r, z) = \sum_m \left(C'_{7m} e^{-\xi_{2m} z} + C'_{8m} e^{\xi_{2m} z} \right) J_0(\lambda_{2m} r) \quad (23)$$

Next, the total current condition given by Ampere's law (equation (19)) yields:

$$2\pi r_0 H_\phi(r, z) \Big|_{r=r_0} = I_0 \quad (24)$$

Substituting for $H_\phi(r, z)$ from equation (21), we have:

$$\left(\frac{\partial E_z}{\partial r} - \frac{\partial E_r}{\partial z} \right)_{(r_0, z)} = \frac{j\omega\mu}{2\pi r_0} I_0 \quad (25)$$

Since $E_r(r, z) \Big|_{(r_0, z)} = 0$, the above expression reduces to:

$$\left(\frac{\partial E_z}{\partial r}\right)_{(r_o, z)} = \frac{j\omega\mu}{2\pi r_o} I_o \quad (26)$$

The right hand side (RHS) term in equation (26) being a constant, $E_z(r, z)$ must contain at least one term that is just a function of r and independent of z . Therefore, the expression for $E_z(r, z)$ is modified as follows:

$$E_z(r, z) = f(r) + \sum_m \left(C'_{7m} e^{-\xi_{2m} z} + C'_{8m} e^{\xi_{2m} z} \right) J_o(\lambda_{2m} r) \quad (27)$$

Inserting this expression back into equation (25), it is seen that only $f(r)$ contributes to total current and therefore, $\left(\frac{\partial J_o(\lambda_{2m} r)}{\partial r}\right) = 0$. A non-trivial solution to this equation (see

Appendix) is given by $\lambda_{2m} = \frac{\beta_{1m}}{r_o}$ ($m = 1, 2, 3, \dots$), where β_{1m} is a root of $J_1(x)$. Thus λ_i 's

and ξ_i 's appearing in the field expressions - $E_r(r, z)$ and $E_z(r, z)$ given by equations (22)

and (27) are determined as $\lambda_{1m} = \lambda_{2m} = \frac{\beta_{1m}}{r_o}$ and $\xi_{1m}^2 = \xi_{2m}^2 = \gamma^2 + \lambda_{1m}^2$.

5.1.3.3.1 Symmetry and anti-symmetry conditions

The remaining unknowns that need to be determined in the field expressions are the pre-exponential coefficients - C_i 's. The number of unknown coefficients that need to be determined can be reduced by exploiting the symmetry of the problem. The problem geometry is symmetric about $z = \left(\frac{t_o}{2}\right)$ because the source and sink electrodes are positioned on opposite circular faces of the specimen, centered about the axis of symmetry. A schematic illustrating the symmetric current flow contour incorporating constriction and skin effects is depicted in Figure 5.1 (b). Based on the schematic, it is

evident that $E_z(r, z)$ should be symmetric about $z = \left(\frac{t_o}{2}\right)$, whereas, $E_r(r, z)$ should be

anti-symmetric. Thus, we can write the following conditions:

$$E_r(r, z) = -E_r(r, t_o - z) \quad (28)$$

$$E_z(r, z) = E_z(r, t_o - z) \quad (29)$$

These symmetry expressions yield the following relations between the coefficients for the axial and radial fields:

$$C'_{8m} = C'_{7m} e^{-\xi t_o} \quad (30)$$

$$C'_{6m} = -C'_{5m} e^{-\xi t_o} \quad (31)$$

Incorporating these relationships, the field expressions are now modified to be:

$$E_r(r, z) = \sum_m C'_{5m} \left(e^{-\xi_{1m} z} - e^{-\xi_{1m}(t_o - z)} \right) J_1(\lambda_{1m} r) \quad (32)$$

$$E_z(r, z) = f(r) + \sum_m C'_{7m} \left(e^{-\xi_{1m} z} + e^{-\xi_{1m}(t_o - z)} \right) J_0(\lambda_{1m} r) \quad (33)$$

5.1.3.3.2 Validation of 1-D solution for $f(r)$

Let us consider the case of an alternating current $I_o \exp(-j\omega t)$, flowing through an infinitely long thin cylindrical wire in the z direction. In this case, the distribution of current is governed entirely by skin-effect and the solution for the electric field is given by¹⁷:

$$E_z(r) = \alpha J_o(\kappa r), \quad (34)$$

where $\alpha = \frac{\kappa I_o}{2\pi\sigma_o J_1(\kappa r_o)}$ and $\kappa^2 = -j\omega\mu\sigma = -\gamma^2$.

Let us for the moment assume that this solution adequately describes $f(r)$ in the expression for $E_z(r, z)$. This assumption will be validated by testing for the total current condition specified in equation (26). The expression for $E_z(r, z)$ now becomes:

$$E_z(r, z) = \alpha J_o(\kappa r) + \sum_m C'_{7m} \left(e^{-\xi_{1m} z} + e^{-\xi_{1m}(t_o - z)} \right) J_o(\lambda_{1m} r) \quad (35)$$

Substituting this expression for $E_z(r, z)$ on the left hand side (LHS) of equation (26) (see Appendix for derivative of $J_o(x)$),

$$\left(\frac{\partial E_z}{\partial r} \right)_{(r_o, z)} = -\kappa \alpha J_1(\kappa r_o) + \sum_m C'_{7m} \left(e^{-\xi_{1m} z} + e^{-\xi_{1m}(t_o - z)} \right) \left(-\lambda_{1m} J_1(\lambda_{1m} r_o) \right)$$

The second term vanishes as $J_1(\lambda_{1m} r_o) = J_1(\beta_{1m}) = 0$. Therefore, we have:

$$\left(\frac{\partial E_z}{\partial r} \right)_{(r_o, z)} = \frac{-\kappa^2 I_o}{2\pi \sigma r_o} = \frac{j\omega \mu}{2\pi r_o} I_o$$

This is identical to the RHS of equation (26). The first term in the expression for $E_z(r, z)$ as given in equation (35) accounts for skin-effect and the summation signifies the contribution from current constriction at the contacts. The expression for $E_z(r, z)$ in equation (35) can also be verified alternately. Consider $E_z(r, z)$ at $z = \frac{t_o}{2}$:

$$E_z\left(r, \frac{t_o}{2}\right) = \alpha J_o(\kappa r) + \sum_m 2C'_{7m} e^{-\frac{\xi_{1m} t_o}{2}} J_o(\lambda_{1m} r) \quad (36)$$

Since the constriction effect diminishes away from the contacts, it is to be expected that the summation term contributes less and less at $\left(\frac{t_o}{2}\right)$ as the cylinder grows longer. As t_o increases to very large values ($t_o \gg r_o$), the second term in the above equation tends to

zero, rendering the solution to be identical to the case of an infinitely long cylindrical wire described earlier. This completes the validation of the expression for $E_z(r, z)$.

The constants that are left to be determined are the pre-exponential coefficients in equations (32) and (35). Now we make use of the source condition listed in equation (17).

$$\left(\frac{\partial E_z}{\partial r}\right)_{z=0^-} = -\frac{I_o}{\pi r_c^2 \sigma} \delta(r_c - r) \quad (37)$$

The derivative of $E_z(r, z)|_{z=0^+}$ from equation (35) is (see Appendix):

$$\left(\frac{\partial E_z}{\partial r}\right)_{z=0^+} = -\kappa \alpha J_1(\kappa r) + \sum_m C'_{7m} \left(1 + e^{-\xi_{1m} t_o}\right) (-\lambda_{1m} J_1(\lambda_{1m} r)) \quad (38)$$

Consider the evaluation of $\int_0^{r_o} \left(\frac{\partial E_z}{\partial r}\right)_{z=0} J_1(\lambda_{1p} r) r dr$ independently using the expressions

in equations (37) and (38). The result of integral evaluation (see Appendix) via equation (37) is given as:

$$\int_0^{r_o} \left(\frac{\partial E_z}{\partial r}\right)_{z=0^-} J_1(\lambda_{1p} r) r dr = -\frac{I_o J_1(\lambda_{1p} r_c)}{\pi r_c \sigma} = X_1 \quad (39)$$

The evaluation of the integral expression via equation (38) is possible by making use of orthogonality relations for Bessel functions^{50, 51, 53} (see Appendix). The final result is given as:

$$\begin{aligned} \int_0^{r_o} \left(\frac{\partial E_z}{\partial r}\right)_{z=0^+} J_1(\lambda_{1p} r) r dr &= \frac{-\kappa \alpha r_o}{(\kappa^2 - \lambda_{1p}^2)} \left[\kappa J_2(\kappa r_o) J_1(\lambda_{1p} r_o) - \lambda_{1p} J_1(\kappa r_o) J_2(\lambda_{1p} r_o) \right] \\ &\quad - \frac{C'_{7p} \left(1 + e^{-\xi_{1p} t_o}\right) \lambda_{1p} r_o^2 [J_2(\beta_{1p})]^2}{2} \\ &= X_2 + C'_{7p} X_3 \end{aligned} \quad (40)$$

Comparing the RHS terms in equations (39) and (40), the pre-exponential coefficient, C'_{7p} , corresponding to $E_z(r, z)$ is evaluated as:

$$C'_{7p} = \frac{X_1 - X_2}{X_3} \quad (41)$$

The final unknown to be determined is the coefficient, C'_{5m} , in the expression for $E_r(r, z)$. Faraday's law⁴⁸ will be made use of in evaluating this constant:

$$\bar{\nabla} \times \bar{H} = \sigma \bar{E} \Rightarrow -\left(\frac{\partial H_\phi}{\partial z}\right) \hat{r} + \left(\frac{\partial H_\phi}{\partial r}\right) \hat{z} = \sigma E_r \hat{r} + \sigma E_z \hat{z} \quad (42)$$

Comparing the r component on both sides of the equation:

$$-\left(\frac{\partial H_\phi}{\partial z}\right) = \sigma E_r; \text{ substituting for } H_\phi \text{ from equation (21), we have:}$$

$$\left(\frac{\partial^2 E_z}{\partial z \partial r} - \frac{\partial^2 E_r}{\partial z^2}\right) = -j\omega\mu\sigma E_r \quad (43)$$

Substituting the expressions for $E_r(r, z)$ and $E_z(r, z)$ from equations (32) and (35), the above equation becomes:

$$\begin{aligned} \sum_m \left(C'_{7m} \lambda_{1m} \xi_{1m} - C'_{5m} \xi_{1m}^2 \right) J_1(\lambda_{1m} r) \left[e^{-\xi_{1m} z} - e^{-\xi_{1m}(t_o - z)} \right] \\ = -j\omega\mu\sigma \sum_m C'_{5m} J_1(\lambda_{1m} r) \left[e^{-\xi_{1m} z} - e^{-\xi_{1m}(t_o - z)} \right] \end{aligned} \quad (44)$$

By comparing the coefficients on both sides of the equation, C'_{5m} is obtained as:

$$C'_{5m} = \frac{C'_{7m} \lambda_{1m} \xi_{1m}}{\xi_{1m}^2 - j\omega\mu\sigma} \quad (45)$$

This completes the determination of the electric field distribution (equations (32) and (35)) inside a metallic cylindrical disk specimen caused by current injection and extraction via source and sink electrodes.

5.1.3.4 Semi-infinite solution

Let us consider the case when the cylinder is infinitely long in the thickness (z) direction. The solution for the electric field distribution in this case can be developed as a corollary to the derivation for the disk case. All the boundary conditions listed for the disk problem are equally valid here. Therefore, the approach for obtaining the final solution is similar to that used for the disk problem. However, the only major difference between the solutions is that, terms involving $e^{+\xi_i z}$ are excluded from z -solutions (equations (12) and (13)) for the present case. This essentially means that the probability of a return wave originating from the opposite boundary is negligible, which is a good approximation for large values of t_o .

The solutions for field expressions, viz. $E_r(r, z)$ and $E_z(r, z)$ for this problem can then be written as follows:

$$E_r(r, z) = \sum_m C'_{8m} e^{-\xi_{1m} z} J_1(\lambda_{1m} r) \quad (46)$$

$$E_z(r, z) = \alpha J_o(\kappa r) + \sum_m C'_{9m} e^{-\xi_{1m} z} J_o(\lambda_{1m} r) \quad (47)$$

The coefficients C'_{8m} and C'_{9m} may be solved for in a similar manner as treated in the disk solution. The expressions listed above are valid only from $z = 0$ to $\left(\frac{t_o}{2}\right)$; the solution for other half of the cylinder is readily obtained by using the symmetry

conditions listed in equations (27) and (28). Therefore, this problem will hereafter be referred to as the ‘semi-infinite’ case.

5.1.4 Finite element approach

As mentioned earlier, a finite element solution obtained using the Electromagnetics Module of FEMLAB package⁵⁸ is presented in order to validate the analytical field expressions. The Meridional Currents/Potentials mode is chosen for modeling, which ensures symmetry about the ϕ direction. Additionally, symmetry about the z -axis is also preserved by enforcing the condition that there is no non-zero radial current density or a gradient in the axial current density on the z axis, i.e. $J_r|_{r=0} = 0$ and

$$\left(\frac{\partial J_z}{\partial r} \right) \Big|_{r=0} = 0^{11}. \text{ The finite element model is formulated as a time-harmonic quasistatic}$$

application in terms of magnetic and electric potentials. The modeling space consists of one-half of r - z cross-section of the specimen (boundary 1 shows axial symmetry), which has been subdivided into two sub-domains as shown in Figure 5.2. The edges of sub-domain I at $z=0$ (boundary 3) and $z=t_o$ (boundary 2) correspond to the source and sink electrode contacts respectively. Continuity of electric and magnetic fields is specified across the vertical boundary (boundary 4) at $r=r_c$. Electric and magnetic insulation is specified at all boundaries (boundaries- 5,6,7) excepting the electrode contacts, where, a constant current density, is specified. A Direct UMFPACK linear stationary linear solver capable of handling time-harmonic problems is employed for obtaining the solution of the dependent variables, viz. the vector magnetic potential (\bar{A}) and the electric potential (V), for the following PDE:

$$\begin{aligned}
& (j\omega\sigma - \omega^2 \varepsilon_o \varepsilon_r) \bar{A} + \bar{\nabla}_x \left(\frac{\bar{\nabla}_x \bar{A}}{\mu_o \mu_r} \right) - \sigma \bar{\nabla}_x (\bar{\nabla}_x \bar{A}) + \\
& + (\sigma + j\omega \varepsilon_o \varepsilon_r) \nabla V - \bar{J}^e = 0
\end{aligned} \tag{48}$$

In the above equation, ε_o and ε_r refer to the absolute and the relative permittivity respectively. Subsequently, the electric and magnetic fields are obtained as:

$$\bar{E} = -\nabla V - \frac{\partial \bar{A}}{\partial t} \text{ and} \tag{49}$$

$$\bar{B} = \bar{\nabla}_x \bar{A} \tag{50}$$

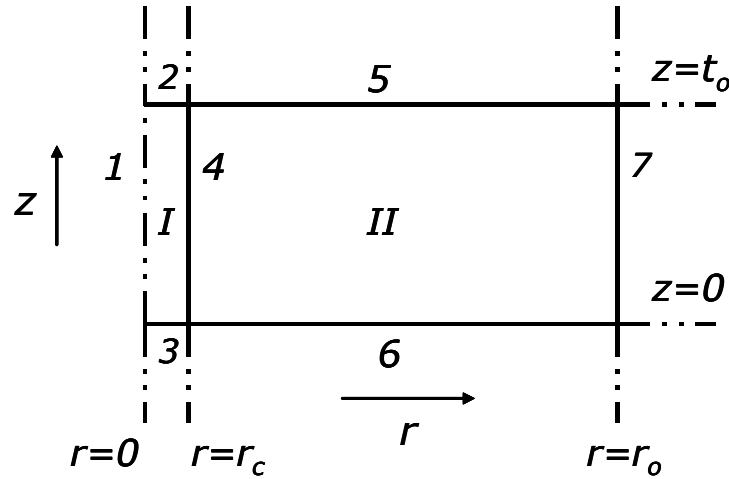


Figure 5.2. Illustration of the problem geometry (r - z cross-section) detailing the various sub-domains and boundaries as modeled in FEMLAB. Sub-domains I and II are parts of the complete specimen and are differentiated in order to indicate the electrode contacts on boundaries ($z=0$ and $z=t_o$) of sub-domain I. Sub-domain boundaries are numbered using Arabic numerals.

5.1.5 Simulation results and discussion

First, the electric field profiles (E_z and E_r) obtained via analytical and finite element approaches are presented and compared at various frequencies. Next, the effects of varying one or more geometric parameters on the field profiles are studied systematically. Finally, the notion of a limiting thickness, $t_{o,lim}$, is introduced, which is useful in assessing the applicability of the disk and semi-infinite analytical solutions for a given geometric configuration.

5.1.5.1 Electric field profiles

The following set of material properties and geometric parameters is used for computing of the profiles: $\sigma = 8.34 \times 10^5$ [S/m], $\mu_r = 1.004$, $r_o = 5$ [mm], $r_c = 0.5$ [mm] and $t_o = 2$ [mm]. A current of constant amplitude, $I_o = 50$ [mA] is also assumed. A total of 53288 elements and 3126 boundary elements corresponding to a simulation space of 5×2 [sq.mm] were used for finite element computations. Figure 5.3 shows the comparison between the analytical and the FEMLAB solutions in terms of axial field profiles (E_z vs r) at frequencies of 10^4 , 2×10^5 and 10^6 Hz. Plots showing the radial field profiles (E_r vs r) are shown in Figure 5.4. For frequencies below 10^4 Hz, the profiles are approximately the same as the one at 10^4 Hz. It is clear from these figures that the analytical and FEMLAB solutions are in excellent agreement with one another.

As discussed earlier, due to symmetry about $z = \frac{t_o}{2}$, field profiles will be the same on either half of the disk. For this reason, field profiles are only shown from $z = 0$ to $\left(\frac{t_o}{2}\right)$ at intervals of $\left(\frac{t_o}{6}\right)$ in z . At any given frequency, the impressed field is always a

step function at $z = 0$. With increase in z , it is seen that $E_z(r, z)|_{r=0}$ decreases progressively from $z = 0$ to $\left(\frac{t_o}{2}\right)$. This is due to progressive attenuation of the signal as it propagates within the medium. With increasing r , it is noted that there is a declining gradient in $E_z(r, z)$ with respect to r , at all frequencies, initially. This initial gradient is due to constriction of current flow lines near the contacts. The gradient diminishes in magnitude as z increases from 0 to $\left(\frac{t_o}{2}\right)$, because the effect of constriction progressively decreases away from the contacts. The constriction effect in essence signifies the extent of radial spreading of the current. That this is the case, can be seen from Figure 5.4, where the radial field, $E_r(r, z)$, is plotted versus r . It is clear from the plots that the constriction effect is a maximum at $r = r_c$, where the contacts terminate. The diminishing effect of constriction with increase in z or r is manifested again as a reduction in $E_r(r, z)$.

The constriction drop-off is modified to a significant extent upon changing the frequency as is noted from Figure 5.3. Increasing the frequency has the effect of lowering the fields in the constriction region and enhancing the rate of drop-off. The effect of frequency is also noted in the tail regions of the profiles (higher values of r), as is evident from Figures 5.3 and 5.4. At 10^4 Hz, the profile for $E_z(r, z)$ remains fairly flat beyond the initial drop off. However as frequency increases, the profile rises near the tail region. The extent of rise is greater, the higher the frequency. This behavior is due to the skin-effect, which forces the current to propagate closer to the surface, resulting in higher fields near the surface^{47, 57}. Thus at high frequencies, the interplay between constriction and skin

effects determines the overall field distribution, whereas constriction is the only predominant effect at low frequencies.

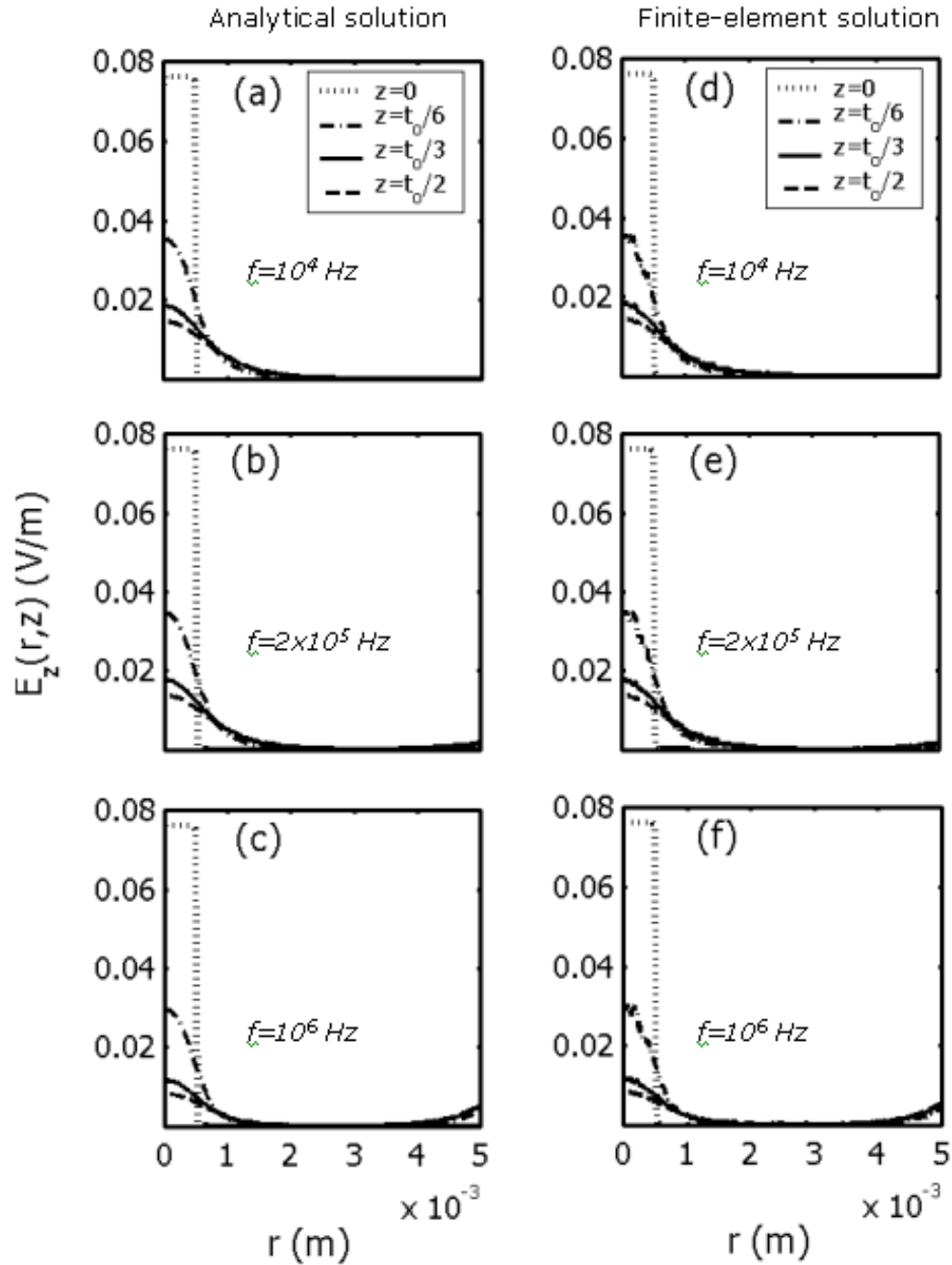


Figure 5.3. Plots showing the axial field profiles- $E_z(r, z)$ obtained via analytical (cases-(a), (b) and (c)) and FEMLAB (cases-(d), (e) and (f)) solutions at frequencies of 10^4 , 2×10^5 and 10^6 Hz respectively.

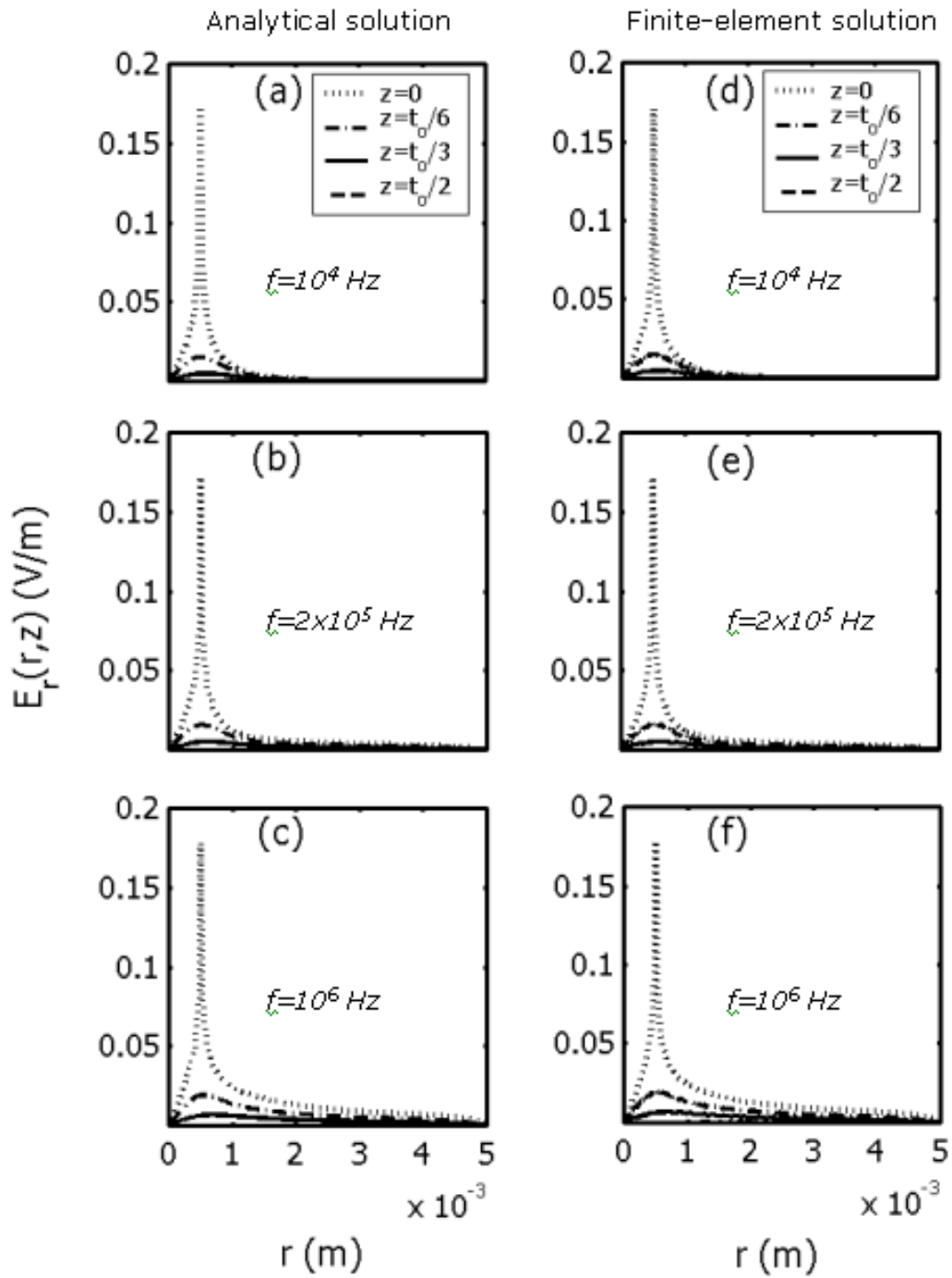


Figure 5.4. Plots showing the radial field profiles- $E_r(r,z)$ obtained via analytical calculations ((a), (b) and (c)) and FEMLAB simulations (d), (e) and (f)) at frequencies of 10^4 , 2×10^5 and 10^6 Hz respectively. In this set of plots, the peak position for $z = 0$ case is at $r = r_c$.

5.1.5.2 Geometric effects on field distribution

The effects of systematically varying the different geometrical parameters on the field profiles are presented next. For this study, the material parameters (σ, μ) and the total injected current (I_o) are unaltered from earlier values.

Simulations for studying the skin-effect behavior (at large r) were conducted by fixing r_c and systematically varying r_o and t_o . The field on the boundary, viz.

$E_z(r, z) \Big|_{(r_o, \frac{t_o}{2})}$, was chosen as the representative parameter for studying the skin-effect

behavior. This is because, the constriction effect is minimal at the center ($z = \frac{t_o}{2}$),

whereas the field due to skin-effect is a maximum on the boundary ($r = r_o$). Therefore,

the field parameter, $E_z(r, z) \Big|_{(r_o, \frac{t_o}{2})}$, will hereafter be referred to as the skin-effect field.

Figure 5.5 (a) shows the skin-effect field at 1 MHz plotted versus t_o at three different values of r_o . The electrode contact radius- r_c is fixed at 0.1 [mm] for these simulations. It is evident from the plot that the skin-effect field is primarily influenced by a change of r_o . Next, a maximum in the skin-effect field at $t_o = t_{o, cri}$ is noted upon progressively increasing t_o which ultimately reaches a steady value. These inferences may be understood by examining the expression for the skin-effect field, which is given as:

$$E_z(r_o, \frac{t_o}{2}) = \alpha J_o(kr_o) + \sum_m 2C'_m e^{-\frac{\xi_{1m} t_o}{2}} J_o(\lambda_{1m} r_o) \quad (51)$$

In general both the terms in this expression are complex quantities. The first term actually describes the skin-effect, which for the most part is dependent on α . Therefore, the

magnitude of this term scales inversely with r_o , which is evident from the expression for α , given earlier. The magnitude of the second term that arises due to the constriction effect, is mostly influenced by t_o . The contribution from the constriction term is significant only for small values of t_o . Therefore, the magnitude of the field is governed by both terms at small values of t_o . The maximum occurs when the phase difference between the two complex phasors is minimal. As t_o assumes larger values, the contribution from the constriction term becomes increasingly less significant, which is the reason for the asymptotic behavior. Physically, this implies that at large values of t_o , the constriction effect is insignificant and the situation is therefore identical to 1D skin-effect.

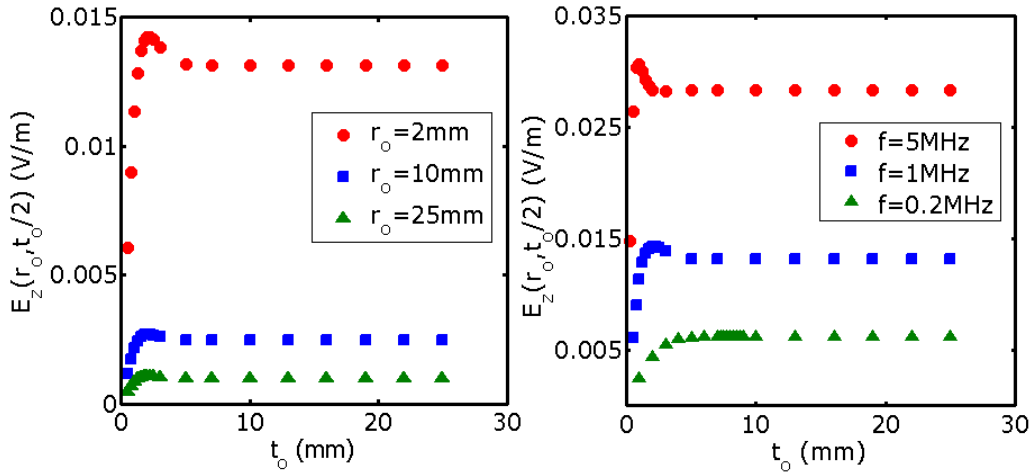


Figure 5.5. Plots showing the skin-effect field $E_z(r, z) \Big|_{(r_o, \frac{t_o}{2})}$ as a function of specimen thickness- t_o by varying the specimen radius- r_o at a fixed frequency of 1 MHz in (a) and by varying the frequency at a fixed r_o of 2 [mm] in (b). The electrode contact radius- r_c was fixed at 0.1 [mm] for both (a) and (b).

From the plot in Figure 5.5 (a), it is noted that the value of $t_{o,cri}$ remains almost unaltered for the three values of r_o investigated. The skin-effect field is found to remain invariant with changes in r_c and therefore, the position of $t_{o,cri}$ also remains the same irrespective of changes in r_c . However, the position of the maximum is found to shift upon varying the frequency as shown in Figure 5.5 (b). The value of $t_{o,cri}$ shifts to larger values with a corresponding decrease in the skin-effect field as the frequency is lowered. The scaling of the field with frequency is because the parameter α is proportional to the square-root of the frequency. Additionally the contribution from the second term is also frequency dependent and therefore the maximum is displaced further along the t_o axis upon lowering the frequency. A good analogy to this situation is that of 1D skin-effect, where the field spreads more into the conductor from the surface as the frequency is lowered. In essence, frequency behaves like a kinetic parameter in controlling the dispersion of the electric field.

Next, the results from studies on constriction behavior are discussed. The value of the field- $E_z(r,z)\Big|_{(r_c, \frac{t_o}{6})}$, is chosen as the representative parameter for studying the constriction behavior. The constriction effect from previous discussion is clearly the largest at $r = r_c$, while the choice of the z co-ordinate is arbitrary. This field parameter will be referred to as the constriction field, hereon. . It is intuitive that r_c should have a major impact on the constriction field, because the constriction field is a consequence of the impressed field, which is dictated by r_c . Next, the effect of systematically varying r_o and t_o on the constriction field is investigated for a fixed value of r_c . Figure 5.6 shows

the constriction field plotted as a function of t_o for three different values of r_o . It is clear from the plot that for a given r_o , a monotonous decrease in the constriction field is noted until it reaches an asymptote. Additionally, the asymptote occurs at a higher value of t_o as r_o increases. This may be understood by looking at the following expression that

governs the constriction field, $E_z(r, z) \Big|_{(r_c, \frac{t_o}{6})}$:

$$E_z(r_c, \frac{t_o}{6}) = \alpha J_o(\kappa r_c) + \sum_m C'_{7m} \left(e^{-\frac{\xi_{1m} t_o}{6}} + e^{-\frac{5\xi_{1m} t_o}{6}} \right) J_o(\lambda_{1m} r_c) \quad (52)$$

The contribution from the summation term decays exponentially with increasing t_o . Therefore, at small values of t_o , the magnitude of the field is entirely determined by the

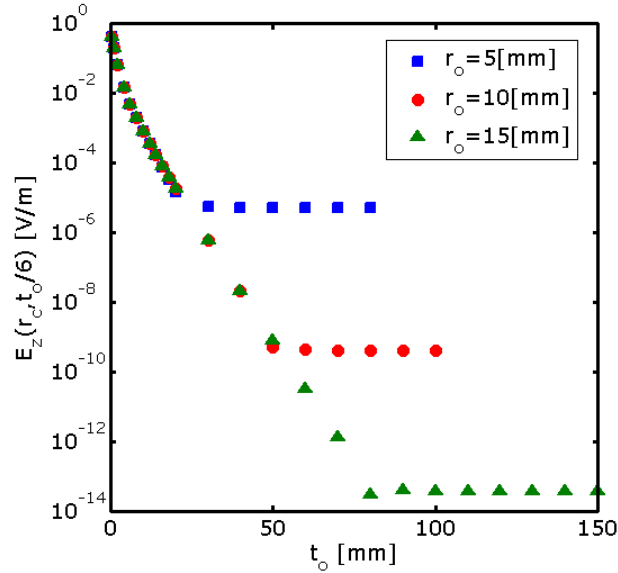


Figure 5.6. Plot showing the constriction field $E_z(r, z) \Big|_{(r_c, \frac{t_o}{6})}$ versus t_o for three different values of the specimen radius- r_o . The electrode contact radius r_c is fixed at 0.1 [mm] for these simulations.

summation term, irrespective of the value of r_o . For large values of t_o , the summation term becomes negligible and therefore the expression is independent of t_o , which explains the asymptotic behavior. In the intermediate regime, contributions from both terms are comparable and the extent of this regime is dependent on the parameter α , which varies inversely with r_o . Therefore, a specimen with a larger radius has an extended intermediate regime and also a smaller asymptotic field directly attributable to the contribution from the first term. Physically this means that the constriction behavior equilibrates at a much smaller thickness in a specimen of smaller radius compared to a larger one. The reason is because the field has to spread out over a larger distance in a specimen of larger radius and consequently equilibrates at a lower asymptote.

5.1.5.3 Limiting thickness analysis

The notion of a limiting thickness, $t_{o,lim}$, is introduced so as to investigate the applicability of the analytical solutions to a particular geometric configuration. The limiting thickness, $t_{o,lim}$, is defined as the minimum thickness of the disk for which a limiting field profile, $E_{z,lim} \Big|_{z=\frac{t_{o,lim}}{2}}$, is reached at the center of the disk. This essentially means that increasing the thickness of the disk beyond $t_{o,lim}$, (say to $t_l > t_{o,lim}$) will yield the same profile, $E_{z,lim} \Big|_{z=\frac{t_{o,lim}}{2}}$, for all values of z between $\left(\frac{t_{o,lim}}{2}\right)$ and $\left(\frac{t_l}{2}\right)$. It is intuitive that the limiting thickness as well as the limiting field profile should be frequency dependent, because the constriction drop off varies with frequency as explained previously.

Since there is no straight forward analytical means for determining $t_{o,lim}$, an optimization procedure was developed for this purpose. The field at the center of the specimen- $E_z(r,z)$ $\Big|_{(0, \frac{t_o}{2})}$ (for any arbitrary t_o), hereafter referred to as the center field, was chosen as the optimization parameter. This is because the field at $\left(0, \frac{t_o}{2}\right)$ was found to be the last to equilibrate of the electric field profile at $z = \frac{t_o}{2}$. The center field is given by the following expression:

$$E_z\left(0, \frac{t_o}{2}\right) = \alpha + \sum_m 2C'_{7m} e^{-\frac{\xi_{1m} t_o}{2}} \quad (53)$$

The procedure begins by initializing lower and upper bounds for t_o , such that $t_{o,upper} \gg t_{o,lower}$. The center fields, viz. $E_{z,lower}$, $E_{z,upper}$ and $E_{z,middle}$ are then determined at corresponding thickness values of $t_{o,lower}$, $t_{o,upper}$ and $t_{o,middle} = \left(\frac{t_{o,lower} + t_{o,upper}}{2}\right)$. Next, a determination of the correct thickness interval ($[t_{o,lower}, t_{o,middle}]$ or $[t_{o,middle}, t_{o,upper}]$) to search for $t_{o,lim}$, is made by examining the relative differences between the corresponding center fields *i.e.* $|E_{z,upper} - E_{z,middle}|$ and $|E_{z,middle} - E_{z,lower}|$. The interval corresponding to the smallest difference in the fields is the obvious choice. The values of the bounds are updated upon choosing the new interval. The procedure is repeated until a good convergence is obtained simultaneously in both the field and thickness values. This uniquely determines the value of $t_{o,lim}$ and the

associated limiting field profile, $E_{z,lim}|_{z=\frac{t_{o,lim}}{2}}$, for a given geometric configuration and a frequency. The results for calculations of the limiting thickness, $t_{o,lim}$, and the limiting center field $E_{z,lim}|_{(0,\frac{t_{o,lim}}{2})}$ are shown in Table 5.1 for several frequencies. These calculations are performed for the same set of material parameters and for values of r_c and r_o of 0.5 [mm] and 5 [mm] respectively. It is clear from the table that both the limiting thickness and the limiting center field increase progressively to an asymptotic quantity with a drop in the frequency.

The limiting thickness parameter thus determined was then used as a reference for comparing the analytical solutions for the disk and the semi-infinite cases with the

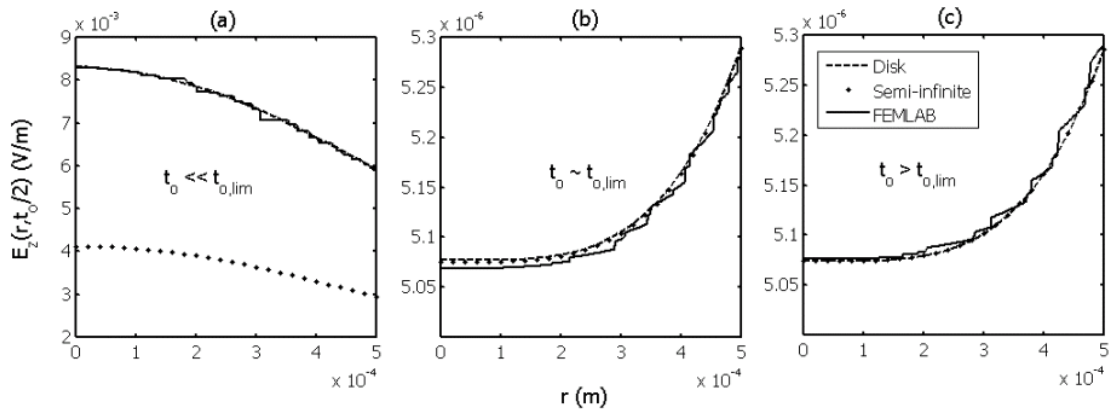


Figure 5.7. Plots showing the axial field at 1MHz as a function of r to show the relative match between the semi-infinite, disk analytical solutions and the FEMLAB solution for the following cases – (a) $t_o \ll t_{o,lim}$, (b) $t_o \cong t_{o,lim}$ and (c) $t_o \geq t_{o,lim}$.

FEMLAB solution. The finite element solution proved indispensable in verifying the assessment of $t_{o,lim}$. Figure 5.7 shows the electric field profiles ($E_z(r,z)$ at 1 MHz) from all three solutions at $z = \frac{t_o}{2}$ for the following cases: $t_o \ll t_{o,lim}$, $t_o \cong t_{o,lim}$ and $t_o > t_{o,lim}$. The cross-section at the center of the disk was chosen because, the discrepancies if present, were always a maximum at the center. For $t_o \ll t_{o,lim}$, there is a clear mismatch between the profiles yielded by the two analytical solutions. As t_o increases, the mismatch becomes progressively smaller and the solutions yield a perfect match at $t_{o,lim}$. The match between the profiles remains intact for $t_o > t_{o,lim}$.

The total number of elements used in the finite element models for the cases - $t_o \ll t_{o,lim}$, $t_o \cong t_{o,lim}$ and $t_o > t_{o,lim}$ were 20824, 67880 and 72017 respectively. The maximum element size (Δ_{max}) on vertical boundaries of the model (spanning a length of t_o) was adjusted so as to enhance the match with the analytical solution(s). The same value of Δ_{max} could not be used for all three cases because of excessive memory demands imposed by the solver. FEMLAB solution yields a nearly identical profile to that of the analytical disk solution for $t_o < t_{o,lim}$. For $t_o \geq t_{o,lim}$, the FEMLAB solution deviates marginally from the two analytical solutions, which match perfectly. The match could be even better provided the amount of memory required by the solver upon lowering Δ_{max} could be met. However, for practical purposes, the analytical disk solution and the FEMLAB solution concur with each other for all values of t_o , while, the semi-infinite analytical solution is clearly a crude approximation for $t_o \ll t_{o,lim}$.

5.1.6 Calculation of specimen impedance for a two-probe measurement

In this section, the procedure for computing the complex impedance of the specimen in the shape of a cylindrical disk is described based on the expressions for the electric field distribution that was presented in section 5.1.3. As before, computation of impedance from the analytical model is validated using the FEMLAB model at a number of frequencies. These will then be compared to the experimentally measured impedance response of a metallic cylindrical disk specimen obtained from a two-probe impedance measurement.

The complex impedance (Z) of a specimen for an alternating current flow situation consists of real (Z') and imaginary (Z'') components, viz. a resistance (R) and a reactance (X).

$$Z = Z' + jZ'' = R + jX \quad (54)$$

In the case of a metallic specimen, the reactance is primarily due to the contribution from the internal inductance (L_i) of the specimen. While the resistance is related directly to the loss of energy due to ohmic heating, the inductance describes the ability of a conductor to store magnetic energy⁴⁹. The expression for the complex impedance in terms of the inductance is written as follows:

$$Z = R + j\omega L_i \quad (55)$$

The computation of R and L_i of a metallic cylindrical disk specimen using the analytical electric field expressions is carried out via energy methods. The resistance and the inductance are obtained by calculating the Joule heat-loss and the total internal magnetic energy respectively⁴⁹. This is restated in the expression formalism as follows⁴⁹:

$$R = \frac{I}{I_{rms}^2} \int_V \overline{\sigma \mathbf{E} \cdot \mathbf{E}_c} dV \quad \text{and} \quad (56)$$

$$L_i = \frac{I}{I_{rms}^2} \int_V \overline{\mathbf{B} \cdot \mathbf{H}_c} dV = \frac{I}{I_{rms}^2} \int_V \overline{\mu \mathbf{H} \cdot \mathbf{H}_c} dV \quad (57)$$

In the above expressions, $\overline{\mathbf{E}}$ and $\overline{\mathbf{H}}$ are the total complex electric and magnetic fields respectively, while the subscript c denotes the complex conjugate. The total magnetization- $\overline{\mathbf{B}}$ is related to the magnetic field $\overline{\mathbf{H}}$ by a magnetic permeability- μ . The total root mean square value of the current of amplitude I_o is given by $I_{rms} = \frac{I_o}{\sqrt{2}}$. The total electric field- $\overline{\mathbf{E}}$ and the magnetic field- $\overline{\mathbf{H}}$ are given in terms of the electric field components- E_r and E_z as follows:

$$\overline{\mathbf{E}} = E_r \hat{r} + E_z \hat{z} \quad \text{and} \quad (58)$$

$$\overline{\mathbf{H}} = \frac{I}{j\omega\mu} \left(\frac{\partial E_z}{\partial r} - \frac{\partial E_r}{\partial z} \right) \quad (59)$$

The expressions for E_r and E_z as a solution to the analytical derivation are given earlier.

The reader is referred to the appendix for further details on evaluation of the volume integrals.

In the case of FEMLAB model, the overall Joule heat loss and the magnetic energy are obtained by integration of the time average resistive heating per unit volume (Q_{av}) and the magnetic energy density (W_{mav}) over the specimen volume respectively⁵⁸. The expressions for the time average quantities, viz. the Joule heat loss per unit volume and the magnetic energy density are given as follows⁵⁸:

$$Q_{av} = \frac{I}{2} \text{Re}(\overline{\mathbf{J} \cdot \mathbf{E}_c}) \quad \text{and} \quad (60)$$

$$W_{mav} = \frac{I}{4} \text{Re}(\overline{H \cdot B_c}) \quad (61)$$

The resistance- R and the inductance- L_i are subsequently obtained by dividing out the time average quantities by I_{rms}^2 .

Plots of R and L_i as a function of the frequency are shown in Figures 5.8 and 5.9 respectively. The perfect match between the quantities computed via the closed-form analytical solution and the finite element FEMLAB solution is evident from both the plots. The resistance behavior as a function of frequency may be understood by examining the plots of $E_z(r, z)$ and $E_r(r, z)$ versus r at different frequencies in Figures 5.3 and 5.4. It is clear from these set of plots that as the frequency increases (from 10 kHz to 1 MHz), the field- $E_z(r, z)$ near the constriction region drops quickly to zero with increasing r and reappears at larger values of r (near the surface). The field- $E_r(r, z)$ on the other hand remains finite beyond the constriction region and is extended for large values of r with increase in the frequency. The variation in the fields for frequencies below 10 kHz is negligible. This redistribution in the axial and radial fields with frequency has the effect of decreasing the Joule loss contribution from $E_z(r, z)$ and increasing that from $E_r(r, z)$. The overall Joule heat loss however, increases drastically with frequency (10 kHz and above) as the predominant effect is that of $E_r(r, z)$. Consequently, the resistance- R remains relatively constant for frequencies up to 10kHz and increases progressively upon further increase in the frequency.

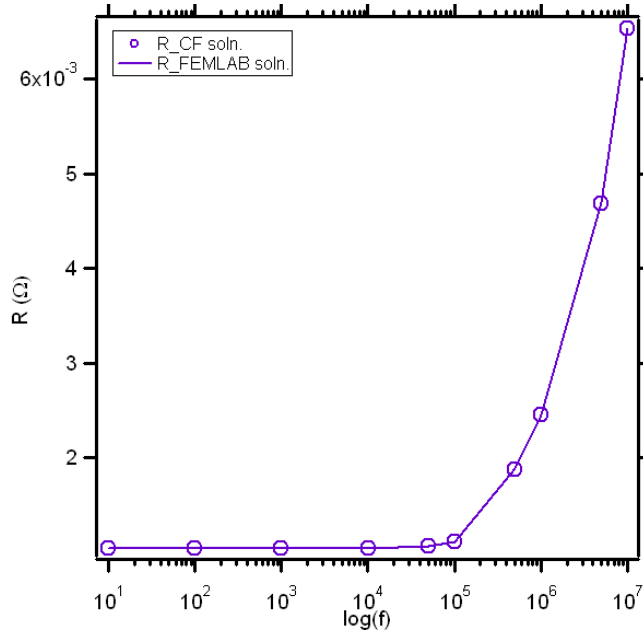


Figure 5.8 Plot of the frequency dependent resistance computed from both analytical (open symbols) and finite element models (solid line).

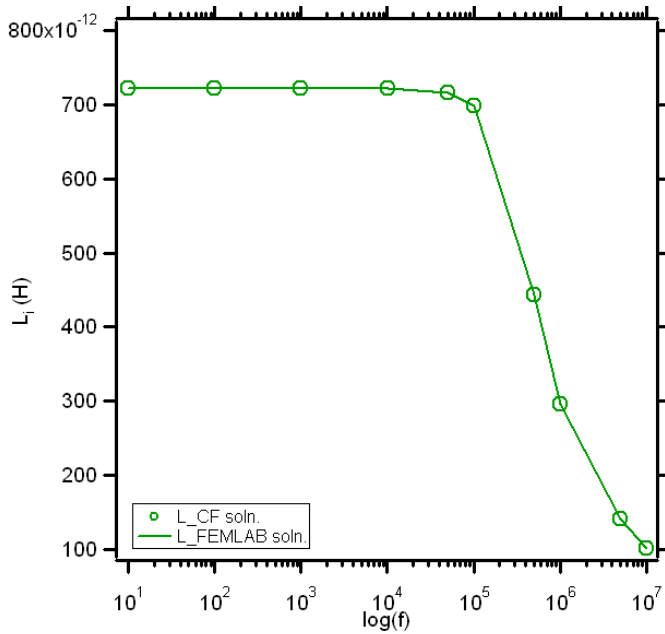


Figure 5.9. Plot of the frequency dependent inductance from both analytical (open symbols) and finite element models (solid line).

The inductance behavior as a function of the frequency is dependent on the distribution of the magnetic field inside the specimen⁴⁹. Figure 5.10 shows plots of the magnetic field- H_ϕ versus r at different z cross-sections starting from the boundary ($z=0$) to the center of the disk ($z=\frac{t_o}{2}$). It is evident from the plots that H_ϕ is a maximum at $r=r_c$, (where the constriction effect is maximum) and reaches a constant value on the curved boundary ($r=r_o$). As the frequency increases, it is noted that H_ϕ decreases in magnitude significantly near the constriction region as z increases from 0 to $\frac{t_o}{2}$. Thus the internal magnetic field weakens as the field penetrates less and less with increasing frequency. This results in a lower overall magnetic energy for the specimen and consequently a lower internal inductance with a rise in the frequency. In fact, the internal inductance decreases as the inverse of the square root of the angular frequency⁴⁹. The reactance- X on the other hand is a product of the internal inductance and the angular frequency and therefore increases with increasing frequency⁴⁹.

The magnitude of the overall impedance ($|Z| = \sqrt{R^2 + X^2}$) as a function of the frequency, is shown in Figure 5.11, for the closed-form analytical and the finite-element solutions respectively. The excellent match between the two solutions is again obvious.

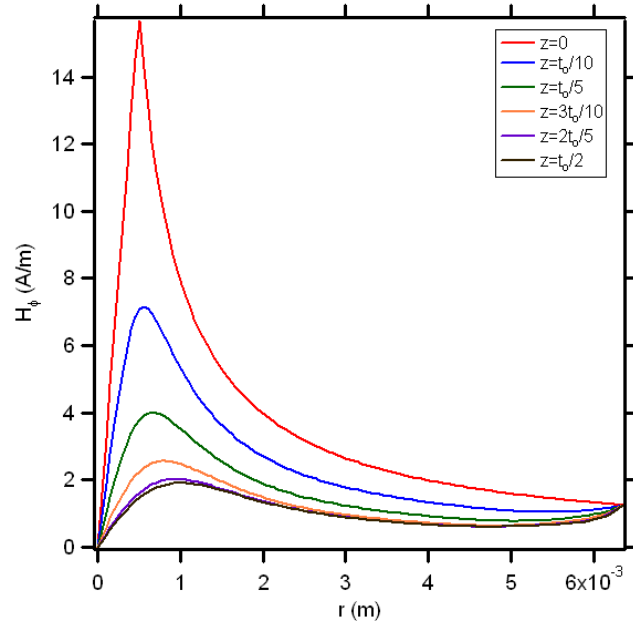


Figure 5.10 Plot showing the magnetic field- $H_{\phi}(r, z)$ versus r_o at different z cross-sections from the surface to the center of the conductor in steps of $\frac{t_o}{10}$. The frequency was set to be 1 MHz for these computations.

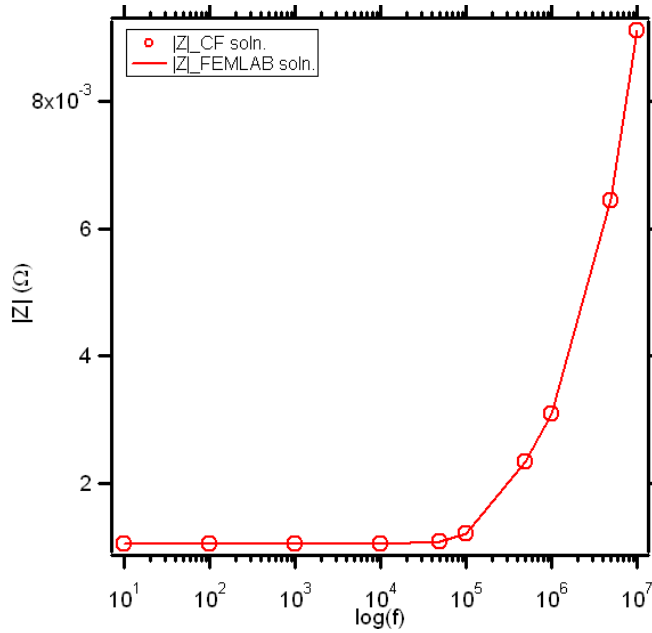


Figure 5.11. Plot of the complex impedance magnitude versus frequency from both analytical (open symbols) and finite element models (solid line).

5.1.7 Conclusions

Closed-form analytical expressions for the electric field distribution inside a cylindrical metallic disk specimen were derived for the problem of a two-probe impedance measurement. The specimen was treated to be a homogeneous material medium with average electrical and magnetic properties. As a corollary to the disk solution, the case of an infinitely long cylinder is also treated. A finite element solution obtained using a commercially available finite element package is also presented for comparison with the analytical solutions.

The field expressions consist of terms that incorporate both the skin effect and the constriction effect. In an expected manner, the skin effect term becomes prominent at high frequencies (10^4 Hz to 10^6 Hz) near the end regions of the disk (large r), while the constriction term dominates in regions near the contacts (small r). The magnitude of the field due to constriction decreases away from the electrode contacts in both the r and the z directions.

The effects of varying the electrode contact radius, r_c , the disk radius r_o , and the disk thickness, t_o , were also investigated in a systematic fashion. The skin effect behavior at high frequencies is found to be dependent only on the dimensions of the disk (r_o and t_o) and remains unaffected by a variation in r_c . The skin effect field reaches a maximum in t_o , before decreasing to an asymptotic value with increasing t_o . The constriction behavior is generally dependent on the geometry of the disk; however, the dominant effect is that of the contact radius, r_c . The dependency on r_o can be ruled out only for small values of t_o .

The concept of a limiting thickness, $t_{o,lim}$, for the disk and the associated limiting field profile, $E_{z,lim}\big|_{z=\frac{t_{o,lim}}{2}}$, is proposed in order to assess the range of validity of the disk and semi-infinite analytical solutions. Simulations indicate that the disk solution is a good match for the FEMLAB solution for all values of t_o . The semi-infinite solution also converges very well with the other solutions for $t_o \geq t_{o,lim}$. However, for $t_o \ll t_{o,lim}$, the semi-infinite solution diverges considerably from the actual profile yielded by the disk solution.

The real and imaginary parts of the complex impedance for an ideal two-probe impedance measurement were computed using the closed-form analytical and finite-element solutions via energy-based methods. The frequency dependent resistance of a Waspaloy disk specimen was found to remain unchanged up to 100 kHz and increased monotonically with further increase in the frequency. The internal inductance on the other hand showed a monotonic decrease after 100 kHz. These effects were explained as due to the increase in the overall Joule heat-loss and a decrease in the magnetic energy storage with rise in the frequency.

5.2 Determination of correction factors for a DC four-point probe measurement

5.2.1 Introduction

A four-point resistivity measurement may be described as the measurement of voltage drop between a pair of probes contacting the specimen by making the current to flow through a second set of probes, namely the source and sink contacts respectively. This scheme essentially allows for measuring the true specimen resistance without

including the contact resistance between the probes and the specimen. This is made possible by making the voltage probes part of a high impedance circuit, thus allowing only negligible current to flow through this circuit⁵⁹. As the name implies, the current and the voltage probe contacts are assumed to be point contacts. Additionally, the point-contacts are assumed to be ohmic to facilitate the injected current to flow uninterrupted³⁴. Four-point resistivity measurements have traditionally been used to characterize the uniformity of silicon wafers in the semiconductor industry^{35, 60}. Researchers have also used four-point measurements for conducting resistivity studies in precipitation-hardening metallic systems^{7, 8}. In these alloys, the microstructural variations induced by heat-treatments as a function of time and temperature are related to the measured changes in resistivity. More recently, the four-point technique is made applicable on a much finer scale by the use of micro-probes that have spacings in the range of a few microns to tens of microns^{61, 62}. The fabrication of these micro-probes enables the characterization of microstructural features such as whiskers, bulk nanostructures etc. that is not possible using the traditional four-point probe. The measured resistance in a four-point probe measurement is related to the specimen resistivity by a geometric correction factor that accounts for the finite geometry of the specimen³². It is therefore important to apply accurate correction factors to be able to trust the observed changes in resistivity with enough confidence.

The present analytical derivation deals with the evaluation of correction factors for cylindrical specimens for a random placement of the four probes on a circular face of the specimen. A closed-form analytical expression is obtained for the potential difference between the voltage probes via the solution of Laplace's equation⁴⁸ using the variable-

separation technique^{50, 53}. The potential difference thus obtained is subsequently used to compute the geometric correction factor. The solution presented here is valid for any given cylindrical geometry and for any random placement of the four probes. It is similar to the well known van der Pauw method⁶³, which enables the determination of the resistivity of a specimen of arbitrary shape and uniform thickness using four point contacts. The point contacts in the van der Pauw method⁶³ can also be randomly located. However, they should all lie on the circumference of the specimen.

Golubev et al.⁶⁴ presented closed-form solutions for four-point probe measurements on a tubular cylinder applicable for collinear and square probe arrays. The derivation is based on obtaining a solution for Laplace's equation by integrating the boundary value problem using Green's function. The factors are expressed in terms of modified Bessel functions and their derivatives. Correction factor curves are given in this reference⁶⁴ for different arrangements of collinear and square probe arrays for cylinders of semi-infinite length. However, correction factors that were computed for the present research using the equations listed by Golubev et al., yielded incorrect values for solid cylinders of finite thickness. Additionally, small thicknesses resulted in large arguments for the modified Bessel terms in the series solution. Asymptotic expansion⁵¹ of modified Bessel terms for large arguments shot up rapidly to infinity for a relatively small number of series of terms. Yamashita⁶⁵ obtained a closed-form solution for the potential distribution as a solution to Poisson's equation for a four-probe measurement on a thick cylinder, which is the same problem dealt with in the present research. Expressions for correction factors were presented separately for regions of the specimen enclosed by the probe array and those outside. Correction factor behavior was studied systematically by

varying the specimen thickness, specimen radius, probe spacing and probe displacement. Additionally, the author also accounted for variations introduced by the probe tip radius⁶⁵. In a second publication⁶⁶, the author presented the correction factor for the same problem using the ‘method of images’. The correction factor derived using the ‘method of images’ was reported to yield faster convergence in case of thicker specimens⁶⁶.

In addition, several researchers have computed geometric correction factors for different circular cylindrical geometries using the ‘method of images’³⁴, which will be referred to as analytical approximation factors. These will be detailed in a later section. However, the specific case of a four-point probe measurement on a cylindrical specimen of finite thickness has not been dealt with using the method of images.

The applicability of the present derivation is illustrated for two specific cases using a collinear probe-array viz.- probes arranged along a radius and perpendicular to a radius. Simulations are conducted by systematically varying the specimen radius- r_o , the thickness- d and the probe-array displacement- L for the above probe arrangements. Correction factors obtained from the closed-form solution are validated in each case by a finite-element simulation solution obtained using COMSOL Multiphysics 3.2. Additionally, the correction factors from the two methods are compared to analytical approximation factors, the expressions for which are available in the literature. A range for the analytical approximation factors defined by a lower and an upper bound approximation, is computed for each specific case. Correction factors from the closed-form solution and the COMSOL solution show an excellent match with each other and lie within the analytical approximation bounds in all cases.

5.2.2 Problem Formulation

The specimen is assumed to be a uniform solid cylinder of radius r_o and thickness d and of conductivity σ . A cylindrical co-ordinate system- (r,θ,z) with the origin located at the center of one of the circular faces ('A'), as shown in Figure 5.12 is used. The opposite circular face ('B') is assumed to be resting on an insulating support block. The curved surface of the cylinder is also assumed to be insulating. A random placement of probes is considered on the circular face 'A', with probe locations denoted by $(r_i,\theta_i,0)$ for $i=1, 2, 3$ and 4. The subscripts '1' and '2' refer to the source and the sink contacts respectively, transporting a current I_o , while '3' and '4' refer to the voltage pick-up points.

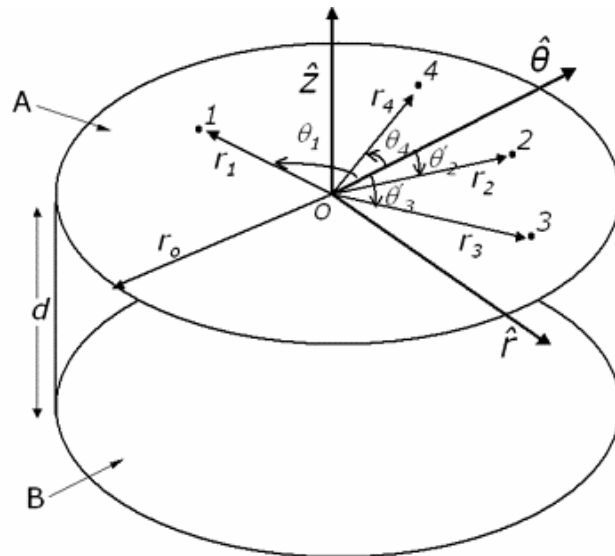


Figure 5.12 Schematic showing the placement of four probes at random locations- $(r_i,\theta_i,0)$ on the circular face-A of a specimen of radius- r_o and thickness- d in a cylindrical co-ordinate system. The opposite circular face-B is assumed to be resting on an insulating support.

The potential distribution $\varphi(r, \theta, z)$ inside the specimen is obtained by a solution of Laplace's equation⁴⁸, written as:

$$\nabla^2 \varphi(r, \theta, z) = 0 \quad (62)$$

Laplace's equation is essentially a restatement of the continuity equation⁴⁸ as given below.

$$\bar{\nabla} \cdot \bar{J} + \left(\frac{\partial \rho}{\partial t} \right) = 0 \quad (63)$$

Here \bar{J} is the current density and ρ is the volume charge density within the specimen.

If a steady current flow is assumed through the specimen, then there is no macroscopic charge residing inside the specimen at any given instant. Therefore, the term describing the time rate of change of charge density in the continuity equation may be set to zero.

The source condition and the boundary conditions governing the problem may now be listed as follows:

$$\left(\frac{\partial \varphi}{\partial z} \right)_{z=0} = \frac{I_o}{\sigma r} [\delta(r - r_1) \delta(\theta - \theta_1) - \delta(r - r_2) \delta(\theta - \theta_2)] \quad (64)$$

$$\left(\frac{\partial \varphi}{\partial z} \right)_{z=-d} = 0 \quad \text{and} \quad (65)$$

$$\left(\frac{\partial \varphi}{\partial r} \right)_{r=r_o} = 0 \quad (66)$$

5.2.3 Analytical Approach

5.2.3.1 Closed-form solution

The solution for the potential distribution $\phi(r, \theta, z)$ governing the above problem is sought using the variable-separation technique^{50, 53}. The preliminary solution for $\phi(r, \theta, z)$ may be expressed as the composite of the component solutions as follows:

$$\phi(r, \theta, z) = \psi(r, \theta)G(z) \quad (67)$$

Substituting this in equation (62) and expanding the Laplacian, we obtain two independent differential equations as follows:

$$\frac{1}{\psi} \left[\frac{\partial^2 \psi}{\partial r^2} + \frac{1}{r} \frac{\partial \psi}{\partial r} + \frac{1}{r^2} \frac{\partial^2 \psi}{\partial \theta^2} \right] = -k^2 \quad (68)$$

$$-\frac{1}{G} \frac{d^2 G}{dz^2} = -k^2 \quad (69)$$

In this equation, $'-k^2'$ is introduced as a separation constant.

The solution for $G(z)$ may readily be written as:

$$G(z) = C_1 e^{-kz} + C_2 e^{kz} \quad (70)$$

The second partial solution $\psi(r, \theta)$ is further split into two component solutions in r and θ as follows:

$$\psi(r, \theta) = R(r)\Theta(\theta) \quad (71)$$

Substituting this in equation (68), the partial differential equation (PDE) in $\psi(r, \theta)$ reduces into two independent ordinary differential equations (ODE's) by the use of a second separation constant, $'-m^2'$:

$$\frac{1}{\Theta} \frac{d^2 \Theta}{d\theta^2} = -m^2 \text{ and} \quad (72)$$

$$\frac{r^2}{R} \frac{d^2 R}{dr^2} + \frac{r}{R} \frac{dR}{dr} + r^2 k^2 = m^2 \quad (73)$$

The standard solutions for equations (72) and (73) may be written down as:

$$\Theta(\theta) = C_3 \sin(m\theta) + C_4 \cos(m\theta) \text{ and} \quad (74)$$

$$R(r) = C_5 J_m(kr) + C_6 Y_m(kr) \quad (75)$$

Here $J_m(x)$ and $Y_m(x)$ are m^{th} order Bessel functions of the first and second kind respectively. Since the function $Y_m(x)$ poses a singularity at the origin⁵³, it may be neglected right away from the radial solution.

The general solution for $\varphi(r, \theta, z)$ may now be written by collecting the component solutions listed in equations (70), (74) and (75) as:

$$\varphi(r, \theta, z) = J_m(kr) [C'_3 \sin(m\theta) + C'_4 \cos(m\theta)] [C_1 e^{-kz} + C_2 e^{kz}] \quad (76)$$

A particular solution for $\varphi(r, \theta, z)$ may be obtained upon determination of the various separation constants and coefficients in equation (76). The unknowns are solved for by making use of the problem constraints listed in equations (64), (65) and (66).

Applying the condition imposed on the radial field expressed in equation (66), we obtain:

$$\left(\frac{dJ_m(kr)}{dr} \right)_{r=r_0} = 0 \quad (77)$$

This equation is essentially the criterion for determining the maxima or minima of $J_m(x)$.

The above equation has an infinite set of roots given by $k_{mn} = \frac{\beta_{mn}}{r_o}$, where β_{mn}

($n=1,2,3,\dots$) is a node corresponding to a maximum or a minimum of $J_m(x)$.

The azimuthal solution- $\Theta(\theta)$ in equation (74) must be a periodic function in θ with a period of 2π in order for it to be single-valued⁵⁰. Therefore –

$$\Theta(\theta) = \Theta(\theta + 2\pi) \quad (78)$$

This condition allows only integer values for m .

From these arguments, a particular solution for $\varphi(r, \theta, z)$ is written as:

$$\varphi(r, \theta, z) = \sum_m \sum_n J_m(k_{mn}r) [C'_{3mn} \sin(m\theta) + C'_{4mn} \cos(m\theta)] [C_{1mn} e^{-k_{mn}z} + C_{2mn} e^{k_{mn}z}] \quad (79)$$

Next, applying the constraint listed in equation (65) on the axial field, a relation between the coefficients- C_{1mn} and C_{2mn} is obtained as follows:

$$C_{1mn} = C_{2mn} e^{-2k_{mn}d} \quad (80)$$

Incorporating this relationship into equation (79), $\varphi(r, \theta, z)$ is rewritten as:

$$\varphi(r, \theta, z) = \sum_m \sum_n J_m(k_{mn}r) [C''_{3mn} \sin(m\theta) + C''_{4mn} \cos(m\theta)] [e^{-k_{mn}(2d+z)} + e^{k_{mn}z}] \quad (81)$$

In the above particular solution for $\varphi(r, \theta, z)$, all integer values are allowed for m , while n can only assume positive values. The summation may therefore be split as follows:

$$\varphi(r, \theta, z) = \varphi_1 + \varphi_2 + \varphi_3 = \sum_{p=-\infty}^{-1} \sum_{n=1}^{\infty} J_p(k_{pn}r) [C''_{3pn} \sin(p\theta) + C''_{4pn} \cos(p\theta)] [e^{-k_{pn}(2d+z)} + e^{k_{pn}z}] +$$

$$\sum_{n=1}^{\infty} C''_{4on} J_o(k_{on}r) [e^{-k_{on}(2d+z)} + e^{k_{on}z}] +$$

$$\sum_{m=1}^{\infty} \sum_{n=1}^{\infty} J_m(k_{mn}r) [C''_{3mn} \sin(m\theta) + C''_{4mn} \cos(m\theta)] [e^{-k_{mn}(2d+z)} + e^{k_{mn}z}] \quad (82)$$

The first double summation in $\varphi(r, \theta, z)$ can be reduced to a positive index by the following property of Bessel functions⁵⁰:

$J_{-m}(x) = (-1)^m J_m(x)$; therefore, the nodes that correspond to the maxima or the minima of $J_{-m}(x)$ are the same as that of $J_m(x)$, ie., $k_{pn} = k_{mn}$, where $p = -m$. The first double summation may hence be rewritten as:

$$\varphi_1 = \sum_{m=1}^{\infty} \sum_{n=1}^{\infty} (-1)^m J_m(k_{mn}r) [-\overline{C''}_{3mn} \sin(m\theta) + \overline{C''}_{4mn} \cos(m\theta)] [e^{-k_{mn}(2d+z)} + e^{k_{mn}z}] \quad (83)$$

In this equation, $\overline{C''}_{3mn}$ and $\overline{C''}_{4mn}$ refer to coefficients computed with a value of $-m$. The first and the third double summations may now be combined as follows:

$$\varphi_1 + \varphi_3 = \sum_{m=1}^{\infty} \sum_{n=1}^{\infty} J_m(k_{mn}r) \left\{ \sin(m\theta) (C''_{3mn} + (-1)^{m+1} \overline{C''}_{3mn}) + \cos(m\theta) (C''_{4mn} + (-1)^m \overline{C''}_{4mn}) \right\}$$

$$\times [e^{-k_{mn}(2d+z)} + e^{k_{mn}z}]$$

$$= \sum_{m=1}^{\infty} \sum_{n=1}^{\infty} J_m(k_{mn}r) [C^*_{3mn} \sin(m\theta) + C^*_{4mn} \cos(m\theta)] [e^{-k_{mn}(2d+z)} + e^{k_{mn}z}] \quad (84)$$

Here C^*_{3mn} and C^*_{4mn} are introduced to replace the composite coefficients without any loss of generality. The final expression for the particular solution of $\varphi(r, \theta, z)$ is given as:

$$\varphi(r, \theta, z) = 2C''_{4o1} + \sum_{n=2}^{\infty} C''_{4on} J_o(k_{on}r) [e^{-k_{on}(2d+z)} + e^{k_{on}z}] +$$

$$\sum_{m=1}^{\infty} \sum_{n=1}^{\infty} J_m(k_{mn}r) [C^*_{3mn} \sin(m\theta) + C^*_{4mn} \cos(m\theta)] [e^{-k_{mn}(2d+z)} + e^{k_{mn}z}] \quad (85)$$

The coefficients in the above equation are to be found by making use of the source condition expressed in equation (64). The axial field on the surface of the specimen ($z = 0$) may be found from equation (85) as:

$$\left(\frac{\partial\varphi}{\partial z}\right)_{z=0} = \sum_{n=2}^{\infty} C''_{4on} k_{on} J_o(k_{on}r) [1 - e^{-2k_{on}d}] + \sum_{m=1}^{\infty} \sum_{n=1}^{\infty} k_{mn} J_m(k_{mn}r) [C^*_{3mn} \sin(m\theta) + C^*_{4mn} \cos(m\theta)] [1 - e^{-2k_{mn}d}] \quad (86)$$

The constants C''_{4on} , C^*_{3mn} and C^*_{4mn} resemble coefficients of a Fourier series¹³ and may be found by evaluating the following integrals using equations (64) and (86):

(See appendix for details)

$$C''_{4on} : \int_0^{r_o} \int_0^{2\pi} \left(\frac{\partial\varphi}{\partial z}\right)_{z=0} d\theta r J_o(k_{on}r) dr \quad (87)$$

$$C^*_{3mn} : \int_0^{r_o} \int_0^{2\pi} \left(\frac{\partial\varphi}{\partial z}\right)_{z=0} \sin(m\theta) d\theta r J_m(k_{mn}r) dr \quad (88)$$

$$C^*_{4mn} : \int_0^{r_o} \int_0^{2\pi} \left(\frac{\partial\varphi}{\partial z}\right)_{z=0} \cos(m\theta) d\theta r J_m(k_{mn}r) dr \quad (89)$$

The constant C''_{4o1} is indeterminate due to the absence of a Dirichlet condition⁵⁰ for $\varphi(r, \theta, z)$. This however is not of much concern because it is the potential difference between the voltage probes that is used in the calculation of the geometric correction factor and not the absolute value of the potential.

For a four-probe measurement, the specimen conductivity σ is related to the measured resistance R by a geometric correction factor (GCF) as follows³²:

$$[GCF] = \frac{I}{R\sigma} = \frac{I_o}{\sigma\Delta\varphi} \quad (90)$$

where $\Delta\varphi$ is the potential difference between the pair of voltage probes and I_o is the source current. The geometric correction factor accounts for the finite specimen geometry as well as the arrangement (collinear or square) and the placement of the four-probe array. For a specific placement of the four-probe array upon the circular face of a cylindrical specimen, the geometric correction factor may now be obtained by computing the potential difference from the closed-form analytical solution (equation (85)) and inserting it into the above equation. It should be mentioned that the *GCF* in equation (90) has dimensions of length. All the physical quantities for computing *GCF* are converted to SI units and therefore, *GCF* is expressed in meters.

The application of the closed-form analytical solution for computing the exact geometric factor derived in this paper is only applicable for conducting or semi-conducting materials. In the case of dielectrics or insulators, which impede the free flow of charge, the charge density term in the continuity equation (given in equation 63) cannot be set to zero. Therefore, the problem equations presented here do not adequately describe the physics of charge flow in materials with limited or minimal conductivity.

5.2.3.2 Determination of a convergent solution

The application of the closed-form solution to specific cases of probe arrangement is discussed in a later section. Herein, the procedure for arriving at the final value of $\Delta\varphi$ computed using equation (85) is outlined. The infinite series in equation (85) are truncated at 601 orders for m (including zero) and 10000 roots for n , corresponding to each order m . The roots $k_{mn} = \frac{\beta_{mn}}{r_o}$ are determined by finding the maxima and minima of $J_m(x)$ for each order m as stated in equation (77). Subsequently, the value of $\Delta\varphi$ is

computed separately for each successive additional n from 1, 2, ... up to 10,000. A plot of $\Delta\phi(n)$ vs n is generally oscillatory, with the amplitude of oscillations falling with increasing n . The decrease in amplitude of the oscillations though, is not monotonic. However, it may be shown that the oscillatory series is bounded by an envelope in which the series terms are monotonically decreasing and hence convergent. Therefore, the original series must also converge for this reason.

The centerline or the mean of the oscillations is taken to be the convergence value of the series. In order to determine the centerline, the maxima and minima of the oscillatory series are first identified. Then a new series with smaller oscillations is constructed by joining the mid-points of consecutive maxima and minima of the original series. This procedure is repeated until the oscillations are completely damped out resulting in a convergent solution. Alternately, the convergent value in some cases is approximated by calculating the mean of the maxima and the minima of the oscillations in the original series.

The value of $\Delta\phi$ is also computed by reversing the order of the indices in the double summation in equation (85) for a few cases of a collinear probe array. The deviation in the computed values of $\Delta\phi$ upon interchanging the summation is less than 3%.

5.2.4 Finite Element Approach

The task of computing the geometric correction factors for four-point measurement on a finite cylindrical specimen has also been conducted using the finite element method to serve as a validation for the analytical derivation. COMSOL Multiphysics 3.2, a commercially available finite element package was used to obtain a

finite element solution to the problem of finding the potential distribution inside a cylindrical specimen induced by source and sink current contacts. The Conductive media DC mode of the Electromagnetics module was used to formulate and obtain a solution for the present problem in three dimensions (3D).

The problem geometry as described before consists of a cylindrical specimen with the source and sink contacts placed on the top circular face. The specimen was treated as a single sub-domain, while the contacts were embedded in the sub-domain as boundaries. In the finite element treatment, the contacts were modeled with a finite radius of 50 μm instead of idealized point contacts. All the specimen boundaries were specified to be insulating excepting the source and sink contacts, where a constant current density corresponding to the total current was specified.

The maximum mesh element size and the element growth rate factor on the boundaries and the edges of the electrode contacts were fixed at 10 μm and 1.005 respectively for all the simulations. Mesh sizes smaller than 10 μm for the contacts resulted in incomplete meshing of the sub-domain for a number of different cases of r_o and d (see more details below). The maximum mesh element size and the element growth rate factor for the sub-domain itself (global parameters) were not forced to be a constant across all the simulation cases. Instead, the global parameters were adjusted to limit the total number of elements below 300,000 in each simulation case. This procedure was followed to allow for dealing with the memory limitations of the solver.

The Conductive Media DC mode obtains a solution for the electric potential (V) by solving for the Poisson's equation:

$$-\nabla \cdot (\sigma \nabla V - J^e) = Q_j \quad (91)$$

Here J^e is the external current density and Q_j is the current density which, are both set to zero in the model. Instead, the total current is specified as an average normal current density at the contacts. A Stationary Linear solver based on the Conjugate Gradients algorithm⁶⁷ was used to obtain a solution for the 3D Conductive Media DC problem. The Conjugate Gradients solver obtains a solution for the linear system of equations $Ax = b$ via iteration as opposed to Direct solvers⁶⁷. Iterative solvers are particularly useful and more memory efficient in case of 3D systems with a large number of degrees of freedom. The Conjugate Gradients solver can handle linear systems where the matrix A is positive definite and Hermitian⁶⁷. Iterative solvers by themselves are less stable and require the use of a preconditioner algorithm⁶⁷ to enable faster convergence. The preconditioner generates a second matrix- M , which is an approximation to A and performs all subsequent element operations on M . In this case, the Incomplete Cholesky (TAUCS) algorithm⁶⁷ with a drop tolerance of 0.03 was used as the preconditioner for the Conjugate Gradients algorithm.

5.2.5 Analytical Approximations to Geometric Correction Factors

Analytical approximations of geometric correction factors for measurements using a collinear four-probe unit on cylindrical specimens are listed by Topsoe³². Most of the analytical approximation factors were derived based on the ‘method of images’³⁴. The method of images is an elegant technique for obtaining solutions of problems in potential theory based on symmetry considerations. Typically, the technique consists of mapping current injection or extraction points by a scheme of point or line sources on the problem domain. Subsequently, the potential at the point of interest is evaluated by the principle of superposition^{34, 48}.

The two cases that are pertinent to measurement on a cylindrical specimen using a collinear probe unit are (a) a probe unit centered and perpendicular to a radius and (b) a probe unit along a radius as shown in Figures 5.2.2 and 5.2.3 respectively. In general, for a cylindrical specimen of radius- r_o and finite thickness- d , the correction factor- GCF is defined to lie within a range bounded by a lower and an upper bound analytical approximation factor as follows³²:

$$\frac{2\pi s}{C_L\left(\frac{r_o}{s}, \frac{\Delta}{s}\right)T_L\left(\frac{d}{s}\right)} \leq GCF \leq \frac{2\pi s}{T_U\left(\frac{x}{d}, \frac{s}{d}\right)} \quad (92)$$

The lower bound is a combination of the contour factor³³- C_L for a thin specimen $\left(d < \frac{s}{2}\right)$ and the thickness factor³⁴- T_L defined for a specimen of thickness- d that extends to infinity in-plane. In the lower bound factor, s is the probe spacing and Δ is the displacement of the center of the probe array from the specimen center. The upper bound³⁴ is defined for a semi-infinite specimen of thickness- d , where the probe unit or the nearest probe is at a distance x from the edge of the specimen.

The expressions for the different thickness and contour factors listed in the table are given as follows:

1. Lower bound Thickness factor- $T_L\left(\frac{s}{d}\right) = 1 + \frac{s}{d} \left[M\left(\frac{s}{d}\right) - M\left(\frac{s}{2d}\right) \right]$ (93)

2. Upper bound Thickness factor- $T_U\left(\frac{x}{d}, \frac{s}{d}\right) = T_L\left(\frac{s}{d}\right) + \Delta T_I\left(\frac{x}{d}, \frac{s}{d}\right)$ (94)

where

$$\Delta T_I = \frac{s}{2d} \left(\frac{1}{\alpha} + \frac{1}{\beta} - \frac{1}{\gamma} - \frac{1}{\delta} + M(\gamma) + M(\delta) - M(\alpha) - M(\beta) \right), \quad \text{and} \quad (95)$$

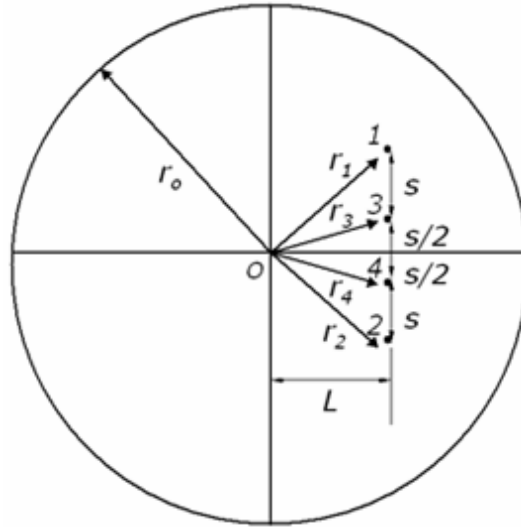


Figure 5.13 Schematic showing the top view of a cylindrical specimen of radius- r_o , on which a collinear probe array displaced by L from the specimen center, is positioned normal to a radius. This arrangement of probes is referred to as the PNR (probes normal to a radius) type. Also shown are the position vectors to the current probes- 1 and 2 and the voltage probes- 3 and 4 respectively.

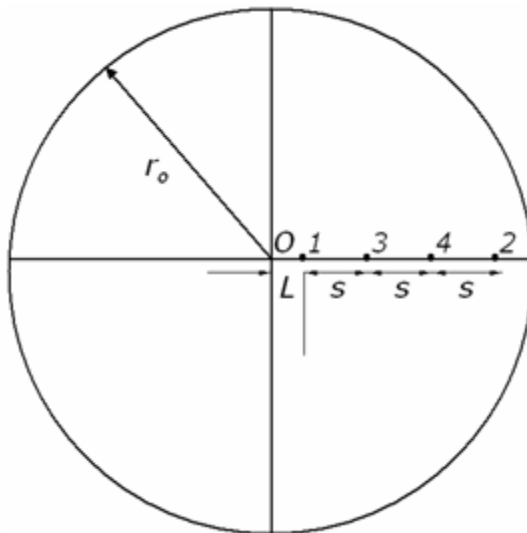


Figure 5.14 Schematic showing the top view of a cylindrical specimen of radius- r_o , on which a collinear probe array displaced by L from the specimen center, is positioned along a radius. This arrangement of probes is referred to as the PAR (probes along a radius) type. Probes 1 and 2 are used as current contacts, while voltage drop is measured between 3 and 4.

where α , β , γ and δ are given as $\frac{x+\frac{s}{2}}{d}$, $\frac{x+\frac{5s}{2}}{d}$, $\frac{x+s}{d}$ and $\frac{x+2s}{d}$ respectively.

$$3. \text{ Thickness factor- } T_U\left(\frac{x}{s}, \frac{s}{d}\right) = T_L\left(\frac{s}{d}\right) + \Delta T_2\left(\frac{x}{s}, \frac{s}{d}\right) \text{ where} \quad (96)$$

$$\Delta T_2 = \frac{I}{\sqrt{\eta^2 + \frac{I}{4}}} - \frac{I}{\sqrt{\eta^2 + I}} + \zeta \left[M\left(\zeta \sqrt{\eta^2 + I}\right) - M\left(\zeta \sqrt{\eta^2 + \frac{I}{4}}\right) \right], \quad (97)$$

and where, $\zeta = \frac{s}{d}$ and $\eta = \frac{x}{s}$.

In equations (93), (95) and (97), the function $M(\lambda)$ is a dimensionless function of the parameter $\lambda = \frac{s}{d}$ that corresponds to a scheme of two parallel infinite line charges of opposite nature. Based on the principle of superposition, it has been defined by Uhlir as follows³⁴:

$$M(\lambda) = 2 \sum_{n=1}^{\infty} \left(\frac{I}{n} - \frac{I}{\sqrt{n^2 + \lambda^2}} \right) \quad (98)$$

$$4. \text{ Contour factor- } C_L^o\left(\frac{r_o}{s}\right) = 1 + \frac{I}{\ln 2} \ln \left[\frac{1 + 3\left(\frac{s}{2r_o}\right)^2}{1 - 3\left(\frac{s}{2r_o}\right)^2} \right] \quad (99)$$

$$5. \text{ Contour factor- } C_L^I\left(\frac{s}{r_o}, \frac{\Delta}{r_o}\right)$$

$$C_L^I\left(\frac{s}{r_o}, \frac{\Delta}{r_o}\right) = 1 + \frac{I}{2 \ln 2} \ln \left[\frac{\left[1 - \left(\frac{\Delta + s}{r_o + 2r_o}\right) \left(\frac{\Delta - 3s}{r_o - 2r_o}\right) \right] \left[1 - \left(\frac{\Delta - s}{r_o - 2r_o}\right) \left(\frac{\Delta + 3s}{r_o + 2r_o}\right) \right]}{\left[1 - \left(\frac{\Delta - s}{r_o - 2r_o}\right) \left(\frac{\Delta - 3s}{r_o - 2r_o}\right) \right] \left[1 - \left(\frac{\Delta + s}{r_o + 2r_o}\right) \left(\frac{\Delta + 3s}{r_o + 2r_o}\right) \right]} \right] \quad (100)$$

6. Contour factor- $C_L^2\left(\frac{s}{r_o}, \frac{\Delta}{r_o}\right)$ -the contour correction factor for this case is a

lengthy expression and is listed in the article by Swartzendruber³³.

Table 5.1 List of notations of analytical approximation correction factors for different measurement cases using a collinear probe unit and the corresponding references.

Case	Factor type and notation	Reference
Probe array centered on an infinite plane specimen of finite thickness,- d	Thickness, $T_L\left(\frac{s}{d}\right)$	Uhlir ³⁴
Probe array perpendicular to the edge at a distance x of a semi-infinite specimen of thickness- d	Thickness, $T_U\left(\frac{x}{d}, \frac{s}{d}\right) = T_L\left(\frac{s}{d}\right) + \Delta T_1\left(\frac{x}{d}, \frac{s}{d}\right)$	Uhlir ³⁴
Probe array parallel to the edge at a distance x of a semi-infinite specimen of thickness- d	Thickness, $T_U\left(\frac{x}{s}, \frac{s}{d}\right) = T_L\left(\frac{s}{d}\right) + \Delta T_2\left(\frac{x}{s}, \frac{s}{d}\right)$	Uhlir ³⁴
Probe array centered on a thin cylindrical slice of radius- r_o and thickness- $d < \frac{s}{2}$	Contour, $C_L^o\left(\frac{s}{r_o}\right)$	Smits ⁶⁰
Probe array on the radius and displaced by Δ from the center of a thin cylindrical slice	Contour, $C_L^1\left(\frac{s}{r_o}, \frac{\Delta}{r_o}\right)$	Swartzendruber ³³
Probe array normal to the radius and displaced by Δ from the center of a thin cylindrical slice	Contour, $C_L^2\left(\frac{s}{r_o}, \frac{\Delta}{r_o}\right)$	Swartzendruber ³³

Table 5.1 shows a listing of the correction factor notation and the corresponding reference for several cases of thickness and contour factor derivations relevant to cylindrical geometry. The expressions for the contour and thickness correction factors listed above were used for computing approximate analytical correction factors.

5.2.6 Results and Discussion

In this section, the geometric correction factors computed using the closed-form (CF) analytical solution, the COMSOL finite element solution and the approximate analytical (AA) solution, will be compared first for specific probe arrangements and specimen geometry. Next, the effect of probe displacement along a radius and perpendicular to a radius will be treated for different specimen geometries. A current- I_o of 50 [mA], a conductivity- σ of 8.34×10^5 [$\Omega\text{-cm}$]⁻¹ and a probe spacing- s of 1 [mm] were used in the CF and the COMSOL models for computing the correction factors. In the COMSOL model, this current translates to a current density- J_n of 636.62 [A/cm²] for the assumed electrode contact radius of 50 [μm].

A comparison between the CF, the COMSOL and the AA solutions is presented in Figure 5.15 (a) and (b) via plots of GCF versus the specimen thickness- d for probes aligned normal to a radius (PNR) and along a radius (PAR) respectively (see Figures 5.13 and 5.14). The specimen radius- r_o was fixed at 8 [mm] and the probe displacement- L was set to $\left(\frac{3r_o}{5}\right)$ for these computations. It is seen for both the PNR and the PAR arrangements that the correction factor increases drastically as the specimen thickness is increased from 1 to 2 mm before it levels off to a constant value. This is a direct consequence of the potential distribution inside the specimen that results upon injection of current for specimens of different thicknesses. The measured potential drop between the voltage probes is higher for specimens with a smaller thickness, because the current now spreads over a smaller volume of the material medium. As the thickness increases, the volume for current spreading increases, resulting in progressively lower potentials at

the probes. However, a critical thickness is reached after which the potential distribution on the surface of the specimen remains invariant for all thickness values exceeding the critical thickness (~ 10 mm in both cases). Consequently, the measured voltage difference

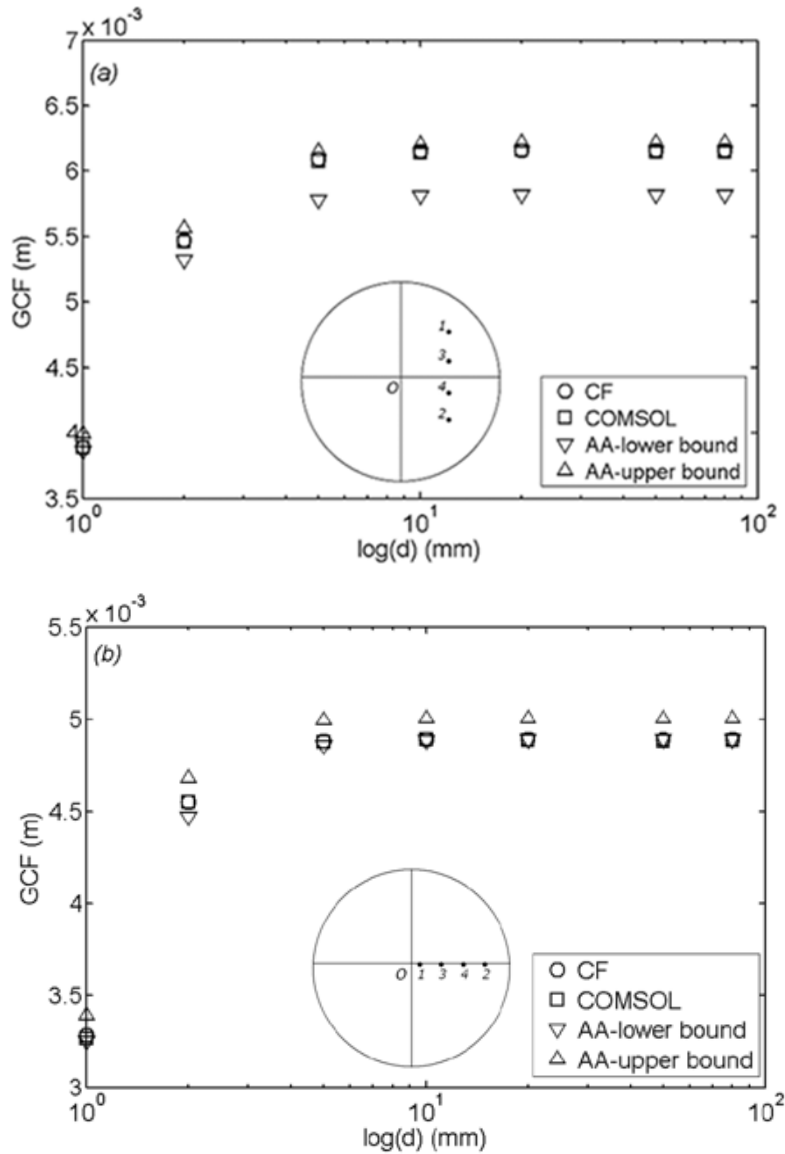


Figure 5.15 Plots showing the comparison between geometric correction factors obtained via the closed-form, COMSOL and analytical approximation solutions as a function of specimen thickness- d for (a) PNR type and (b) PAR type arrangements respectively. The specimen radius- r_o and the probe-displacement- L are fixed at 8 [mm] and 4.8 [mm] respectively.

between the voltage probes also remains unchanged and therefore the correction factor levels off after the critical thickness.

It is clear from the two plots that the correction factors obtained from the CF and the COMSOL solutions show an excellent match with each other. Additionally, the correction factors predicted by the CF and the COMSOL solutions lie between the upper and lower analytical bounds in both cases. For the PNR arrangement (shown in Figure 5.15 (a)), it is seen that the lower analytical bound is a better match with the CF and the COMSOL solutions at low thickness values. The lower analytical bound is a combination of the contour and the thickness correction factors, which are evaluated separately. The contour factor derived by Swartzendruber³³, listed in the previous section, was derived based on the assumption that the specimen thickness was $d < \frac{s}{2}$. Therefore, it is not a surprising result that the lower analytical bound deviates considerably at larger d values. The upper analytical bound was derived (by Uhlir³⁴) for a semi-infinite specimen of finite thickness, where the probes are at a fixed distance from a chosen boundary. Therefore, the upper bound is a good approximation for specimens with large radii irrespective of the specimen thickness. The disparity between the upper bound approximation and the CF solution is larger at small values of d , for the specific choice of r_o displayed in Figure 5.15 (8mm in this case). This is probably due to the fact that the specimen radius- r_o is not large enough for a semi-infinite treatment. The match however improves as d increases, suggesting that the effect of having a finite contour is pronounced at lower specimen thicknesses.

For the PAR arrangement (plot in Figure 5.15 (b)), it is rather surprising to find that the lower analytical bound shows a good match with the factors obtained from the

CF and the COMSOL solutions for all thickness values. In this case, since the probes are aligned along a radius, the outermost probe is closer to the specimen boundary as compared to a PNR scenario, assuming the same probe displacement from the center of the specimen. Due to this reason, the effect of a finite specimen contour should be more pronounced for a PAR arrangement. It is possible that the contour factor (derived by Logan⁶⁸) in this case is more sensitive for larger probe displacements, i.e. as the outermost probe lies closer to the specimen boundary. This is one possible explanation for the good match of the lower analytical bound with the other solutions.

Comparative simulation results from the CF, the COMSOL and the AA models for radius variations at a fixed thickness of 2 [mm] are shown as plots of GCF vs r_o for the PNR and the PAR arrangements in Figures 5.16 (a) and (b) respectively. For this set of plots, the probe displacement- L was set to $\left(\frac{r_o}{5}\right)$. The behavior that is common to both plots is that the correction factor shows a parabolic increase with increasing r_o , however, with a progressively decreasing gradient. This trend may be explained using a similar argument that was used previously to explain the GCF variations as a function of thickness. The effective volume available for current spreading increases upon increasing the specimen radius. In fact, the geometric volume increases much faster with an increase in the radius as compared to an increase in thickness by the same amount. Therefore, the increase in the correction factor with r_o is due to a progressively lower potential difference at voltage probes, associated with an increased volume for current spreading. An added consequence of increasing the radius is that the specimen boundary is moved further from a fixed reference point, say the specimen center. However, the point of

reference that is of interest is defined by the probe displacement- L , which in this case is a function of r_o . With increasing r_o , the probes are also displaced further along the r_o

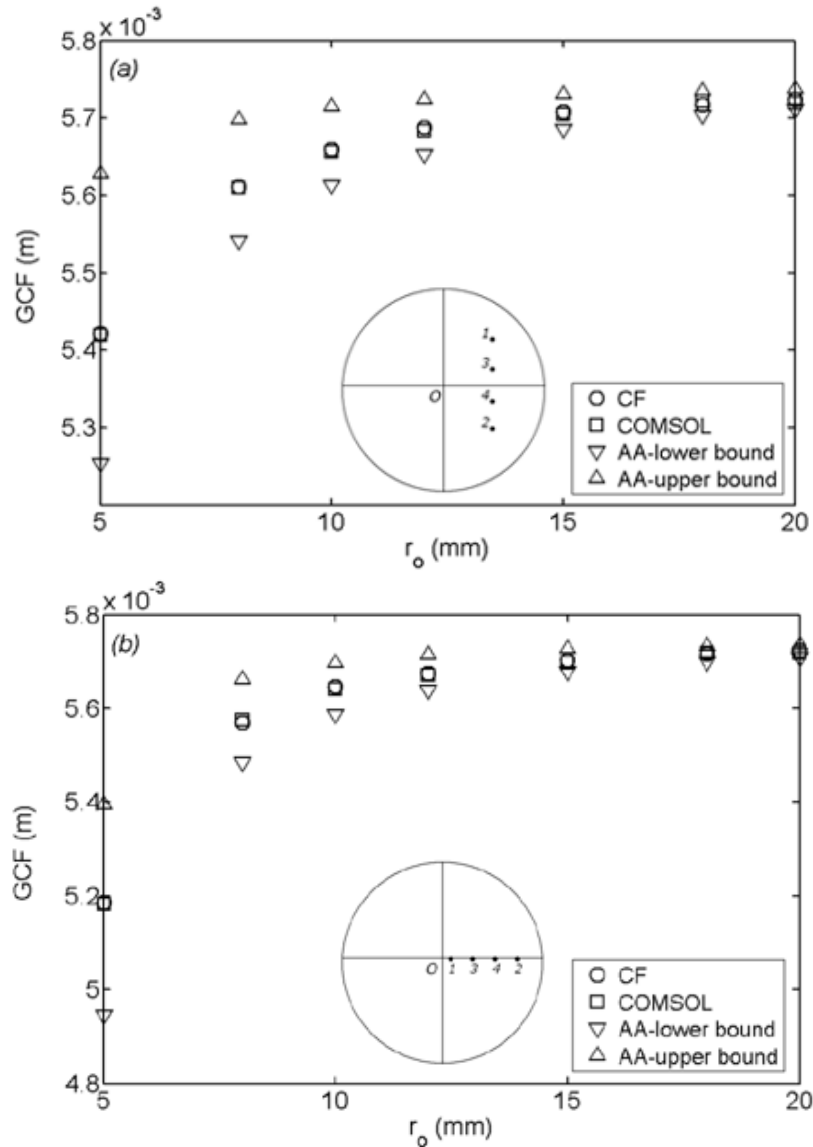


Figure 5.16 Plots showing the comparison between geometric correction factors obtained from the closed-form, COMSOL and analytical approximation solutions as a function of specimen radius- r_o for (a) PNR type and (b) PAR type arrangements respectively. The specimen thickness- d is fixed at 2 [mm] and the probe-displacement- L is specified to be $\left(\frac{r_o}{5}\right)$.

axis. This is the reason why the leveling off of the correction factor occurs over an extended radius range as compared to the thickness variations presented before.

The excellent match between the CF and the COMSOL correction factors is again evident from both Figures 5.16 (a) and (b). At small r_o , both the lower and the upper analytical bounds are poor approximations of the exact correction factor. This means that treating the specimen to be semi-infinite for the upper bound and the combination of the contour and the thickness correction factors for the lower bound are both inexact for small r_o . With increasing r_o , it is seen that both the upper and the lower analytical bound solutions converge closer to the exact solution. As the specimen approaches a semi-infinite situation (in-plane only) upon increasing r_o , the treatment used for the computation of the upper bound is more realistic. The contour factor in the case of the lower bound decreases to a steady asymptote as the effect of the specimen boundary on the voltage drop becomes increasingly less significant upon increasing r_o .

Next, the effects of systematically displacing the probe unit along the specimen radius, is considered for both the PNR and the PAR arrangements. The correction factors in simulations involving probe-displacement were computed using the CF analytical solution only. In the first set of simulations, the effect of probe displacement was studied for specimens of varying thickness, keeping the radius fixed at 8 [mm]. The source current- I_o and the conductivity- σ are the same as before. Figures 5.17 (a) and 5.17 (b) show the geometric correction factor- GCF as a function of the specimen thickness- d at probe displacements of $\left(\frac{r_o}{5}\right)$, $\left(\frac{2r_o}{5}\right)$ and $\left(\frac{3r_o}{5}\right)$ for the PNR and PAR arrangements respectively. It is clear from both the plots that the general behavior of the GCF vs d

remains identical to that described in Figure 5.15 (thickness comparison plots). In the case of the PNR arrangement (plot in Figure 5.17 (a)), as the probe displacement increases, the probe unit lies in close proximity to the specimen boundary. As a result, the

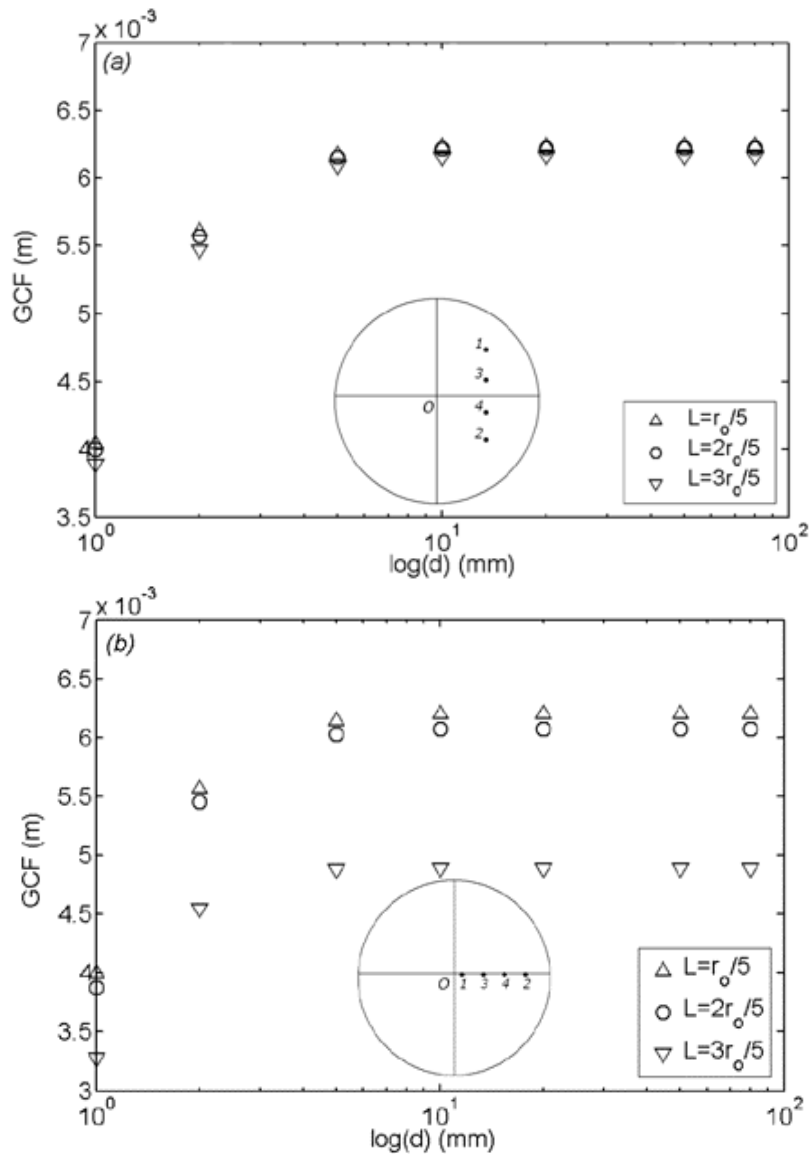


Figure 5.17 Plots showing the geometric factor (CF solution) variations as a function of specimen thickness- d at probe displacements of $\left(\frac{r_o}{5}\right)$, $\left(\frac{2r_o}{5}\right)$ and $\left(\frac{3r_o}{5}\right)$ for (a) PNR type and (b) PAR type arrangements respectively. The specimen radius- r_o is fixed at 8 [mm] for this set of plots.

volume available for current spreading is limited toward the closest boundary. This results in an increased voltage drop between the potential probes. The voltage drop increases progressively with an associated decrease in the correction factor as the probe displacement increases from $\left(\frac{r_o}{5}\right)$ to $\left(\frac{3r_o}{5}\right)$. However, the differences are relatively small here. For the PAR arrangement, where the probes lie along the specimen radius, the outer probe lies much closer to the specimen boundary for the same displacement of the probe unit from the specimen center. Due to this reason, the proximity effect is even more pronounced here. This is evident from Figure 5.17 (b), where a large drop in the GCF is noted upon increasing the probe displacement from $\left(\frac{r_o}{5}\right)$ to $\left(\frac{3r_o}{5}\right)$.

It is seen from Figure 5.17 (a) for the PNR arrangement that the correction factors at the different probe displacements are spread out (although only by a small amount) at small thicknesses and start closing in at larger thicknesses. This suggests that the effect of a finite contour is greater the smaller the thickness, for a PNR arrangement. Interestingly, for the PAR arrangement (plot in Figure 5.17 (b)), the correction factors corresponding to the different probe displacements are spaced out further at larger thicknesses than at smaller values. In this case, the effect of the finite contour is maximum at larger thicknesses in contrast to the PNR arrangement. This suggests that the relative differences in the voltage drop at the different probe displacements affected by increasing the thickness are larger for the PAR arrangement as compared to a PNR arrangement. The plots shown in Figure 5.18 (a) and (b) are results from simulations at different probe displacements in conjunction with radius variations. The specimen thickness was fixed at 2 [mm] in this set of computations. The correction factor behavior as a function of

increasing r_o is the same as that described earlier for Figures 5.16 (a) and 5.16 (b). The effect of displacing the probe unit by θ , $\left(\frac{2r_o}{5}\right)$ and $\left(\frac{3r_o}{5}\right)$ is nearly the same for both

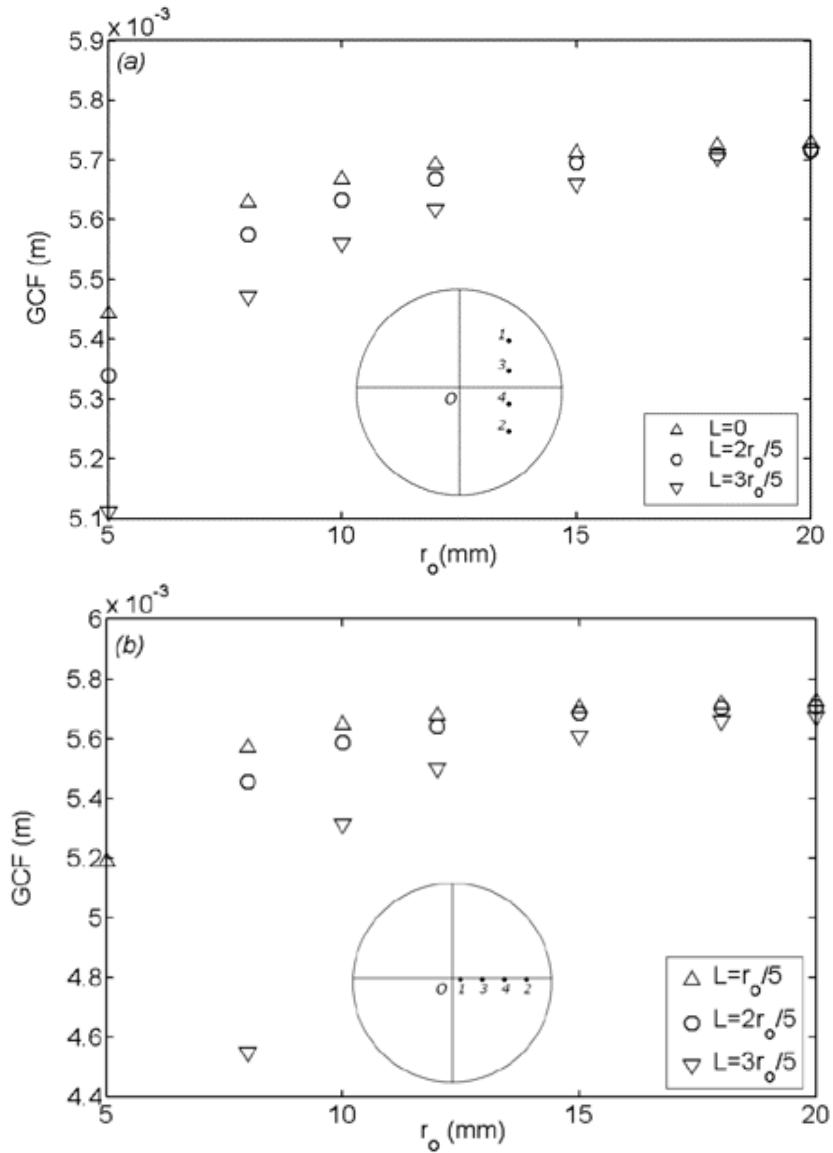


Figure 5.18 Plots showing the geometric factor (CF solution) variations as a function of specimen radius- r_o at probe displacements of $\left(\frac{r_o}{5}\right)$, $\left(\frac{2r_o}{5}\right)$ and $\left(\frac{3r_o}{5}\right)$ for (a) PNR type and (b) PAR type arrangements respectively. The specimen radius- d is fixed at 2 [mm] for this set of plots.

the PNR and the PAR type arrangements. The discrepancies among the correction factors at the three displacements are greater at smaller radii and decrease progressively with increasing radius. The effect of displacing the probe unit (as a fraction of r_o) in terms of the voltage drop is obviously greater at small r_o because of the proximity to the boundary. The effect due to proximity decreases in significance as the specimen radius increases and as a result, the disparity among the voltage drops at the three displacements decreases progressively. Therefore, the geometric correction factors corresponding to the three displacements converge together as the radius increases. This was the only dominant effect observed as the thickness of the cylinders is held a constant.

5.2.7 Conclusions

A closed-form analytical expression for the potential difference at the voltage probes was derived for a four-point probe measurement on a cylindrical specimen. The closed-form expression was obtained as a solution to Laplace's equation using the variable-separation technique. The solution is generally valid for a random placement of the four probes on a circular face of the cylinder. The geometric correction factor, which is dependent on the specific specimen geometry and the probe arrangement, was then evaluated using the computed potential difference.

The general closed-form solution was then applied to two specific arrangements of a collinear probe array- (a) a probe unit lying on a radius and (b) a probe unit centered and perpendicular to a radius. Simulations were conducted by varying the specimen radius, specimen thickness and the displacement of the probe unit from the specimen center in a systematic fashion. Correction factors computed using the closed-form solution are in excellent agreement with those obtained via finite-element method

calculation using COMSOL Multiphysics 3.2. The factors from the closed-form and the COMSOL solutions lie within the bounds predicted by the approximate analytical correction factors in all cases.

For fixed values of r_o and L , the correction factor rises initially as a function of d until a critical thickness is reached and remains constant thereafter. In a second set of simulations with fixed d , the correction factor shows a parabolic increase with increasing r_o , with a progressively decreasing slope. In this set of simulations, L was specified to be a constant fraction of r_o . The correction factor behavior in both sets of simulations is due to progressively lower values of potential difference at the voltage probes as a consequence of increasing specimen volume. The increase in specimen volume affected by increasing r_o or d facilitates easier current spreading, thereby leading to a lower potential drop. Simulations conducted by increasing the probe displacement- L , specified as a fraction of r_o , resulted in progressively lower values of the correction factors. As the probe unit is displaced closer to the specimen boundary, the potential difference increases because of a reduction in the volume for current spreading near the boundary. Thus the increased potential difference directly leads to a lower geometric correction factor.

It is useful to remember that the closed-form correction factor presented here assumes that four point measurements are being made on homogeneous extended microstructures (i.e. with features much larger than the spacing between the measuring probes) so that a measurement of a bulk feature may be made; or with features much smaller than the spacing between the measuring probes so that the measurement will be a representative average of the heterogeneous microstructure. The latter scenario is

particularly true of controlled Waspaloy microstructures, where the nanometer sized precipitate distribution is representative of an average microstructure for the measurement. In case of bulk microstructural features such as whiskers or nanobelts, even if one uses micron-sized probe sizes and/or spacings, the measurements will be affected by several factors. These may be: (a) depth dimension and homogeneity of the feature, (b) conductivity of the material medium surrounding the feature, (c) proximity of the probes to the surrounding medium and (d) size of the probe contacts in relation to the probe spacing and the feature size. Lastly, the orientation of the feature relative to the direction of probe approach will also need to be accounted for in the computation of accurate geometric correction factors.

5.3 Calculation of specimen impedance for AC four-point probe measurements

5.3.1 Measurements on Wire Specimens

The method for computing the complex impedance of a specimen wire of radius- r_o and length- l_o will be described briefly based on a closed-form analytical solution for the electric field distribution developed by Giacoletto⁴⁷. The electric field distribution for alternating current (I_o) flow (of angular frequency ω) through the wire was derived as a solution to Maxwell's electrodynamic equations^{48, 49}. In this specific case, the electric field is present only along the axial direction, for which the solution was given as⁴⁷:

$$E_z = \alpha J_o(\kappa r) \quad (101)$$

where, r is the radial co-ordinate, $\kappa^2 = -j\omega\mu\sigma$ and $\alpha = \frac{\kappa I_o}{2\pi\sigma r_o J_1(\kappa r_o)}$. Here μ and σ refer to the magnetic permeability and the electrical conductivity of the wire and $J_\nu(x)$ is a Bessel function⁵⁰ in x of order ν .

From the above equation, it may be inferred that the axial field distribution is not homogeneous across the wire cross-section and is dependent on the radial distance. Additionally the degree of non-homogeneity is also dictated by the parameter κ , which depends on the frequency ω of the alternating current.

The solution for the complex impedance of a wire specimen of length- l_o and radius- r_o is obtained by an integration of the electric field given in equation (101) over the length of the wire as follows:

$$Z = \frac{I}{I_o} \int_0^{l_o} E_z(r_o) dz = \alpha J_o(\kappa r_o) l_o = R_{dc} \frac{\kappa r_o J_o(\kappa r_o)}{2 J_1(\kappa r_o)} \quad (102)$$

In the above equation for the complex impedance, R_{dc} is the dc resistance of the wire, given by $R_{dc} = \frac{l_o}{\pi r_o^2 \sigma}$. The frequency dependent resistance and inductance of the specimen wire are then obtained as follows:

$$R = \text{real}(Z) \text{ and} \quad (103)$$

$$L_i = \frac{I}{\omega} \text{imag}(Z) \quad (104)$$

5.3.2 Measurements on Cylindrical Disk Specimens

The objective of a four-probe AC measurement, as explained in an earlier chapter, is to measure the impedance of the specimen by isolating the effects of electrode contact

resistance and induced voltage due to the magnetic field. In this section, a procedure is described for computing the impedance from a four-probe AC measurement via a closed-form analytical solution.

Analytical computation of the specimen impedance in a four-probe AC measurement requires a knowledge of the electromagnetic field distribution inside the specimen induced by current flow through source and sink current contacts. The problem of calculating the electromagnetic field distribution in a conducting half space due to a point current injection at the surface has been treated by Bowler⁶⁹ and Mitrofanov⁷⁰ separately. Mitrofanov's approach⁷⁰ is based on obtaining a solution for Maxwell's second order diffusion equation for the electric field by using Fourier transforms. Bowler⁶⁹ formulated the original second order differential equation in terms of a single transverse magnetic potential. The solution for the transverse magnetic potential was derived first by using the Hankel transform and the electric field distribution was obtained subsequently from the potential. The solutions discussed thus far are only applicable for infinite specimens i.e. the specimen dimensions both in-plane and perpendicular to the plane of probe placement are much larger compared to the probe spacing.

In a different publication, Bowler³⁹ presented a closed-form analytical solution for the electric field distribution inside a metal plate of finite thickness, induced by current injection at the surface through a wire. The problem is treated in a cylindrical co-ordinate system- (r, θ, z) by assuming rotational symmetry about the wire through which the current is injected and the specimen, both sharing the same axis of symmetry. A similar procedure, as described for an infinite specimen, was followed for obtaining the solution

for the electric field distribution in this case. The final closed-form expression for the radial electric field derived by Bowler³⁹ is given as follows:

$$E_r(p) = -\frac{jkI_o}{2\pi\sigma_o r} \left(\sum_{n=0}^N \left\{ e^{jk(z+2nd)} - \frac{e^{jkp_n}}{jkp_n} \left[1 + \frac{[jk(z+2nd)]^2}{jkp_n} \left(1 - \frac{1}{jkp_n} \right) \right] \right\} + \sum_{n=0}^{N-1} \left\{ e^{-jk[z-2(n+1)d]} - \frac{e^{jkp'_n}}{jkp'_n} \left[1 + \frac{\{jk[z-2(n+1)d]\}^2}{jkp'_n} \left(1 - \frac{1}{jkp'_n} \right) \right] \right\} \right) \quad (105)$$

In the above expression valid for $0 \leq z \leq d$, $p_n = \sqrt{r^2 + (z + 2nd)^2}$ and $p'_n = \sqrt{r^2 + (z - 2(n+1)d)^2}$.

This expression for the radial electric field for a semi-infinite metal plate is made use of in the present research for computing the potential difference between the voltage probes in a four probe AC measurement. Even though the specimens used for measurement were of a finite size (laterally), the above expression for the electric field yielded a good approximation of the voltage difference. This is because the distance between the specimen edge and the outer probe was large enough (typically greater than $4s$, $s =$ probe spacing) to discount effects of having a finite contour. Consider the centered arrangement of a linear probe array on the circular face of a cylindrical specimen as shown in Figure 5.19. The procedure for computing the voltage difference between probes at $\left(\pm \frac{s}{2}, 0, 0\right)$, upon current injection and extraction at $(\pm s, 0, 0)$ respectively, will now be described. The expression for the total electric field at any point $(x_o, 0, 0)$ lying on the same diameter as the probe unit is placed, is given by the principle of superposition⁴⁸ as:

$$E_r^T = E_{r_1} - E_{r_2} \quad (106)$$

where, $r_{1,2} = x_o \pm s$ are the radial distances from the source and sink electrodes to the point $(x_o, 0, 0)$. The distances p_n and p_n' in equation (105) are defined as $p_n = \sqrt{r^2 + (2nd)^2}$ and $p_n' = \sqrt{r^2 + (2(n+1)d)^2}$ for each value of r as the probes lie on the $z = 0$ plane.

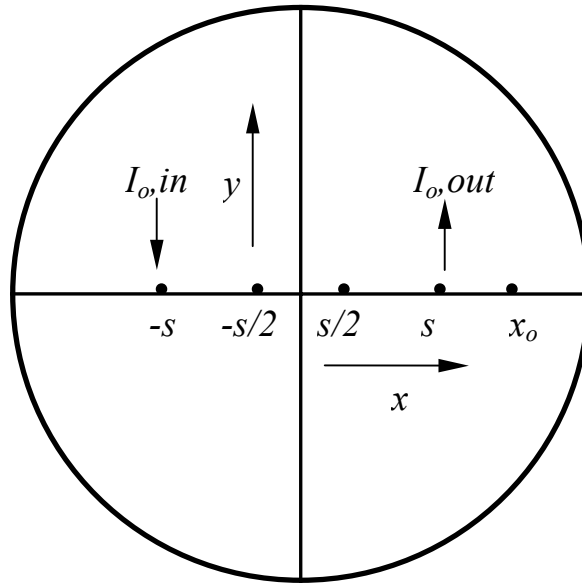


Figure 5.19 Schematic showing the arrangement of current probes (at $\pm s$) and voltage probes (at $\pm s/2$) on the circular face of a cylindrical specimen. The point $(x_o, 0, 0)$ is arbitrarily chosen for computing the total superimposed field due to sources at $(s, 0, 0)$ and $(-s, 0, 0)$.

The voltage difference between probes 3 and 4 can now be obtained as follows:

$$\Delta V_{3,4} = - \int_{-\frac{s}{2}}^{\frac{s}{2}} E_r^T dr \quad (107)$$

where E_p^T is obtained from equations (105) and (106). Description on the computation of the integral for obtaining $\Delta V_{3,4}$ is provided in the appendix.

The resistance and the inductance of the specimen from a four probe impedance measurement can now be obtained as follows:

$$R = \operatorname{Re}\left(\frac{\Delta V_{3,4}}{I_o}\right) \text{ and} \quad (108)$$

$$L_i = \frac{1}{\omega} \operatorname{Im}\left(\frac{\Delta V_{3,4}}{I_o}\right). \quad (109)$$

CHAPTER 6

AC ELECTRICAL MEASUREMENTS ON CONDUCTING SPECIMENS

In this chapter, the results from ac measurements on cylindrical disk-shaped Waspaloy specimens using two-probe and four-probe approaches are described. Additionally, the four-probe measurements on wire specimens, which were conducted as a precursor to four-probe measurements on disk specimens, are also discussed. The experimentally measured impedance response for each measurement/specimen type is compared to a computed response obtained from closed-form analytical solutions or finite-element based solutions.

6.1 AC Two Probe Impedance on Cylindrical Disk Specimens

The results from two-probe impedance measurement of a typical Waspaloy disk specimen are shown in Figures 6.1 (a) and (b) as plots of R vs $\log(f)$ and X vs $\log(f)$, where R and X refer to the real and imaginary components of the measured impedance. The frequency-dependent real resistance R is more or less invariant up to 100 kHz and then shows a drastic rise for higher frequencies. A similar behavior is noted in terms of the frequency for X for frequencies above 50 Hz. The computed responses for R and X are shown in Figures 6.2 (a) and (b) respectively, which were obtained based on the closed-form analytical solution for the two-probe measurement as detailed in the previous chapter. The computed response for R shows the same trend with frequency as the

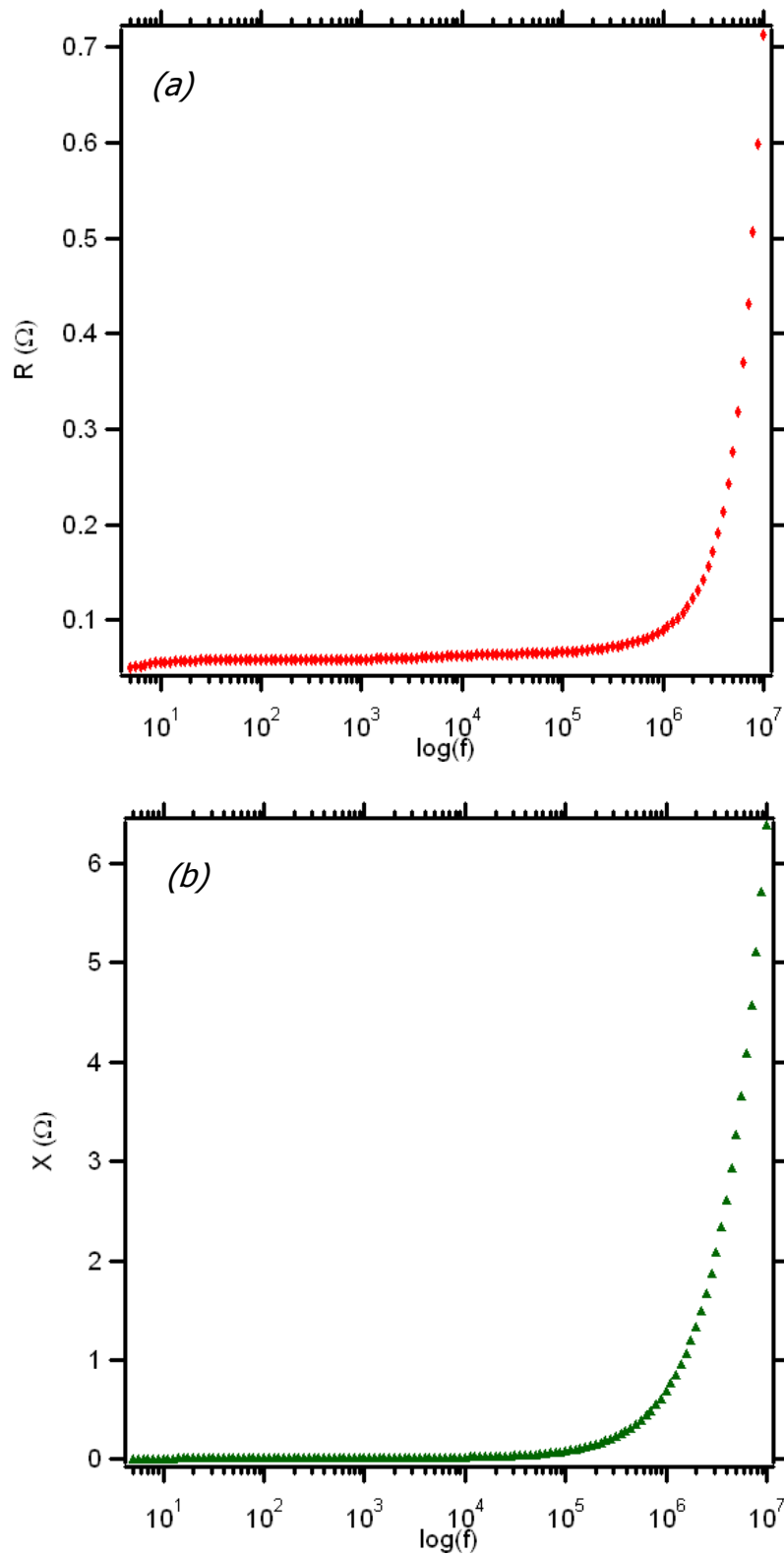


Figure 6.1 Plots of experimentally measured resistance- (a) and reactance- (b) as a function of the frequency of a cylindrical Waspaloy disk specimen in a two-probe impedance measurement.

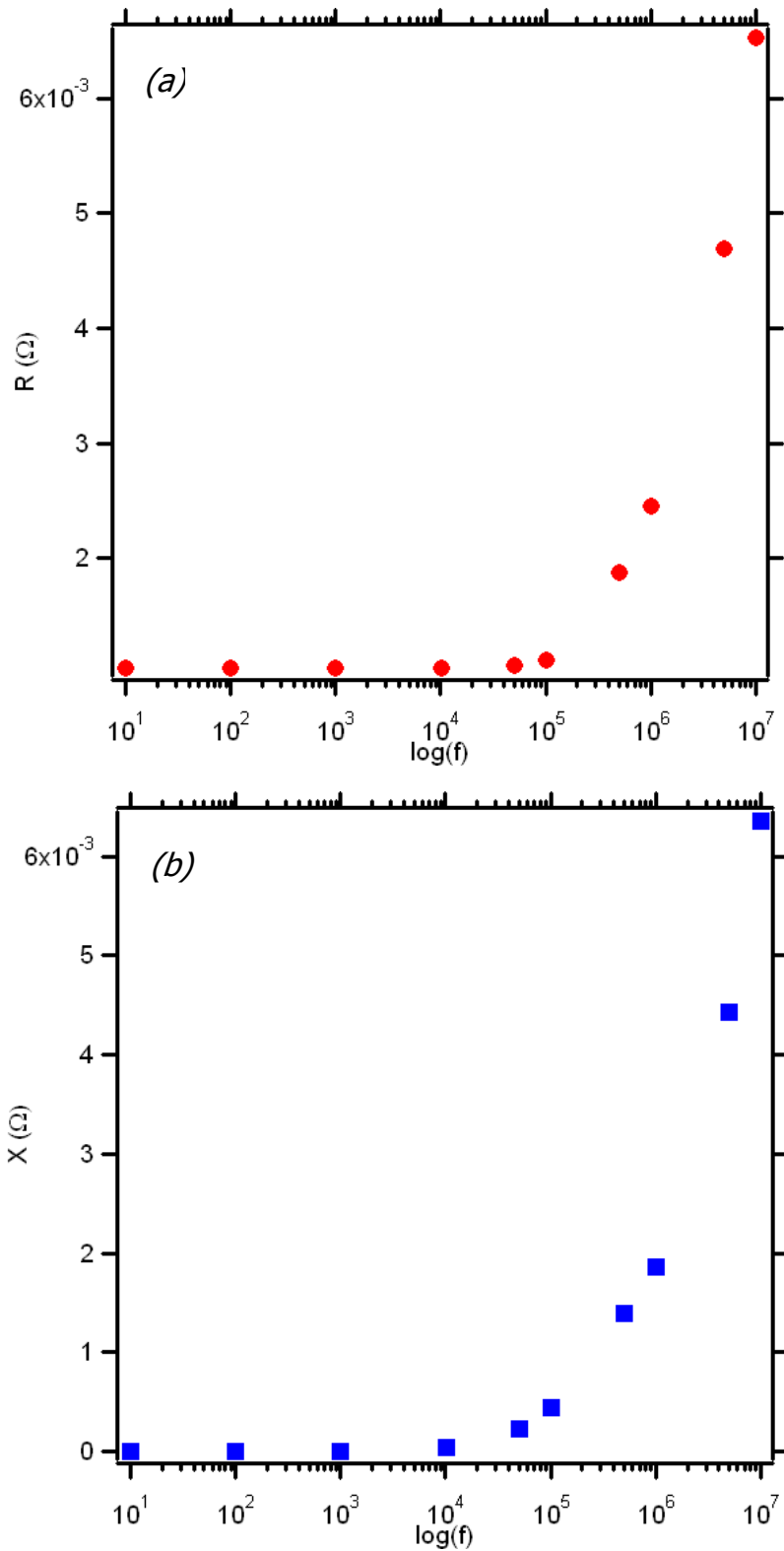


Figure 6.2 Plots of computed resistance- (a) and reactance- (b) as a function of the frequency of a cylindrical Waspaloy disk specimen, obtained from the analytical treatment of an ideal two-probe impedance measurement.

measured response (see Figure 6.1(a)); but, the actual resistance values are markedly different in both cases. Figure 6.2 (b) shows the computed reactance (X) as a function of the frequency. Upon comparison with the measured reactance in Figure 6.1 (b), it is seen that there is a huge discrepancy in the reactance values, especially at high frequencies, even though the trends are similar.

The increasing behavior in R and X after the initial flat regime is related to the rearrangement of the electromagnetic field distribution with rising frequency. The specific reasons pertinent to the frequency behavior in R and L are discussed in section 5.1.6. The reactance- X is the internal inductance- L multiplied by the angular frequency- ω , which is related to the weakening of the internal magnetic field⁴⁹.

The causes for the above mentioned discrepancy between the computed and measured values in the frequency spectra of both R and X will be discussed now. In a two-probe measurement, the measured response includes the contact resistance between the electrodes and the specimen. Although, this may be safely ignored for dielectric specimens, the contact resistance may completely dominate the signal of interest in the case of conducting specimens. This is precisely the reason why the measured resistance is much higher than the computed value over the entire frequency range.

Secondly, the flow of alternating current generates a time-varying magnetic field, as a consequence of Faraday's law^{48, 49}. This magnetic field is responsible for an induced voltage besides that from the specimen, if any loops are present in the circuitry. While the contact resistance offsets the specimen resistance, the induced voltage from the magnetic field primarily affects the reactance. In the measurement scheme used, the reactance measurement is dominated by the induced voltage due to the magnetic field, which is

orders of magnitude higher than the voltage drop from the specimen, especially at high frequencies.

6.2 AC Four-point Probe Impedance on Wire Specimens

AC four-point probe measurements were conducted on copper wire specimens as a precursor to extending this measurement scheme for actual cylindrical disk specimens. The measurements were conducted on two different 12 AWG wires of lengths 12.2 cm and 6.9 cm. The computed responses were based on the analytical treatment of 1-D skin-effect developed by Giacoletto⁴⁷ that was presented in the previous chapter. The measured resistance at 200 Hz which was the lowest measured frequency was taken to be the *dc* resistance of the wire for the model. Additionally, a wire diameter of 2 mm and a resistivity of 1.663×10^{-8} [Ω -m] for copper were also used as model inputs.

The measured and computed responses for resistance and inductance of the two wires are shown in Figures 6.3 and 6.4 respectively. It is seen from Figure 6.3 that the measured resistance for both the wires remains flat for frequencies up to 8 kHz and then starts to increase monotonically for higher frequencies. The match between the measured and the computed profiles is remarkably good considering the wide range of frequencies (200 Hz to 100 kHz) measured. The measurement set-up used in this research (shown in Figure 3.3) was replicated from that used by Gosselin et al.³⁶, who reported similar measurements only up to 10 kHz. It is also seen from Figure 6.3 that the ratio of the measured resistances of the two wires at any given frequency is nearly equal to the ratio of their lengths. This is in agreement with the predicted values from the analytical model (see equations (102) and (103) in Chapter 5.3.1). The reason for the rise in the resistance for frequencies higher than 8 kHz is because of the redistribution in the electric field,

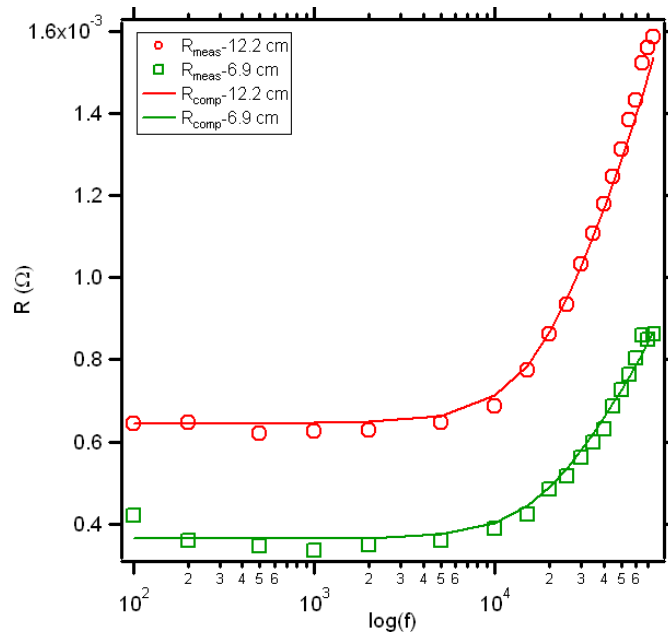


Figure 6.3 Plot of the resistance versus frequency showing the measured (open symbols) and the computed profiles (solid line) for wires of two different lengths in a four-probe AC measurement. Wires 1 and 2 measured 12.2 cm and 6.9 cm in length respectively.

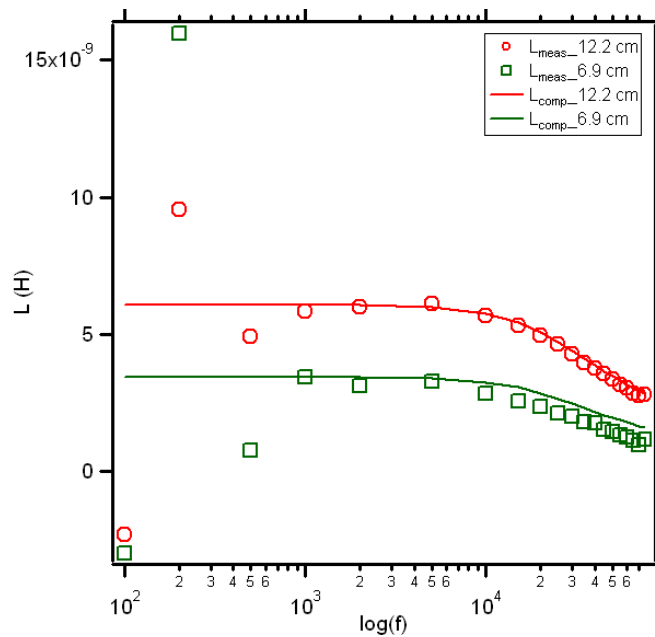


Figure 6.4 Plot of the inductance versus frequency showing the measured (open symbols) and the computed profiles (solid line) for wires of two different lengths in a four-probe AC measurement. Wires 1 and 2 measured 12.2 cm and 6.9 cm in length respectively.

which occurs in response to the increasing frequency. Specifically, the axial electric field starts to become non-uniform across the cross-section of the wire, in that the field starts to diminish near center regions of the wire at modestly high frequencies of 10 kHz. For higher frequencies, the field is pushed further away from the center until the point where the field is prevalent only near regions very close to the surface of the wire. This may be seen from Figure 6.5 (a)-(c) where surface plots of the axial electric field distribution across the wire cross-section are shown at progressively increasing frequencies of 0.1 MHz, 0.5 MHz and 1MHz. This phenomenon is generally referred to as the ‘skin-effect’ in the literature^{47, 57}. The magnitude of the axial electric field also increases progressively with rising frequency as a consequence of redistribution in smaller and smaller cross-sectional area of the wire. This is expressed analytically by equation (101) in Chapter 5.3.1.

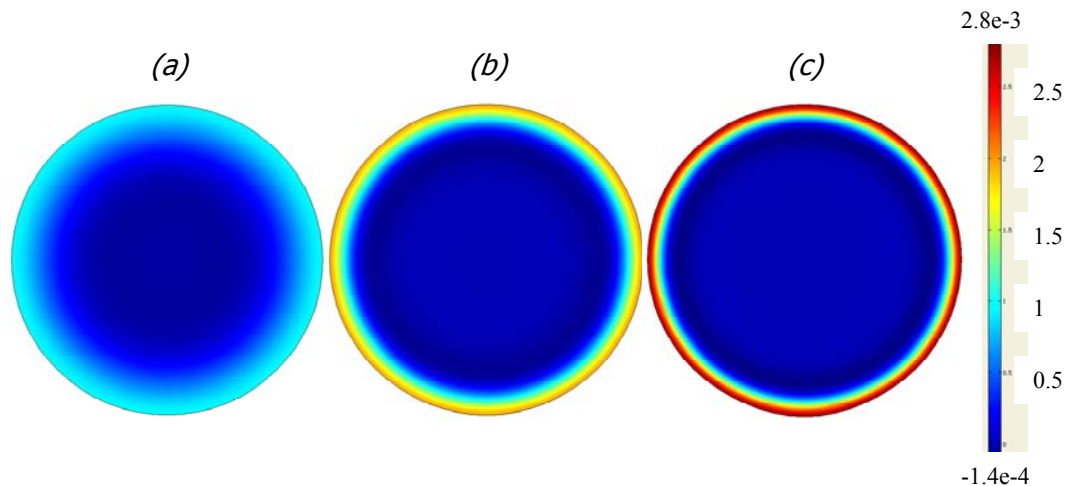


Figure 6.5 Surface plots of the axial electric field- E_z at frequencies of 0.1 MHz-(a), 0.5 MHz-(b) and 1 MHz-(c) respectively. The range for E_z in the above plots is from $E_{z,min} = -1.4 \times 10^{-4}$ [V/m] to $E_{z,max} = 2.8 \times 10^{-3}$ [V/m].

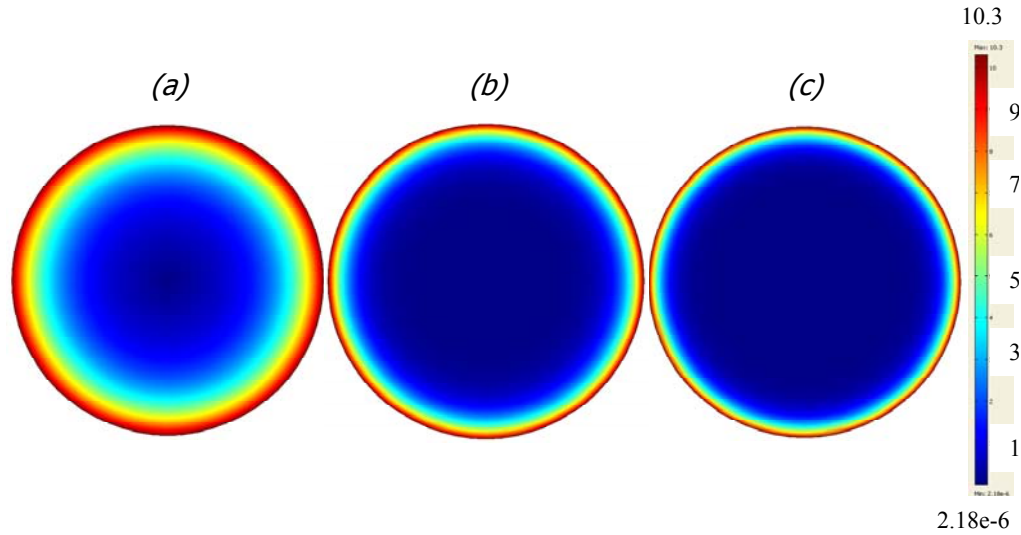


Figure 6.6 Surface plots of the axial normalized magnetic field- H_{norm} at frequencies of 0.1 MHz-(a), 0.5 MHz-(b) and 1 MHz-(c) respectively. The range for H_{norm} in the above plots is from $H_{norm, min} = 2.18 \times 10^{-6}$ [A/m] to $H_{norm, max} = 10.3$ [A/m].

Figure 6.4 shows a plot of the internal inductance of the wires as a function of the frequency for both measured and computed cases. The general inductance behavior may be described as being invariant up to 8 kHz and then decreases monotonically with frequency. The scatter observed in the measured data points at low frequencies may be related to interference arising from multiples of line signal frequency and any other noise signals prevailing at the measurement frequencies. The deviations in the measured response from the computed response at higher frequencies are related to imperfect cancellation of inductance contributions from the circuitry. The scaling of the inductance with the length of the wires is also evident here (see Figure 6.4).

The reason for the decrease in the internal inductance of the wires with rising frequency is associated with the skin-effect^{47, 57}, which was explained earlier. The lines of internal magnetic flux which encircle the wire axis tend to counteract the axial electric

field around the center regions of the wire cross-section⁴⁹. With rising frequency, the internal magnetic field weakens which is responsible for the decreasing inductance⁴⁹. The decrease in the magnetic field in the interior regions of the conductor with rising frequency is shown in Figures 6.6 (a)-(c) as surface plots of the normalized magnetic field.

6.3 AC Four-point Probe Impedance on Cylindrical Disk Specimens

AC four-point probe measurements on Waspaloy specimens in the shape of a cylindrical disk were conducted by a suitable modification of the experimental set-up used for wire measurements. The specifics of the set-up are described in the experimental chapter (see Figure 3.4 in section 3.6). In here, the experimentally measured impedance response using the lock-in amplifier will be compared to the computed response using the closed-form analytical solution developed by Bowler³⁹, described in the previous chapter. A nominal conductivity- σ of 8.34×10^5 [S/m] for Waspaloy, was used as an input for the analytical model.

Figure 6.7 shows a plot of the resistance- R as a function of the frequency for the as-measured, short-corrected and computed cases. It is seen that R shows a flat behavior with frequency up to ~ 25 kHz and then continues to increase for higher frequencies up to 100 kHz. The reason for the increasing behavior beyond 25 kHz is because of the redistribution of the electromagnetic fields with increasing frequency. The as-measured experimental resistance shows a rather large deviation from the computed response for higher frequencies (25 kHz to 100 kHz). This is presumably due to contributions to the measured voltage from the instrumentation in addition to the actual specimen voltage.

The short-corrected profile is the difference between the as-measured resistance and the residual resistance associated with the instrumentation. The latter component was

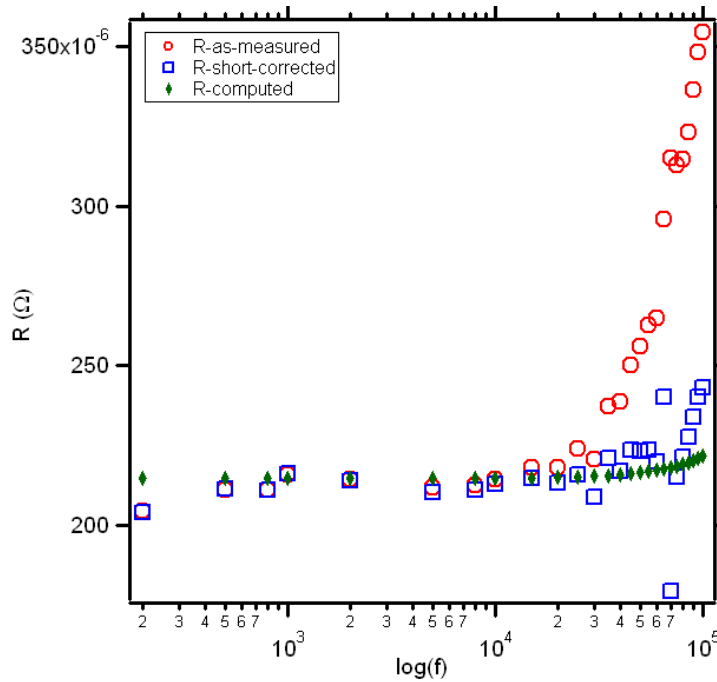


Figure 6.7 Plot of the resistance versus frequency showing the as-measured, short-corrected and computed profiles of a cylindrical Waspaloy disk specimen in a four-probe AC measurement.

determined by a separate short measurement on a copper sheet specimen, which is described in detail in the experimental procedure chapter. The short-corrected specimen resistance overall shows an increasing behavior with frequency and is a more reasonable comparison to the computed response. Nevertheless, discrepancies still exist between the short-corrected and the computed resistances because of the imperfect cancellation of the residual resistance.

The as-measured, short-corrected and computed reactances- X as a function of frequency are shown in Figure 6.8. The reactance also shows a similar increasing

behavior with frequency as the resistance associated with the redistribution of the electromagnetic fields. It is seen from Figure 6.8 that the short-correction scheme is of

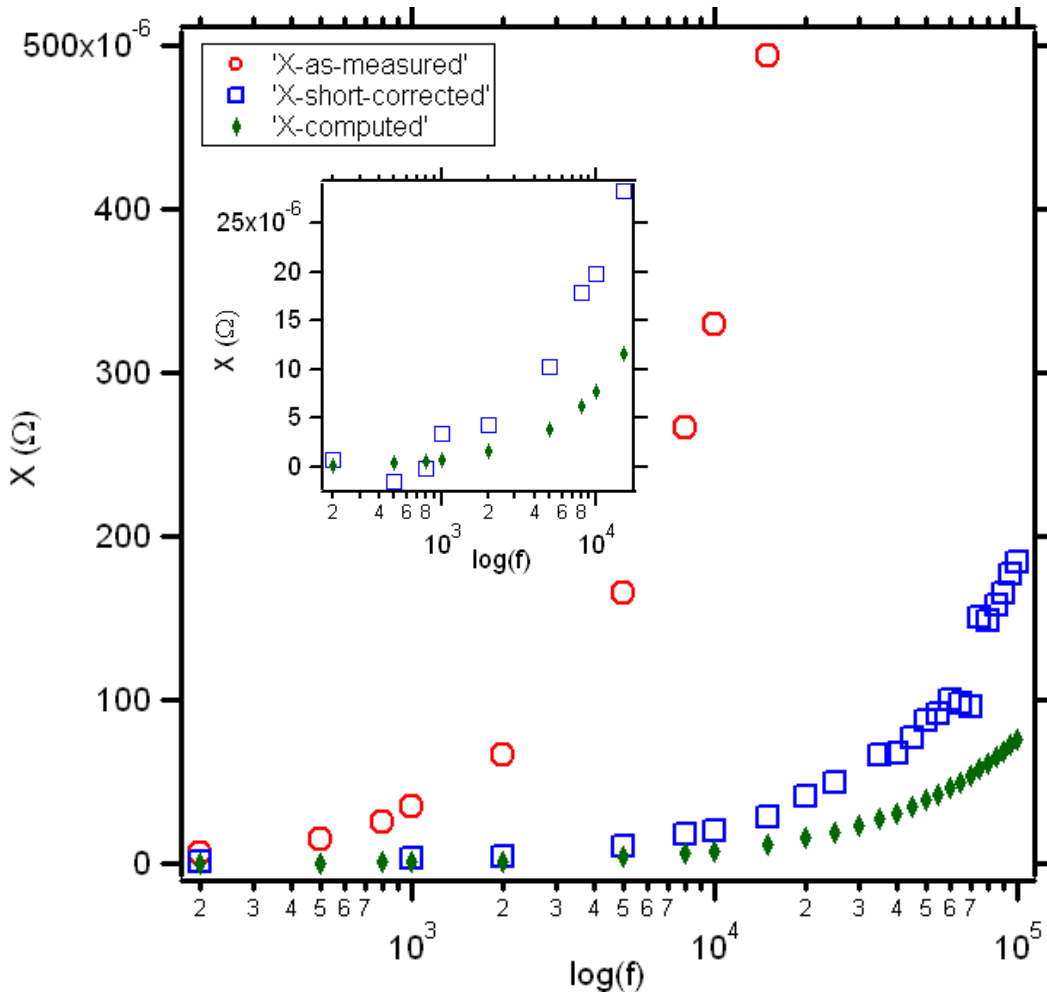


Figure 6.8 Plot of the reactance versus frequency showing the as-measured, short-corrected and computed profiles of a cylindrical Waspaloy disk specimen in a four-probe AC measurement. The inset is a magnified view of the data at low frequencies.

utmost importance in this case to disregard the reactance associated with the instrumentation. Even after the short-correction, the measurements do not confirm to the theoretically predicted values at any of the measured frequencies. The mismatch at lower frequencies is shown in the inset in Figure 6.8.

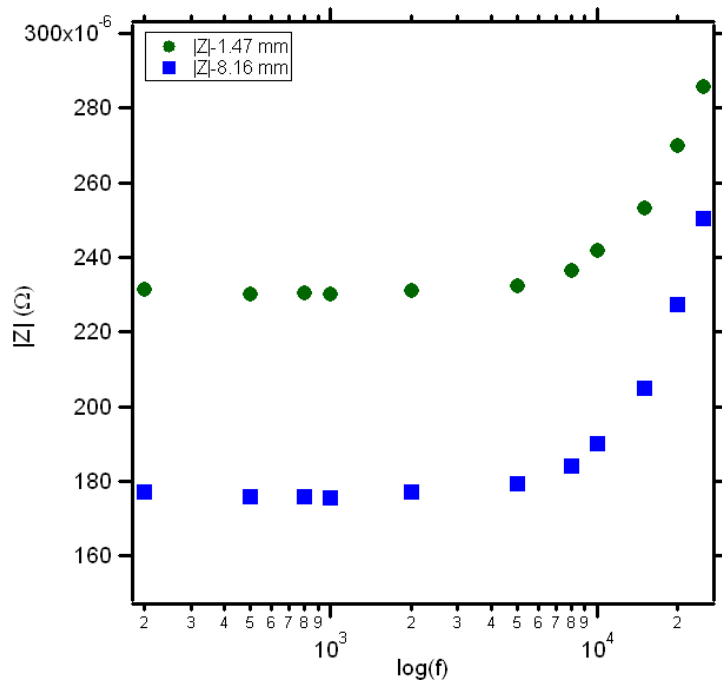


Figure 6.9 Plot of the absolute value of the impedance as a function of the frequency showing the effect of thickness variations for four-point probe measurement of cylindrical Waspaloy specimens.

Next, the effect of varying the thickness is shown in Figure 6.9 as a plot of the magnitude of the complex impedance, $|Z|$ vs frequency for two Waspaloy specimens of thickness 1.47 [mm] and 8.16 [mm] respectively. The measured response is only presented up to 25 kHz because the response at higher frequencies changed drastically with a minimal shift of the voltage pick-up circuitry. As before, the impedance response as a function of the frequency shows an increasing trend. It is seen that the effect of decreasing the thickness results in an increased impedance for all the frequencies shown.

This is to be expected because decreasing the thickness results in a decreased volume for current spreading inside the specimen, thereby resulting in a higher value of the measured voltage. Consequently, the measured impedance is higher for the thinner specimen as compared to the thicker one for the same value of the source current. Thus the effect of the specimen thickness is demonstrated for a very limited range of frequencies.

6.4 Conclusions

The experimentally measured two-probe impedance response and the computed response for an ideal two-probe impedance measurement show similar trends as a function of the measured frequency. The experimentally measured resistance is dominated by the contact resistance between the specimen and the electrodes at all measurement frequencies. The measured reactance behavior is dominated by induced voltage contributions from the magnetic field due to the presence of loops in the circuitry.

For AC four-point probe measurements on wire specimens, the experimentally measured and the computed profiles of the frequency dependent resistance and the inductance show a good agreement with each other. The resistance remained flat for frequencies below 10 kHz and increased monotonically with further rise in the frequency, whereas, the inductance decreased correspondingly. These effects are due to the skin-effect, which forces the electric field near regions close to the surface and also causes a decrease in the internal magnetic field of the conductor. Upon changing the length of the conductor, both the resistance and the inductance scaled by nearly the same amount as the fractional change in length at all frequencies.

AC four-point probe measurements on cylindrical disk specimens showed an increasing behavior in the resistance for higher frequencies (>20 kHz approximately) after an initial flat regime at lower frequencies. The resistance measurements conformed to the theoretically predicted values only at relatively low frequencies (up to 25 kHz). The reactance measurements deviated largely from the theoretically predicted values over the entire frequency regime, which is due to the imperfect cancellation of induced voltage contributions arising from the circuitry, after the short-measurement. The effect of decreasing the specimen thickness resulted in a higher value of the measured impedance because of the lower volume available for current flow.

CHAPTER 7

AFM-BASED LOCALIZED ELECTRICAL CHARACTERIZATION

Sub-grain level localized electrical characterization using the AFM was conducted in order to investigate the electrical contrast between the different microstructural constituents in heat-treated Waspaloy microstructures. The underlying principle in AFM-based electrical measurements is based on mapping the electrical variations in the specimen in response to an applied bias between a conductive AFM tip and the specimen⁷¹. The electrical variations arise from the differences in the interaction between the AFM tip and the features on the surface of the specimen⁷¹. Localized AFM characterization of heat-treated Waspaloy microstructures on the XE 100 SPM were conducted in three different electrical modes, viz. Electrostatic Force Microscopy (EFM), Scanning Kelvin Probe Microscopy (SKPM) and Current-Atomic Force Microscopy (I-AFM).

7.1 Description of Measurement Techniques

In EFM, as the name implies, the electrostatic force between the biased AFM tip and the specimen surface is sensed as the AFM cantilever scans the surface topography in non-contact mode^{71, 72}. The key to successful EFM imaging lies in the separation of the topography and the electrical signals arising from the interaction between the AFM tip and the specimen^{71, 72}. In non-contact mode, the topographic signal is due to the attractive van der Waals force between the atoms on the AFM tip and the surface atoms, that varies as $\frac{1}{r^6}$ ^{72, 73}. The electrostatic force on the other hand is a Coulombic interaction, that

varies as $\frac{I}{r^2}$ ^{71, 73}. Thus at small separation distances, the topographic signal dominates the overall response, where as at larger distances, the van der Waals force decreases rapidly with the electrostatic force becoming more significant. Usually a two-pass technique is used to separate the contributions arising from topographic and electrical signals^{71, 72}. In the first pass, the AFM tip scans at a relatively small separation distance, rendering the topographic signal to be dominant. In the second pass, the AFM tip is lifted up to a predetermined height, where the electrostatic force is dominant and the scan is repeated by retracing the stored topographic profile from the first pass. Thus, the two-pass technique allows effective separation of the topographic and electrostatic signals^{71, 72}.

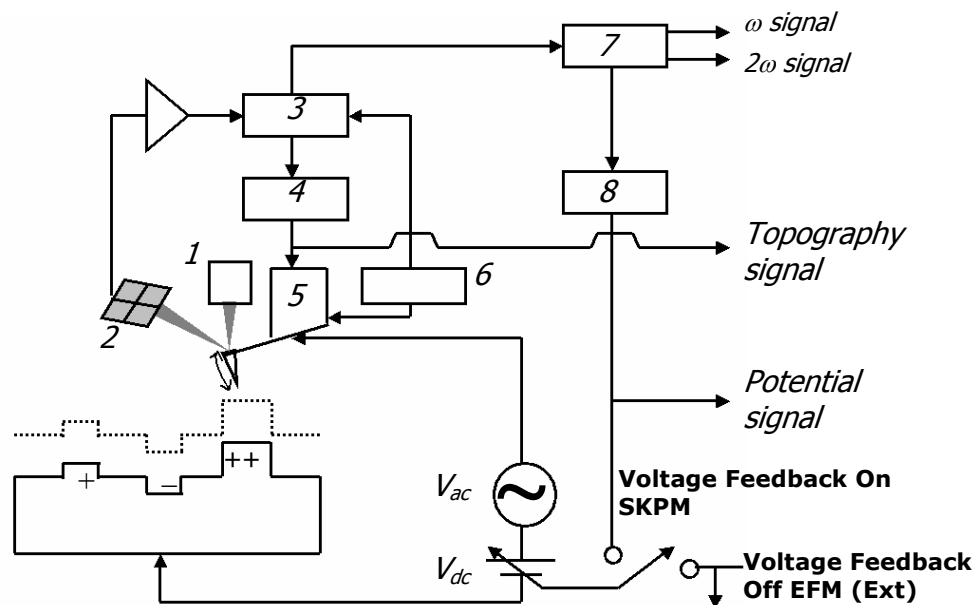


Figure 7.1 Schematic showing the experimental set-up of an EFM/SKPM measurement⁷². The numerals denote the following: (1) laser diode, (2) position sensitive photo diode detectors, (3) internal lock-in amplifier, (4) feedback loop for amplitude/phase, (5) ‘Z’ piezoelectric actuator, (6) oscillator, (7) external lock-in amplifier and (8) feedback loop for *dc* bias.

PSIA Inc. has developed a new technique known as the Enhanced EFM^{71, 72} that allows separation of the topographic and the electrostatic signals in a single pass. The experimental set-up of Enhanced EFM measurement technique is shown in Figure 7.1. In the Enhanced EFM mode, an external lock-in amplifier is connected to the XE 100 controller for isolating the electrostatic signal from the topographic signal^{71, 72}. The lock-in amplifier is used to apply an alternating bias of frequency ω , in addition to any *dc* bias applied from the XE 100 controller to the conductive AFM tip. The overall bias between the AFM tip and the specimen may then be written as follows⁷³:

$$V(t) = V_{dc} - V_S + V_{ac} \sin(\omega t) \quad (1)$$

where, V_S is the potential on the surface of the specimen, V_{dc} and V_{ac} are the applied DC and AC potentials respectively. The above equation for the voltage is under the assumption that the tip and the sample can be treated as two parallel plates. The electrostatic force- $F(z)$ between the tip and the sample by assuming a tip-surface capacitance $C(z)$ and a separation distance- z , can then be written as⁷³:

$$\begin{aligned} F(z) = \frac{1}{2} \left(\frac{\partial C}{\partial z} \right) V(z)^2 &= \frac{1}{2} \left(\frac{\partial C}{\partial z} \right) \left[(V_{dc} - V_S)^2 + \frac{1}{2} V_{ac}^2 \right] \\ &+ \left(\frac{\partial C}{\partial z} \right) (V_{dc} - V_S) V_{ac} \sin(\omega t) \\ &- \frac{1}{4} \left(\frac{\partial C}{\partial z} \right) V_{ac}^2 \cos(2\omega t) \end{aligned} \quad (2)$$

Thus the overall electrostatic force between the AFM tip and the specimen consists of a *dc* component and components at the first and second harmonic frequencies. The *dc* component of the force can be obtained directly from the signal channels accessible using the data acquisition software. The ω and the 2ω components of the electrostatic force can

be monitored using the lock-in amplifier. In the Enhanced EFM mode, an electrical image representing the amplitude and the phase of either the ω and 2ω components of the force may be generated^{71, 72}.

The operating principle of surface potential microscopy (SKPM) is similar to the Enhanced EFM. The measurement set-up used for SKPM⁷² is the same as that for an EFM measurement (see Figure 7.1). In SKPM, the ω component of the force is made use of to obtain a potential map of the surface of the specimen⁷². The first harmonic of the force will be identically zero when V_{DC} and V_S are equal to each other^{72, 73}. In the SKPM mode, a feedback loop is enabled during the scan to vary the DC offset voltage (see Figure 7.1), V_{DC} , so as to set the ω component of the force to zero, also referred to as the null force approach⁷². This approach allows for obtaining the true potential distribution on the surface of the specimen.

Localized electrical examination of heat-treated Waspaloy microstructures in the Enhanced EFM and SKPM modes were conducted at frequencies of 17.5 kHz and 54.65 kHz and at amplitudes of AC voltage ranging from 1V to 4V. The choice of the experimental parameters is based on obtaining the best response in terms of the EFM amplitude, EFM phase or the potential in relation to the observed topographic signal. Besides the frequency and the voltage amplitude, other parameters that were adjusted on the lock-in amplifier include the time-constant and the slope of the filter. The time-constant and the slope determine the variability in the measured signal and were typically set at 1-3 msec and 12 dB roll-off respectively. In the SKPM mode, the phase of the applied signal was also optimized prior to image collection.

In the I-AFM mode^{74, 75}, a conductive AFM tip scans the surface of the specimen in contact mode to map the topography, while also sensing the current flow from the specimen simultaneously. The measurement set-up of an I-AFM experiment is shown in Figure 7.2. A bias is applied to the specimen in the I-AFM mode, while the tip is left unbiased and only acts as a sensor. The current map produced upon imaging correlates directly to the variations in resistivity of features on the surface^{74, 75}. Regions corresponding a higher current flow are indicative of a lower resistivity compared to regions yielding lower currents.

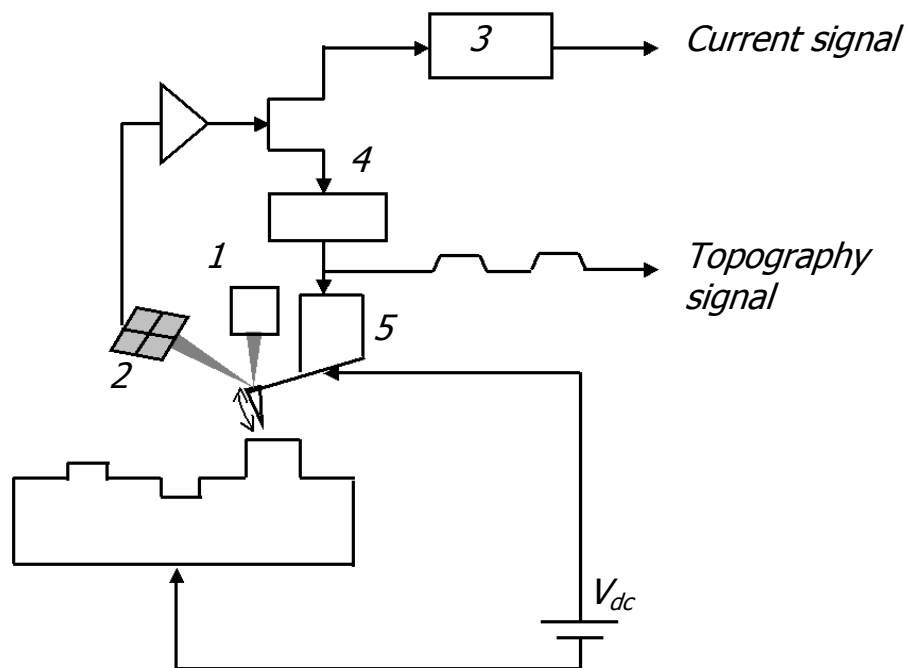


Figure 7.2 Schematic showing the experimental set-up of an I-AFM measurement⁷⁴. The numerals denote the following: (1) laser diode, (2) position sensitive photo diode detectors, (3) external current gain amplifier, (4) feedback loop for height and (5) 'Z' piezoelectric actuator.

The magnitude of current flow from the specimen to the tip is generally very low and is magnified by a current amplifier before representing the current data in the form of an image. I-AFM experiments on the XE 100 SPM were conducted using an external DLCPA-200 variable gain low noise current amplifier^{74, 75}. This mode of electrical imaging is also referred to as the External I-AFM for this reason. The gain setting on the current amplifier determines the measurable range of current values in an I-AFM experiment⁷⁵. By modulating the gain suitably, current values ranging from 1pA to 10mA are measurable in External I-AFM experiments. Generally speaking, the gain setting varies from one specimen to another and is sensitive to the surface condition of the specimen. I-AFM experiments on Waspaloy specimens were conducted at values of sample bias ranging from 0.34 V to 2 V and gain settings of 10^4 to 10^9 .

7.2 Results and Discussion

In this section, the results of AFM-based localized investigations of the electrical characteristics of the γ and γ' phases and that of the etch-pit features will be discussed. The microstructures are highlighted differently using two different etchants as follows- 'A-etchant' that preferentially etches the γ' phase and 'B-etchant' that preferentially etches the γ phase, leaving out the γ' phase. The compositions of these etchants are specified in an earlier chapter. Additionally, imaging was also conducted on as-polished specimens, where the contrast was given rise due to the mild etching effect caused by colloidal silica that was used in the final polishing step.

Figures 7.3 through 7.5 show the topographic and EFM amplitude micrographs of Waspaloy under different etching conditions, in order to demonstrate the electrical contrast between the γ and γ' phases. The specimens in the different etched conditions

and the corresponding experimental parameters that were used for acquiring the EFM micrographs are listed in Table 7.1.

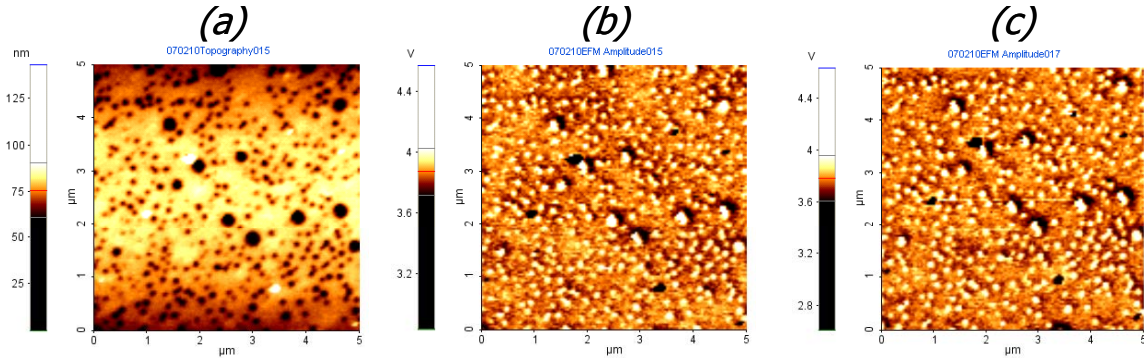


Figure 7.3 AFM micrographs of IIDS-875-75 specimen with a preferential γ' etch showing γ - γ' contrast in terms of (a) surface topography, (b) EFM amplitude at $V_{dc} = -1V$ and (c) EFM amplitude at $V_{dc} = 1V$ respectively. An oscillating bias of $V_{ac} = 2V$ was also applied at a frequency of 52.65 kHz.

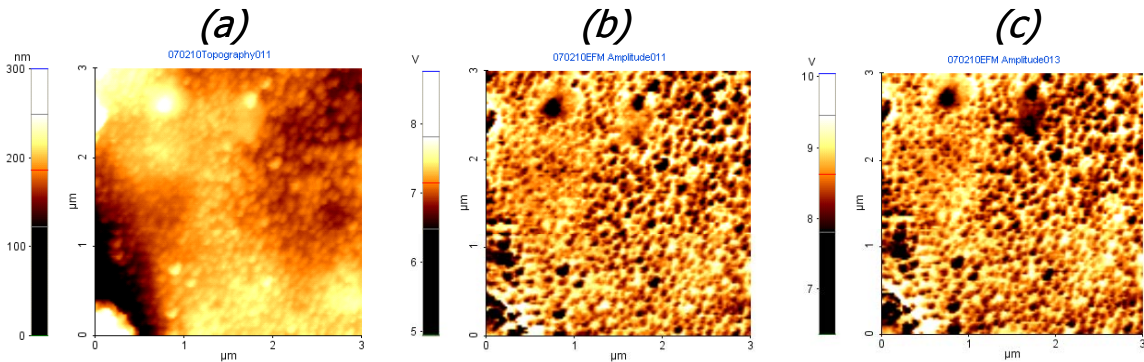


Figure 7.4 AFM micrographs of IBS-800-100 specimen with a preferential γ etch showing γ - γ' contrast in terms of (a) surface topography, (b) EFM amplitude at $V_{dc} = 1V$ and (c) EFM amplitude at $V_{dc} = -1V$ respectively. An oscillating bias of $V_{ac} = 1.5V$ was also applied at a frequency of 52.65 kHz.

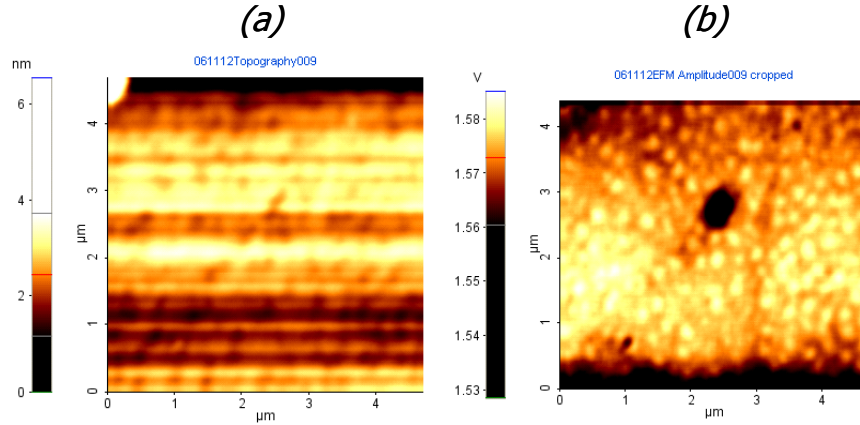


Figure 7.5 AFM micrographs of IID-875-100 specimen in the as-polished condition showing γ - γ' contrast in terms of (a) surface topography and (b) EFM amplitude response at $V_{dc} = 0V$ and $V_{ac} = 3V$ at a frequency of 52.65 kHz.

Table 7.1 List of specimens with the specific surface finish and the corresponding measurement parameters for EFM experiments

Specimen	Figure(s)	Preferential etch	V_{ac} (V)	Frequency (kHz)	V_{dc} (V)
IIDS-875-75	6.1 (a)-(c)	γ' etch	2	52.65	± 1.0
IID-875-100	6.3 (a)&(b)	As-polished	3	52.65	0
IBS-800-100	6.2 (a)-(c)	γ etch	1.5	52.65	± 1.0
IID-725-5	6.4 (a)-(c)	γ' etch	2	52.65	± 1.0

An EFM image in general contains information regarding the potential or the charge distribution on the surface of the specimen⁷². The EFM amplitude micrographs shown here represent the amplitude of the first harmonic (ω) component- $F_{1\omega}$ of the total electrostatic force interaction between the tip and the surface or equivalently the total cantilever deflection⁷². As may be noted from equation (2), $F_{1\omega}$ contains contributions from the applied AC and DC voltages- V_{ac} and V_{dc} , the voltage on the surface of the specimen- V_s and the gradient in the capacitance- $\left(\frac{\partial C}{\partial z}\right)$. Therefore, the measured signal

is a convoluted response of these different terms and there is no straight forward interpretation of an EFM amplitude image^{72, 73}.

Figure 7.3 shows the topographic and EFM amplitude micrographs of the IIIDS-875-75 specimen which is highlighted using a preferential γ' etch (A-etchant). It is clear from the topographic image (Figure 7.3 (a)) that the precipitates are etched much deeper than the surrounding γ regions. The polarity of the *dc* voltage was reversed for EFM amplitude images in Figures 7.3 (b) and 7.3 (c), keeping the other parameters fixed as indicated in the table. It is seen that the EFM voltage amplitude near the γ' regions is higher than the surrounding γ regions in both cases. As seen from the micrographs, this reversal in polarity causes only a slight shift in the voltage scale but importantly, the γ - γ' amplitude contrast is unaffected. It is experimentally observed that the reversal of polarity of the dc bias caused a phase shift of $\sim 180^\circ$, leaving the sign of the EFM amplitude unaffected.

The set of micrographs in Figure 7.4 show the topographic scan and the corresponding EFM amplitude response of IBS-800-100 specimen with a preferential γ etch. The topographic image (Figure 7.4 (a)) clearly shows the precipitates to be at a greater height relative to the surrounding γ matrix. The γ - γ' amplitude contrast is notably reversed from the earlier case upon inverting the etch effect. This clearly confirms that the presence of γ' in this case is responsible for a different EFM interaction compared to the IIIDS-875-100 specimen where most of the γ' is etched out. It is also possible that the presence of opposite topographies might contribute to different EFM interactions. Even though the topographic interaction resulting from van der Waals forces is effectively separated by using a lock-in amplifier^{71, 72}, the EFM response is indirectly affected by the

topography introduced by the etch. This is because the electrical interaction between the tip and the surface is dependent on both the geometric and the electric properties of the tip and the surface and can be non-linear⁷³, as explained later. Next, the relative difference in the voltage scales of EFM amplitude micrographs in Figures 7.4 (b) and 7.4 (c) is clearly due to the reversal of the dc bias. As before, the γ - γ' contrast remained, but a phase shift of 180° was noted when the polarity was reversed.

Topographic and EFM amplitude images of IID-875-100 specimen in the as-polished condition are shown in Figure 7.5. Even though the topographic contrast (Figure 7.5 (a)) is poor, the EFM amplitude image in Figure 7.5 (b) shows a clear γ - γ' contrast. It is also noted that the γ - γ' amplitude contrast is represented in terms of smaller variations in the voltage compared to the etched specimens. This is again an indication that the interaction is dependent on the preferential presence of one phase versus another and additionally the indirect effect of topography, as mentioned previously.

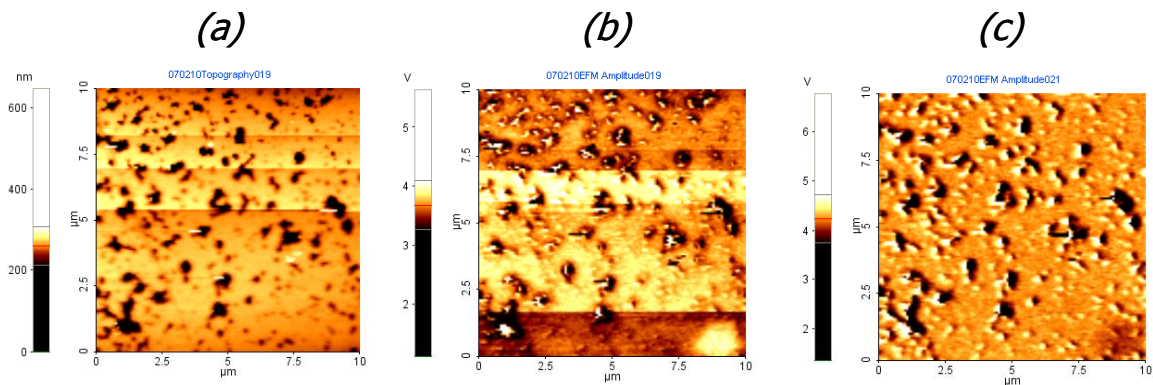


Figure 7.6 AFM micrographs of IID-725-5 specimen with a preferential γ' etch showing etch-pit contrast in terms of (a) surface topography, (b) EFM amplitude at $V_{dc} = -1V$ and (c) amplitude at $V_{dc} = 1V$ respectively. An oscillating bias of $V_{ac} = 2V$ was also applied at a frequency of 52.65 kHz.

Figure 7.6 shows the topographic scan and the corresponding EFM amplitude images of the IID-725-5 specimen highlighted using the B-etchant in order to demonstrate the etch-pit contrast. The polarity of the applied dc bias is reversed from Figures 7.6 (b) to 7.6 (c) as indicated in Table 7.1. The EFM amplitude contrast between the etch-pit regions and the surrounding regions is clear from both Figures 7.6 (b) and (c). In an earlier chapter, it was argued that the etch-pits in fact consisted of γ' precipitates, which upon gradual coarsening, contributed to the evolution of the etch-pits from polygonal to more irregular shapes and eventual annihilation. Therefore, the contrast observed in the etch-pit regions both in terms of the topography and EFM amplitude is because of complete or partial removal of γ' material within the pits. It is not to say that the surrounding regions are devoid of γ' precipitates, however, the contrast is unclear using this specific etchant, considering the fine scale of the precipitates. As in the previous sets of specimens, reversal of the dc bias resulted in the phase shift of 180° , without any changes in the γ - γ' contrast (see Figures 7.6 (b) and (c)).

Next, the micrographs representing γ - γ' electrical contrast obtained using SKPM are discussed. The specimens used for SKPM experiments in different etch contrasts and the experimental parameters are given in Table 7.2.

Table 7.2 List of specimens with the specific surface finish and the corresponding measurement parameters for SKPM experiments

Specimen	Figure(s)	Preferential etch	V_{ac} (V)	Frequency (kHz)	Phase ($^\circ$)
IIDS-875-75	6.6 (a)-(c)	γ' etch	3	52.65	-2.92
IIDS-875-100	6.7 (a)-(b)	As-polished	2.5	52.65	-0.86
IBS-800-100	6.8 (a)-(d)	γ etch	3	52.65	-3.24
IID-725-5	6.9 (a)-(b)	γ' etch	2.86	17.5	4.62

As explained before, SKPM is a null force technique^{71, 73} that is based on modulating the dc bias applied to the tip to equal the surface voltage of the specimen, so as to render the ω component of the total force to zero. Therefore, the voltage map produced in an SKPM scan is a direct representation of the absolute voltage on the surface of the specimen^{71, 72}. In this simple treatment, the surface potential signal is independent of the geometric properties of the tip-surface system and the *ac* measurement parameters. However, for a more realistic system, the surface potential distribution as well as the topography can be non-uniform. In this scenario, the tip-surface interaction becomes complex and non-linear, as not only the region directly under the tip but also the surrounding regions impact the overall interaction⁷³. This is schematically shown in Figure 7.7. In fact, the region that is directly under the tip interacts with a smaller tip area than do the

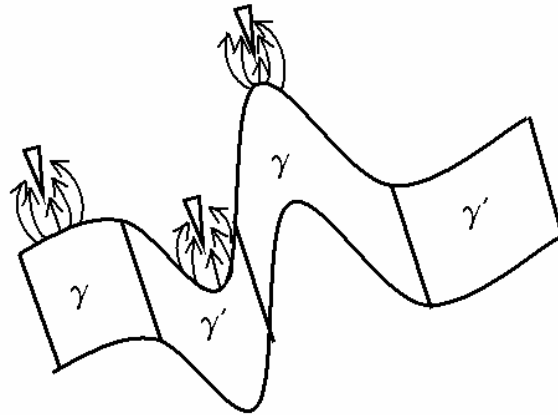


Figure 7.7 Schematic illustrating the topography dependent non-linear tip-surface interaction⁷³ during EFM/SKPM measurement. The voltage distribution is non-homogeneous because of the inhomogeneous surface topography and due to the presence of different phases.

surrounding regions⁷³. The ω component of the total force- $F_{I\omega}$ is now expressed as the sum of several capacitive interactions between the tip and the different regions of the surface as follows⁷³:

$$F_{I\omega} = V_{ac} \sum_{i=1}^n \frac{\partial C_{eff,i}}{\partial z} (V_{dc} - V_{S,i}) \quad (3)$$

The effective surface potential that is measured is therefore⁷³:

$$V_{dc} = \frac{\sum_{i=1}^n \frac{\partial C_{eff,i}}{\partial z} V_{S,i}}{\sum_{i=1}^n \frac{\partial C_{eff,i}}{\partial z}} \quad (4)$$

where- $C_{eff,i}$ is the partial capacitance between the tip and the i^{th} region on the surface and $V_{S,i}$ is the local potential of the i^{th} region.

Figure 7.8 shows the topographic image and the associated surface potential and phase images of the IBS-800-100 specimen with a preferential γ etch to demonstrate the γ - γ' contrast in the SKPM mode. The surface potential scan (Figure 7.8 (b)) indicates a higher voltage near γ' relative to the surrounding γ regions. It is also interesting to note the γ - γ' contrast in terms of the EFM phase here (Figure 7.8 (c)). The as-polished IIIDS-875-100 specimen shows a good γ - γ' contrast in terms of the surface potential (Figure 7.9 (b)) despite the weak topographic contrast (Figure 7.9(a)). The relative γ - γ' surface potential contrast is the same here as for the IBS-800-100 specimen (see Figure 7.9 (b)). In the case of the IIIDS-875-75 specimen with a preferential γ' etch (Figure 7.10), surface potential scans were acquired from two different regions of the specimen. It is seen from Figure 7.10 (b) and 7.10 (e) that the surface potential responses from the two different regions show opposite γ - γ' contrasts for the same experimental parameters. γ - γ' contrast

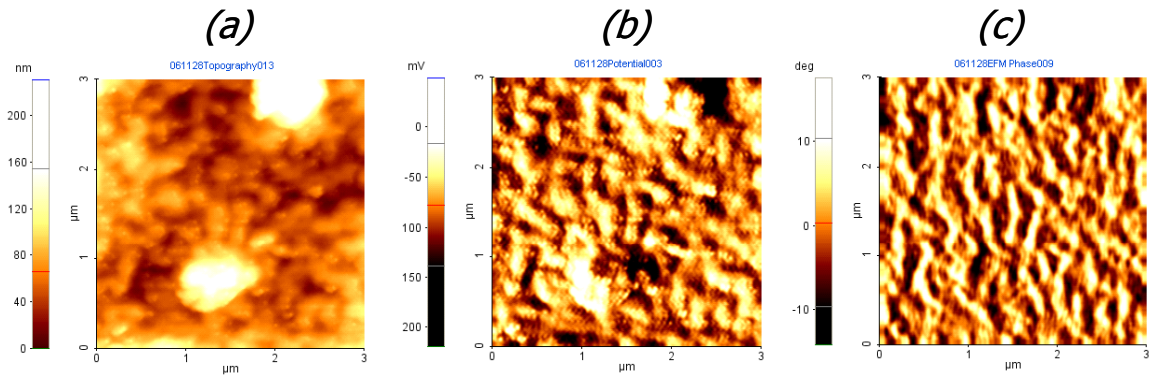


Figure 7.8 AFM micrographs of IBS-800-100 specimen with a preferential γ etch showing γ - γ' contrast in terms of (a) surface topography, (b) surface potential and (c) EFM phase. The scan was acquired using a sinusoidal input signal of $V_{ac} = 3V$, frequency = 52.65 kHz and phase = -3.24° .

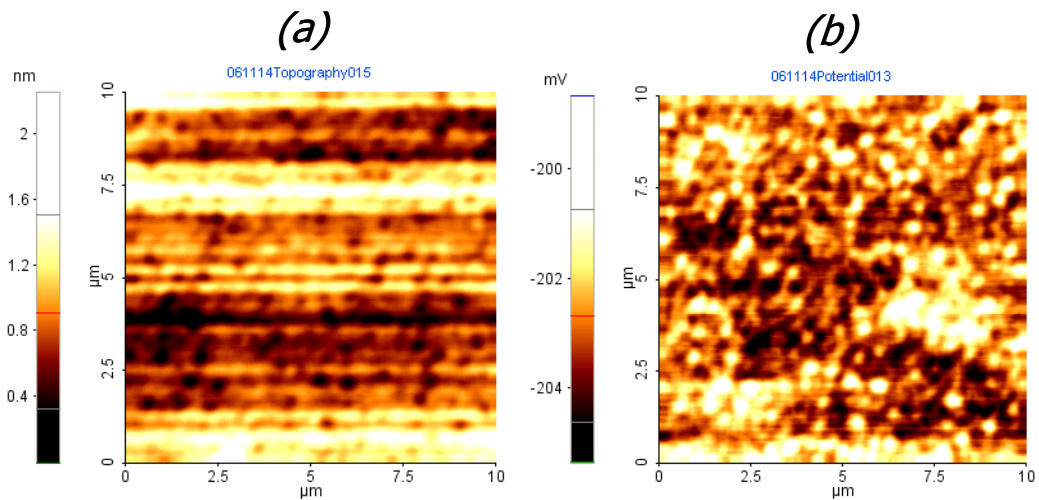


Figure 7.9 AFM micrographs of IIIDS-875-100 specimen in the as-polished condition showing γ - γ' contrast in terms of (a) surface topography and (b) surface potential. The scan was acquired using a sinusoidal input signal of $V_{ac} = 2.5V$, frequency = 52.65 kHz and phase = -0.86° .

in terms of the EFM phase is also observed here (see Figure 7.10 (c)) by using a preferential γ' etch.

It should be noted that the relative γ - γ' topography introduced by the different etching conditions are markedly different among the specimens. Based on the preceding paragraph, it is clear that the non-uniform surface topography in addition to the non-uniform voltage distribution, result in a complex and non-linear tip-surface interaction.

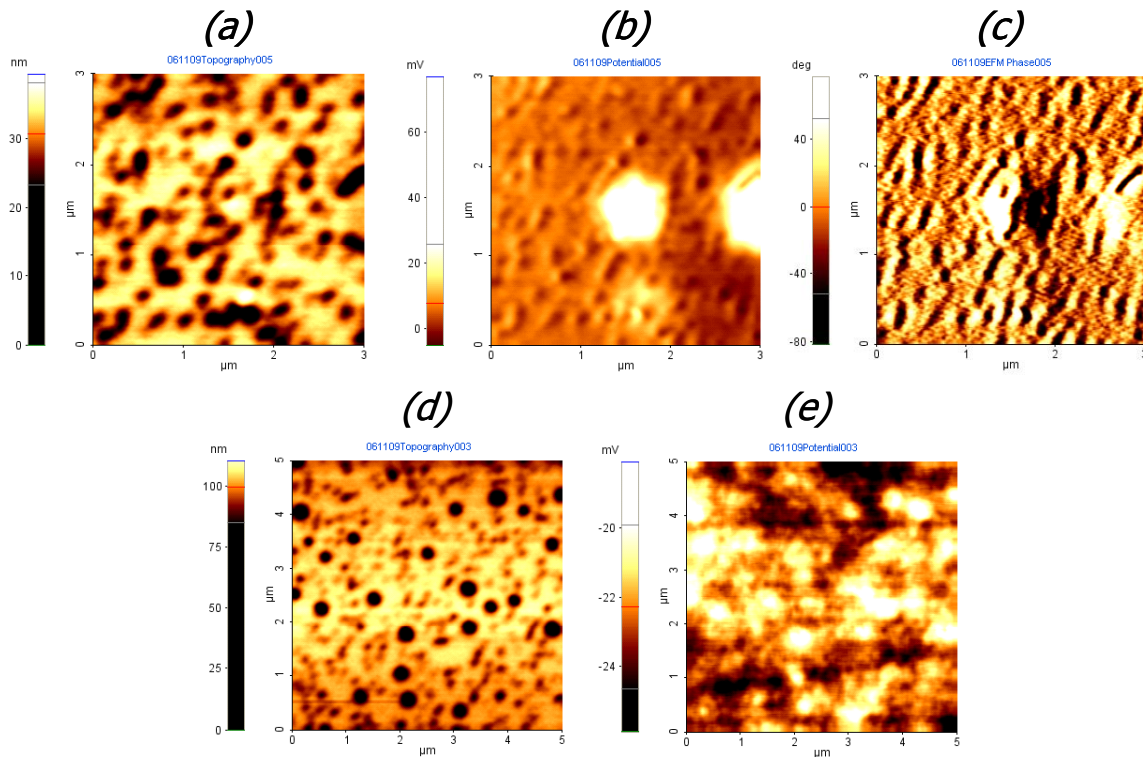


Figure 7.10 AFM micrographs of IIIDS-875-75specimen with a preferential γ' etch showing γ - γ' contrast in terms of (a) surface topography (region 1), (b) surface potential (region 1), (c) EFM phase (region1), (d) surface topography (region 2) and (e) potential (region 2). The scan was acquired using a sinusoidal input signal of $V_{ac} = 3V$, frequency = 52.65 kHz and phase = -2.92° .

The non-uniform surface potential distribution here, is attributed to the presence of multiple phases and additionally, the preferential removal of one phase versus another based on the etchant used. Besides this, the surface potential distribution may also be

affected by the specific grounding configuration that varies from one specimen to another.

The EFM phase images shown in Figures 7.8 (c) and 7.10 (c) represent the changes in the phase of the ω component of the force (see equation (2)) measured by the lock-in amplifier. In the SKPM mode, the phase changes are with reference to the optimized phase of the input signal, which is listed in Table 7.2.

The electrical contrast of the etch-pits observed in the SKPM mode is presented in Figure 7.11. As mentioned previously for the EFM images, the observed voltage contrast is due to the inhomogeneous surface potential distribution arising from the preferential loss of γ' within the pits and the indirect effect of topography.

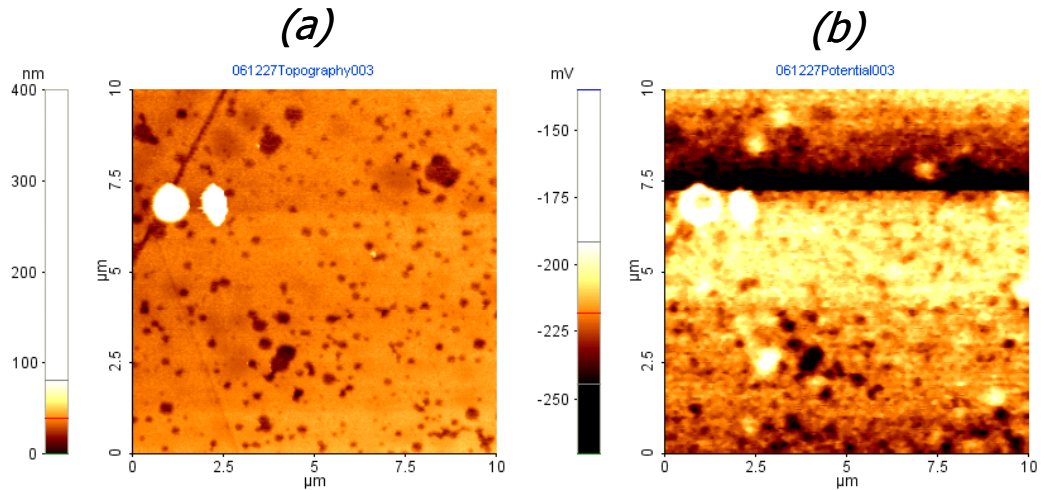


Figure 7.11 AFM micrographs of IID-725-5 specimen with a preferential γ' etch showing etch-pit contrast in terms of (a) surface topography and (b) surface potential. The scan was acquired using a sinusoidal input signal of $V_{ac} = 2.86\text{V}$, frequency = 17.5 kHz and phase = 4.62° .

Table 7.3 List of specimens with the specific surface finish and the corresponding measurement parameters for I-AFM experiments

Specimen	Figure(s)	Preferential etch	Sample bias (V)	Amplifier gain
IID-725-5	6.10 (a)-(b)	γ'	0.34	10^9
IIDS-875-75	6.11 (a)-(b)	γ'	0.22	10^5
IID-875-100	6.12 (a)-(b)	γ	0.57	10^4
IID-875-100	6.13 (a)-(b)	As-polished	2	10^7

The final AFM-based electrical imaging mode that was investigated for studying the electrical contrast between the different microstructural features in Waspaloy was current-AFM or I-AFM. The I-AFM mode allows for mapping the resistivity variations of the surface features, by sensing the current through a conductive AFM tip simultaneously during a contact mode topographic scan^{74, 75}. As stated previously, a *dc* bias is applied to the specimen in an I-AFM scan and the tip only acts as a sensor. The specimens investigated using the I-AFM mode in the different etched conditions are given in Table 7.3.

Figures 7.12 and 7.13 show the topographic and current-AFM scans of the IID-725-5 and the IIDS-875-75 specimens with a preferential γ' etch demonstrating the etch-pit contrast and γ - γ' contrast respectively. Firstly, it is clear from the set of micrographs in Figure. 7.12 and 7.13 that the current contrast is definitely seen at locations of the etch-pits and the γ' precipitates. It should however be noted that the contrast indicated by the higher current regions is not uniform throughout the feature, but is predominant around the edges of the γ' precipitates and the etch-pits. Secondly, the magnitude of the current scale differs by four orders of magnitude between the current image representations of the etch-pits and γ' precipitates. This is clearly a consequence of using different amplifier

gains- 10^9 and 10^5 in the case of the etch-pits and γ' precipitates respectively. Accounting for this factor of the amplifier gain, it is also seen from the current images of the etch-pits and the γ' precipitates that the current scale is more or less proportional to the applied dc bias (see Table 7.3).

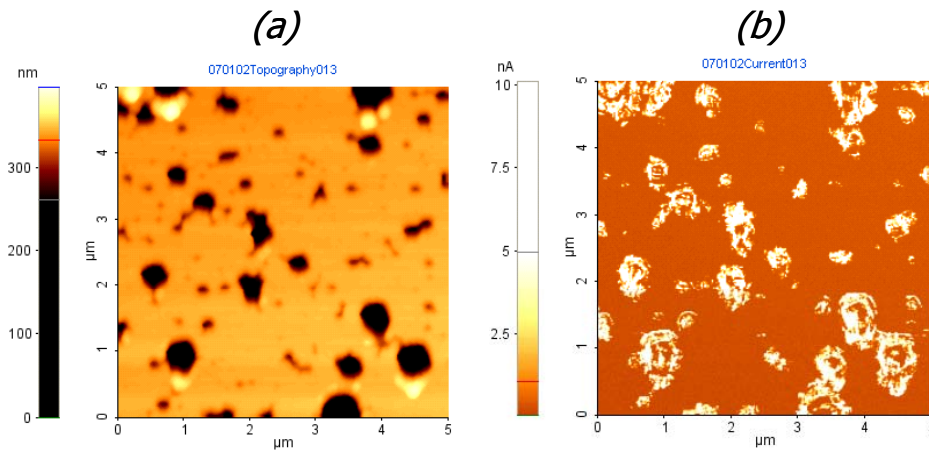


Figure 7.12 AFM micrographs of IID-725-5 specimen with a preferential γ' etch showing etch-pit contrast in terms of (a) surface topography and (b) tip-current. The scan was acquired at a sample bias of 0.34V and an amplifier gain of 10^9 .

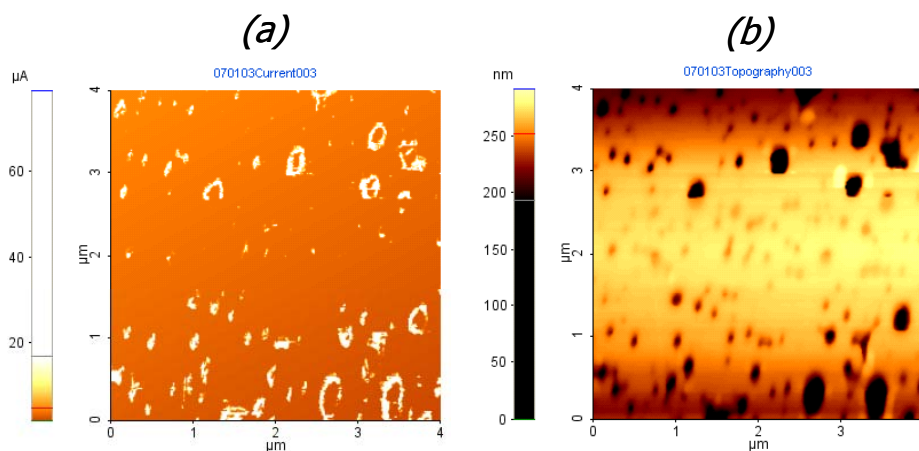


Figure 7.13 AFM micrographs of IIIDS-875-75 specimen with a preferential γ' etch showing γ - γ' contrast in terms of (a) surface topography and (b) tip-current. The scan was acquired at a sample bias of 0.22V and an amplifier gain of 10^5 .

Topography and current images showing γ - γ' contrast highlighted using the B-etchant are shown in Figure 7.14. As noted in the case for the A-etchant, the high current regions are pronounced around the γ' precipitates. Given that higher current regions are always observed in the immediate vicinity of the features delineated by the etch, it is suggested that this is a geometric effect rather than due to resistivity variations. If the current variations were in fact due to resistivity differences between the γ and γ' phases, then it would be expected that regions of higher current would be uniform throughout either the γ or the γ' phase. However, this is clearly not the case as is evident from the micrographs presented for the two cases with opposite γ - γ' etch contrasts.

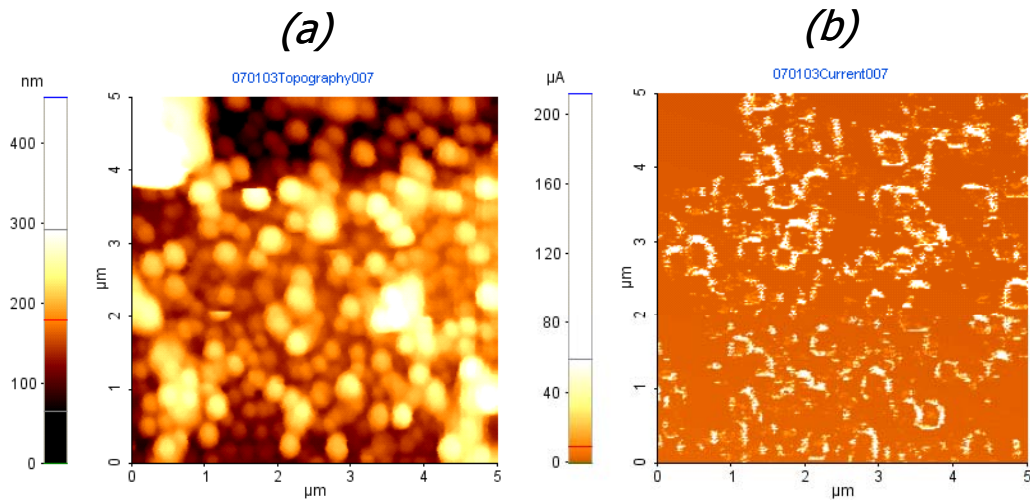


Figure 7.14 AFM micrographs of IID-875-100 specimen with a preferential γ etch showing γ - γ' contrast in terms of (a) surface topography and (b) tip-current. The scan was acquired at a sample bias of 0.57V and an amplifier gain of 10^4 .

Another observation that may be made is that the topography introduced by a specific etchant seems to affect the measured current, as may be noted from Figures 7.13 and 7.14. Accounting for the discrepancy in the amplifier gain and the applied dc bias, the

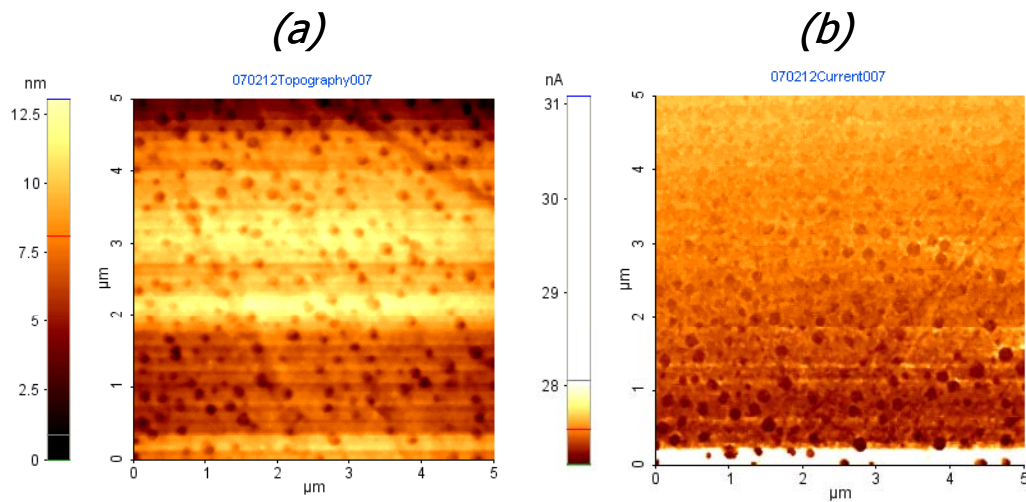


Figure 7.15 AFM micrographs of IID-875-100 specimen in the as-polished condition showing γ - γ' contrast in terms of (a) surface topography and (b) tip-current. The scan was acquired at a sample bias of 2V and an amplifier gain of 10^7 .

measured current is still disparate between these two specific cases. Therefore, it is clear that the disparity is due to the differences in the topography- the absence of γ' in the IIIDS-875-75 specimen (Figure 7.13 (b)) and the presence of γ' in the IID-875-100 specimen respectively (Figure 7.14 (b)).

Finally, the last set of topographic and current micrographs corresponding to the IID-875-100 specimen in the as-polished condition is shown in Figure 7.15. The final polishing step using colloidal silica causes a mild etching effect, resulting in the observed topographic contrast of up to 12.5 nm (see Figure 7.15 (a)). The corresponding current AFM image shows a clear contrast between the γ' precipitates and the surrounding matrix regions. Unlike previous cases, where the current contrast was primarily due to geometric effects arising from the topography introduced by the specific etchants, the contrast here is mostly due to the resistivity differences between the γ and γ' phases. Based on the

current image of the as-polished specimen, it may be concluded that the γ' precipitates should have relatively lower conductivity than the γ phase, indicated by lower current regions in the image. As a final remark, resistivity mapping of microstructures consisting of phases with similar resistivities, should preferably be performed on specimens with minimal surface topography as indicated by the present results.

7.3 Conclusions

AFM-based electrical characterization of heat-treated Waspaloy microstructures was conducted using EFM, SKPM and I-AFM operating modes. Specifically, γ - γ' electrical contrast was observed in all the modes in three different surface conditions- preferential γ' etch, preferential γ etch and in the as-polished condition. The electrical contrast of the etch-pits was observed primarily by using a preferential γ' etch.

In both EFM and SKPM modes, the tip-surface interaction is non-linear due to the presence of inhomogeneous topography and surface potential distribution. As a consequence, the presence of topography indirectly affects the final interaction, even though the van der Waals forces that correspond to topographic interaction are separated from the electrostatic forces. In EFM imaging, the effect of using a preferential γ' etch versus a γ etch resulted in opposite γ - γ' electrical contrasts. Additionally, the effect of reversing the polarity of the applied dc bias resulted in a phase shift of the amplitude signal by $\sim 180^\circ$, leaving the γ - γ' amplitude contrast unchanged. The same behavior was also noted in case of specimens showing etch-pit contrast.

I-AFM response of as-polished specimens clearly showed lower current regions near γ' precipitates indicative of a relatively lower conductivity compared to the

surrounding γ phase. However, specimens that were preferentially etched to remove the γ or the γ' phase showed higher currents in the immediate vicinity of the precipitates as delineated by the etch. The same phenomenon was also noted in case of etch-pits. This was attributed to a geometric tip-surface interaction effect rather than detection of resistivity differences.

CHAPTER VIII

CONCLUSIONS AND FUTURE WORK

8.1 Conclusions

Controlled Waspaloy microstructures with systematically varying matrix (γ) grain size and γ' precipitate size distributions were successfully synthesized with the objective of studying/developing microstructure-electrical property correlations in this alloy. A combination of non-destructive (NDE) *ac/dc* electrical testing methods, ultra small angle x-ray scattering and conventional microscopy techniques was used to obtain a quantitative understanding of microstructural transformations and the associated kinetics, induced by systematic heat-treatments. Using the combination of these techniques, it was possible to distinguish the transition from nucleation-growth to coarsening and between different stages of coarsening. Coarsening in Waspaloy proceeded at a rate smaller than that evidenced in binary Ni-Al alloys, probably related to the presence of multiple solute elements.

DC four-point probe resistivity technique was the most sensitive of all the electrically based techniques investigated in tracking the resistivity variations caused by microstructural transformations. The microstructural features which impacted the measured DC four-probe resistivity were primarily the γ' precipitate distribution and γ' forming solute elements present in the matrix during initial and later stages of coarsening respectively. The effect of carbides, grain/twin boundaries and quenched-in vacancies on the measured resistivity was deemed to be minimal because of the large scale of dispersion of the former and the insignificantly small concentration of the latter. In

general, the closer the size scale of dispersion of an impurity type to the mean free path of conduction electrons, the greater is the contribution towards the overall resistivity from that impurity.

The applicability of two-probe and four-probe *ac* impedance techniques as potential non-destructive means of microstructural examination in Waspaloy was also investigated. The measured impedance of a representative Waspaloy specimen showed a rising behavior with frequency after an initial flat regime. It was shown via analytical and finite-element simulations that the same frequency dependent impedance response in a two-probe measurement was true of any metallic material treated as a continuum. The frequency response was therefore caused by an electrodynamic effect and not unique to the microstructure of Waspaloy, consisting of interfaces at multiple size scales due to the presence of grain boundaries, carbides and γ' precipitates. Two-probe measurements were found unsuitable for NDE studies of controlled Waspaloy microstructures because of dominating effects of electrode contact resistance and induced voltage contributions. Even though contact resistance effects were eliminated in a four-probe impedance measurement, induced voltage effects still prevailed, which drastically affected the imaginary impedance component.

It was demonstrated qualitatively using I-AFM experiments on unetched specimens that the conductivity of the γ' phase was lower than the surrounding γ phase.

8.2 Future Work

1. In this research, it was demonstrated that DC four-point probe electrical resistivity measurements were adequately sensitive to microstructural transformations that occurred during γ' nucleation-growth and coarsening regimes respectively. The aging temperatures used here were significantly higher than service temperatures which the alloy would normally encounter, in order to study the kinetics of microstructural transformations in a reasonable period of time. The present research lays the ground work for studying more complicated real-world serviced microstructures, in that the primary microstructural attributes impacting the measured resistivity have been discussed in detail.

The initial microstructure of an alloy to be used as a service component usually consists of a unimodal or a bimodal distribution of γ' precipitates. Upon thermal exposure during service at lower temperatures, the formation of a tertiary γ' distribution will result in addition to the evolution of the existing distributions. Prolonged thermal exposure may possibly result in the evolution of all three distributions to the point where only a single distribution might be present finally. Developing microstructure-resistivity correlations in such a series of microstructures will be interesting and more challenging than the controlled microstructures dealt with in the present research. However, the general procedure that may be adopted for such a study will be very similar to that used in the present research, viz. combining information from multiple non-destructive and conventional techniques. It may also be useful to develop simple models which account for the scattering efficiency of each class of impurities and their contribution to overall measured resistivity, along similar lines of White et al. This is essential for establishing a general framework and understanding of how the resistivity changes are linked to the

microstructural transformations. Upon completing such a study, electrical resistivity measurements may be used on a routine basis for a non-destructive examination of service components.

2. The nucleation stage of γ' needs a more thorough study by completing the set of heat-treatments at 600°C and possibly extending the studies to additional temperatures. Conducting the nucleation studies at several temperatures enables the determination of the activation energy of migration of vacancies in Waspaloy via electrical resistivity measurements.

3. USAXS analysis of specimens fabricated in set III, viz. 725°C, 800°C and 875°C sets of specimens with 1145°C pre-solution-treatment, needs to be completed. The activation energy of coarsening in Waspaloy may then be determined from an Arrhenius plot of the coarsening rate-constants at each of these temperatures. This may be compared to the activation energy values quoted in the literature for diffusion of Al and Ti in Ni to resolve the lower diffusion coefficients seen from the present data compared to Ardell's analysis. Extended long-term thermal exposure experiments of an alloy with an initial unimodal distribution of γ' obtained upon aging at temperatures used in this research is definitely worth investigating. The thermal exposure experiments should be carried out at relatively lower temperatures in relation to the aging temperatures used.

4. TEM investigations could be carried out on microstructures that show the etch-pit evolution in response to γ' coarsening, in order to determine the chemical composition of γ' inside the etch-pits versus that in the surrounding matrix.

APPENDIX A

INTEGRALS AND IDENTITIES

I. Derivative of Bessel functions

$$[x^{-\nu} J_{\nu}(x)]' = -x^{\nu} J_{\nu+1}(x)$$

II. Orthogonality of Bessel functions

For a given ν , the Bessel functions $J_{\nu}(\lambda_{1\nu}x)$, $J_{\nu}(\lambda_{2\nu}x)$, $J_{\nu}(\lambda_{3\nu}x)$, ... with

$$\lambda_{m\nu} = \frac{\beta_{m\nu}}{R} \quad (m = 1, 2, 3, \dots)$$

form an orthogonal basis on the interval $0 \leq x \leq R$ with

respect to the weight function $p(x) = x$. This property is expressed as:

$$\int_0^R x J_{\nu}(\lambda_{m\nu}x) J_{\nu}(\lambda_{n\nu}x) dx = 0 \quad (m \neq n)$$

$$= \frac{R^2}{2} J_{\nu+1}^2(\lambda_{m\nu}R) \quad (m = n)$$

III. Indefinite integral of the product of Bessel functions

$$(a) \int_z^{\infty} \left\{ (k^2 - l^2)t - \frac{(\mu^2 - \nu^2)}{t} \right\} J_{\mu}(kt) J_{\nu}(lt) dt$$

$$= z \left\{ k J_{\mu+1}(kz) J_{\nu}(lz) - l J_{\mu}(kz) J_{\nu+1}(lz) \right\} - (\mu - \nu) J_{\mu}(kz) J_{\nu}(lz)$$

$$(b) \int_0^z t J_0^2(t) dt = \frac{z^2}{2} \left[J_0^2(z) + J_1^2(z) \right]$$

IV. Sifting property of the delta function

$$\int f(x) \delta(x_0 - x) dx = f(x_0)$$

V. Complex identities

If u and v are any two complex numbers, then the following identities hold true for operations on their complex conjugates- \bar{u} and \bar{v} .

$$(a) \overline{(u \pm v)} = \bar{u} \pm \bar{v}$$

$$(b) \overline{(uv)} = \bar{u}\bar{v}$$

$$(c) \overline{J_\mu(u)} = J_\mu(\bar{u}), \text{ where } J_\mu(x) \text{ is a Bessel function in } x \text{ of order } \mu.$$

VI. Variable substitution and separation of the integrand into partial fractions-computation of voltage in a four-probe AC measurement.

$$(a) y^2 = \rho^2 + (2nT)^2$$

$$(b) \int \frac{(2nT)^2 y dy}{y^2(y^2 - 4n^2T^2)} = \int \frac{y dy}{y^2 - 4n^2T^2} - \int \frac{y dy}{y^2}$$

$$(c) \int \frac{(2nT)^2 y dy}{y^3(y^2 - 4n^2T^2)} = \int \frac{dy}{y^2 - 4n^2T^2} - \int \frac{dy}{y^2}$$

VII. Definite and indefinite integrals for computing the integrals in VI:

$$(a) E_1(z) = \int_z^\infty \frac{e^{-t}}{t} dt \quad (|\arg z| < \pi)$$

$$(b) \int \frac{e^{ix} dx}{a^2 + x^2} = \frac{i}{2a} [e^{-a} E_1(-a - ix) - e^a E_1(a - ix)]$$

$$(c) \int \frac{x e^{ix} dx}{a^2 + x^2} = -\frac{1}{2} [e^{-a} E_1(-a - ix) + e^a E_1(a - ix)]$$

VIII. Evaluation of Fourier coefficients

If $f(x)$ is a periodic function with a period 2π , a Fourier series representation for $f(x)$ may be written as follows:

$$f(x) = a_0 + \sum_{n=1}^{\infty} (a_n \cos nx + b_n \sin nx)$$

The Fourier coefficients- a_0 , a_n and b_n are then computed as follows:

$$a_0 = \frac{1}{2\pi} \int_0^{2\pi} f(x) dx, \quad a_n = \frac{1}{2\pi} \int_0^{2\pi} f(x) \cos(nx) dx \quad \text{and} \quad b_n = \frac{1}{2\pi} \int_0^{2\pi} f(x) \sin(nx) dx$$

APPENDIX B

NOMENCLATURE USED IN MODELING CHAPTER

r_o :	Specimen radius
r_c :	Electrode contact radius
t_o or d :	Specimen thickness
r :	Radial coordinate
z :	Axial coordinate
s :	Probe spacing
Δ :	Displacement of center of probe array from specimen center
L :	Distance from the specimen center to the nearest probe when the probe unit is displaced.
x :	Distance from the specimen edge to the nearest probe when the probe unit is displaced.
p :	Position vector
ϕ or θ :	Tangential coordinate
ω :	Angular frequency
t :	Time
μ_o :	Absolute magnetic permeability
μ_r :	Relative magnetic permeability
ϵ_o :	Absolute permittivity
ϵ_r :	Relative permittivity

σ :	Specimen conductivity
ρ :	Charge density
R :	Resistance
X :	Reactance
Z :	Impedance
L_i :	Internal inductance
\bar{v} :	Velocity of conductor
I_o :	Current
I_{rms} :	Root mean square value of current
E_r :	Radial electric field
E_z :	Axial electric field
J_r :	Radial current density
J_z :	Axial current density
J_n :	Normal current density
J^e :	External current density
Q_j :	Current density
H_φ :	Tangential magnetic field
\bar{B} :	Magnetization vector
\bar{A} :	Vector magnetic potential
V or φ :	Electric potential
Q_{av} :	Joule heat loss per unit volume
W_{mav} :	Magnetic energy density

APPENDIX C

MATLAB CODE IMPLEMENTATION IN ANALYTICAL MODELS

C.1 Two-probe Impedance Spectroscopy

* Routine for computing the electric fields (E_z and E_r) in a two-probe impedance measurement *

```
Ro = 5e-3; % Specimen radius %
Rc = 5e-4; % Electrode contact radius %
Lo = 2e-3; % Specimen thickness %
delr = Ro/250;
rSteps = transpose([0:delr:Ro]);
zSteps = [0:(Lo/6):(Lo/2)];

sigmao = 8.34e5; % Electrical conductivity of Waspaloy%
muo = 4*pi*1e-7; % Magnetic permeability of free space %
muWaspaloy = 1.004*muo; %Magnetic permeability of Waspaloy %
Io = 50e-3;

nRoots = 2000; % Total no. of roots of J1(x) %
roots_J1 = besselRootsII(nRoots); % Links to function- besselRoots %
lambda = roots_J1/Ro;
f = 1e4; % Frequency %
omega = 2*pi*f; % Angular frequency %
alphaSquared = complex(0,omega*muWaspaloy*sigmao);
beta = sqrt(-alphaSquared);
A = (beta*Io)/(2*pi*sigmao*Ro*besselVal(1,beta*Ro));
% Links to function- besselVal %

C = coefficientsOfE(A,beta,lambda,Io,sigmao,Rc,Ro,Lo,nRoots);
% Links to function- coefficientsOfE %

EzCoeff = C(1,:); % Coefficients in  $E_z$  summation %
Zeta = C(2,:);
ErCoeff = C(3,:); % Coefficients in  $E_r$  summation %

zIndex = 1;
while (zIndex<=4)
    rIndex = 1;
    while (rIndex<=251)
        skinEffectTerm = A*besselVal(0,beta*rSteps(rIndex,1));
```

```

constrictionZterm = 0;
constrictionRterm = 0;
p=1;
for (p=1:nRoots)
    fzz = exp(-Zeta(1,p)*zSteps(1,zIndex)) + exp(-Zeta(1,p)*(Lo-zSteps(1,zIndex)));
    fzs = exp(-Zeta(1,p)*zSteps(1,zIndex)) - exp(-Zeta(1,p)*(Lo-zSteps(1,zIndex)));
    constrictionZterm = constrictionZterm +
    EzCoeff(1,p)*fzz*besselVal(0,lambda(1,p)*rSteps(rIndex,1));
    constrictionRterm = constrictionRterm +
    ErCoeff(1,p)*fzs*besselVal(1,lambda(1,p)*rSteps(rIndex,1));
end
Ez(rIndex,zIndex) = abs(skinEffectTerm + constrictionZterm);
Er(rIndex,zIndex) = abs(constrictionRterm);
rIndex = rIndex + 1;
end
zIndex = zIndex + 1;
end

```

* Function to compute the roots of $J_1(x)$ *

```

function Y = besselRootsII(nRoots)
m = 4;
poly3 = [7 -38 31];
% Coefficients of a second-order polynomial of the form  $p(x) = a_1x^2 + a_1x + a_0$  %

poly4 = [83 -982 3779];
poly5 = [6949 -153855 1585743 -6277237];
p2 = (m-1);
p3 = polyval(poly3,m);

% polyval is an inbuilt MATLAB function, which computes the value of a polynomial at
a specified value %

p4 = (m-1)*polyval(poly4,m);
p5 = (m-1)*polyval(poly5,m);

rootCount = 1;
while (rootCount <= nRoots)
    beta = (pi/4)*(2 + 4*rootCount -1);
    Y(1,rootCount) = beta - p2/(8*beta) - (4*p3)/(3*((8*beta)^3)) -
    (32*p4)/(15*((8*beta)^5)) - (64*p5)/(105*((8*beta)^7));
    rootCount = rootCount + 1;
end

```

* Function to compute the Bessel function value of a given argument *

```
function out = besselVal(nu,z)
    if (abs(z) < 80) % Complex z with abs(z) < 80 %
        out = besselj(nu,z);
    else
        out = besselLarge(nu,z);
    end
```

* Function to compute the coefficients of $E_z(r,z)$ and $E_r(r,z)$ *

```
function C = coefficientsOfE(A,beta,lambda,Io,sigmao,Rc,Ro,Lo,nRoots)

    p = 1;
    for (p = 1:nRoots)
        J1_lambdaRc = besselVal(1,lambda(1,p)*Rc);
        J2_lambdaRo = besselVal(2,lambda(1,p)*Ro);
        zeta = sqrt(-(beta^2) + (lambda(1,p)^2));

        LHS = (-Io/(pi*Rc*sigmao)) * J1_lambdaRc; % LHS term %
        RHS_I = (-beta*A)*integralOfJJ(1,1,beta,lambda(1,p),Ro); % First term on RHS %
        RHS_II_Coefficient = lambda(1,p)*(1 + exp(-
zeta*Lo))*0.5*((Ro*J2_lambdaRo)^2);
        % Coefficient of second term on RHS %

        % Coefficient of Ez and Er%
        C(1,p) = (RHS_I - LHS)/RHS_II_Coefficient; % Coefficients in Ez summation %
        C(2,p) = zeta;
        C(3,p) = (C(1,p)*lambda(1,p)*zeta) / ((zeta^2) + (beta^2)); % Coefficients in Er
summation %
    end
```

* Function to compute the integral of product of two Bessel functions *

```
function Z = integralOfJJ(mu,nu,k,l,zmax)
    Jmuo = besselVal(mu,k*zmax);
    Jmu1 = besselVal(mu+1,k*zmax);
    Jnuo = besselVal(nu,l*zmax);
    Jnu1 = besselVal(nu+1,l*zmax);

    if (mu==0 & nu==0 & k==1)
        Z = 0.5*(zmax^2)*(Jmuo^2 + Jmu1^2);
    elseif (mu==1 & nu==1 & k==1)
```

```

    Z = 0.5*(zmax^2)*(Jmu1^2);
else
    Iom = zmax*((k*Jmu1*Jnuo)-(l*Jmuo*Jnu1)) - (mu-nu)*Jmuo*Jnuo;
    Z = Iom/(k^2 - l^2);
end

* Routine for computing the magnetic field ( $H_\phi$ ) for a two-probe measurement *

Ro = 6.35e-3;
Rc = 5e-4;
Lo = 2e-3;
rZero = 0;
lZero = 0;
rSteps = [rZero:(Ro-rZero)/125:Ro];
zSteps = [lZero:Lo/10:Lo];

sigmao = 8.34e5;
muo = 4*pi*1e-7;
muWaspaloy = 1.004*muo;
Io = 50e-3;

nRoots = 2000;
roots_J1 = bessellRootsII(nRoots);
lambda = roots_J1/Ro;
f = 1e6;
omega = 2*pi*f;
alphaSquared = complex(0,omega*muWaspaloy*sigmao);
beta = sqrt(-alphaSquared);
A = (beta*Io)/(2*pi*sigmao*Ro*besselVal(1,beta*Ro));

C = coefficientsOfEz(A,beta,lambda,Io,sigmao,Rc,Ro,Lo,nRoots);
EzCoeff = C(1,:);
Zeta = C(2,:);
ErCoeff = C(3,:);

for (q=1:nRoots)
    sTermCoeff(1,q) = (-lambda(1,q)*EzCoeff(1,q)) + (Zeta(1,q)*ErCoeff(1,q));
end

zIndex = 1;
while (zIndex<=6)
    rIndex = 1;
    while (rIndex<=126)
        fTerm = -A*beta*besselVal(1,beta*rSteps(1,rIndex));
        sTerm = 0;
    end
end

```

```

    p=1;
    for (p=1:nRoots)
        fz = exp(-Zeta(1,p)*zSteps(1,zIndex)) + exp(-Zeta(1,p)*(Lo-zSteps(1,zIndex)));
        sTerm = sTerm +
sTermCoeff(1,p)*fz*besselVal(1,lambda(1,p)*rSteps(1,rIndex));
    end
    Hphi(zIndex,rIndex) = complex(0,-1)*(fTerm + sTerm)/(omega*muWaspaloy);
    rIndex = rIndex + 1;
end
zIndex = zIndex + 1;
end

```

* Routine for computing the limiting thickness value *

```

Ro = 5e-3;
Rc = 5e-4;
loLower = 1e-3; % Lower limit of specimen thickness %
loUpper = 100e-3; % Upper limit of specimen thickness %

loMiddle = (loLower+loUpper)/2;

sigmao = 8.34e5;
muo = 4*pi*1e-7;
muWaspaloy = 1.004*muo;
Io = 50e-3;
EzImpressed = Io/(sigmao*pi*(Rc^2));

nRoots = 2000;
roots_J1 = besselRootsII(nRoots);
lambda = roots_J1/Ro;
f = 1e6;
omega = 2*pi*f;
alphaSquared = complex(0,omega*muWaspaloy*sigmao);
beta = sqrt(-alphaSquared);
A = (beta*Io)/(2*pi*sigmao*Ro*besselVal(1,beta*Ro));

cDiskLower = coefficientsOfEz(A,beta,lambda,lo,sigmao,Rc,Ro,loLower,nRoots);
cDiskUpper = coefficientsOfEz(A,beta,lambda,lo,sigmao,Rc,Ro,loUpper,nRoots);
cDiskMiddle = coefficientsOfEz(A,beta,lambda,lo,sigmao,Rc,Ro,loMiddle,nRoots);

EzCoeffDiskLower = cDiskLower(1,:);
EzCoeffDiskUpper = cDiskUpper(1,:);
EzCoeffDiskMiddle = cDiskMiddle(1,:);
zeta = cDiskLower(2,:);

```

```

ifIndex = 0;
elseIndex = 0;
delta = 1e-3;
rLim = 0;

EzSkin = A*besselVal(0,beta*rLim);
EzConstrDiskLower =
ConstrictionComponentofEz(EzCoeffDiskLower,lambda,zeta,loLower,rLim,nRoots);
% Links to the function ConstrictionComponentofEz() %
EzConstrDiskUpper =
ConstrictionComponentofEz(EzCoeffDiskUpper,lambda,zeta,loUpper,rLim,nRoots);
EzConstrDiskMiddle =
ConstrictionComponentofEz(EzCoeffDiskMiddle,lambda,zeta,loMiddle,rLim,nRoots);

EzDiskLower = EzSkin + EzConstrDiskLower;
EzDiskUpper = EzSkin + EzConstrDiskUpper;
EzDiskMiddle = EzSkin + EzConstrDiskMiddle;

while (abs(EzDiskMiddle-EzDiskUpper)>delta*abs(EzDiskMiddle) | (loUpper-
loLower)>0.001e-3)
    if (abs(EzDiskUpper-EzDiskMiddle)>delta*abs(EzDiskMiddle))
        ifIndex = ifIndex + 1;
        loLower = loMiddle;
        EzDiskLower = EzDiskMiddle;
        loMiddle = (loLower + loUpper)/2;
        cDiskMiddle = coefficientsOfEz(A,beta,lambda,lo,sigmao,Rc,Ro,loMiddle,nRoots);
        EzCoeffDiskMiddle = cDiskMiddle(1,:);
        EzConstrDiskMiddle =
ConstrictionComponentofEz(EzCoeffDiskMiddle,lambda,zeta,loMiddle,rLim,nRoots);
        EzDiskMiddle = EzSkin + EzConstrDiskMiddle;
    else
        elseIndex = elseIndex + 1;
        loUpper = loMiddle;
        EzDiskUpper = EzDiskMiddle;
        loMiddle = (loLower + loUpper)/2;
        cDiskMiddle = coefficientsOfEz(A,beta,lambda,lo,sigmao,Rc,Ro,loMiddle,nRoots);
        EzCoeffDiskMiddle = cDiskMiddle(1,:);
        EzConstrDiskMiddle =
ConstrictionComponentofEz(EzCoeffDiskMiddle,lambda,zeta,loMiddle,rLim,nRoots);
        EzDiskMiddle = EzSkin + EzConstrDiskMiddle;
    end
end

EzLimiting = abs(EzDiskMiddle)
loLimiting = loMiddle

```

* Function to compute the constriction term (summation) of $E_z(r,z)$ *

```
function Z = ConstrictionComponentofEz(EzCoeffDisk,lambda,zeta,Lo,rLim,nRoots)
p = 1;
Z = 0;
for (p=1:nRoots)
    fzzDisk = 2*exp(-zeta(1,p)*(Lo/2));
    Z = Z + EzCoeffDisk(1,p)*fzzDisk*besselVal(0,lambda(1,p)*rLim);
end
```

* Routine for computing the real impedance of a metallic cylindrical specimen in a two-probe impedance measurement- based on computing the overall Joule heat loss *

```
Ro = 6.35e-3;
Rc = 5e-4;
Lo = 2e-3;
sigmao = 8.34e5;
muo = 4*pi*1e-7;
muWaspaloy = 1.004*muo;
Io = 50e-3;

nRoots = 1000;
roots_J1 = besselRootsII(nRoots);
lambda = roots_J1/Ro;
f = 5*1e1;
omega = 2*pi*f;
alphaSquared = complex(0,omega*muWaspaloy*sigmao);
beta = sqrt(-alphaSquared);
A = (beta*Io)/(2*pi*sigmao*Ro*besselVal(1,beta*Ro));
conjbeta = conj(beta); % conj(z) yields the complex conjugate of a complex number z %
conjA = conj(A);

C = coefficientsOfEz(A,beta,lambda,Io,sigmao,Rc,Ro,Lo,nRoots);
conjC = conj(C);
EzCoeff = C(1,:);
Zeta = C(2,:);
ErCoeff = C(3,:);
conjEzCoeff = conjC(1,:);
conjZeta = conjC(2,:);
conjErCoeff = conjC(3,:);

% Term I – from Ez %
term1 = 2*pi*Lo*(abs(A)^2)*integralOfJJ(0,0,beta,conjbeta,Ro);
% Links to function integralOfJJ() %
```

```

% Term II – from Ez %
m = 1;
sum1 = 0;
for (m=1:nRoots)
    rIntegral = integralOfJJ(0,0,beta,lambda(1,m),Ro);
    zIntegral = integralOfFz(conjZeta(1,m),Lo);
    % Links to function integralOfFz() %

    sum1 = sum1 + conjEzCoeff(1,m)*rIntegral*zIntegral;
end
term2 = 2*pi*A*sum1;

% Term III – from Ez %
n = 1;
sum2 = 0;
for (n=1:nRoots)
    rIntegral = integralOfJJ(0,0,conjbeta,lambda(1,n),Ro);
    zIntegral = integralOfFz(Zeta(1,n),Lo);
    sum2 = sum2 + EzCoeff(1,n)*rIntegral*zIntegral;
end
term3 = 2*pi*conjA*sum2;

% Term IV – from Ez %
outerSum = 0;
for (p=1:nRoots)
    q = 1;
    innerSum = 0;
    for (q=1:nRoots)
        rIntegral = integralOfJJ(0,0,lambda(1,p),lambda(1,q),Ro);
        zIntegral = integralOfFzFz(Zeta(1,p),conjZeta(1,q),Lo);
        % Links to function integralOfFzFz() %

        innerSum = innerSum + conjEzCoeff(1,q)*rIntegral*zIntegral;
    end
    outerSum = outerSum + EzCoeff(1,p)*innerSum;
end
term4 = 2*pi*outerSum;

% Term V – from Er %
outerSum = 0;
for (p=1:nRoots)
    q = 1;
    innerSum = 0;
    for (q=1:nRoots)
        rIntegral = integralOfJJ(1,1,lambda(1,p),lambda(1,q),Ro);

```

```

zIntegral_1 = integralOfFz3((Zeta(1,p)+conjZeta(1,q)),Lo);
% Links to function integralOfFz3() %

zIntegral_2 = exp(-conjZeta(1,q)*Lo)*integralOfFz3((Zeta(1,p)-conjZeta(1,q)),Lo);
zIntegral_3 = exp(-Zeta(1,p)*Lo)*integralOfFz3((conjZeta(1,q)-Zeta(1,p)),Lo);
zIntegral_4 = exp(-(Zeta(1,p)+conjZeta(1,q))*Lo)*integralOfFz3(-
(conjZeta(1,q)+Zeta(1,p)),Lo);
zIntegralSum = zIntegral_1 - zIntegral_2 - zIntegral_3 + zIntegral_4;
innerSum = innerSum + conjErCoeff(1,q)*rIntegral*zIntegralSum;
end
outerSum = outerSum + ErCoeff(1,p)*innerSum;
end
term5 = 2*pi*outerSum;

volumeIntegral = (1/(sqrt(2)^2))*sigmao*(term1 + term2 + term3 + term4 + term5)
Resistance = 2*volumeIntegral/(Io^2) % The factor of '2' accounts for Irms=Io/sqrt(2) %

* Routine for computing the imaginary impedance of a metallic cylindrical specimen in a
two-probe impedance measurement- based on computing the overall internal magnetic
energy of the conductor *

Ro = 6.35e-3;
Rc = 5e-4;
Lo = 2e-3;

sigmao = 8.34e5;
muo = 4*pi*1e-7;
muWaspaloy = 1.004*muo;
Io = 50e-3;

nRoots = 1000;
roots_J1 = besselRootsII(nRoots);
lambda = roots_J1/Ro;
f = 1e7;
omega = 2*pi*f;
alphaSquared = complex(0,omega*muWaspaloy*sigmao);
beta = sqrt(-alphaSquared);
A = (beta*Io)/(2*pi*sigmao*Ro*besselVal(1,beta*Ro));
conjbeta = conj(beta);
conjA = conj(A);

C = coefficientsOfEz(A,beta,lambda,Lo,sigmao,Rc,Ro,Lo,nRoots);
conjC = conj(C);
EzCoeff = C(1,:);
Zeta = C(2,:);

```

```

ErCoeff = C(3,:);
conjEzCoeff = conj(EzCoeff);
conjZeta = conj(Zeta);
conjErCoeff = conj(ErCoeff);

% Term I %
term1 = 2*pi*Lo*(abs(A)^2)*(abs(beta)^2)*integralOfJJ(1,1,beta,conjbeta,Ro);

% Term II%
m = 1;
sum1 = 0;
for (m=1:nRoots)
    rIntegral = integralOfJJ(1,1,beta,lambda(1,m),Ro);
    zIntegral = integralOfFz(conjZeta(1,m),Lo);
    t2_Coeff = (-lambda(1,m)*conjEzCoeff(1,m)) + (conjZeta(1,m)*conjErCoeff(1,m));
    sum1 = sum1 + t2_Coeff*rIntegral*zIntegral;
end
term2 = -2*pi*A*beta*sum1;

% Term III%
n = 1;
sum2 = 0;
for (n=1:nRoots)
    rIntegral = integralOfJJ(1,1,conjbeta,lambda(1,n),Ro);
    zIntegral = integralOfFz(Zeta(1,n),Lo);
    t3_Coeff = (-lambda(1,n)*EzCoeff(1,n)) + (Zeta(1,n)*ErCoeff(1,n));
    sum2 = sum2 + t3_Coeff*rIntegral*zIntegral;
end
term3 = -2*pi*conjA*conjbeta*sum2;

% Term IV %
outerSum = 0;
for (p=1:nRoots)
    q = 1;
    innerSum = 0;
    t4_outerCoeff = (-lambda(1,p)*EzCoeff(1,p)) + (Zeta(1,p)*ErCoeff(1,p));
    for (q=1:nRoots)
        rIntegral = integralOfJJ(1,1,lambda(1,p),lambda(1,q),Ro);
        zIntegral = integralOfFzFz(Zeta(1,p),conjZeta(1,q),Lo);
        t4_innerCoeff = (-lambda(1,q)*conjEzCoeff(1,q)) +
(conjZeta(1,q)*conjErCoeff(1,q));
        innerSum = innerSum + t4_innerCoeff*rIntegral*zIntegral;
    end
    outerSum = outerSum + t4_outerCoeff*innerSum;
end

```

```
term4 = 2*pi*outerSum;
```

```
volumeIntegral = (term1 + term2 + term3 +  
term4)/(2*(sqrt(2)^2)*(omega^2)*muWaspaloy)  
Inductance = volumeIntegral/(Io^2)  
Reactance = omega*Inductance
```

```
* Function to compute the definite integral of  $f(z) = (e^{-\xi z} + e^{-\xi(L-z)})$  from 0 to  $z_{\max}$  *
```

```
function Y = integralOfFz(zetao,zmax)  
Y = 2*(1 - exp(-zetao*zmax))/(zetao);
```

```
* Function to compute the definite integral of  $f(z) = (e^{-\xi_1 z} + e^{-\xi_1(L-z)})(e^{-\xi_2 z} + e^{-\xi_2(L-z)})$  from 0  
to  $z_{\max}$  *
```

```
function X = integralOfFzFz(zeta1,zeta2,zmax)  
fTerm = (1 - exp(-(zeta1+zeta2)*zmax))/(zeta1+zeta2);  
sTerm = (exp(-zeta1*zmax) - exp(-zeta2*zmax))/(zeta2-zeta1);  
X = 2*(fTerm + sTerm);
```

```
* Function to compute the definite integral of  $f(z) = e^{-\xi_1 z}$  from 0 to  $z_{\max}$  *
```

```
function Y = integralOfFz3(zetao,zmax)  
if (isnan(1/zetao)==1)  
    Y=zmax;  
else  
    Y = (1 - exp(-zetao*zmax))/(zetao);  
end
```

C.2 Impedance of a Wire Specimen

```
* Routine for computing the impedance of a wire *
```

```
Rdc = 3.639e-04; % DC resistance of the specimen wire %  
rho = 120e-8; % Electrical resistivity %  
ro = 1e-3; % Specimen radius %
```

```
mu_o = 4*pi*1e-7; % Magnetic permeability of free space %  
mu = mu_o*1; % Magnetic permeability of the conductor %
```

```
frequency = 1e6;  
angular_frequency = 2*pi*frequency;
```

```

alpha_squared = complex(0,angular_frequency*mu/rho);
beta = sqrt(-alpha_squared);

Jof = besselj(0,beta*ro);
J1f = besselj(1,beta*ro);
mfactor = (ro*beta*Jof)/(2*J1f);

Z = Rdc*mfactor;
resistance = real(Z);
reactance = imag(Z)/angular_frequency;
inductance = imag(Z)/angular_frequency;

```

C.3 Four-probe Impedance Measurement

* Routine for computing the potential difference between the pair of voltage probes in a four-probe impedance measurement *

```

T = 8.16e-3; % Specimen thickness %
xSp = 1e-3; % Probe spacing %
s = 1.5*xSp; % Source/sink location %
sigma = 8.34e5; % Electrical conductivity %
mu = 4*pi*1e-7; % Magnetic permeability %
F = load('FrequencyFile.txt');
Io = load('CurrentFile.txt');

fIndex = 1;
for (fIndex=1:26)
    f = F(fIndex,1);
    I = Io(fIndex,1);
    omega = 2*pi*f;
    k = sqrt(complex(0,omega*mu*sigma));
    kp = complex(0,1)*k;

    N = 85;
    nIndex = 0;
    zerothTerm = 0;
    firstTerm = 0;
    secondTerm = 0;
    thirdTerm = 0;
    fourthTerm = 0;
    fifthTerm = 0;
    sixthTerm = 0;
    seventhTerm = 0;

    % First summation with N terms %

```

```

for (nIndex=0:N)
    pSquared = (2*nIndex*T)^2;
    yMin1 = sqrt((2*s/3)^2 + pSquared);
    yMax1 = sqrt((4*s/3)^2 + pSquared);
    yMin2 = sqrt((4*s/3)^2 + pSquared);
    yMax2 = sqrt((2*s/3)^2 + pSquared);

    zerothTerm = zerothTerm + exp(2*kp*nIndex*T)*(log(2)-log(0.5));
    firstTerm = firstTerm +
(integralOfFirstTerm(kp,yMin1,yMax1,pSquared) -
    integralOfFirstTerm(kp,yMin2,yMax2,pSquared));
    % Links to the function integralOfFirstTerm() %

    secondTerm=secondTerm + (kp^2*pSquared)*
    (integralOfSecondTerm(kp,yMin1,yMax1,pSquared) -
    integralOfSecondTerm(kp,yMin2,yMax2,pSquared));

    % Links to the function integralOfSecondTerm() %

    thirdTerm = thirdTerm + (kp^2*pSquared)*
    (integralOfThirdTerm(kp,yMin1,yMax1,pSquared) -
    integralOfThirdTerm(kp,yMin2,yMax2,pSquared));

    % Links to the function integralOfThirdTerm() %

    mIndex = nIndex - 1;

% Second summation with (N-1) terms %
if (mIndex>=0)
    qSquared = (2*(mIndex+1)*T)^2;
    yMin3 = sqrt((2*s/3)^2 + qSquared);
    yMax3 = sqrt((4*s/3)^2 + qSquared);
    yMin4 = sqrt((4*s/3)^2 + qSquared);
    yMax4 = sqrt((2*s/3)^2 + qSquared);

    fourthTerm = fourthTerm + exp(2*kp*(mIndex+1)*T)*(log(2)-log(0.5));
    fifthTerm = fifthTerm + (integralOfFirstTerm(kp,yMin3,yMax3,qSquared) -
    integralOfFirstTerm(kp,yMin4,yMax4,qSquared));
    sixthTerm = sixthTerm + (kp^2*qSquared)*
    (integralOfSecondTerm(kp,yMin3,yMax3,qSquared) -
    integralOfSecondTerm(kp,yMin4,yMax4,qSquared));
    seventhTerm = seventhTerm + (kp^2*qSquared)*
    (integralOfThirdTerm(kp,yMin3,yMax3,qSquared) -
    integralOfThirdTerm(kp,yMin4,yMax4,qSquared));

end
end

```

```

V = ((-kp*I)/(2*pi*sigma))*(zerothTerm - firstTerm - secondTerm + thirdTerm +
fourthTerm -
    fifthTerm - sixthTerm + seventhTerm);
realV(fIndex,1) = 1e-3*real(V)/1e-6; % Answer in microV %
imagV(fIndex,1) = 1e-3*imag(V)/1e-6; % Answer in microV %
end

```

* Function to compute the definite integral of *

```

function X = integralOfFirstTerm(kp,yMin,yMax,pSquared)
a = sqrt(kp^2*pSquared);
xMax1 = -a-(kp*yMax);
xMax2 = a-(kp*yMax);
xMin1 = -a-(kp*yMin);
xMin2 = a-(kp*yMin);

if (a==0)
    firstTerm = (1/kp)*(-(exp(kp*yMax)/yMax) + (exp(kp*yMin)/yMin));
    secondTerm = integralOfFourthTermB(kp,yMin,yMax,0);
    X = firstTerm+secondTerm;
else
    firstTerm = exp(-a)*(expint(xMax1) - expint(xMin1));
    secondTerm = exp(a)*(expint(xMax2) - expint(xMin2));
    X = (1/(2*a))*(firstTerm - secondTerm);
end

```

* Function to compute the definite integral of *

```

function X = integralOfSecondTerm(kp,yMin,yMax,pSquared)
a = sqrt(kp^2*pSquared);
xMax1 = -a-(kp*yMax);
xMax2 = a-(kp*yMax);
xMin1 = -a-(kp*yMin);
xMin2 = a-(kp*yMin);
xMax3 = -(kp*yMax);
xMin3 = -(kp*yMin);

if (a==0)
    firstTerm = (-1/(2*(kp^2)))*((exp(kp*yMax)/(yMax^2)) - (exp(kp*yMin)/(yMin^2)));
    secondTerm = (-1/(2*kp))*((exp(kp*yMax)/yMax) - (exp(kp*yMin)/yMin));
    thirdTerm = (1/2)*integralOfFourthTermB(kp,yMin,yMax,0);
    X = firstTerm + secondTerm + thirdTerm;
else

```

```

firstTerm = expint(xMax3) - expint(xMin3);
secondTerm = exp(-a)*(expint(xMax1) - expint(xMin1));
thirdTerm = exp(a)*(expint(xMax2) - expint(xMin2));
X = (1/(a^2))*(firstTerm - (1/2)*(secondTerm + thirdTerm));
end
* Function to compute the definite integral of *

function X = integralOfThirdTermC(kp,yMin,yMax,pSquared)
if (pSquared==0)
    firstTerm = (-1/(3*(kp^3)))*((exp(kp*yMax)/(yMax^3)) - (exp(kp*yMin)/(yMin^3)));
    secondTerm = (-1/(6*(kp^2)))*((exp(kp*yMax)/(yMax^2)) -
(exp(kp*yMin)/(yMin^2)));
    thirdTerm = (-1/(6*kp))*((exp(kp*yMax)/yMax) - (exp(kp*yMin)/yMin));
    fourthTerm = (1/6)*integralOfFourthTermB(kp,yMin,yMax,0);
    X = firstTerm + secondTerm + thirdTerm + fourthTerm;
else
    firstTerm = (-1/kp)*((exp(kp*yMax)/yMax) - (exp(kp*yMin)/yMin));
    secondTerm = integralOfFourthTermB(kp,yMin,yMax,0);
    thirdTerm = integralOfFirstTermB(kp,yMin,yMax,pSquared);
    X = (-1/((kp^2)*pSquared))*(firstTerm + secondTerm - thirdTerm);
end

```

* Function to compute the definite integral of *

```

function X = integralOfFourthTermB(kp,yMin,yMax,pSquared)
a = sqrt(kp^2*pSquared);
xMax1 = -a-(kp*yMax);
xMax2 = a-(kp*yMax);
xMin1 = -a-(kp*yMin);
xMin2 = a-(kp*yMin);

firstTerm = exp(-a)*(expint(xMax1) - expint(xMin1));
secondTerm = exp(a)*(expint(xMax2) - expint(xMin2));
X = (-1/2)*(firstTerm + secondTerm);

```

C.4 Geometric Correction Factors for a DC Four-point Probe Measurement

* Routine for computing the potential difference between the pair of voltage probes for four-point probe measurement on a cylindrical specimen, PNR arrangement *

```

Ro = 8e-3; % Specimen radius %
d = 2e-3; % Specimen thickness %
s = 1e-3; % Probe spacing %
sigma = 8.34e5; % Electrical conductivity %

```

```

Io = 50e-3; % Source Current %
L = 0; % Probe Displacement %

r1 = sqrt((L^2)+((1.5*s)^2)); % Distance from origin to current-probe (1) %
r3 = sqrt((L^2)+((0.5*s)^2)); % Distance from origin to voltage-probe (3) %
r2 = r1; % Distance from origin to current-probe (2) %
r4 = r3; % Distance from origin to voltage-probe (4) %

theta1 = acos(L/r1);
theta3 = acos(L/r3);
theta2 = -theta1;
theta4 = -theta3;

mOrders = 600; % No. of orders of Bessel functions %
nRoots = 10000; % No. of roots for each order %

flag = 0
beta = load('nodesJmn'); % 600 x 10000 roots of Bessel functions-  $J_\mu(x)$ , for  $\mu = 1$  to 600
%

for (p=1:mOrders)
    Wm(1,p) = 0;
    Sm(1,p) = 0;
    for (q=1:nRoots)
        Vmn(p,q) = 0;
    end
end

flag = 1
A=FcoeffOfPotential_Fc(Io,sigma,Ro,d,r1,r2,theta1,theta2,beta,mOrders,nRoots);
% Links to the function FcoeffOfPotential_Fc() %

flag = 2

% Double summation for potential difference %

for (mIndex=1:mOrders)
    for (nIndex=1:nRoots)
        zTerm = (1 + exp(-2*beta(mIndex,nIndex)*d/Ro));
        rTerm = besselj(mIndex,beta(mIndex,nIndex)*r3/Ro);
        thetaTerm = 2*(A(mIndex,nIndex)*sin(mIndex*theta3));
        Vmn(mIndex,nIndex) = (zTerm*rTerm*thetaTerm);
        Wm(1,mIndex) = Wm(1,mIndex) + Vmn(mIndex,nIndex);
    end
end

```

```

for (pIndex=1:mOrders)
    for (ppIndex=1:pIndex)
        Sm(1,pIndex) = Sm(1,pIndex) + Wm(1,ppIndex); % Progressive outer sum %
    end
end

```

```

save('Amn_ro5mm_d2mm_L3mm_M600_N10000','A','-ASCII');
save('Smn_ro5mm_d2mm_L3mm_M600_N10000','Sm','-ASCII');
save('Vmn_ro5mm_d2mm_L3mm_M600_N10000','Vmn','-ASCII');
save('Wm_ro5mm_d2mm_L3mm_M600_N10000','Wm','-ASCII');

```

* Function to compute A_{mn} coefficients *

```

function A =
FcoeffOfPotential_Fc(Io,sigma,Ro,d,r1,r2,theta1,theta2,beta,mOrders,nRoots)
alpha = (2*Io)/(pi*sigma*(Ro^2));

```

```

for (m=1:mOrders)
    for (n=1:nRoots)
        A(m,n) = 0;
    end
end

```

% Amn and Bmn coefficients %
 % Bmn are all zero %

```

for (mIndex=1:mOrders) % mIndex corresponds to p in beta(p,q) %
    for (nIndex=1:nRoots)
        kpFactor = (beta(mIndex,nIndex)/Ro)*(1-exp(-2*beta(mIndex,nIndex)*d/Ro));

        LHS1 = (besselj(mIndex,beta(mIndex,nIndex)*r1/Ro)*sin(mIndex*theta1)) -
            (besselj(mIndex,beta(mIndex,nIndex)*r2/Ro)*sin(mIndex*theta2));
        RHS1 = ((beta(mIndex,nIndex)^2) -
            (mIndex^2))*(besselj(mIndex,beta(mIndex,nIndex))^2)*
            kpFactor/(beta(mIndex,nIndex)^2);
        A(mIndex,nIndex) = alpha*LHS1/RHS1;
    end
end

```

* Routine for computing the potential difference between the pair of voltage probes for four-point probe measurement on a cylindrical specimen, PAR arrangement- Double summation only *

```

Ro = 8e-3;

```

```

d = 2e-3;
s = 1e-3;
sigma = 8.34e5;
Io = 50e-3;
L = (3*Ro/5);

r2 = L;
r4 = r2 + s;
r3 = r4 + s;
r1 = r3 + s;

theta1 = 0;
theta2 = 0;
theta3 = 0;
theta4 = 0;

mOrders = 600;
nRoots = 10000;

flag = 0
beta = load('nodesJmn');
% 600 x 10000 roots of Bessel functions-  $J_\mu(x)$ , for  $\mu = 1$  to 600 %

for (p=1:mOrders)
    for (q=1:nRoots)
        Umn(p,q) = 0;
        Xm(1,q) = 0;
        SSmn(p,q) = 0;
    end
end

flag = 1
B = FcoeffOfPotential_Fe(Io,sigma,Ro,d,r1,r2,theta1,theta2,beta,mOrders,nRoots);
% Links to the function FcoeffOfPotential_Fe() %

flag = 2

% Double summation for potential difference %

for (mIndex=1:mOrders)
    for (nIndex=1:nRoots)
        zTerm = (1 + exp(-2*beta(mIndex,nIndex)*d/Ro));
        rTerm1 = besselj(mIndex,beta(mIndex,nIndex)*r3/Ro);
        rTerm2 = besselj(mIndex,beta(mIndex,nIndex)*r4/Ro);
        thetaTerm1 = B(mIndex,nIndex)*cos(mIndex*theta3);
        thetaTerm2 = B(mIndex,nIndex)*cos(mIndex*theta4);
    end
end

```

```

        Umn(mIndex,nIndex) = (zTerm*((rTerm1*thetaTerm1) - (rTerm2*thetaTerm2)));
        Xm(1,mIndex) = Xm(1,mIndex) + Umn(mIndex,nIndex);
    end
end

for (pIndex=1:mOrders)
    for (ppIndex=1:pIndex)
        SSmn(1,pIndex) = SSmn(1,pIndex) + Xm(1,ppIndex); % Progressive outer sum %
    end
end

save('SSmn_ro8mm_s1mm_d2mm_L1.6mm_M600_N10000_PAR','SSmn','-ASCII');
save('Bmn_ro8mm_s1mm_d2mm_L1.6mm_M600_N10000_122106','B','-ASCII');
save('Umn_ro8mm_s1mm_d2mm_L1.6mm_M600_N10000_PAR','Umn','-ASCII');
save('Xm_ro8mm_s1mm_d2mm_L1.6mm_M600_N10000_PAR','Xm','-ASCII');

```

* Routine for computing the potential difference between the pair of voltage probes for four-point probe measurement on a cylindrical specimen, PAR arrangement- Single summation only *

```

Ro = 8e-3;
d = 2e-3;
s = 1e-3;
sigma = 8.34e5;
Io = 50e-3;
L = (3*Ro/5);

r2 = L;
r4 = r2 + s;
r3 = r4 + s;
r1 = r3 + s;

theta1 = 0;
theta2 = 0;
theta3 = 0;
theta4 = 0;

nRoots = 10000;

flag = 0
gamma = load('nodesJon'); % 1 x 10000 roots of J0(x) %

for (q=1:nRoots)
    Vn(1,q) = 0;
    Sn(1,q) = 0;

```

```

end

flag = 1
C = FcoeffOfPotential_Fd(Io,sigma,Ro,d,r1,r2,theta1,theta2,gamma,nRoots);
% Links to the function FcoeffOfPotential_Fe() %

flag = 2

for (nIndex=2:nRoots)
    zTerm = (1 + exp(-2*gamma(1,nIndex)*d/Ro));
    rTerm = besselj(0,gamma(1,nIndex)*r3/Ro) - besselj(0,gamma(1,nIndex)*r4/Ro);
    Vn(1,nIndex) = (C(1,nIndex)*rTerm*zTerm);
    for (npIndex=2:nIndex)
        Sn(1,nIndex) = Sn(1,nIndex) + Vn(1,npIndex); % Progressive sum %
    end
end

save('Sn_ro8mm_d2mm_L4.8mm_N10000','Sn','-ASCII');
save('Vn_ro8mm_d2mm_L4.8mm_M600_N10000','Vn','-ASCII');

* Function to compute Bmn coefficients *

function B =
FcoeffOfPotential_Fe(Io,sigma,Ro,d,r1,r2,theta1,theta2,beta,mOrders,nRoots)
alpha = (2*Io)/(pi*sigma*(Ro^2));

for (m=1:mOrders)
    for (n=1:nRoots)
        B(m,n) = 0;
    end
end

% Bmn coefficients %

for (mIndex=1:mOrders) % mIndex is an index for beta(p,q) %
    for (nIndex=1:nRoots)
        kpFactor = (beta(mIndex,nIndex)/Ro)*(1-exp(-2*beta(mIndex,nIndex)*d/Ro));

        LHS2 = (besselj(mIndex,beta(mIndex,nIndex)*r1/Ro)*cos(mIndex*theta1)) -
            (besselj(mIndex,beta(mIndex,nIndex)*r2/Ro)*cos(mIndex*theta2));
        RHS1 = ((beta(mIndex,nIndex)^2) - --
(mIndex^2))*(besselj(mIndex,beta(mIndex,nIndex))^2)*
            kpFactor/(beta(mIndex,nIndex)^2);
        B(mIndex,nIndex) = alpha*LHS2/RHS1;
    end
end

```

end

* Function to compute C_{on} coefficients *

```
function C = FcoeffOfPotential_Fd(Io,sigma,Ro,d,r1,r2,theta1,theta2,gamma,nRoots)
alpha = (2*Io)/(pi*sigma*(Ro^2));
```

```
for (n=1:nRoots)
    C(1,n) = 0;
end
```

% Con coefficients %

```
for (nIndex=2:nRoots)
    kpFactor = (gamma(1,nIndex)/Ro)*(1-exp(-2*gamma(1,nIndex)*d/Ro));
    LHSo = besselj(0,gamma(1,nIndex)*r1/Ro) - besselj(0,gamma(1,nIndex)*r2/Ro);
    RHSo = 2*(besselj(0,gamma(1,nIndex))^2)*kpFactor;
    C(1,nIndex) = alpha*LHSo/RHSo;
end
```

* Routine for finding the first 2000 roots of $J_\mu(x)$, for $\mu = 1$ to 601 *

```
mOrders = 601; % 0 to 600 orders %
nRoots = 2000; % 1 to 2000 roots %
```

```
for (mIndex=1:mOrders)
    nuIndex = mIndex-1; % 0 to 600 %
    if (nuIndex==0)
        for (nIndex=1:nRoots)
            zeta(1,nIndex)=0; % 1x2000 array %
        end
    else
        for (nIndex=1:nRoots)
            kappa(nuIndex,nIndex) = 0; % 600x2000 array %
        end
    end
end
```

```
for (mIndex=1:mOrders)
    nuIndex = mIndex-1;
    if (nuIndex==0)
        zeta(1,:) = bessellMaxMin(nuIndex,nRoots);

        nuIndex
    else
```

```

        kappa(nuIndex,:) = besselMaxMin(nuIndex,nRoots);
    nuIndex
end
end

```

```

save('besselMaxMin_xo','zeta','-ASCII')
save('besselMaxMin_xmn','kappa','-ASCII')

```

* Routine for finding the maxima and minima of $J_m(x)$ *

```

function Y=besselMaxMin(m,nRoots)
delta = 0.005;
epsilon = 0.001;
X = [0:delta:100000];
nLim = (100000-lowerBound)/delta;
rootCount = 0;
xIndex = 1;

while ((rootCount<nRoots) & (xIndex<=(nLim-2)))
    deltaY1 = besselj(m,X(1,xIndex+1)) - besselj(m,X(1,xIndex));
    deltaY2 = besselj(m,X(1,xIndex+2)) - besselj(m,X(1,xIndex+1));
    deltaY3 = besselj(m,X(1,xIndex+3)) - besselj(m,X(1,xIndex+2));

    if ((deltaY1*deltaY3<0) & (abs(deltaY2)<=epsilon))
        rootCount = rootCount+1;
        Y(1,rootCount) = (X(1,xIndex+3) + X(1,xIndex+1))/2;
        xIndex = xIndex+1;
    end

    xIndex = xIndex + 1;
end

```

* Routine to find the convergence value from a series summation *

```

S = load('Sm_SP_ro10mm_d2mm_L4mm_M600_N10000');
x = [1:1:600];
xIndex = 1;
mmIndex = 1;
Mx(1,mmIndex) = 1;
My(1,mmIndex) = S(1,1);

% Finding maxima and minima of Smn %
while (xIndex<=598)
    deltaY1 = S(1,xIndex+1) - S(1,xIndex);

```

```

deltaY2 = S(1,xIndex+2) - S(1,xIndex+1);
if ((deltaY1*deltaY2)<0)
    mmIndex = mmIndex+1;
    Mx(1,mmIndex) = xIndex+1;
    My(1,mmIndex) = S(1,xIndex+1);
    xIndex = xIndex+1;
else
    xIndex = xIndex+1;
end
end

% Finding mid-points of My %
sizeOfMy = size(My,2);
for (yIndex=1:(sizeOfMy-1))
    midMy(1,yIndex) = (My(1,yIndex)+My(1,yIndex+1))/2;
    midMx(1,yIndex) = (Mx(1,yIndex)+Mx(1,yIndex+1))/2;
end

% Finding maxima and minima of midMy %
zIndex = 1;
nnIndex = 1;
Nx(1,nnIndex) = midMx(1,1);
Ny(1,nnIndex) = midMy(1,1);
midLength = size(midMy,2);

while(zIndex<=(midLength-2))
    deltaY3 = midMy(1,zIndex+1)-midMy(1,zIndex);
    deltaY4 = midMy(1,zIndex+2)-midMy(1,zIndex+1);
    if ((deltaY3*deltaY4)<0)
        nnIndex = nnIndex+1;
        Nx(1,nnIndex) = midMx(1,zIndex+1);
        Ny(1,nnIndex) = midMy(1,zIndex+1);
        zIndex = zIndex+1;
    else
        zIndex = zIndex+1;
    end
end

% Finding mid-points of Ny %
sizeOfNy = size(Ny,2);
for (yIndex=1:(sizeOfNy-1))
    midNy(1,yIndex) = (Ny(1,yIndex)+Ny(1,yIndex+1))/2;
    midNx(1,yIndex) = (Nx(1,yIndex)+Nx(1,yIndex+1))/2;
end

% Finding maxima and minima of midNy %

```

```

zIndex = 1;
ppIndex = 1;
Px(1,ppIndex) = midNx(1,1);
Py(1,ppIndex) = midNy(1,1);
midLengthb = size(midNy,2);

while(zIndex<=(midLengthb-2))
    deltaY3 = midNy(1,zIndex+1)-midNy(1,zIndex);
    deltaY4 = midNy(1,zIndex+2)-midNy(1,zIndex+1);
    if ((deltaY3*deltaY4)<0)
        ppIndex = ppIndex+1;
        Px(1,ppIndex) = midNx(1,zIndex+1);
        Py(1,ppIndex) = midNy(1,zIndex+1);
        zIndex = zIndex+1;
    else
        zIndex = zIndex+1;
    end
end

% Finding mid-points of Py %
sizeOfPy = size(Py,2);
for (yIndex=1:(sizeOfPy-1))
    midPy(1,yIndex) = (Py(1,yIndex)+Py(1,yIndex+1))/2;
    midPx(1,yIndex) = (Px(1,yIndex)+Px(1,yIndex+1))/2;
end

% Finding maxima and minima of midPy %
zIndex = 1;
ooIndex = 1;
Ox(1,ooIndex) = midPx(1,1);
Oy(1,ooIndex) = midPy(1,1);
midLengthc = size(midPy,2);

while(zIndex<=(midLengthc-2))
    deltaY3 = midPy(1,zIndex+1)-midPy(1,zIndex);
    deltaY4 = midPy(1,zIndex+2)-midPy(1,zIndex+1);
    if ((deltaY3*deltaY4)<0)
        ooIndex = ooIndex+1;
        Ox(1,ooIndex) = midPx(1,zIndex+1);
        Oy(1,ooIndex) = midPy(1,zIndex+1);
        zIndex = zIndex+1;
    else
        zIndex = zIndex+1;
    end
end
end

```

```

% Finding mid-points of Oy %
sizeOfOy = size(Oy,2);
for (yIndex=1:(sizeOfOy-1))
    midOy(1,yIndex) = (Oy(1,yIndex)+Oy(1,yIndex+1))/2;
    midOx(1,yIndex) = (Ox(1,yIndex)+Ox(1,yIndex+1))/2;
end

% Plotting %
plot(x,S)
hold on
plot(Mx,My,'or')
plot(midMx,midMy,'-k')
plot(Nx,Ny,'db')
plot(midNx,midNy,'-g')
plot(Px,Py,'sk')
plot(midPx,midPy,'-m')
plot(Ox,Oy,'ok')
plot(midOx,midOy,'-r')

```

REFERENCES

1. C. T. Sims and W. C. Hagel, *The Superalloys*, John Wiley & Sons, Inc., 1972.
2. W. F. Smith, *Structure and Properties of Engineering Alloys*, McGraw-Hill Inc., New York, 1993.
3. S. Mannan, S. Patel and J. deBarbadillo, Special Metals Corporation, Huntington.
4. S.-I. Komazaki, T. Shoji, I. Abe and I. Okada, *Nondestructive Characterization of Materials*, 1999, **IX**, 113-119.
5. R. Ferragut, A. Somoza and I. Torriani, *Materials Science and Engineering*, 2002, **A 334**, 1-5.
6. J. W. Martin, R. D. Doherty and B. Cantor, *Stability of Microstructure in Metallic Systems*, Cambridge University Press, New York, 1997.
7. C. Panseri and T. Federeghi, *Acta Metallurgica*, 1960, **8**, 217-238.
8. R. J. White, S. B. Fisher, K. M. Miller and G. A. Swallow, *Journal of Nuclear Materials*, 1974, **52**, 51-58.
9. N. W. Ashcroft and N. D. Mermin, *Solid State Physics*, Saunders College, Philadelphia, 1976.
10. R. C. Dorward, *Materials Science and Technology*, 1999, **15**, 1133-1138.
11. A. J. Ardell, *Materials Science and Engineering A*, 1997, **A238**, 108-120.
12. R. A. Swalin, *Thermodynamics of Solids*, John Wiley and Sons Inc., New York, 1972.
13. B. Noble and S. E. Bray, *Materials Science and Engineering*, 1999, **A266**, 80-85.
14. F. Yu and P. B. Nagy, *Journal of Applied Physics*, 2004, **96**, 1-10.
15. F. Yu and P. B. Nagy, *Journal of Applied Physics*, 2004, **95**, 1-12.
16. A. I. Lavrentyev and W. A. Veronesi, *Review of Quantitative Nondestructive Evaluation*, 2002, **21**, 1659-1666.
17. P. Haldipur, F. J. Margetan and R. B. Thompson, *Review of Quantitative Nondestructive Evaluation*, 2003, **22**, 1355-1362.

18. J. Kang, J. Qu, A. Saxena and L. Jacobs, *Review of Quantitative Nondestructive Evaluation*, 2004, **23**, 1248-1255.
19. M. V. Nathal, R. A. Mackay and R. G. Garlick, *Scripta Metallurgica*, 1988, **22**, 1421-1424.
20. D. Q. Wang, S. S. Babu, E. A. Payzant, P. G. Radaelli and A. C. Hannon, *Metallurgical and Materials Transactions*, 2001, **32 A**, 1551-1552.
21. A. Royer and P. Bastie, *Acta Metallurgica*, 1997, **36**, 1151-1159.
22. P. R. Jemian, R. A. Gerhardt and G. G. Long, *Anomalous USAXS investigation of Ni-base superalloys, Unpublished Work*.
23. A. Baldan, *Journal of Materials Sciences*, 2002, **37**, 2379-2305.
24. A. J. Ardell, *Acta Metallurgica*, 1972, **20**.
25. K. B. S. Rao, V. Seetharaman, S. L. Mannan and R. P., *Materials Science and Engineering*, 1983, **58**, 93-106.
26. R. A. Stevens and P. E. J. Flewitt, *Materials Science and Engineering*, 1979, **37**, 237-247.
27. A. Ges, O. Fornaro and H. Palacio, *Journal of Materials Science*, 1997, **32**, 3687-3691.
28. S. Q. Xiao and P. Haasen, *Acta Metallurgica Materialia*, 1991, **39**, 651-659.
29. A. J. Ardell, *Scripta Metallurgica et Materialia*, 1990, **24**, 343-346.
30. G. Petzow, *Metallographic Etching*, ASM International, Materials Park, Ohio, 2001.
31. *Keithley Low Level Measurements Handbook*, Keithley Instruments Inc.
32. H. Topsoe, *Geometric Correction Factors in Four Point Resistivity Measurement* 1968.
33. L. J. Swartzendruber, *Solid State Electronics*, 1964, **7**, 413-422.
34. A. Uhlir Jr., *The Bell System Technical Journal*, 1955, 105-128.
35. L. G. Valdes, *Proc. I. R. E.*, 1954, **42**, 420-427.
36. J. R. Gosselin, P. Rochon and N. Gauthier, *American Journal of Physics*, 1981, **50**, 440-443.

37. L. Jansak, *Review of Scientific Measurements*, 1999, **70**, 3087-3091.
38. *Operating Manual for SR830 DSP Lock-in Amplifier*, Stanford Research Systems, Sunnyvale, California, 2005.
39. N. Bowler, *Journal of Applied Physics*, 2004, **96**, 4607-4613.
40. E. L. Megchiche, S. Perusin, J.-C. Barthelat and C. Mijoule, *Physical Review B*, 2006, **74**.
41. Z. Hashin and S. Shtrikman, *Journal of Applied Physics*, 1962, **33**, 3125-3131.
42. Y. Terada, K. Ohkubo and T. Mohri, *Journal of Applied Physics*, 1996, **81**, 2263-2268.
43. E. A. Brandes and G. B. Brook, eds., *Smithells Metals Reference Book*, Reed Educational and Professional Publishing Ltd., Boston, 1992.
44. J. I. Goldstien, D. E. Newbury, P. Echlin, D. C. Joy, C. Fiori and E. Lifshin, *Scanning Electron Microscopy and X-ray Micoanalysis*, Plenum Press, New York, 1981.
45. D. A. Porter and K. E. Easterling, *Phase Transformations in Metals and Alloys*, Nelson Thornes, Ltd., Cheltenham, UK, 2001.
46. V. S. K. G. Kelekanjeri, L. K. Moss and R. A. Gerhardt, *in preparation for Acta Materialia*, 2007.
47. L. J. Giacoletto, *IEEE Transactions on Magnetics*, 1996, **32**, 220-229.
48. W. N. Cottingham and D. A. Greenwood, *Electricity and Magnetism* Cambridge University Press, New York, 1991.
49. E. Hallen, *Electromagnetic Theory* Wiley & Sons Inc., 1962.
50. H. J. Weber and G. B. Arfken, *Essential Mathematical Methods for Physicists* Elsevier, San Diego, 2004.
51. M. Abramowitz and I. A. Stegun, eds., *Online Version of Handbook of Mathematical Functions*, U. S. Government Printing Office, Washington, 1964.
52. A. Gray and G. B. Mathews, *A Treatise on Bessel Functions and Their Applications to Physics*, Macmillan and Co., Limited, London, 1952.
53. E. Kreyszig, *Advanced Engineering Mathematics* Wiley Eastern Limited, New Delhi, 1994.

54. www.mathworld.com.
55. M. M. Ney, in *IEEE Transactions on Electromagnetic Compatibility*, 1991, p. 321.
56. G. I. Costache and M. M. Ney, in *Symposium on Antenna Technology and Applied Electromagnetics*, Winnipeg, Canada, 1988.
57. H. B. G. Casimir and J. Ubbink, *Philips Technical Reviews*, 1967, **28**.
58. *User's Guide to Electromagnetics Module, FEMLAB 3.1* COMSOL AB, 2004.
59. *Handbook on Low Level Measurements*, Keithley Instruments Inc.
60. F. M. Smits, *The Bell System Technical Journal*, 1958, 711-718.
61. Y. Ju, Ju, B-F., and Saka, M., *Review of Scientific Instruments*, 2005, **76**.
62. L. Shiraki, T. Nagao and S. Hasegawa, *Surface Review and Letters*, 2000, **(5) and (6)**.
63. L. J. van der Pauw, *Philips Research Reports*, 1958, **13**.
64. V. I. Golubev, Polyakov, N. N., and Pavlov, N. I., *translated from Zavodskaya Laboratoriya*, 1972, **38**.
65. M. Yamashita, *Japanese Journal of Applied Physics*, 1987, **26**, 1550-1554.
66. M. Yamashita, *Japanese Journal of Applied Physics*, 1988, **27**, 1317-1321.
67. *User's guide to COMSOL Multiphysics 3.2*, COMSOL AB, 2005.
68. M. A. Logan, *The Bell System Technical Journal*, 1961, **40**.
69. N. Bowler, *Journal of Applied Physics*, 2004, **95**, 344-348.
70. V. A. Mitrofanov, *Russian Journal of Non-destructive Testing*, 1998, **34**, 183-189.
71. *Operating Manual for Electrostatic Force Microscopy, XE Series SPM*, PSIA Inc., Santa Clara, California, 2004.
72. EFM Mode Notes, <http://www.psiainc.com>.
73. D. A. Bonnell, *Scanning Probe Microscopy and Spectroscopy*, John Wiley & Sons Inc., New York, **2001**.

74. I-AFM Mode Notes, <http://www.psiainc.com>.
75. *Operating Manual for External I-AFM, XE Series SPM*, PSIA Inc., Santa Clara, California, 2004.

VITA

The author was born in the south Indian coastal city of Chennai on 22nd July, 1979. He received his primary and secondary school education in Hyderabad, situated in south central India, known for its diverse culture and rich cuisine. His genuine interests in physical sciences paved the way for college level education in St. Mary's Junior College, Hyderabad, majoring in Maths, Physics and Chemistry. During his school and college years, the author became proficient in Telugu, Hindi and English and articulate in Tamil. He took the Joint Entrance Examinations for entry into the Indian Institute of Technology, one of the premier institutes for engineering education in India, after a two-year intensive preparation during his college term. He joined the Metallurgical Engineering program at IIT, Chennai and graduated with a Bachelor of Technology in July 2000. With a foundation in Metallurgy, he decided to pursue his graduate studies in Materials Science and Engineering at Georgia Institute of Technology, Atlanta. He graduated with a Masters degree in December 2002, during which time, he conducted research on the Deposition of Alpha-Alumina using Combustion CVD, under the guidance of Dr. Brent Carter. In May 2003, after his PhD qualifiers, he teamed up with Dr. Rosario Gerhardt, also in the School of Materials Science and Engineering at Georgia Tech, for conducting doctoral research. His doctoral research deals with Non-Destructive Electrical Studies of Controlled Waspaloy Microstructures and will be graduating in May 2007.